New Concepts in Energy and Mass Transport within Carbon Nanotubes

by

Wonjoon Choi

B.S. Mechanical and Aerospace Engineering
Seoul National University, Republic of Korea, 2003

SUBMITTED TO THE DEPARTMENT OF MECHANICAL ENGINEERING IN PARTIAL FULFILLMENT OF THE REQUIREMENTS FOR THE DEGREE OF

DOCTOR OF PHILOSOPHY IN MECHANICAL ENGINEERING
AT THE
MASSACHUSETTS INSTITUTE OF TECHNOLOGY

FEBRUARY 2012

Signature of Author:_____
Department of Mechanical Engineering
January 20, 2012

Certified by:_____
Michael S. Strano
Professor of Chemical Engineering
Thesis Supervisor

Certified by:_____
Sang-Gook Kim
Professor of Mechanical Engineering
Committee Chair

Accepted by:_____
David E. Hardt
Chairman, Department Committee on Graduate Students

New Concepts in Energy and Mass Transport within Carbon Nanotubes

by

Wonjoon Choi

Submitted to the Department of Mechanical Engineering
on January 20, 2012 in Partial Fulfillment of the
Requirements for the Degree of Doctor of Philosophy in
Mechanical Engineering

Abstract

The unique structure of carbon nanotubes (CNTs) contributes to their distinguished properties, making them useful in nanotechnology. CNTs have been explored for energy transport in next-generation, such as light-emitting diodes, field-effect transistors, and phonon wave guides due to their high axial electrical and thermal conductivity. Also, their sub-nanometer scale with atomically smooth surfaces is promising for selective mass transport in nanoscale, such as molecular transport, selective gas permeation, and nanofluidics.

The first part of this thesis considers CNTs as substrates for guided chemical reactivity and thermal waves for energy generation. Coupling an exothermic chemical reaction with a nanowire possessing a high axial thermal conductivity creates a self-propagating reactive wave. Such waves are realized using a 7-nm cyclotrimethylene-trinitramine (TNA) annular shell around a CNT and are amplified by 10^4 times the bulk TNA value, propagating more than 2 m/s, with an effective thermal conductivity of 1.28 ± 0.2 kW/m/K at 2860 K. Thermally excited carriers in the direction of the propagating reaction produces a concomitant electrical pulse of high specific power, as large as 7 kW/kg, that we identify as a thermopower wave. The specific power increases with a decreasing system size, resulting in usually efficient sub-micron and nano-sized pulse power sources.

In the second portion, we develop a nanopore platform using the interior of a single walled carbon nanotube (SWNT) for study of single ion transport. Such pores can undergo a resonance in ion transport such that coherent waveforms are generated (CR). The asymmetric electrostatic barriers at their ends show that above the threshold bias, traversing the nanopore end is not rate limiting and that the pore blocking behavior of two parallel nanotubes follows an idealized Markov process. We report two channels undergoing this CR simultaneously, the dynamics of ion transport for different cations (Li+, Na+, K+, Cs+) and the effect of varying the applied voltage on transport across the SWNT channel. Finally, the diameter and temperature dependence (1-2 nm) of ion transport shows the distinct trend in dwell time and blockade current that study its transfer mechanism by proton 'hop' and 'turn', and single ion transport.

Thesis Supervisor : Michael S.Strano
Title : Professor of Chemical Engineering

Acknowledgement

I would hereby like to acknowledge my colleagues, friends and family. Without help from them during long journey for my Ph.D study, this work would not have been completed.

First, I would like to thank my advisor, Professor Michael Strano who has motivated and encouraged me every time not to give up when I was confronted with a lot of difficulties in research. When I started my work in graduate school, I was in difficulty to find my topics as well as the future directions. However, he believed in me and opened his mind for new stuff that I brought, and it was the starting point of this work. Also, I really appreciate him giving me a chance to join his lab, even though my background and institution were in mechanical engineering. It was risky choice, but his guidance has lead me to the end of my Ph.D work. He has taught me how to I think about and look at the problems, as well as the insight for research. Also, he was always happy when I reported some interesting results. It was quite impressive for me, and I felt like he really loved the research, and it made me move forward.

Also, I would like to express my gratitude to my thesis committee members, Professor Sang-Gook Kim and Professor Rohit Karnik for valuable comments with new insights and supports for my graduation. They helped me to find new analysis about my experimental dataset. Also, they have cared about my graduation as well as the future career paths. They provided good recommendation during the job search period for my postdoc, and it was really helpful for me.

Next, I appreciate many people in our lab. The seniors in the lab at the time that I joined the lab, Paul Barone, Esther Jeng, Daniel Heller, Nitish Nair, Richa Sharma and Hong Jin helped me to settle in the lab, and taught me many valuable things for my graduate work. Also, my coworkers, Joel Abrahamson, Steven Shimizu, Darin Bellisario and Zack Ulissi who worked together gave me the opportunities for great discussions and new insights for many experiments and simulations.

Many koreans in our lab always supported my life for 6 years. Postdocs, Jonghyun Choi, Woojae Kim, Jaehee Han, Changsik Song, Joonhyun Baik, Jongho Kim, Moonho Ham, Jin-Ho Ahn, Hyeonseok Yoon, Sangwook Kang, Byung-Seon Kong, J, Taeyun Kwon and Kyungsuk Yum gave many advices and encouragement to me. Former graduate student, Changyoung Lee motivated me to join Strano Research Group, and guided my research and career path as well as the 2nd part of my thesis. I deeply appreciate his support and advice for both research and private stuff. Also, I would like to thank Professor Seunghyun Baik who was a coworker for the 1st part of my thesis, and the colleague at the end of my graduate life. I was not alone with them. I shared worries of my own with them, and their warm comforts made me overcome many difficulties.

Also, I would like to thank my friends in KGSA, KGSA-ME, and Boston 3040. When I needed to take a rest from my research, they have always provided many fun stuff and great gathering with good friends. They refreshed me, and I really enjoyed all moments with my friends.

Finally, I owe my large debt of gratitude for my family. My older sisters have always taken care of me, and encouraged me to overcome many obstacles. I deeply appreciate they have always cared about our family issues even after their marriages. My parents have always devoted themselves to me with unconditional love. Also, they always believed and supported me. Without their support, I would not have accomplish anything. Also, without them, any accomplishment is not meaningful for me.

Table of Contents

List of Figures

List of Tables

1. Introduction, Background and Thesis Objectives

1.1. Introduction to Carbon Nanotubes (CNTs)

Elemental carbon can be classified into different allotropes based on the nature of its bonding. The chemical bonding of the well-known diamond consists of sp^3 hybridization in a tetrahedral lattice arrangement. In graphite, carbon forms sp^2 hybridization in two-dimensional sheets of a hexagonal lattice called graphene, which are stacked on top of each other, bound by weak van der Waals forces. Elemental carbon in sp^2 hybridization can form many other intriguing structures, like the cylindrical shape seen in carbon nanotubes (CNTs). In 1991, Iijima first found tens of graphitic shells with an adjacent shell separation of ~ 0.34 nm, diameters of ~ 1 nm and a high length-to-diameter ratio, which came to be known as multi-walled carbon nanotubes (MWNTs).[1] Two years later, Iijima, Ichihashi and Bethune et al. synthesized what are now known as single-walled carbon nanotubes (SWNTs).[2] The SWNT consists of a graphene sheet seamlessly wrapped into a cylindrical tube. The MWNT comprises an array of such nanotubes that are concentrically nested like rings of a tree trunk.[3] The diameter of a CNT is on the order of a few nanometers, approximately 5×10^4 times smaller than the width of a human hair, while its tube length can be up to several millimeters. Therefore, their length-to-diameter ratio(aspect ratio) can be up to 10^8:1, which is significantly larger than any other material.[3] Unlike graphite that exists in 3-D bulk, the cylindrical arrangement of an ultra-thin carbon layer constitutes a 1-D cylinder.

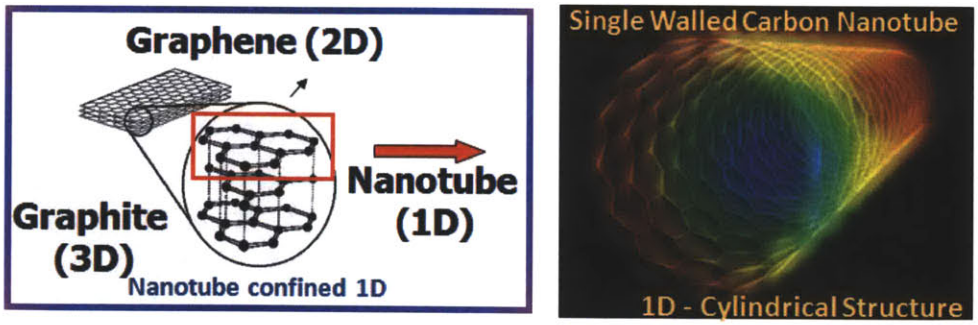

Figure 1.1. Dimensionalities of carbon materials and CNTs. The graphene sheet can be rolled more than one way, and it can produce different types of carbon nanotube depending on its chirality. Since it is confined in 2-directions, and open only 1-direction, it has very special thermal and electrical properties. (Right figure is from Science Photo Library).

1.1.1. CNT Basic Structure

The structure of CNTs has been verified by High Resolution Transmission Electron Microscopy (HRTEM) and Scanning Tunneling Microscopy (STM) techniques.[4] The structure of a SWNT can be conceptualized by 'rolling up' an atomic layer of graphene and 'gluing' in back to itself to form a seamless cylinder. Since graphene comprises an infinite atomic sheet, there are many ways of matching up the carbon atoms along the edge to construct a CNT.

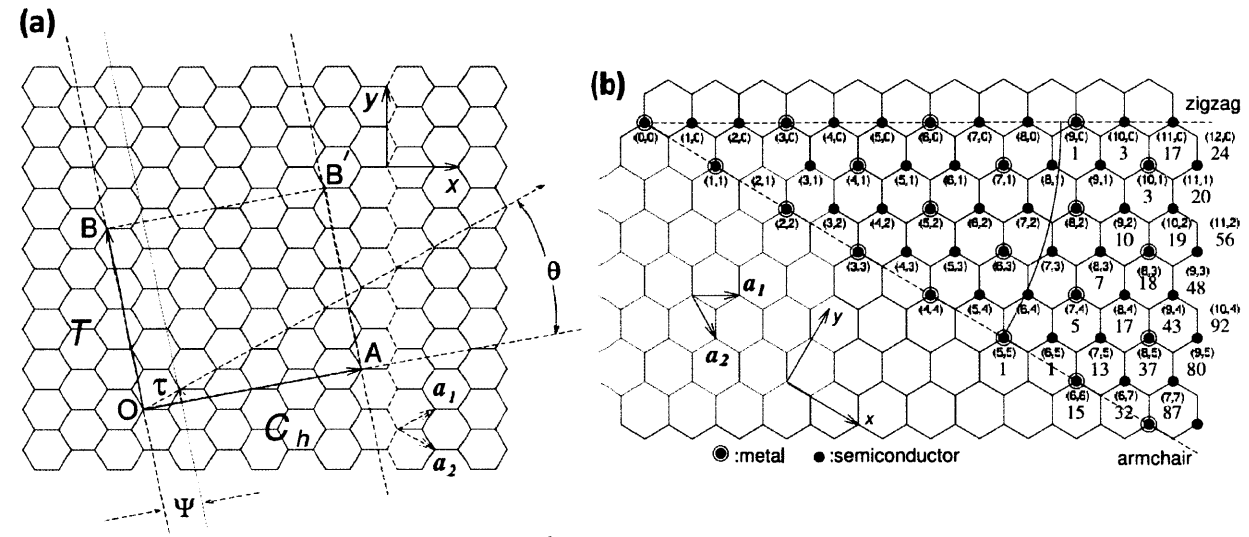

Figure 1.2. Formation and structure of CNTs [3] (a): A graphene sheet is chosen to be rolled up in such a way that the chiral vector $\overrightarrow{OA}$ will end up on top of each other. Also shown are the hexagonal unit vectors a_1 and a_2 that span the infinite honeycomb crystal lattice. The angle θ is the *chiral angle*. (b): Each pair of integers (n, m)[5] denotes a CNT created by joining the points (0,0) and (n, m). The encircled dots denote metallic CNTs, and the small dots are for semiconducting CNTs.[6]

In Figure 1.2a, the choice of a vector $\overrightarrow{OA}$ in the plane specifies a particular direction for rolling the sheet. $\overrightarrow{OA}$ is called the *chiral vector* and denoted by a pair of integer indices (n,m) where O-A = $na_1 + ma_2$. The segment O-A will constitute the circumference of the tube, and the tube axis will be along O-B (or A-B'), the length of which can be chosen arbitrarily. The diagram is constructed for (4,2) nanotube. Symmetry shows that we only need to consider n≥m because (2,4) nanotube will have the same circumference as (4,2) nanotube. A particular choice of (n,m) uniquely determines the diameter of a CNT. The diameter d_t is given by:

$$d_t = \frac{\sqrt{3}a_{C-C}\sqrt{m^2+mn+n^2}}{\pi} = \frac{C_h}{\pi} \qquad (1\text{-}1)$$

where C_h is the length of its circumference and a_{C-C} refers to the C–C bond length (=1.42A). The chiral angle is given by

$$\theta = \tan^{-1}\left(\frac{\sqrt{3}n}{2m+n}\right) \qquad (1\text{-}2)$$

It turns out that in the actual synthesis process, SWNTs cannot take a diameter larger than ~5 nm, putting a practical upper bound on the (n,m) indices. The diameter of the outermost cylinder of MWNTs can range up to ~80 nm. Figure 1.2b shows some of the possible small CNTs that can be created. The tubes with m=0 are called *zigzag* (θ=0) and the tubes with n=m are called *armchair* (θ=30°). Other nanotubes are called *chiral* (0<θ<30°). The names *armchair* and *zigzag* simply reflect the shape of the open edges of the CNTs (Figure 1.3).[7] The (n,m) indices also determine the electronic type for CNTs. For a given choice of n and m, if n−m is a multiple of 3, that CNT is metallic. If n−m is not a multiple of 3, then it is semiconducting (Figure 1.2b).

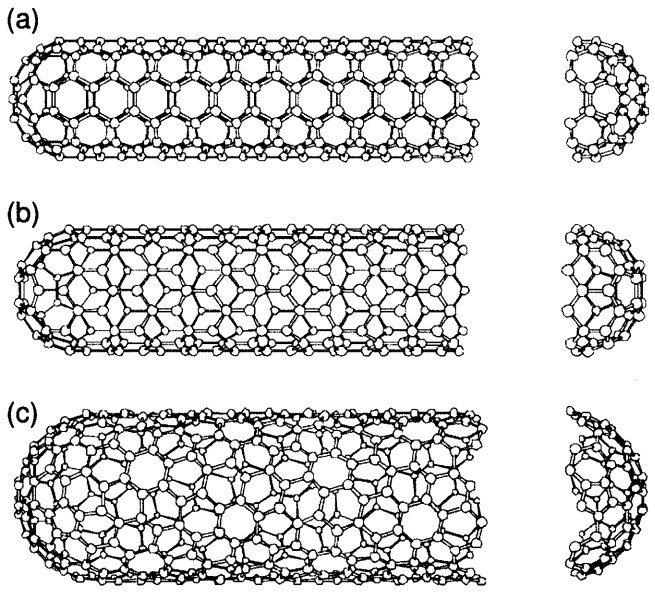

Figure 1.3. The distinct shapes[3] of the armchair (a), zigzag (b) and chiral (c) CNTs

1.1.2. Synthesis of CNTs via Chemical Vapor Deposition (CVD)

There are different methods of synthesizing CNTs, including arc discharge, laser ablation, high pressure carbon monoxide (HiPCO), and chemical vapor deposition (CVD).[8] Of all, CVD is the most effective method for the controlled structures of CNTs because it allows for a relatively desirable yield, producing vertically aligned, rather than randomly oriented, CNTs with little defect (Figure 1.4).[8] CVD takes a bottom-up approach, in which the 'root' catalysts of metal-nanoparticles are exposed to carbon sources at a high temperature to give rise to CNT 'stems'. First, a substrate is prepared with a layer of metal catalyst particles, such as nickel, cobalt, iron, or a combination of these, and is heated to approximately 700°C.[8] Then, two kinds of gases are bled into the reactor: a process gas, such as ammonia, argon, and nitrogen, which constitutes the surrounding atmosphere and an actual hydrocarbon source, such as acetylene, ethylene, ethanol or methane. Subsequently, in a process called pyrolysis, the hydrogen carbon source is decomposed by plasma or resistivity metal coil and is made to contact with the metal catalyst to initiate the growth of CNTs.

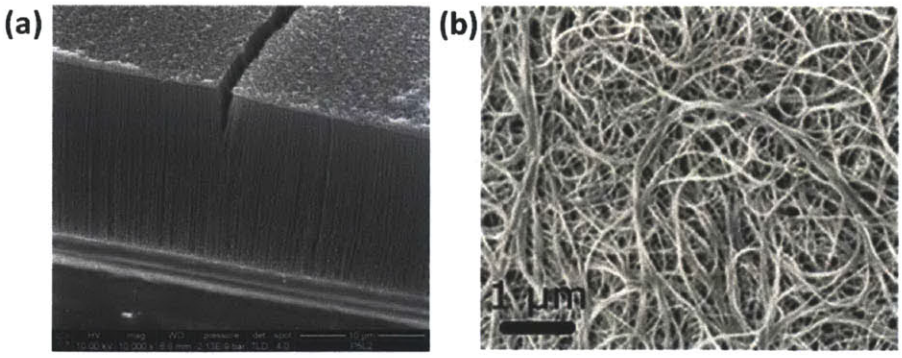

Figure 1.4. Comparison of grown CNTs in CVD and other methods. [8-9] (a) Highly, vertically aligned SWNTs fabricated by CVD. (b) Unaligned, mixed SWNTs produced by arc discharge

In 2006, Brukh and Mitra studied reaction pathways of CVD with C_2H_4 as the carbon precursor.[10] It is now commonly accepted that ethylene goes through the following reactions to produce elemental carbon. First, C_2H_4 decomposes to form acetylene (C_2H_2) via:

$$C_2H_{4\,(g)} \Rightarrow C_2H_{2\,(g)} + H_{2\,(g)} \qquad (1\text{-}3)$$

Acetylene then reacts with hydrogen radical (H) to form vinyl radical (CH_3) and elemental carbon (C), which will end up as either CNTs or non-tubular carbon:

$$C_2H_{2\,(g)} + H_{(g)} \Rightarrow CH_{3\,(g)} + C_{(g)} \qquad (1\text{-}4)$$

It turns out that the identity of CNT formation does not solely depend on the nature of hydrocarbon source, but it also depends on other parameters, such as properties and composition method of the metal catalyst, metal-support interactions, and reaction conditions like temperature, pressure, inert/hydrocarbon gas ratio and gas flow rate.[8] However, with present technology, researchers have limited control of the parameters, making it difficult to synthesize one specific type of CNT exclusively. Thus, a proper identification process is needed to extract the target CNT from a mix of all sorts of newly synthesized CNTs.

1.2. Carbon Nanotubes Properties

The unique structure of CNTs contributes to their distinguished thermal and electrical properties, making them potentially useful in nanotechnology, electronics, optics and other fields of materials science. Especially, CNTs have been explored as the main components of energy transport in next-generation devices, such as light-emitting diode (LED), field-effect transistor (FET), thermal rectifier[11], and phonon wave guide[12] due to their high axial electrical

conductivity[13-14] and thermal conductivity[15-17] in high aspect ratio, 1-D structures[18-19]. Also, sub-nanometer scale with the atomically smooth surfaces[20] have proposed CNTs as ideal candidates for mass transport in nanoscale, such as molecular transport, selective gas permeation, and nanofluidics.

1.2.1. CNTs Thermal Properties

Thermal properties of a substance can be explained by a combination of phonon effects and electron excitations at varying temperatures. In quantum mechanics, phonon refers to a quasiparticle characterized by lattice vibrations of periodic and elastic crystal structures of solids, similar to the mechanism of spring oscillation.[21-22] In CNTs, phonon effects dominate thermal properties, especially at low temperatures, where the contribution of electron energy levels becomes insignificant. This section will thus focus primarily on the phonon effects, and the electron excitations in CNTs will be discussed in greater detail in the next section.

At moderate temperatures, the phonon contribution to the specific heat[23] is given by:

$$C_{ph} = \frac{3k_B{}^2T}{\pi v\hbar\rho_m} \times \frac{1}{3}\pi^2 \qquad (1\text{-}5)$$

where ħ: Planck's constant, ρ_m : mass per unit length of CNT, k_B : Boltzmann constant, T : temperature in Kelvin, v : acoustic phonon velocity ($\approx 10^4$ m/s) . [21] Acoustic phonon velocity refers to the rate at which phonons propagate in CNTs. At low temperatures, CNTs have an electronic heat capacity that is linear in temperature, with a magnitude given by:

$$C_e = \frac{4\pi k_B{}^2T}{3\hbar v_F\rho_m} \qquad (1\text{-}6)$$

v_f : Fermi velocity. Fermi velocity refers to the fastest velocity of electrons in the conducting CNT with a kinetic energy equal to the Fermi energy, or the highest occupied quantum state.[21] The ratio between the phonon and electron specific heats at low temperature can be calculated as:

$$\frac{C_{ph}}{C_e} \approx \frac{v_F}{v} \approx 10^2 \qquad (1\text{-}7)$$

The phonon contribution will dominate the electron contribution by a hundred-fold at low temperatures. Figure 1.5 shows that the specific heats of four carbon-based materials diverge substantially at lower temperatures. In the low temperature region, their distinct phonon structures uniquely determine their specific heats, because quantum effects, specifically, the phonon effects dominate their thermal interactions. C(T) of isolated CNT is linear in T, marking a direct signature of the 1-D phonon structure. Interlayer couplings in graphite and similar intertube-couplings in strongly bundled SWNTs (rope) depresses the C(T) at low temperatures. In 3-D bulk form, the carriers of thermal energy are more likely to diffract in different directions, making it easier to diffuse heat, lowering the specific heat. At temperatures above ~ 100 K, the specific heats of all four materials are less distinguished from one another despite their distinct phonon structures because other molecular-level excitation factors outweigh the low-scale quantum effect. The graph predicts that the four different materials will all share a similar heat capacity at room temperature. The calculation of the heat capacity is essential in proving the clearly superior thermal conductivity of CNTs,

$$\kappa = \frac{1}{3}(\rho c_v) v \Lambda \qquad (1\text{-}8)$$

where C_v : heat capacity, v : particle velocity, Λ: mean free path. Mean free path refers to the longest distance a phonon can advance without "colliding" into another particle. The value for

the mean free path of CNTs is significantly higher than that of any other bulk system because the CNTs' 1-D structure allows for "ballistic thermal transport" in which phonons are less likely to collide with one another over 0.5-1.5 μm. [24] When compared with 3-D graphite or even other non-carbon substances, the extraordinarily long mean free path of CNTs serves as a deciding factor resulting in their superior heat conductivity. Indeed, heat conductivity of CNTs mounts up to over 3000 W/mK, while that of most metals resides within ~400 W/mK range.[25] Due to these unique thermal properties, some researchers tried to use CNTs for special thermal applications, such as solid state thermal rectifier[26] and micro cooling devices.

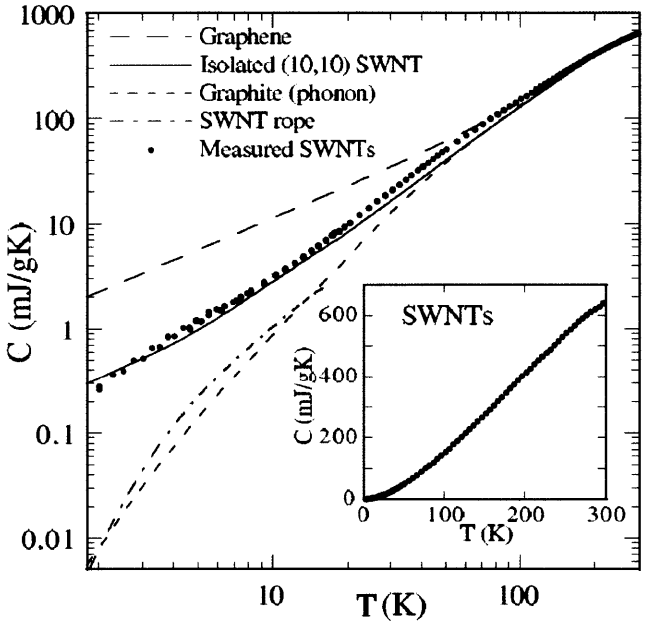

Figure 1.5. Thermal properties in carbon materials. [21] The graph shows the calculated specific heat of graphene, isolated SWNTs, graphite, and strongly coupled, graphite-like SWNT bundles at varying temperatures. The solid points represent the measured specific heat of a bulk sample of SWNTs.[21]

1.2.2. CNTs Electrical Properties

The unique electronic properties of CNTs are also largely attributed to their 1-D character. Generally, resistance occurs when an electron collides with some defect or the boundary of the crystal structure of the material through which it is passing. Such collisions deflect or scatter the electron from its path. In a 3-D conductor, electrons have plenty of opportunities to scatter at any angle, which results in high electrical resistance.[27] In 1-D CNT conductor, however, electrons go through one-dimensional-transport, in which they can travel only forward or backward, resulting in limited scattering, and thus very low resistance and high electric conductivity. CNTs can carry the highest current density of any known material, measured as high as 10^9 A/cm^2. As mentioned earlier, CNTs may be metallic or semiconducting, depending on their (n,m) indices. Generally, in metal, there is no energy barrier for electrons, and therefore any amount of voltage is enough to initiate electric current. In the case of semiconductor, however, there is a threshold voltage that sparks the free movement of otherwise stagnant electrons and holes, the two main carriers of electric flow.[27] Superior electronic properties of CNTs make them a promising alternative to the conventional semiconducting materials. Indeed, CNT-based transistors have effective electronic transport and fast-speed due to their one-dimensional-transport. Additionally, the low dimension of CNTs allows for significant reduction in size of the devices, resulting in smaller integration and ultimately enhancing power efficiency.[28] Electronic gadgets made from CNT transistors also feature reduced heat generation and significantly lower weight per volume, making them more desirable for customer demands.[28] Also, Kong et al[29] demonstrated chemical sensors based on individual SWNTs. Upon exposure to gaseous molecules including the explosive NO group molecules, the electrical resistance of a semiconducting SWNT was found to dramatically increase or decrease. These nanotube sensors

exhibit a fast response and a substantially higher sensitivity than that of existing solid-state sensors at room temperature. An individual nanotube can be used to detect many different types of molecules. The selectivity is achieved by adjusting the electrical gate to set the SWNT in an initial conducting or insulating state.[29]

1.3. Thesis Motivation and Objectives

The goals of this work can be divided into two areas. The first area is to design and develop new and effective nanomaterials for chemical to electrical energy conversion with high specific power (energy transport). The second area is to prove single ion transport and characterize the detailed phenomena in nanofluidic ion channels (mass transport). Applying unique properties of CNTs is the key to promote the fundamental understanding and explore a new class of application for both topics. Specifically, the objectives accomplished in here are :

1. Energy transport

   a. Design and synthesize new nanostructures, CNTs encased in combustible fuel annular coating.

   b. Simulate, and evaluate enhanced 1-D chemical reaction propagation along CNT with chemical fuels.

   c. Realize and measure the generation of electrical energy by 1-D chemical reaction along CNT in the manner of its magnitude of energy and specific power. Study the phenomena with moving thermal gradient in comparison with static, conventional TE effect.

   d. Study other interesting results with exothermic, 1-D chemical reaction with annular coating of fuel around CNTs.

2. Mass transport

   a. Develop a new platform to realize ion transport in high aspect ratio SWNTs.

   b. Study dynamics of single ion transport, such as threshold voltage and ion mobility through SWNT nanopore.

   c. Detect the transport of various molecules, such as cations (K^+, Li^+, Na^+, Cs^+)

   d. Study the SWNTs diameter effect on ion transport driven by an applied electric field

2. Part I. Energy Transport within Carbon Nanotubes : Thermopower Wave

2.1. Introduction to Thermopower Wave

Especially, in MEMS and NEMS devices, the relatively large volume and mass of power source is the big barrier to shrink the size of devices, and use them in many practical applications, while other components can be utilized in extremely small scale. There has been much of research about power sources, such as battery, capacitor, thermoelectrics, but still, the power level, and size are not applicable in small devices. For example, in smart dust device, battery size occupies over half of total volume and mass. So, there have been needs to develop shrinkable, minuscule power source with high power density for MEMS and NEMS devices.

2.1.1. Principle of Thermoelectric (TE) Energy Conversion

German physicist Thomas Johan Seebeck, with the discovery of the phenomena that bears his name, is considered the father of thermoelectricity. Seebeck stumbled upon his discovery by creating a circuit composed of two divergent metals, with junctions at different temperatures that would retract a compass magnet – the detector of electrical current for 19^{th} century physicists. Uncertain of what he had discovered, Seebeck initially believed his effect contributed to magnetism; however, he soon realized an electrical current was produced causing the deflection of the magnet. Today, the theory of the thermoelectric (TE) effect is largely understood and constitutes the direct conversion of a nominally steady-state temperature gradient to electrical current, or the corresponding reverse process. The charge carriers in metals and semiconductors, such as electrons or holes, diffuse from the hotter side to the colder side or the other way when a temperature gradient is applied (Figure 2.1a). A temperature difference at the

junction of two electrodes generates an electrical current as per the Seebeck effect. Conversely, an electrical current drives a temperature gradient in the reverse (or Peltier) effect.

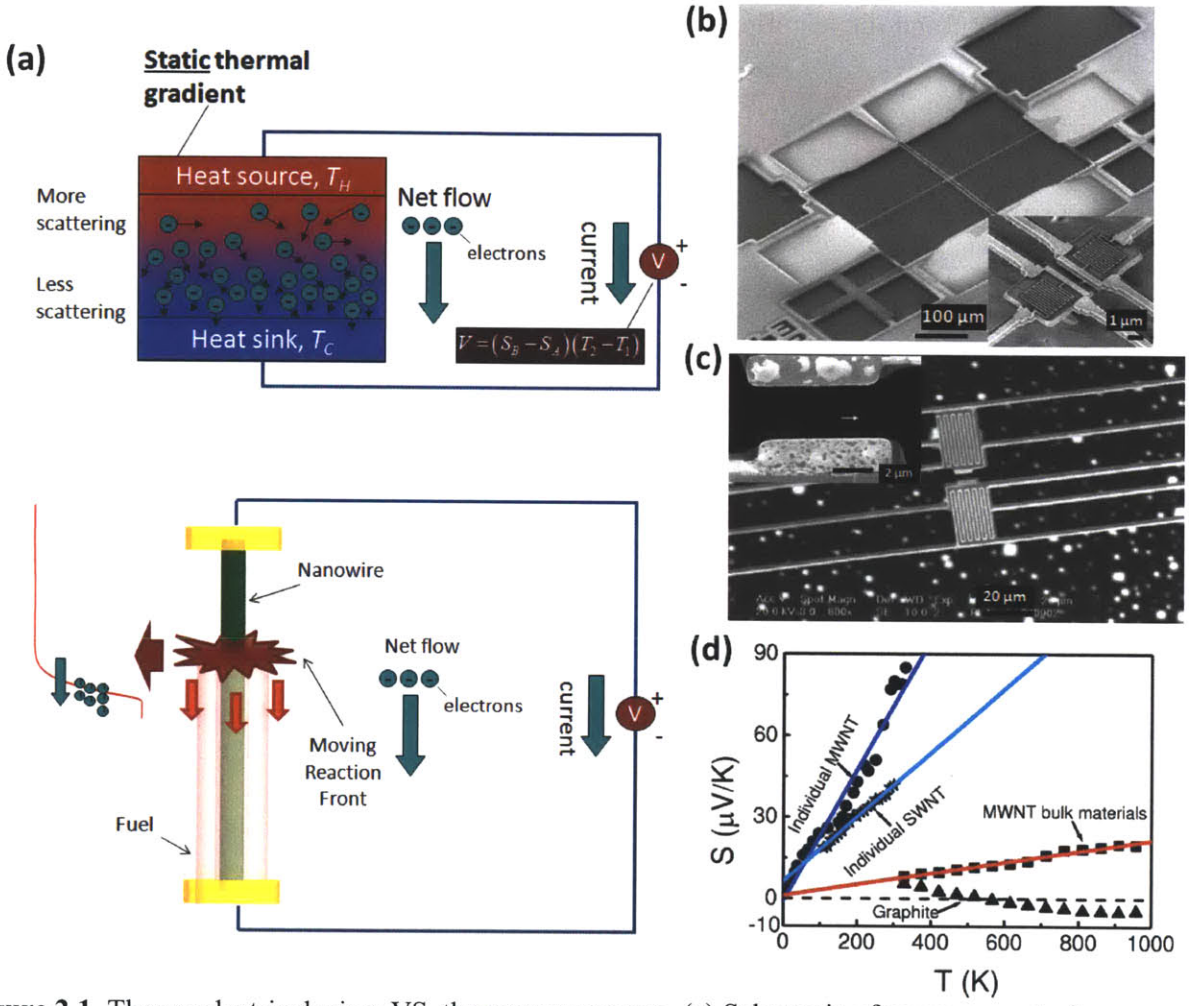

Figure 2.1. Thermoelectric devices VS. thermopower wave. (a) Schematic of measurement of conventional TE effect (top) [30-31] and core/shell nanostructure launching a thermopower wave (bottom). Scanning electron microscopic images of microdevices for thermal transport measurements of (b) individual multiwalled nanotubes (MWNT) [32] and (c) single-walled carbon nanotubes (SWNT). [15] (d) Comparison of TE power generation (MWNT bulk materials, individual SWNT, individual MWNT, and graphite) between 0 K and 958 K. [33] Linear fitting was used on the basis of experimental data.

There are several driving forces that determine the current density through a conductor. The electric field and chemical potential contribute to the current proportional to the conductivity of the solid. Onsager reminds us that there is a driving force related to the temperature gradient across the conductor, and the resulting current is proportional to a coefficient, L_{12}.

$$\text{Current density}: J_e = \sigma\left(E + \frac{\nabla\mu}{e}\right) - L_{12}\nabla T \tag{2-1}$$

$$\text{For } J_e = 0 \rightarrow E = \frac{L_{12}}{\sigma}\nabla T, \Gamma_s = \frac{L_{12}}{\sigma} \tag{2-2}$$

Here, σ is the conductivity, E is the electric field, μ is the chemical potential, L_{12} is the Onsager coefficient, T is the temperature, and $\frac{L_{12}}{\sigma}$ is the seebeck coefficient.

At zero current density, one can calculate the electric field that is induced across the conductor subjected to a temperature gradient and it is proportional to L_{12}/σ. This parameter is also called the Seebeck coefficient, Γs . For one-dimensional conductors, an induced voltage is calculated from a generic temperature gradient via

$$V = \int_{T_C}^{T_H} \Gamma_s dT \tag{2-3}$$

or if Γ_s is constant and the gradient linear,

$$V = \Gamma_s(T_H - T_C) \tag{2-4}$$

Here, V is the voltage developed, T_H is the hot, and T_C is the cold boundary condition of the junction. A TE figure of merit, a criterion of performance of TE materials, is derived from

$$Z = \frac{\Gamma s^2 \sigma}{k} \tag{2-5}$$

Here, k is thermal conductivity of the conductor. Conventional TE devices generate power in the ranges of μW to mW and find applications[34] in heat pumps, refrigeration, and aerospace applications. Efficiencies are generally acknowledged to be low, limiting widespread application[35].

2.1.2. TE Effect in Nanostructured Materials

In recent years, nanostructured materials have played a central role in advancing TE figures of merit[36]. Theoretical and experimental studies have been conducted to nanoscale heat transfer[37] and electronic properties[38] of TE materials. Bulk nanostructured materials have been strong candidates for next generation of TE field because these are compatible with existing TE system[39]. Many types of quantum wells, wires and dots have been studied for new TE materials[40]. Recently, researchers have made the composite materials with nanostructure and bulk samples[41]. Among many nano materials, bismuth-based materials[42] have been strong candidates for an efficient TE system. Boukai *et al.*[43] and Li *et al.*[44] measured TE properties of individual Bi nanowire, and fabricated Bi nanotube arrays, respectively. Bismuth telluride bulk alloys[45], thin films[46-47], nanowires[48-49], and its derivatives[50] have captivated the interests of researchers as promising materials for TE applications. Bismuth antimony-based structures[51-53] were also studied for high figure of merit TE materials. In other materials, rough silicon nanowires[54] and doped silicon nanowires[55-56] have overcome low figure of merit of bulk silicon. Si/Ge superlattice[57] and core/shell[58] nanowires have also been regarded as efficient candidates. Lee *et al.*[59] investigated wide band gap semiconducting nanowires like ZnO and GaN. Other nanostructured materials like PbTe[60], PbSe[61], InSb[62], and InAs[63] have promises as well. The literatures contain many emerging nano/MEMS fabrications[64-65] and devices[66] utilizing the TE

effect for various applications. Among one-dimensional conductors, including conjugated polymers[67] and carbon nanotubes (CNTs), Seebeck coefficients are generally too small for practical application, as shown in Table 2.1, largely excluding these materials as viable candidates for TE devices.

Table 2.1. Conductivities and Seebeck coefficients for example conjugated polymers and multiwalled carbon nanotubes (MWNTs). [67]

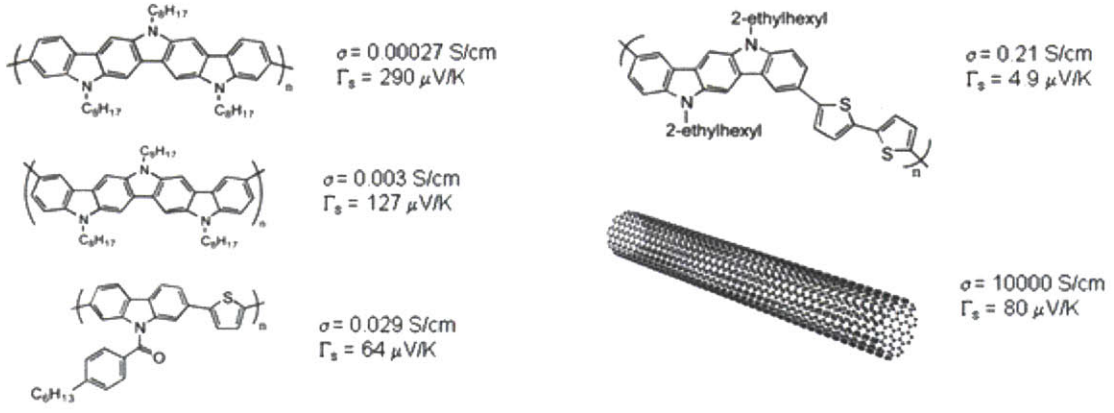

CNTs have been explored as components of TE devices due to their high axial thermal conductivity (3000 W/m/K)[15-17] and electrical conductivity (10000 S/cm) [13-14] in high aspect ratio, one-dimensional structures[18-19]. The typical device for measuring thermoelectricity is composed of TE materials between hot and cold boundaries with metal contacts connected to a temperature controller[30] (Figure 2.1a)[31]. A multimeter or oscilloscope can then measure the Seebeck voltage, current, and resistance. Hone *et al.*[68] measured the TE power of crystalline ropes of single-walled carbon nanotubes(SWNT). Kim *et al.*[32] and Yu *et al.*[15] were the first to measure thermal conductivity and Seebeck coefficient in an individual multiwalled carbon nanotube (MWNT) and a SWNT, respectively (Figure 2.1b, c). These measurements were in the temperature range of 10 K to 300 K. Zhang *et al.*[33] then extended this work by comparing MWNT bundles with

individual MWNT and SWNT up to 958 K (Figure 2.1d). Even though the Seebeck coefficients of both types of nanotubes are higher than graphite, MWNT bundles demonstrated relatively lower Seebeck coefficients than individual MWNT and SWNT due to the low charge carrier concentration that can freely move in bulk materials. Doped CNTs have also been considered as candidates to enhance the TE effect.[69-71] However, the overall TE figures of merit of CNTs have not been competitive in comparison to renowned TE materials such as bismuth telluride (287 μV/K)[44,46,48], silicon nanowires[55], or Bi_2Te_3/Sb_2Te_3 superlattices (243 μV/K)[72].

Lately, new mixed structures of CNTs and other materials, as well as integration in MEMS devices, have been receiving engineering attention. It was reported that the Seebeck coefficient of CNTs coated with polyaniline (Figure 2.2a) was remarkably higher than both of their bulk parent samples (Figure 2.2b)[73]. Dau *et al.*[74] made a CNT/Au junction for a micro-TE device and evaluated its performance (Figure 2.2c, d). However, the TE performance of CNTs lags significantly behind their inorganic counterparts (nanowires) despite these advances. The simultaneously high phonon and electron conductivities in CNTs, combined with their low Seebeck coefficients, limit their use in these applications.

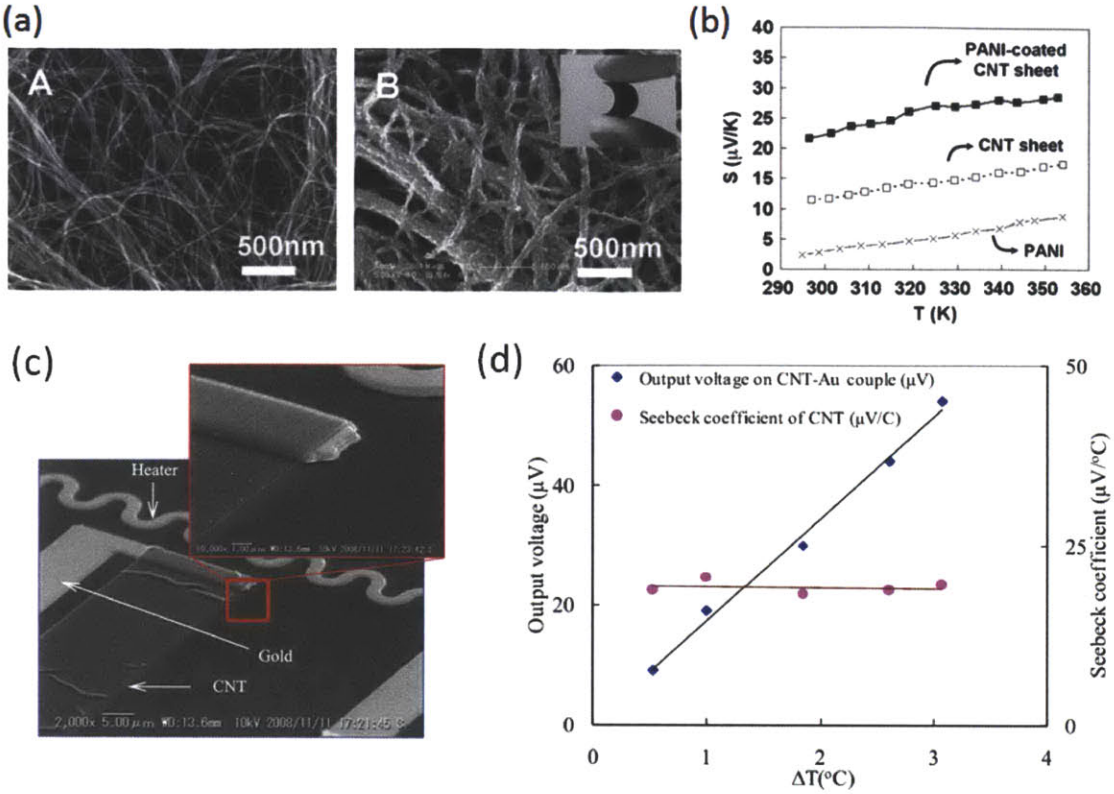

Figure 2.2. Thermoelectric effect in CNTs. (a) Electron micrographs of thick pristine carbon nanotube sheet (left), and polyaniline (PANI) coated sheet (right). [73] (b) Seebeck coefficients of two parent materials (CNT sheet, PANI) and new nanocomposite (PANI-coated CNT sheet). [73] (c) Scanning electron microscopic images of Au-CNT (thermally coupled) device. [74] (d) TE voltage across the junctions of Au-CNT thermocouple plotted as a function of temperature. Calculated Seebeck coefficient is also shown. [74]

2.1.3. Concept of Chemically Driven CNT-guided Self-Propagating Waves

The classical theory of heat conduction predicts that self-propagating chemical waves are possible when a non-linear source term, activated by temperature, is coupled to an exothermic reactive material that is also the heat conductor. The resulting wave velocity that radiates isotropically is known to vary exponentially with the inverse adiabatic reaction temperature [75], a fundamental material property. Such waves were first studied theoretically in 1938 by Zel'dovich and Frank-Kamenetskii [76], and experimentally verified for a wide range of technological applications, such as propulsion [77], chemical synthesis [78] and combustion [79]. The

emergence of nanotube and nanowire systems, where phonons are quantum confined and scattering processes are minimized, has resulted in observations of thermal conductivity that are exceedingly high [80]. The properties of such systems are surprisingly invariant to mechanical deformation [81], even showing thermal rectification for anisotropically loaded specimens [11]. The question of how such systems support or modify a neighboring reaction wave has thus far been unexplored. It is known, for example, that only the thermal conductivity in the vicinity of the narrow reaction zone contributes to wave propagation [82]. If the phonon mean free path becomes commensurate with the length of this zone, a possibility for many one dimensional nanotube systems, an enormous acceleration of the reactive wave may result. This thesis demonstrates the existence of such accelerated thermal waves and introduce a new phenomenon that results from their effect on carrier propagation, namely concomitant thermopower waves that yield a substantial specific power from a micro- or nano-scale source.

2.1.4. Design of Thermopower Wave in CNTs

The challenge with conventional TE devices is maintaining a large thermal gradient while allowing a large electrical current to flow through the interface. In devices designed to harvest electrical power from waste heat, the goal of materials scientists has been to select materials that conduct heat primarily as phonons but block their propagation across an interface where electrical conduction is large. An alternate means of creating a large thermal gradient, even in a material that conducts both heat and electrical current well, is to create a self-sustaining reaction wave, called as thermopower wave. [83] (Figure 2.3). This can be achieved by thermally coupling an exothermic fuel with an anisotropic heat conductor, as depicted schematically in Figure 3a. The suggested structure is annular coating of energetic fuel on nanowire shape. In this design,

nanowire is a thermal conduit for 1d chain reaction. It forms anisotropic reaction along its length axis and enhances the reaction velocity by means of fast thermal transport. When this material is ignited at one end, the released heat energy is transferred into both of CNTs and energetic material. But, most energetic material (fuel) has low thermal conductivity in the range of 0.05 to 0.3 w/mK, and the reaction speed is not fast. In this design, CNTs can make fast heat transfer along its length axis, and this heat will be transferred into exothermic fuel before the reaction. By this mechanism, this reaction will be accelerated as the anisotropic reaction in attached energetic fuel layer.

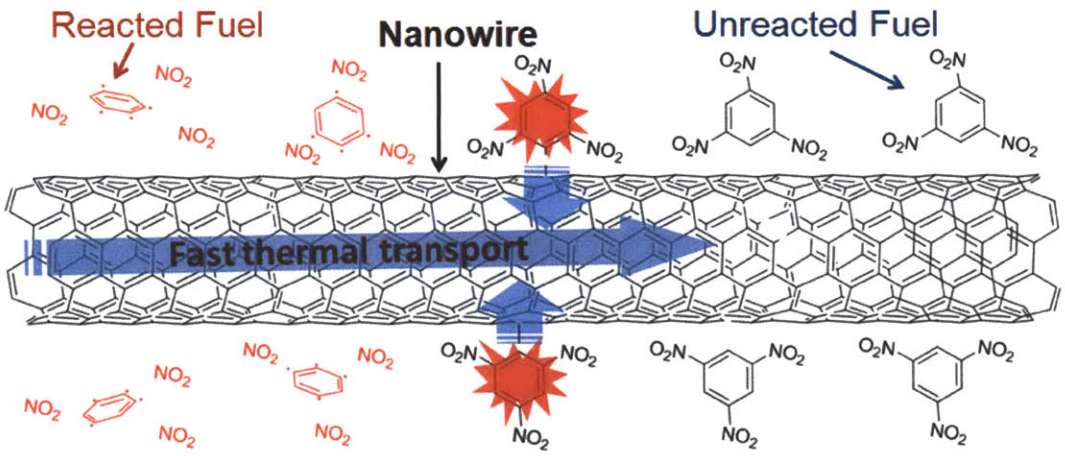

Figure 2.3. Schematic of a coaxial nanocomposite for anisotropic reaction waves. An exothermic chemical fuel is wrapped around a thermal conduit, such as a nanotube or nanowire. Initiation at one end of the conduit induces a one-dimensional chain reaction with amplified velocity due to fast thermal transport in the conduit.

2.2. Synthesis of Thermopower Wave Materials

We verified the existence of thermopower waves experimentally by creating both isolated and aligned arrays of multi-walled carbon nanotubes (MWNT) encased in a 7-nm-thick cyclotrimethylene-trinitramine (TNA) annular coating (Figure 2.4). The synthesis procedure is

based on a wet impregnation of a 90-mM TNA in acetonitrile solution into pre-synthesized vertically aligned MWNT arrays.

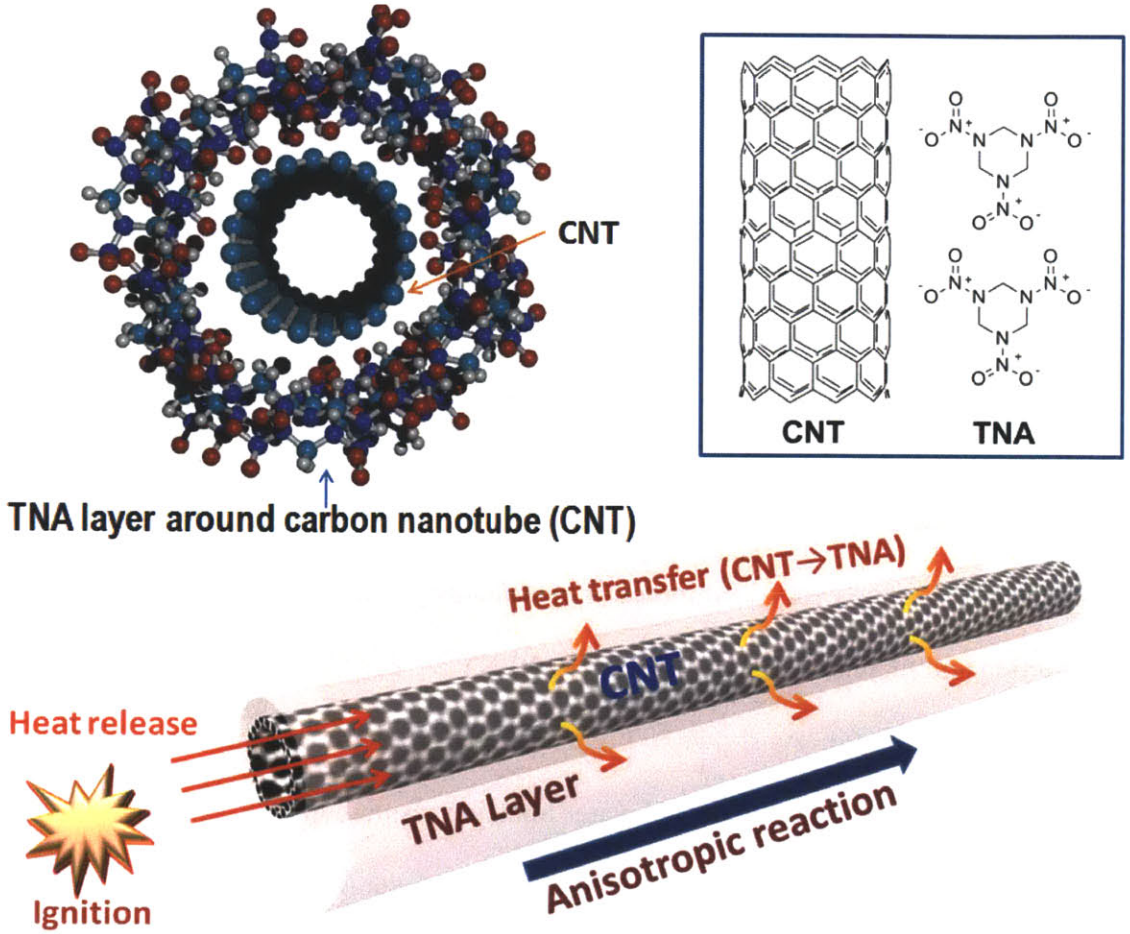

Figure 2.4. An accelerated, anisotropic reaction wave of TNA confined to an annular region around a nanotube thermal waveguide. Ignition at one end of TNA-CNT results in an exothermic reaction and heat transfer along the length of the CNT, with feedback creating an anisotropic reaction wave of amplified velocity.

2.2.1. Synthesis of Vertically Aligned CNTs by CVD

Vertically aligned multi-walled carbon nanotubes (VAMWNT) were synthesized by the chemical vapor deposition (CVD) method in a horizontal quartz tube furnace with an inner diameter of 29 mm. Catalyst layers, 0.5 – 1 nm Fe and 10 nm Al_2O_3, were deposited on a silicon

wafer by electron beam evaporation [84]. Ethylene (C_2H_4) was the carbon source. Hydrogen (H_2) and argon (Ar) were used as catalytic and carrier gases, respectively [85]. The gases were preheated by a tungsten filament (12 – 14 amps) to induce the decomposition of the hydrocarbons [86]. The key steps in this fabrication process are described below.

a. For 28 minutes, the furnace temperature was increased from 25 to 750 °C with Ar gas flow (400 sccm).
b. Next, the temperature was maintained at 750 °C for 10 minutes while H_2 (100 sccm) and Ar (400 sccm) were injected. During this process, the Fe layer changed form to Fe nanoparticles.
c. C_2H_4 (147 sccm), H_2 (100 sccm) and Ar (400 sccm) were introduced into the furnace at 750 °C and 1 atm. To grow 22 nm-diameter MWNT, bubbling water (50 sccm) was injected for 1 minute every 15 minutes or continuously to decrease amorphous carbon production and increase the straightness of MWNT [84]. For 13 nm-diameter MWNT, water was not injected. As shown in Figure 2.5a, SEM confirmed that the final lengths of MWNT were similar and that pulsed water injection resulted in well aligned VAMWNT. Figure 2.6 shows the comparison between 22 nm-diameter MWNT and 13 nm-diameter MWNT. The method for growing 13 nm-diameter MWNT has a lower degree of alignment and a higher quantity of amorphous carbon compared to the 22 nm sample.
d. At the end of the CVD process, the Ar flow rate was decreased to 50−100 sccm in order to weaken bonding between the MWNT array and substrate [87] and create a free-standing aligned MWNT array.

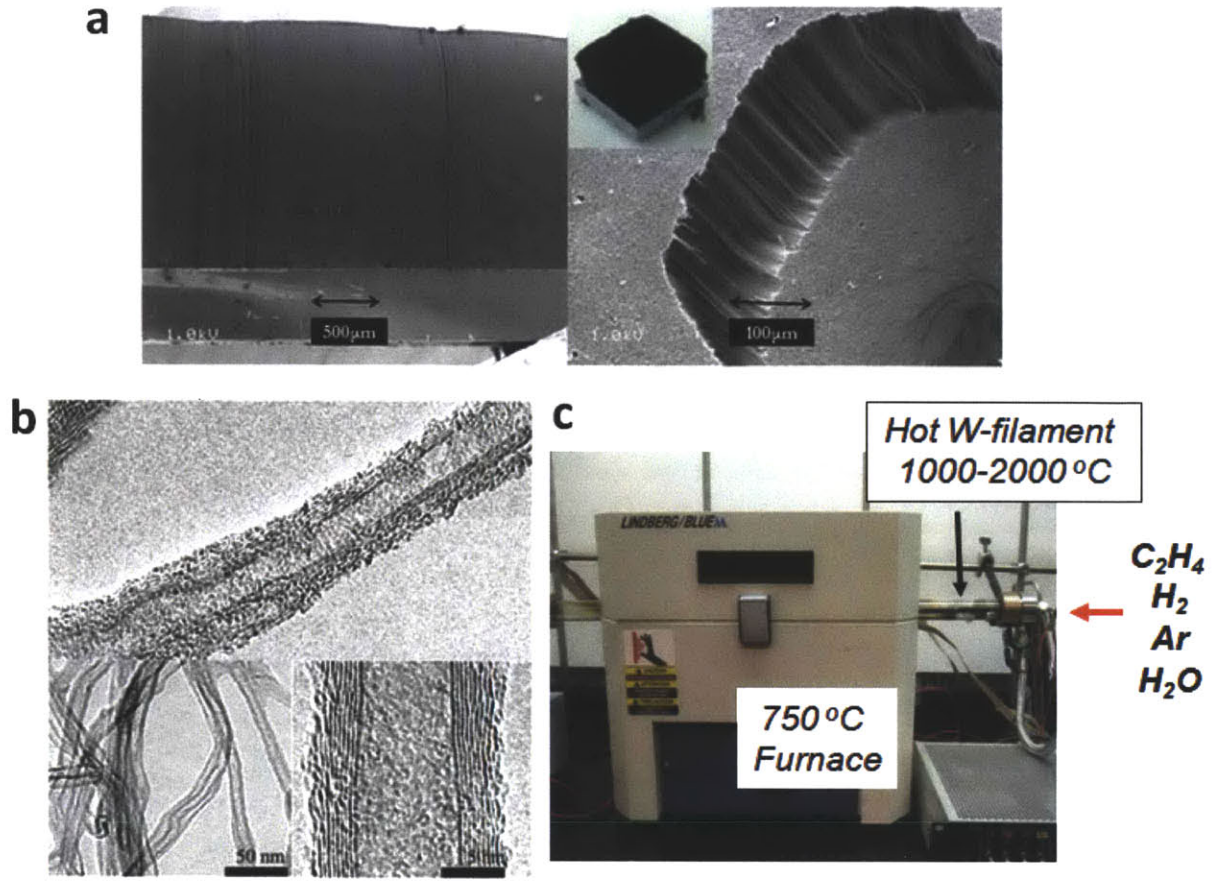

Figure 2.5. Microscopic images of VAMWNT. (a) Scanning electron microscopic images of nanotubes synthesized using water injection method. Cross-section is 5 x 5 mm and average height is 3 to 5 mm. (b) Transmission microscopic images. Inner diameter is 7 to 8 nm, and outer diameter is 11 to 13 nm. (c) Chemical vapor deposition set up for CNT growth.

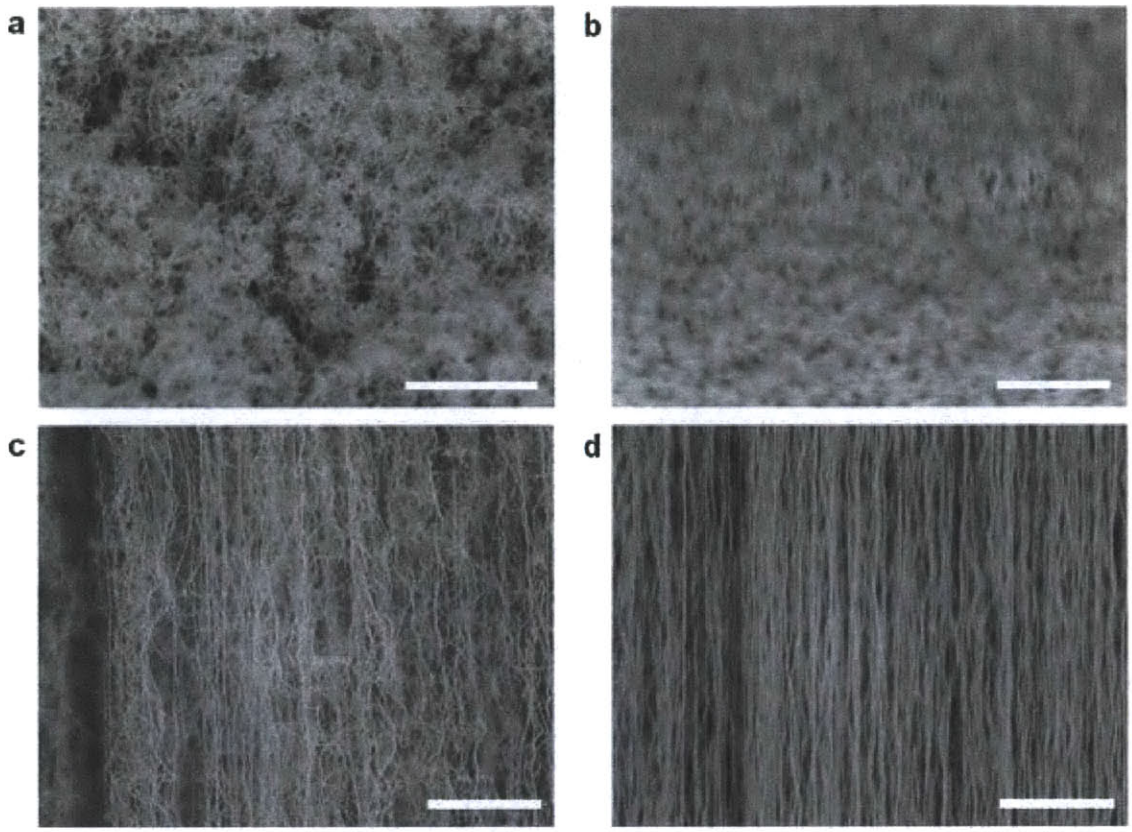

Figure 2.6. Scanning electron microscope images of VAMWNT with (22 nm-diameter MWNT) or without water-assisted method (13 nm-diameter MWNT). (a) Tilted view of VAMWNT without water-assisted method. A great deal of amorphous carbon exists on the top surface. (b) Tilted view of VAMWNT with water-assisted method. The top surface of the VAMWNT is clear. (c) Side view of VAMWNT without water-assisted method. The array is relatively poorly aligned. (d) Side view of VAMWNT with water-assisted method. The array is relatively well aligned. All scale bars indicate 1 μm.

The resulting films were 3 to 5 mm tall on a silicon wafer approximately 5x5 mm in cross-section (Figure 2.5a). The MWNT were either dispersed as individual nanotubes for characterization or kept in an array form for further reaction testing. We calculated the porosity of the VAMWNT using a previously published protocol [88]. The mass and volume of the VAMWNT were measured directly. The information about tube diameter and number of walls was obtained from TEM images (Figure. 2.5b). The 22 nm-MWNT had an average of ten walls, an inner radius of 7.6 nm, and an outer radius of 11 nm, giving them a cross-sectional area of

197.6 nm^2. The porosity was estimated as 99%. Alternative growth conditions (Furnace tube diameter: 29mm, Fe: 0.5 nm, Al_2O_3: 20nm, C_2H_4: 30 sccm, H_2: 55 sccm, Ar: 150 sccm) produced 13 nm-diameter MWNT with an average of nine walls. TEM images are shown in Figure. 2.5b. The inner radius was 3.4 nm and outer radius was 6.5 nm. The cross-sectional area was 96.4 nm^2 and the porosity was 97%.

2.2.2. Method for Wrapping Exothermic Fuel Layer around CNTs

A subsequent sodium azide (NaN_3)/water solution applied after wet impregnation allowed for facile initiation after drying for 24 hours at ambient temperature and pressure. The detail procedures are in below. TNA was received in a sand mixture. Washing the mixture with acetonitrile dissolved TNA. The solution was filtered to eliminate impurities, resulting in pure TNA solution. Wet impregnation is the basic method to coat fuel on CNTs and produce the coaxial structure (Figure 2.7). 0.2 g of TNA was dissolved in 10 mL of acetonitrile. TNA in acetonitrile solution was dropped into the pores of a MWNT array. When liquids are introduced into sparse VAMWNT and evaporated, the cross-section of VAMWNT significantly shrinks due to the surface tension of the liquid and strong van der Waals interactions between nanotubes [89]. 5 μL of NaN_3 in aqueous solution with a concentration of 50 mg/mL was then added to serve as a primary igniter, since NaN_3 has a much lower activation energy (40 kJ/mol) [90] than TNA (140–200 kJ/mol) [91]. The VAMWNT were dried under atmospheric conditions (300 K, 1 atm) for 24 hours. After the evaporation, the MWNT array had densely contracted, its volume decreasing by about an order of magnitude, and annular coatings of TNA crystals were deposited on the sidewalls of the MWNT.

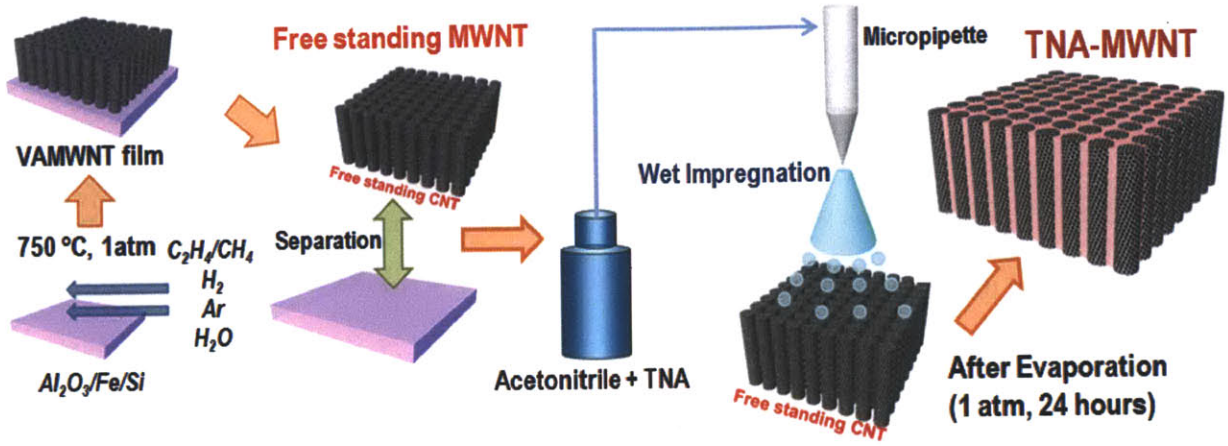

Figure 2.7. Synthesis process for TNA-MWNT arrays by wet impregnation.

2.2.3. Characterization of Trinitramine-Multi Walled CNTs (TNA-MWNTs)

The aligned structure of TNA-MWNT was maintained after the wet impregnation as shown in Figure 2.8a. The TNA shows up as a bright coating compared to the nanotubes (Figure 2.8b). Transmission electron microscopy (Figure. 2.9) indicates annular coatings of TNA crystals between 6 to 9 nm in thickness wrapping MWNTs of approximately 22 nm in diameter with an average of 10 walls. Alternate growth conditions (Figure. 2.5b) produce 13-nm-diameter MWNTs with an average of nine walls, also explored in this work. The TNA coatings were uniform, although larger crystallites with defined grain boundaries were frequently visible along the side-walls of MWNTs, as shown in Figure 2.9, from homogeneous crystallization in the bulk impregnation solution before adsorption to the nanotubes. The x-ray diffraction (Figure 2.10) spectra shows that both the crystal structures of the bulk MWNT array and the TNA are preserved in the composite, with little evidence of organic intercalation [92-94]. The diffraction peak at 26° (002) corresponds to a typical inter-planar spacing of graphite (0.34 nm), and 42.4° (100) yields a 2.12 nm nanotube pitch [95-97]. The mass of the array was measured with a microbalance before and after impregnation to determine the mass ratio of TNA to MWNT. The

mass ratio could be controlled by the concentration and amount of TNA solution added to the VAMWNT.

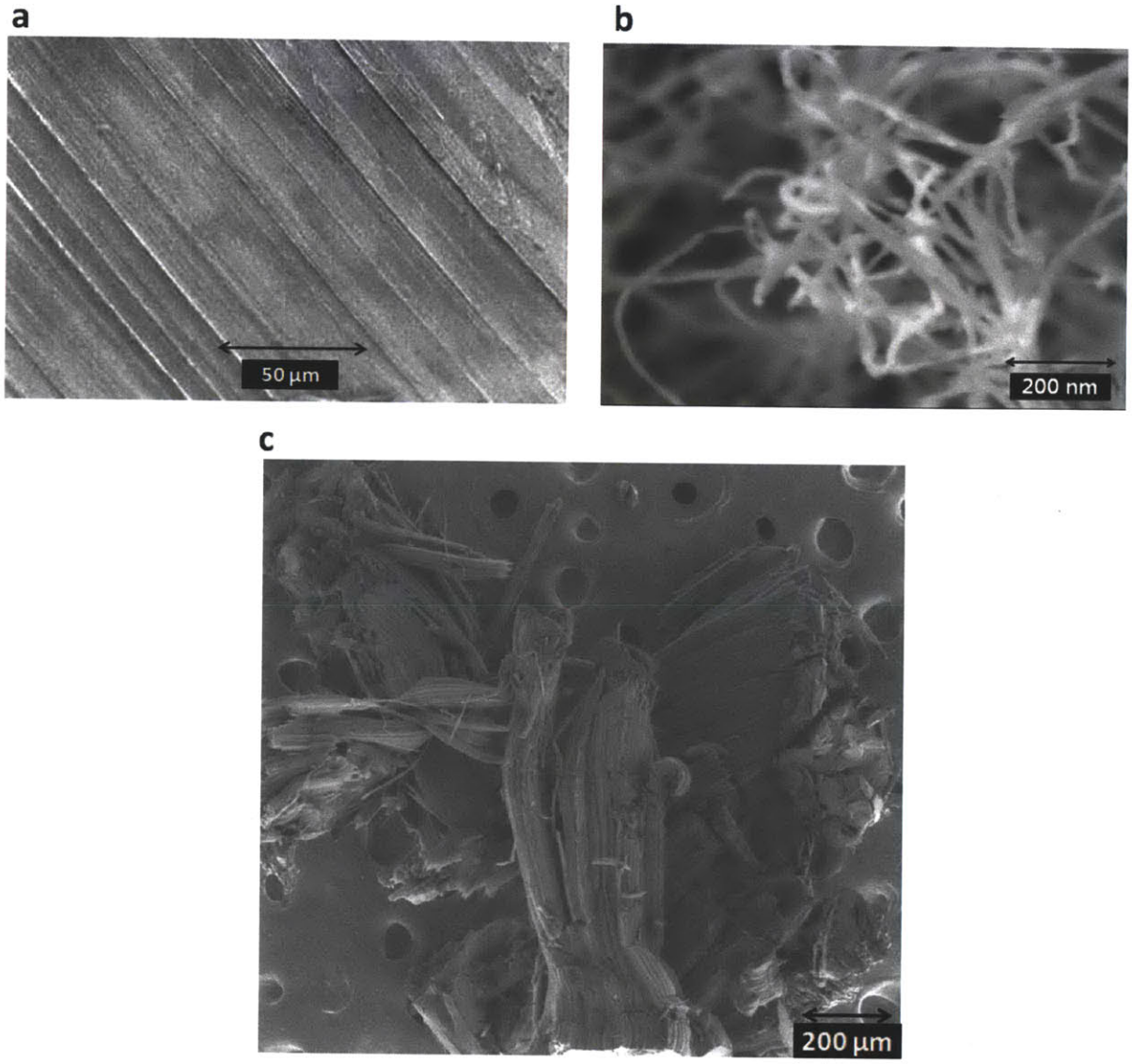

Figure 2.8. TNA-MWNT scanning electron microscopic images. Each TNA-coated MWNT was dispersed from the bundles before electron microscopy. **a,** The aligned structure was maintained after the wet impregnation. In several places, larger crystallites of TNA were visible. **b,** The TNA shows up as a bright coating compared to the nanotubes. **c,** Bulk TNA-MWNT arrays were aligned along length axis, and were more densely packed in comparison with MWNT arrays lacking TNA, due to capillary forces during evaporation.

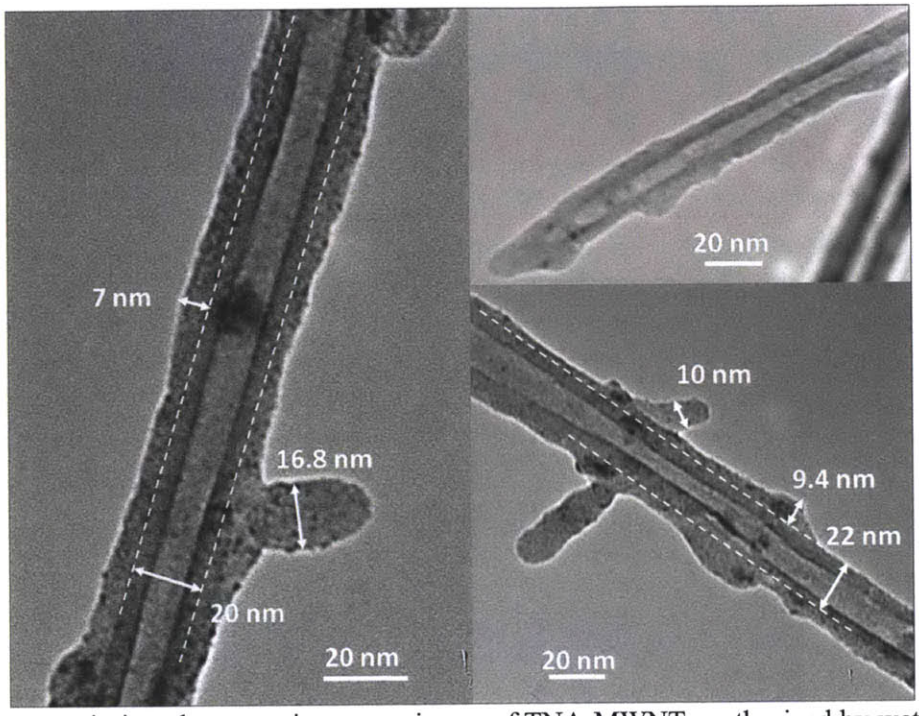

Figure 2.9. Transmission electron microscopy image of TNA-MWNT synthesized by wet impregnation. The dashed line indicates the boundary between MWNT and TNA layers.

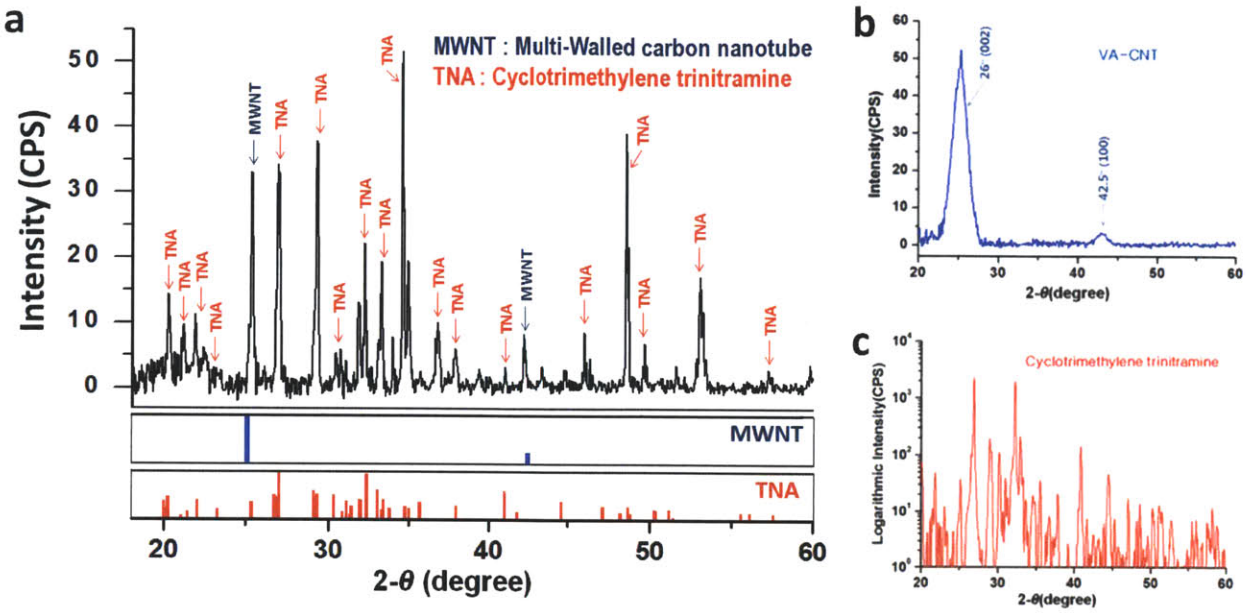

Figure 2.10. (a) X-ray diffraction showing TNA-MWNT after synthesis (black), MWNT only (blue) and TNA only (red). (b) VAMWNT have two peaks. 26° (002) corresponds to the inter-tube spacing of 0.34 nm and 42.4° (100) to 2.12 nm crystal spacing [95-97]. The (002) plane peak depends on the alignment of the MWNT; the peak will shift away from 26° with decreasing degree of alignment. (c) TNA has many XRD peaks since it has numerous crystal polymorphs.

2.3. One Dimensional, Self-Propagating Chemical Reaction along CNTs

2.3.1. Initiation and Propagation of Chemical Reaction in CNTs

Energy input above the minimum barrier of the chemical reaction of fuel is required to launch thermopower waves. Notably, the composite structures of CNTs and fuel described above sharply reduce the required initiation energy for propagating chemical reaction waves[98-99]. Here, I describe four methods: two contact-less heating (laser irradiation and high voltage electrical discharge), and two direct contact (Joule heating and butane torch). A laser pulse can heat a spot at one end of an array, and the exothermic chemical reaction wave will propagate from the heating spot to the opposite end. Another contact-less method is high voltage electrical discharge, where a thin tungsten wire fixes the array in place, keeping a small gap between it and a tungsten plate below. The two tungsten elements serve as electrodes for the sub-millisecond

discharge, briefly creating a high-energy plasma that starts the reaction wave. A thin tungsten wire can be used as a Joule (resistance) heater, directly supplying energy *via* conduction to a sample. When a voltage is applied, the tungsten wire heats rapidly due to its resistance, and the point of contact with the array is ignited. Perhaps the simplest method is to "jump start" the reaction wave with another exothermic reaction. A small torch burning a hydrocarbon fuel (e.g. butane) will easily initiate thermopower waves, although care must be taken to precisely heat only one end of the sample. Among them, two methods were mainly used for initiating reactive waves in this system: laser irradiation and high voltage electrical discharge. Either laser irradiation (785 nm, 300 to 400 mW) or high voltage electrical discharge (up to 2.8 kV, 5 mA) was used to ignite samples (Figure 2.11, Figure 2.12). For the high voltage electrical discharge, a thin tungsten wire was fixed to the TNA-MWNT, keeping a small gap between them and the tungsten plate below (Figure 2.12a). The two tungsten elements served as electrodes for the sub-ms high voltage discharge.

Two methods have been employed to measure the reaction velocity of thermopower waves. First, an optical fiber array can detect light emitted from a series of spots in the reaction region. The optical fiber array is positioned above the array parallel to the expected reaction region, and it measures the time differences between successive fibers as the reaction wave propagates across the sample. Both position and velocity of the reaction wave can be precisely measured over time. The TNA-MWNTs were attached to a metallic fixture with a temperature control apparatus. TNA-MWNT were preheated on the fixture and ignited with a 785 nm, 400 mW laser pulse. Figure 2.11 shows a schematic of setup and signals acquired from two optical fibers. A second method is high-speed photography. A high-speed CCD camera with a microscopic lens can record the reaction wave propagation in real time. Snapshots of the reaction wave record its

position at the time of each frame. A high speed CCD camera (CPL-MS70K, Canadian Photonic Labs) with a microscopic lens (Macro 60 mm, f/2.8D micro Nikkor Autofocus lens, Nikon) recorded the reaction at 90,000 frames per second (Figure 2.12).

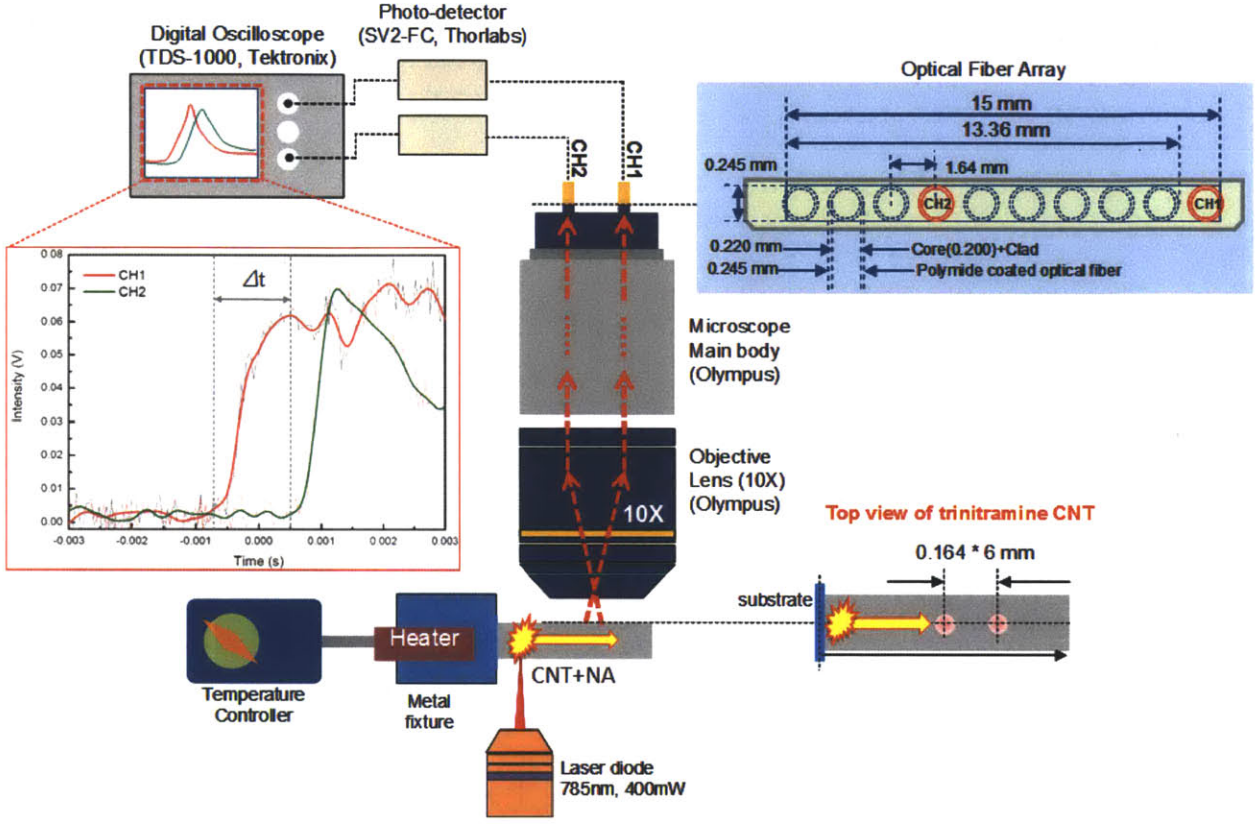

Figure 2.11. Reaction velocity measurements using an optical fiber array with microscopic lens system. Reaction propagation was monitored using optical fibers connected to a microscope. A photo-detector (SV2-FC, Thorlabs, rise and fall time < 150 ps) converted optical signals into electrical signals, which were then digitized with an oscilloscope (TDS-1000, Tektronix, 1 GS/s). The time delay between the two channel signals (CH1 and CH2) was used to calculate reaction velocity. The distance between the two channel spots on the surface of the sample was 984 μm. The optical fiber array was aligned along the length axis of the VAMWNT to measure the parallel reaction velocity. For an orthogonal reaction velocity measurement, the fiber array was rotated by 90 degrees.

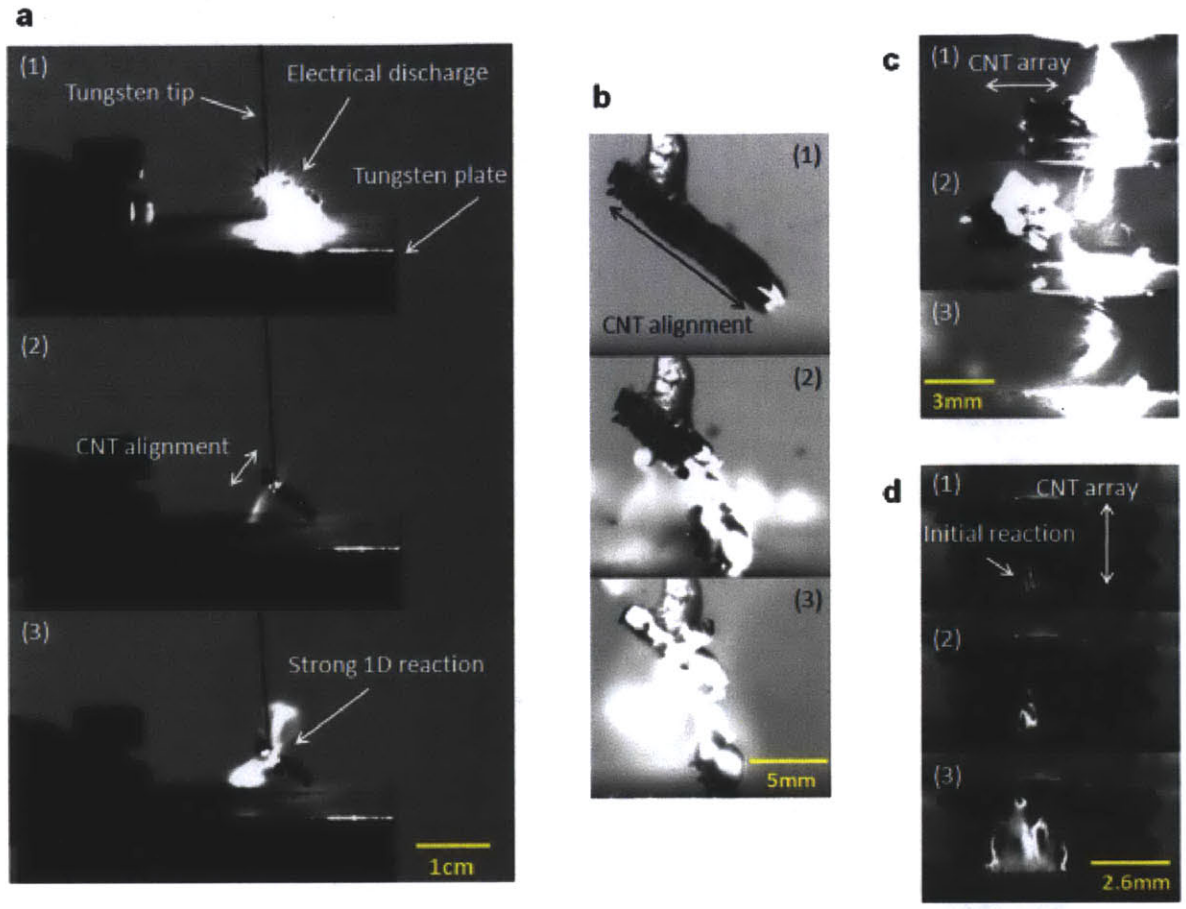

Figure 2.12. High speed photographic images. (a) TNA-MWNT were attached to a thin tungsten wire. A tungsten plate was placed below the sample, leaving a small gap. A high voltage power supply (up to 2.8 kV, 5 mA) was connected to the tungsten wire and the plate. This produced an electrical discharge between the TNA-MWNT and the tungsten plate that ignited the reaction. (b) The reaction front velocity was measured from magnified high speed photographic images. (c) Launching TNA-MWNT in the direction of their alignment for free body experiment. A laser (785nm, 340 mW) ignited the sample on the top surface. Thrust force in the direction of alignment of the MWNT was generated, which launched the sample towards the left of the image. (d) Flame propagation in TNA-MWNT bulk array. An electrical discharge ignited the sample at its base. The reaction propagated in the direction of nanotube alignment initially (images 1 and 2), but eventually spread outward in the radial direction.

2.3.2. Measurement and Evaluation of Propagating Velocity

Sustained reaction waves specifically along the direction of the nanotube orientation (Figure 2.13a, inset) were observed at velocities more than four orders of magnitude larger than the bulk combustion rate of TNA of 0.2 – 0.5 mm/s [100-103] at an atmospheric condition (1 atm). Several control materials confirm that the reaction wave requires the aligned nanotubes and TNA. Randomly oriented arrays, or those lacking TNA or NaN_3, showed no such sustained reaction in any direction under any condition. In the example in Figure 2.13a, the aligned TNA-MWNT produced a steadily propagating wave with velocity 1.2 ± 0.4 m/s along the nanotube length. The MWNT generally survive the propagation of the wave intact, consistent with the high temperature stability of MWNT observed up to 3800 K[104-105]. To confirm that the mechanism of amplification involves the nanotube specifically as a thermal conduit, the reaction velocity dependence on preheating temperature (Figure 2.13b) was measured both in parallel and orthogonal directions to the nanotube alignment. Both orientations demonstrated an increase in reaction velocity with increasing preheat temperature, but in the parallel orientation, where the external heat directly supplements that supplied by the reactive wave, the enhancement is nearly 10 times faster than the orthogonal orientation. This result agrees with those of an earlier study, showing that thermal diffusivity in vertically aligned MWNT strongly depends on the direction of thermal transport, varying by up to a factor of 70 [106]. I found that 22-nm (10 walls) MWNT amplified the reaction velocity by more than 10^4 times, while for 13-nm (9 walls) MWNT the enhancement was about 10^3 times the TNA value. The difference is greater than what is predicted by the factor of 3 larger cross-sectional area of the 22-nm MWNT. A lower degree of alignment and higher quantity of amorphous carbon generated during synthesis of the 13-nm

samples compared to the 22-nm samples accounts for apparent differences in conductances (Figure 2.6).

The reaction velocity of the thermopower wave varies with many factors, including thickness of fuel, diameter of thermal conduit, and the dimensions of the sample. A higher degree of alignment, lower quantity of amorphous carbon, and small cross-sectional area of the sample increases the average reaction velocity. With the optimal conditions (based on present tests), the average reaction velocity can reach 1 to 2 m/s (Figure 2.13a). Across a greater range of conditions and samples, most reaction velocities are 0.1 to 2 m/s. Reaction velocity is strongly dependent on the thermal diffusivity of the conduit. In addition, the macroscale TNA-MWNT array has a relatively large number of bulk paths for orthogonal heat transfer *via* extended two-dimensional flame dissipation. A very thin TNA layer cannot supply enough heat from its exothermic reaction to aid reaction propagation, although the unreacted region of TNA requires small total amount of energy for reaction. On the contrary, when TNA layer is very thick, the exothermic reaction can provide more heat energy, but the unreacted region needs large amounts of energy for reaction. Consequently, we might expect that there is an optimal ratio to promote fast reaction velocities. Since all the arrays were roughly the same length and density, the total MWNT mass is determined mostly by the cross-sectional area of the array.

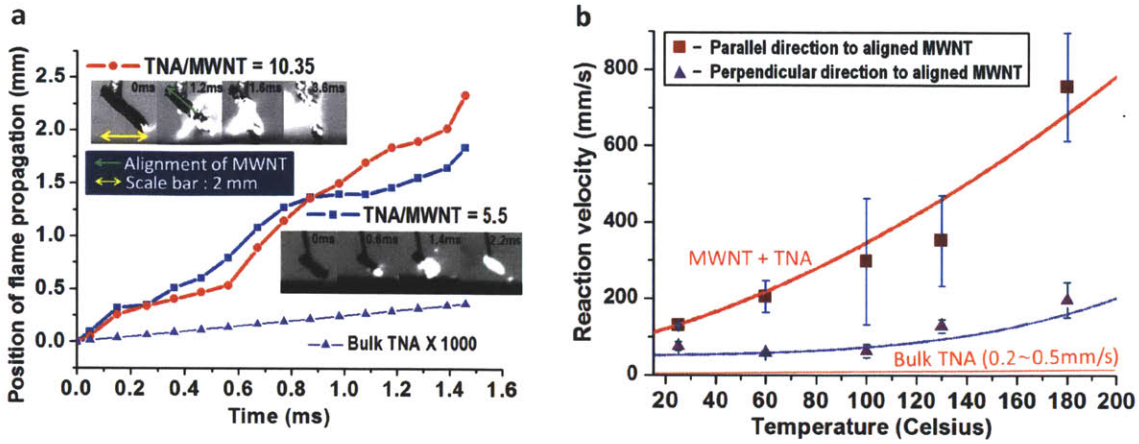

Figure 2.13. Propagating velocity of 1D chemical reaction. (a) Reaction propagation along an aligned MWNT array (average diameter 22 nm) after ignition by electrical discharge (no preheating). The height of the TNA-MWNT array is ~2 mm, and its cross-section is about 0.1 mm^2 (frame rate = 3.33 kHz). (b) The reaction velocity differs between samples preheated parallel and orthogonal to the aligned direction (average MWNT diameter 13 nm) as measured with an optical fiber array along the array length (Figure 2.11). The x-axis shows the preheating temperature of the TNA-MWNT array (Table 2.2).

Table 2.2. Data used in Fig.

Orientation	Temp. (°C)	Specimens	Time delay between two signals (s)	Reaction velocity (m/s)	Avg.velocity (m/s)	Std. Dev. (m/s)
Parallel	25	PA-25-1	0.00776	0.127	0.130	0.003
		PA-25-2	0.00736	0.134		
		PA-25-3	0.00752	0.131		
	60	PA-60-1	0.00392	0.251	0.205	0.041
		PA-60-2	0.00512	0.192		
		PA-60-3	0.00576	0.171		
	100	PA-100-1	0.00408	0.241	0.297	0.165
		PA-100-2	0.00588	0.167		
		PA-100-3	0.00204	0.482		
	130	PA-130-1	0.00244	0.403	0.353	0.119
		PA-130-2	0.00212	0.464		
		PA-130-3	0.00276	0.357		
		PA-130-4	0.00528	0.186		
	180	PA-180-1	0.00156	0.631	0.755	0.143
		PA-180-2	0.00108	0.911		
		PA-180-3	0.00136	0.724		
Perpendicular	25	PE-25-1	0.01300	0.076	0.066	0.011
		PE-25-2	0.01476	0.067		
		PE-25-3	0.01812	0.054		
	60	PE-60-1	0.01700	0.058	0.059	0.002
		PE-60-2	0.01612	0.061		
		PE-60-3	0.01708	0.058		
	100	PE-100-1	0.01572	0.063	0.067	0.017
		PE-100-2	0.01144	0.086		
		PE-100-3	0.01896	0.052		
	130	PE-130-1	0.00764	0.129	0.147	0.018
		PE-130-2	0.00600	0.164		
		PE-130-3	0.00664	0.148		
	180	PE-180-1	0.00500	0.197	0.174	0.046
		PE-180-2	0.00816	0.121		
		PE-180-3	0.00484	0.203		

2.3.3. Chemical Reactions in Other Structures

The presence and alignment of CNT are very important for creating and maintaining thermopower waves, respectively. Comparisons between TNA-MWNT samples of aligned, unaligned CNTs, or activated carbon (AC) demonstrates these roles. AC and unaligned MWNT were coated with TNA by the same wet impregnation method described earlier, producing contiguous solid materials similar to aligned TNA-MWNT. TNA-AC needed much more energy

to initiate reaction than TNA-MWNT. The reaction did not propagate completely but rather stopped, even though the AC contained no large pores. In the case of TNA-unaligned MWNT, the initiation energy requirement was similar to aligned TNA-MWNT, though the reaction wave was not continuous. Part of the array separated due to a pressure wave (Figure 2.14a) created by the reaction, and the velocity was significantly lower than TNA-aligned MWNT case. The alignment and porosity of the MWNT arrays helps to shape the TNA coatings around the MWNT walls continuously. Finally, Raman spectroscopy indicates that the MWNT array is still intact (Figure 2.14b) after thermopower wave propagation. If fuel were coated on a MWNT array repeatedly between thermopower wave reactions, it would be reusable—a new concept for a "fuel cell."

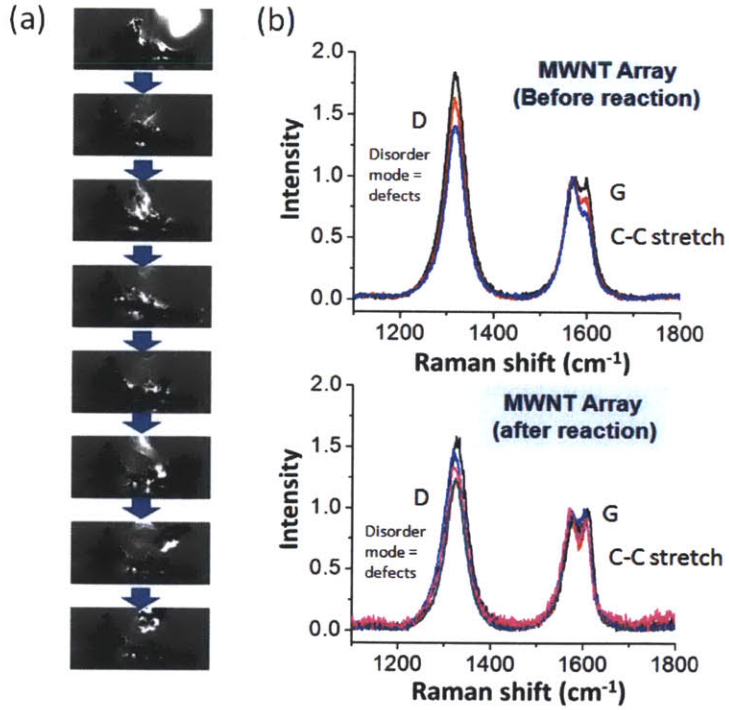

Figure 2.14. Random distribution of TNA-MWNT and Raman spectra before and after the reaction. (a) High-speed photographs of TNA on unaligned MWNT. The reaction wave did not propagate solely in one direction. Part of the TNA-MWNT sample could not withstand the pressure wave created by the reaction and separated from the main body. (b) Raman spectra of MWNT array before and after reaction of TNA. The original structure and properties of the carbon nanotubes are preserved.

2.4. Understanding the Dynamics of One Dimensional Chemical Reaction

2.4.1. Mathematical Formula and Boundary Conditions

I adapt the theory of conventional combustion waves to describe the nanotube-coupled thermal wave. Consider a first order reactive annulus at dimensionless temperature u surrounding a nanotube or nanowire (Figure. 2.4) at temperature u_2 where both are thermally coupled via a dimensionless interfacial conductance, γ. The Fourier description of this system is to model a coupled TNA-MWNT system. I begin with a standard one-dimensional heat balance for the TNA, including terms for heat conduction, reaction, and coupling with the nanotube.

$$\frac{\rho C_p}{M_W}\frac{\partial T}{\partial t} = \chi\frac{\partial^2 T}{\partial x^2} - (Qk_o y)Exp\left(-\frac{E_a}{RT}\right) - G_1(T-T_2) - \frac{hS}{V}(T-T_{atm}) - \frac{\varepsilon\sigma S}{V}(T^4 - T_{atm}{}^4) \qquad (2\text{-}6)$$

where $G_1 = G_0\frac{4d_N}{d_M{}^2 - d_N^2}$.

Variables with no subscript refer to TNA, subscript "2" refers to the nanotube, T is temperature, t is time, x is distance, χ is thermal conductivity, ρ is density, Q is the enthalpy of combustion, C_p is the (molar) specific heat, M_W is molecular weight, y is the molar concentration of TNA , k_0 is the Arrhenius prefactor, R is the universal gas constant, and E_a is the activation energy, h is convective heat transfer coefficient, S/V is surface area to volume ratio for TNA configuration, ε is the emissivity, σ is the Stephan-Boltzmann constant, T_{amb} is the temperature of the surroundings, d_M is the total diameter of the TNA-MWNT system, d_N is the nanotube diameter, and G_0 is the interfacial conductance. The aspect ratio of the TNA-MWNT system is large enough that other spatial dimensions are unimportant. Phase changes can be neglected by using material parameters averaged over multiple phases.

Likewise, we can write a heat balance for the nanotube

$$\frac{\rho_2 C_{p,2}}{M_{W2}}\frac{\partial T_2}{\partial t} = \chi_2 \frac{\partial^2 T_2}{\partial x^2} + G_2(T - T_2) \tag{2-7}$$

where $G_2 = G_0 \frac{4}{d_N}$. Reaction and phase changes in the nanotube can be neglected since MWNT are thermally stable up to very high temperatures, even above 2000 K. Furthermore, if the nanotube does break down, it will be after the reaction front passes, so the breakdown will have little effect on the velocity of the reaction front.

We define the reaction kinetics as first-order in TNA:

$$\frac{\partial y}{\partial t} = -k_o y Exp\left(-\frac{E_a}{RT}\right) \tag{2-8}$$

Now we non-dimensionalize temperature, time, distance, and TNA concentration using reaction and thermal parameters to simplify the numerical calculations.

$$u = \left(\frac{R}{E_a}\right)T,\ u_2 = \left(\frac{R}{E_a}\right)T_2,\ \tau = \left(\frac{-Qk_oR}{C_pE_a}\right)t,\ \xi = x\sqrt{\left(\frac{\rho C_p}{\chi M_W}\right)\left(\frac{-Qk_oR}{C_pE_a}\right)},\ \frac{M_W y}{\rho} = 1-\eta \tag{2-9}$$

η is the extent of conversion.

Now it is helpful to define

$$\beta = \frac{C_pE_a}{-QR} \tag{2-10}$$

and thermal diffusivity for each material, α and α_2, in the form

$$\alpha = \frac{\chi M_W}{\rho C_p} \tag{2-11}$$

With these substitutions, the equations become

$$\frac{\partial u}{\partial \tau} = \frac{\partial^2 u}{\partial \xi^2} + (1-\eta)e^{-1/u} - \gamma_1(u-u_2) - l(u-u_{atm}) - w(u^4 - u_{atm}{}^4) \tag{2-12}$$

$$\frac{\partial u_2}{\partial \tau} = \alpha_0 \frac{\partial^2 u_2}{\partial \xi^2} + \gamma_2(u-u_2) \tag{2-13}$$

$$\frac{\partial \eta}{\partial \tau} = \beta(1-\eta)e^{-1/u} \tag{2-14}$$

where $\alpha_0 = \frac{\alpha_2}{\alpha}$, $\gamma_1 = \frac{G_1 \beta M_W}{\rho C_p k_0}$, $\gamma_2 = \frac{G_2 \beta M_{W2}}{\rho_2 C_{p,2} k_0}$, $l = \frac{hSM_W\beta}{V\rho k_0 C_p}$, and $w = \frac{\varepsilon\sigma SM_W\beta}{V\rho k_0 C_p}$

If we neglect convection and radiation, (2-12) would be

$$\frac{\partial u}{\partial \tau} = \frac{\partial^2 u}{\partial \xi^2} + (1-\eta)e^{-1/u} - \gamma_1(u-u_2) \tag{2-15}$$

where η is the extent of chemical conversion of the reactive annulus, α_0 is the dimensionless thermal diffusivity of the nanotube (normalized by that of the annulus), β is the dimensionless inverse adiabatic temperature of the reactive annulus, τ and ξ are dimensionless time and distance (Here, γ_1 and γ_2 are γ scaled by material properties of the annulus and nanotube, respectively.).

We then set initial boundary equations as follows, igniting the left end of the system to launch steady thermal wave propagation by means of a Gaussian temperature pulse. [107]

$\tau = 0$: u = Gaussian temperature pulse centered on $\xi = 0$

$\tau = 0$, $\xi \geq 0$: $u_2 = 0.012425$ (298 K)

$\tau = 0$, $\xi > 0$: $u = 0.012425$ (298 K)

$\tau = 0$, $\xi > 0$: $\eta = 0$

$\tau = 0$, $\xi = 0$: $\eta = 0.999$

2.4.2. Analysis of Fourier Description of TNA-Nanowire Systems

To solve the equations, we assume maximum thermal diffusivity of CNT, α (10^{-5} to 10^{-2}), and β (5 to 35) are varied as parameters for our contour plot (Figure 2.15a). We assume several material properties are constant on the basis of previous literature sources[32,100,108-115]. The molecular weight of TNA is 0.22212 kg/mol, its thermal conductivity [108] is 0.2783 W/m/K, and its density[109] is 1820 kg/m^3. The activation energy for decomposition of TNA is 127 kJ/mol [91], and k_0 is 3.75 x 10^{18} s^{-1}. A system initially at room temperature ($u_{atm} = u = 0.0124$ for TNA) will produce a reactive wave solution if one end is heated to ignition. Numerical solution of (2-12 - 15) demonstrates that, since the thermal conductance in the nanotube exceeds that of the reactive annulus, the reaction velocity along the nanotube component is increased substantially, directing the energy along its length. The interfacial conductance becomes insignificant beyond a minimum threshold ($\gamma_1 > 10^{-3}$, $\gamma_2 > 10^{-2}$ for $\beta > 5$) above which heat exchange between the phases is not rate-limiting (Figure 2.16). In this case, the effect of thermal resistance between TNA and

CNT would be very small, and rapid thermal equilibrium is achieved on the boundary in the narrow reaction zone between the two materials ($T \approx T_2$). Under these conditions, higher interfacial conductance cannot change the temperature profile. The non-linear nature of the source term causes the reaction velocity to increase disproportionately with an increase in nanotube thermal diffusivity above that of the reactive annulus, creating an amplified thermal wave, as shown in Figure 2.15a. The numerical solution of Figure 2.15a can be used in conjunction with the measured reaction velocities to estimate the effective thermal conductances of the MWNT. We find these values to be high, on average $2.1 \pm 0.32 \times 10^{-10}$ W/K for 22-nm-diameter MWNT. The value for 13-nm-diameter MWNT is $2.7 \pm 1.0 \times 10^{-11}$ W/K. For comparison, this is equivalent to a value of about 1,280 ± 200 W/m/K for an effective thermal conductivity of a 22-nm-diameter MWNT of height 2.36 mm (using the total MWNT cross section, including interior void space). The corresponding cross-sectional conductance, 4.5×10^5 W/m^2/K, is substantial, but only 0.01% of the theoretical upper bound of $10^9 - 10^{10}$ W/m^2/K over the range of 300 to 1000 K estimated by quantum constraints [116].

If the temperature dependence is included for thermal conductivities [117-118], heat capacities [102,111] and thermochemical properties [100,110-111,119] of TNA (Table 2.3) and CNT (Table 2.4), one can predict the reaction velocity explicitly. This refined model predicts 1.3 m/s for the wave velocity, in agreement with what is observed experimentally (Figure 2.15b) . Also, we investigated the effect of convection and radiation. The dimensionless heat convection coefficient, l, and dimensionless radiation coefficient, w, depend on k_0. As k_0 decreased, the reaction front velocity decreased (Figure 2.15c). But within the normal range of TNA [110] parameter values, convection and radiation did not affect the results.

Table 2.3. Temperature-dependent thermal properties of TNA [100,108,110-112]

TNA Basic properties	Cp (J/mol/K)	Q (kJ/mol)	α (m^2/s)	β
Temperature (Kelvin)	Specific heat	Heat of combustion	alpha	Beta
300	239.56	876.00	1.42E-07	4.18
400	317.90	874.98	1.07E-07	5.55
500	396.25	881.24	8.57E-08	6.87
600	474.59	894.68	7.16E-08	8.10
700	552.94	915.23	6.14E-08	9.23
800	631.29	942.85	5.38E-08	10.23
900	709.63	977.56	4.79E-08	11.09
1000	787.98	1019.40	4.31E-08	11.81
1100	866.32	1068.41	3.92E-08	12.39
1200	944.67	1124.64	3.60E-08	12.83
1300	1023.02	1188.14	3.32E-08	13.15
1400	1101.36	1258.97	3.08E-08	13.36
1500	1179.71	1337.16	2.88E-08	13.48
1600	1258.06	1422.76	2.70E-08	13.51
1700	1336.40	1515.81	2.54E-08	13.47
1800	1414.75	1616.35	2.40E-08	13.37
1900	1493.09	1724.42	2.27E-08	13.23
2000	1571.44	1840.04	2.16E-08	13.05
2100	1649.79	1963.14	2.06E-08	12.84
2200	1728.13	2094.01	1.97E-08	12.61
2300	1806.48	2232.22	1.88E-08	12.36
2400	1884.82	2378.36	1.80E-08	12.11
2500	1963.17	2532.03	1.73E-08	11.84
2600	2041.52	2693.45	1.66E-08	11.58
2700	2119.86	2862.39	1.60E-08	11.31
2800	2198.21	3039.15	1.55E-08	11.05
2900	2276.55	3223.46	1.49E-08	10.79
3000	2354.90	3415.59	1.44E-08	10.53

Table 2.4. Temperature-dependent thermal properties of MWNT [32,113-115]

MWNT Basic properties	Cp(J/mol/K)	k (W/m-K)	α (m^2/s)
Temperature (Kelvin)	Specific heat	Thermal conductivity	alpha
300	7.8	2347	0.002786
400	10.3	2686.96	0.002415
500	12.8	3000	0.002170
600	15.1	1956	0.001199
700	17	1695	0.000923
800	18.1	1435	0.000734
900	19	1304.35	0.000636
1000	19.8	1148	0.000537
1100	20.5	1017.4	0.000460
1200	21	913.045	0.000403
1300	21.4	834.8	0.000361
1400	21.7	756.2	0.000323
1500	22	717.4	0.000302
1600	22.2	678.3	0.000283
1700	22.4	620	0.000256
1800	22.6	563.91	0.000231
1900	22.8	547	0.000222
2000	23	535	0.000215
2100	23.1	520	0.000208
2200	23.2	508	0.000203
2300	23.3	497	0.000198
2400	23.4	487	0.000193
2500	23.5	478	0.000188
2600	23.6	470	0.000184
2700	23.6	463	0.000182
2800	23.7	457	0.000179
2900	23.7	452	0.000177
3000	23.7	450	0.000176

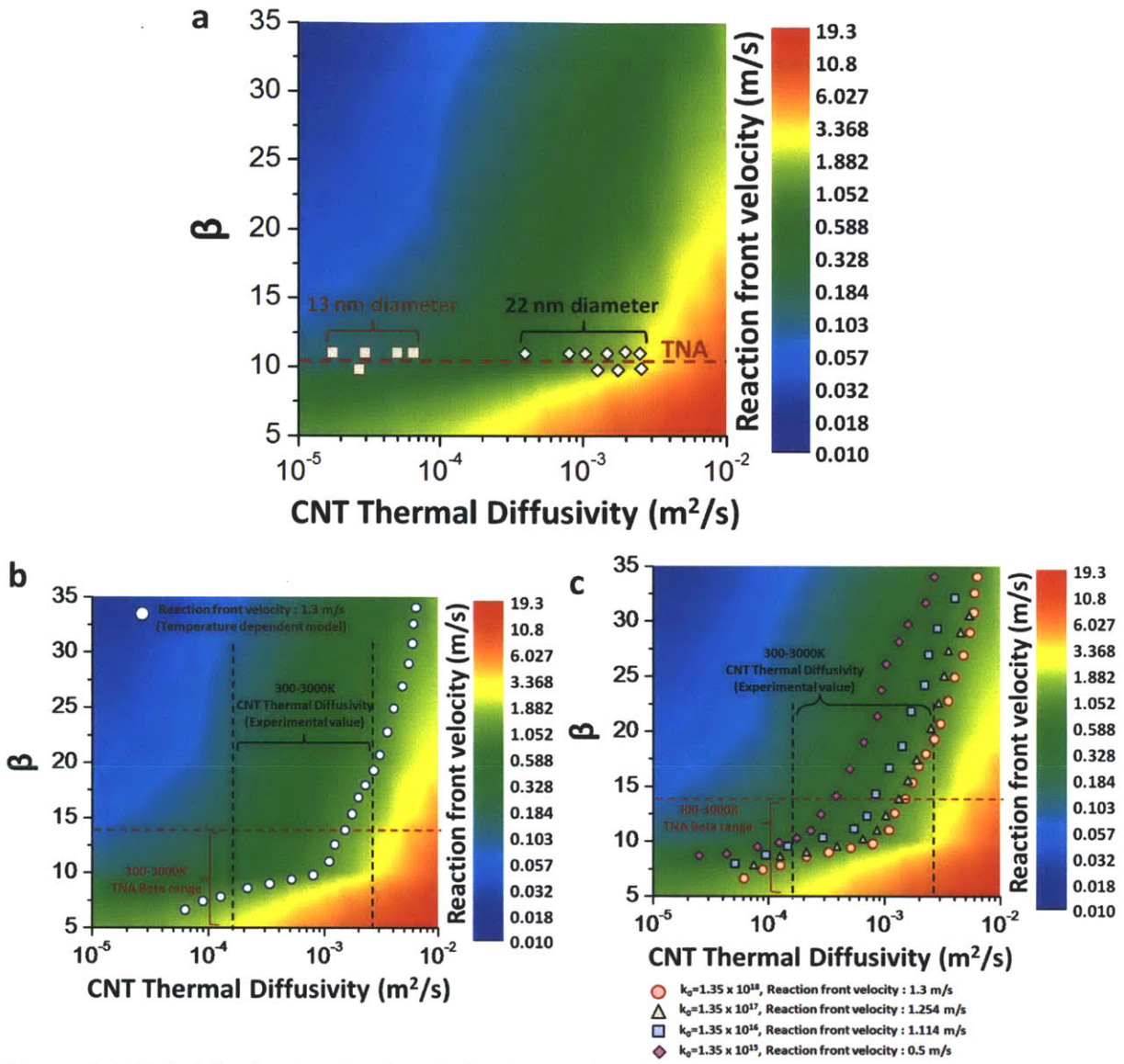

Figure 2.15. Model using Fourier description for 1D chemical reaction along nanowires. (a) Predicted reaction velocity from the Fourier model (equations 2-12-15) as a function of β, the dimensionless inverse adiabatic temperature of the annular material (10.6 for TNA, Table 2.3) versus CNT thermal diffusivity (m^2/s). Note that the reaction velocity increases with increasing CNT thermal conductance. Experimentally observed reaction velocities for both 13- and 22-nm MWNT are plotted for comparison. Low thermal diffusivity of 13-nm diameter case was due to the poorly aligned array of MWNT whereas 22-nm case has high thermal diffusivity from well-aligned array. (b) Reaction front velocity using temperature-dependent thermal properties for TNA and CNT. The reaction front velocity is 1.3 m/s. β and thermal diffusivity values are from other literature sources [108]. β is in the range of 4.2 to 13.5 (Table 2.3), and CNT thermal diffusivity (Table 2.4) is in the range of 0.0002 to 0.002. (c) Reaction front velocity using temperature-dependent thermal properties for TNA and CNT, as well as convection and radiation. The reaction front velocity is 1.3 m/s at $k_0 = 3x10^{18}$ (s^{-1}), the same as our thermal wave propagation model without convection and radiation. A decrease in the reaction rate constant results in a decrease in reaction velocity.

2.4.3. Interfacial Conductivity and Critical Parameters

After steady state wave propagation is attained, the reaction front velocity is constant along the whole MWNT. A dimensionless distance $\xi = 1000$ was sufficient to simulate steady state reaction front velocity. The non-dimensionalized distance of MWNT length 2.36 mm is many orders of magnitude larger than $\xi = 1000$. Thus, for lengths above 1000, the reaction front velocity will be constant. Interfacial thermal conductivity, G, between TNA and MWNT should not be the limiting factor in reaction front velocity enhancement [120], and we confirmed this for this model (Figure 2.16). In the case of low thermal resistance between TNA and MWNT, rapid thermal equilibrium is achieved on the boundary between the two materials ($u \approx u_2$). Higher interfacial conductance does not affect the temperature profiles of the two materials or the reaction front velocity, as long as the interfacial conductance is over some minimum value. Simulation results indicated that the minimum value of G for these conditions is 9×10^5 W/m^2/K. We define the location of the reaction front at each point in time as the point where η (the extent of chemical conversion of the reactive annulus) is 0.5 and calculate reaction front velocity accordingly, since the shape of the η profile is perfectly maintained after steady state wave propagation is achieved.

The parameter β is a significant factor in determining wave properties, such as the average velocity or the presence or form of velocity oscillations[107]. In this coupled system, α_0 determines the acceleration of the reaction wave. Figure 2.15a demonstrates this with simulation results from the numerical solution of equations (2-12 - 15) for a variety of conceivable fuels (β values) and thermal conduits (α_0 values). Most fuels have low thermal diffusivities in the range of 10^{-9} to 10^{-7} m^2/s [121-122], resulting in relatively slow chain reactions. For fuels reacting without a thermal conduit, $\alpha_0 = 1$, and the wave is not accelerated. However, in this coaxial structure, a

nanostructure with high thermal conductivity can rapidly transfer heat along its length, transporting energy to initiate reactions in the unreacted fuel. This mechanism accelerates the one-dimensional chain reaction wave anisotropically in the surrounding fuel layer.

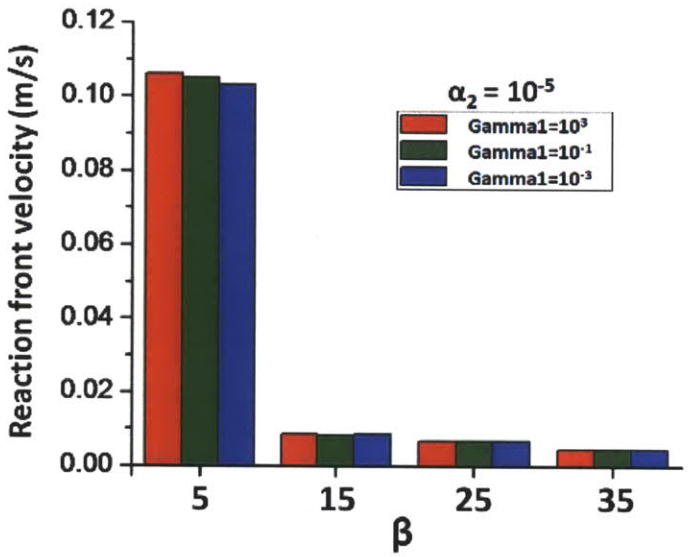

Figure 2.16. Effect of interfacial conductance (γ_1) and TNA properties (β) on reaction front velocity. If γ_1 is larger than 10^{-3}, reaction front velocities are approximately the same no matter the value of γ_1. $\gamma_1 = 10^{-3}$ corresponds to $G_0 = 9x10^5$ W/m^2/K, $\gamma_1 = 10^{-1}$ is $G_0 = 9x10^7$ W/m^2/K, and $\gamma_1 = 10^3$ is $G_0 = 9x10^9$ W/m^2/K. Velocities shown here are the same as Fig. 2c for the $\alpha_2 = 10^{-5}$ m^2/s case.

2.5. Thermopower wave : From Chemical to Electrical Energy Conversion

2.5.1. Measurement of Thermal to Electrical Energy Generation

The directional thermal wave evolves a corresponding thermopower wave in the same direction, creating a high specific power electrical pulse of constant polarity. In order to measure this power generation, the nanotubes were contacted to an oscilloscope with Cu wires and an Ag paste in the arrangement shown in Figure 2.17.

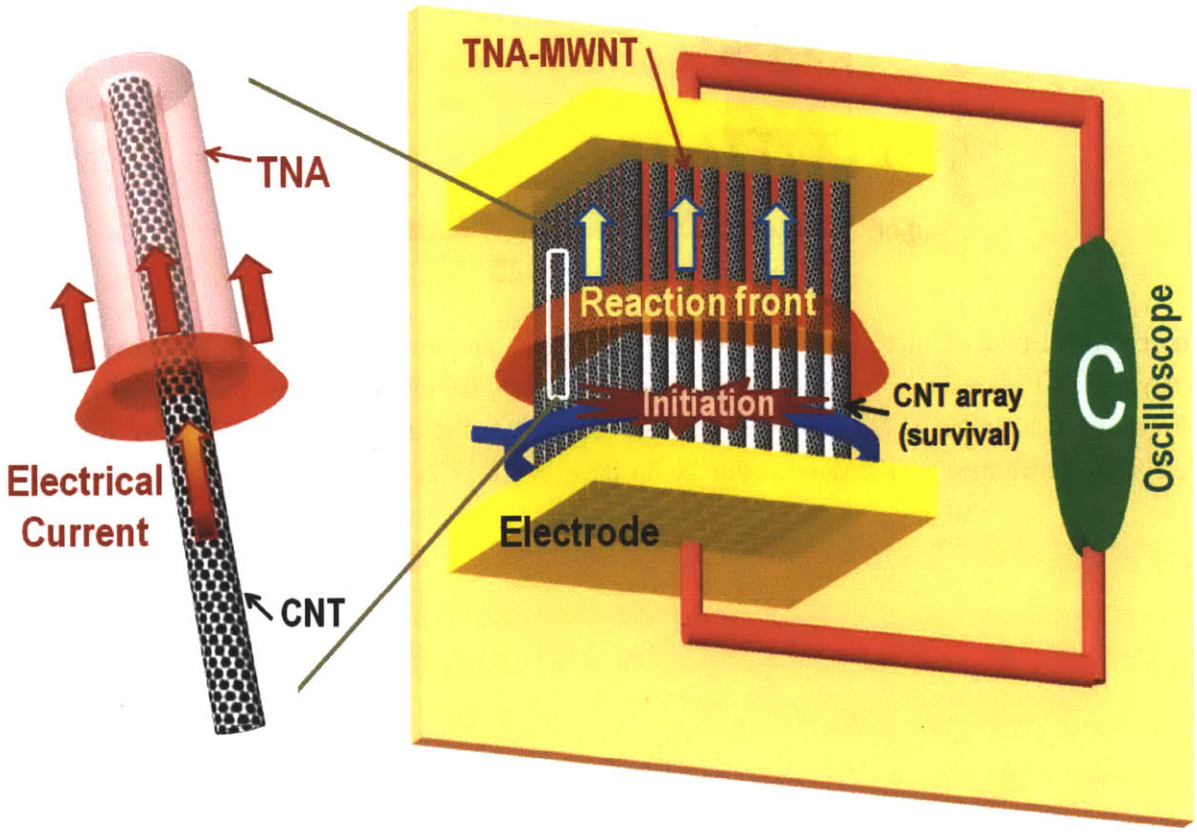

Figure 2.17. Illustration of the experimental setup used for measuring the corresponding thermopower waves that result from reaction wave propagation. Laser ignition (or electric arc discharge) at one end results in a thermopower wave.

2.5.2. Electrical Energy Generation in 1D and 3D Chemical Reaction

A thermal reaction wave leads to a thermopower wave and concomitantly to the generation of a high specific power electrical pulse with constant polarity. In TNA-MWNT, the exothermic decomposition of TNA creates the moving temperature gradient across the MWNT which can then produce electrical energy. The electrical charge carriers tend to move from the reaction front zone (the hottest area) to the unreacted zone in the CNT (the coldest area) as shown in the schematic of Figure 2.18. The voltage was positive for waves emanating from the positive electrode, indicating a pulse of majority electronic carriers traveling toward the negative electrode (Figure 2.19b). This thermopower wave is distinct from conventional, static thermopower in that we see single polarity pulses (positive or negative) over the reaction duration for high velocity waves. A moving thermal gradient across the conductor would produce regions of maximum, minimum and zero voltages based on the Seebeck effect, for example. This is in fact what we observe for samples with larger thermal mass and slower propagation velocities. Also, if the reaction is initiated at the middle of the sample, the current appears to reverse (Figure 2.19c). In contrast, the chemically driven thermopower waves in the high velocity regime (Figure 2.19b) have constant polarity always in the direction of the reaction. The results suggest that the wave traverses the system faster than the cooling time of the posterior region, resulting in a highly efficient energy direction. A small-mass sample with fast reaction velocity generates a sharp electrical pulse of constant polarity (Figure 2.19b). However, a large-mass sample with slow reaction velocity will cool significantly behind the reaction front, creating opposing thermal gradients and thus almost zero voltage (Figure 2.19c). This case can be envisioned as a symmetrical thermal pulse moving across the sample. Likewise, initiating the reaction in the middle of the sample will create two opposing temperature gradients, and the

voltage signal will have peaks of both polarities during the chemical reaction (Figure 2.19c). This cancellation of voltage leads to the loss of electrical energy. Carbon nanotubes have a relatively low Seebeck coefficient (80 μV/K) [123] compared with many thermoelectric materials, such as bismuth telluride (287 μV/K) [124] or Bi_2Te_3/Sb_2Te_3 superlattices (243 μV/K) [125], although modest increases are observed over the temperature range of 300 K and 930 K [126]. Thermopower waves, however, do not necessarily require low phonon and high electron transport rates as the thermal gradient is preserved in the propagation of the wave front. We note that materials with low figures of merit for thermoelectric devices can still produce high efficiencies for guiding thermopower waves, motivating a re-examination of these materials for thermal to electrical energy conversion.

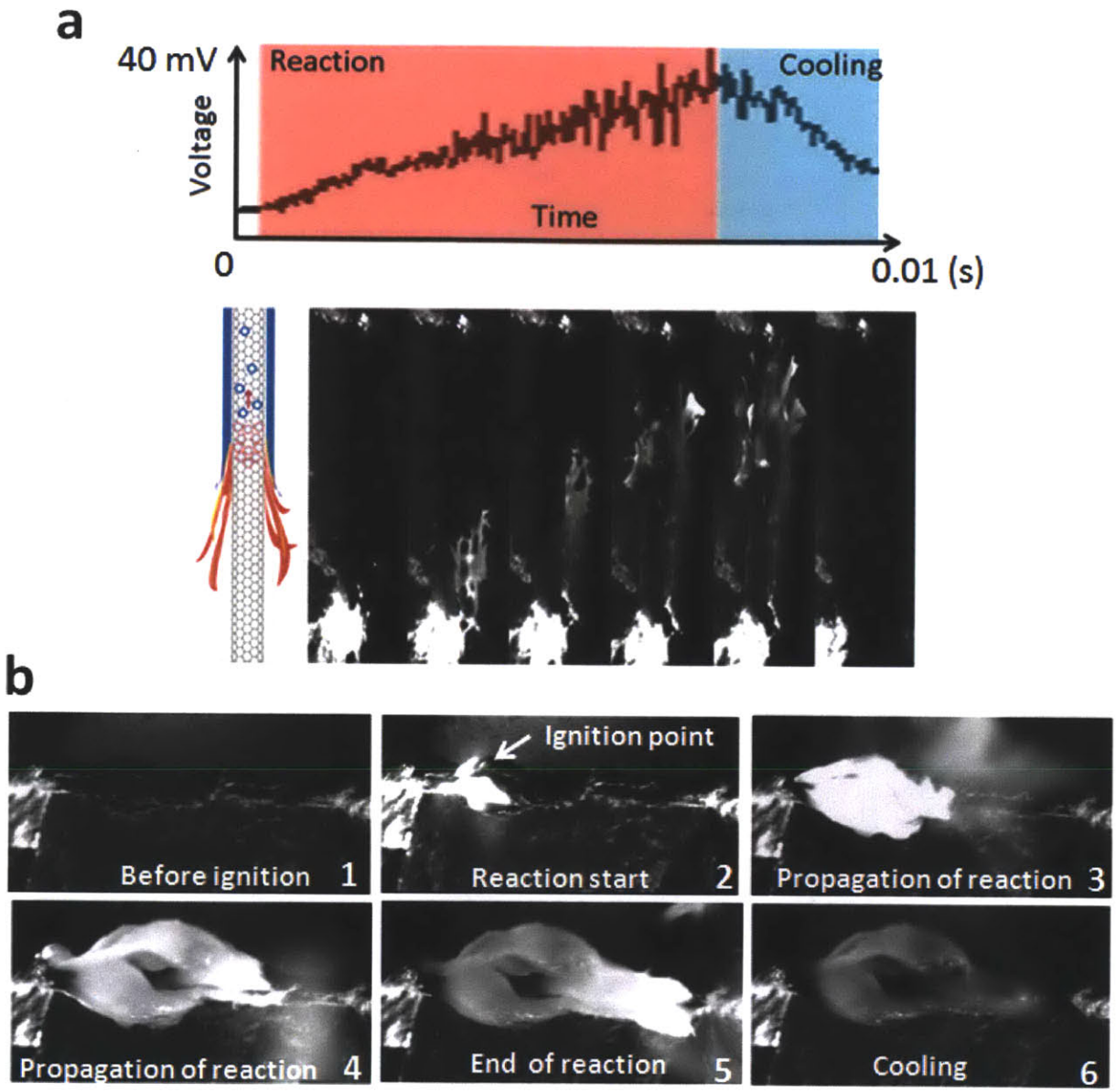

Figure 2.18. (a) Voltage generation synchronized with 1D chemical reaction. (b) High speed microscopic images of thermopower wave propagation in real time.

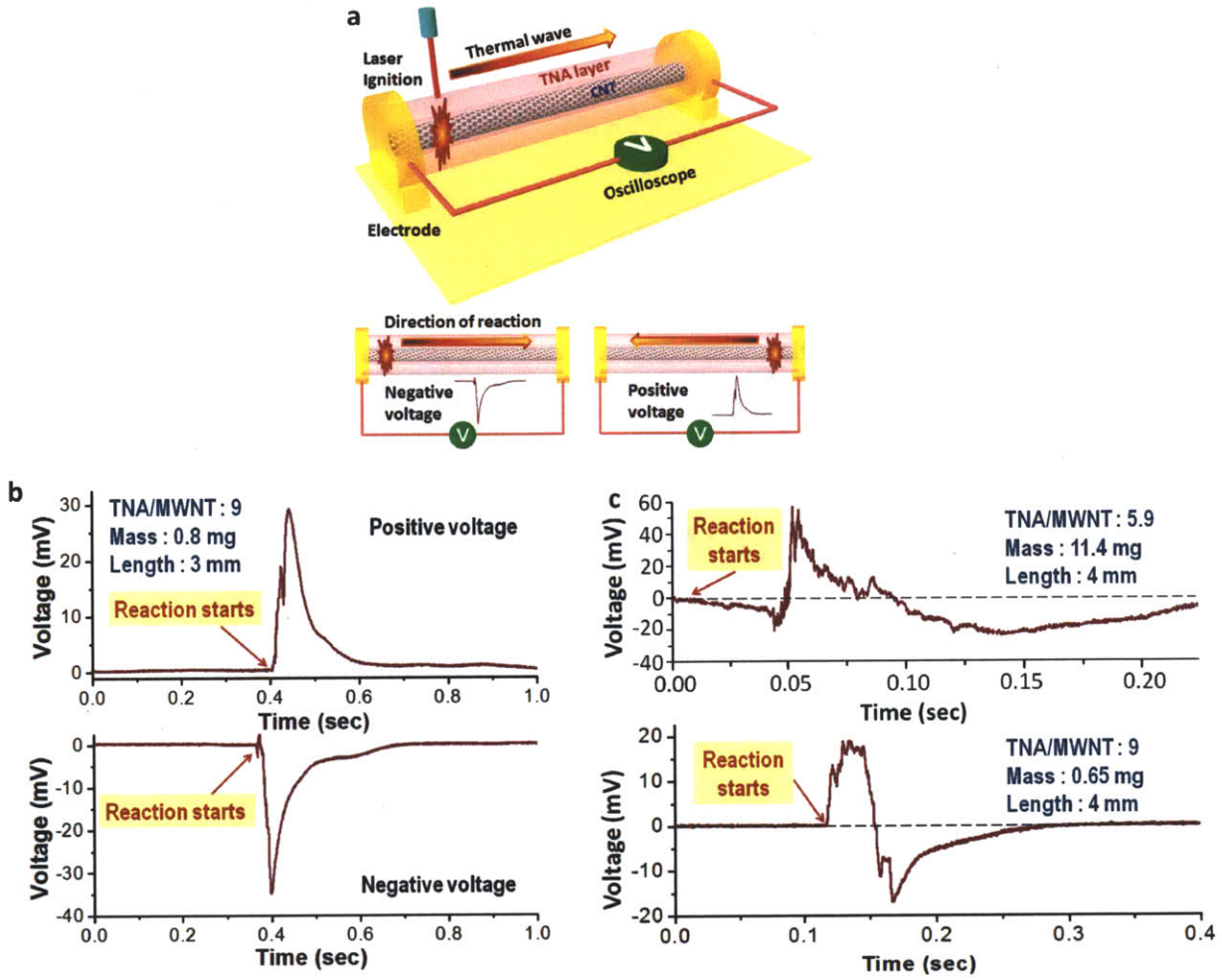

Figure 2.19. A chemically driven thermopower wave. (a) Laser ignition (or electric arc discharge) at one end results in a thermopower wave in the same direction of reaction propagation; either positive or negative voltage generation is observed. (b) The DC voltage generated by exothermic reaction of TNA is observed immediately after laser ignition with a single polarity peak voltage in this experiment of 30 – 35 mV (max observed = 210 mV) in both positive and negative directions for a total system mass of 0.8 mg with a TNA/MWNT ratio of 9. (c) These thermopower waves appear distinct from conventional, static thermopower generation mechanisms. If the system mass is increased, the reaction wave moves slowly and multiple peaks are observed instead, showing a reversal of polarity and an inflection point. Similar behavior is seen if initiation occurs at the center of the sample.

2.5.3. Dynamics of Oscillation : Chemical Reaction and Electrical Signal

Laser initiation at one end resulted in a voltage oscillation peak (Figure 2.20) of the same duration as the corresponding reaction wave, allowing us to calculate reaction propagation velocity for the whole sample volume. During the reaction propagation and subsequent cooling

stages, when a temperature gradient exists, the concomitant voltage signal reflects the electrical energy that the thermopower wave generates. This signal contains much information about the thermopower wave. It can be divided into two regions (Figure 2.20): a strong oscillation region and smooth region. There is a significant body of literature on velocity oscillation in traditional combustion waves[107,127], and most samples exhibited an oscillation region initially. In my measurements, velocity oscillations in a reaction wave can produce visible oscillations in the voltage signal synchronously with the reaction propagation along the length of the sample, regardless of the sign of the voltage. Thus, the reaction time corresponds to the duration of the oscillating voltage signal, and velocity can be calculated accordingly. The smooth region can be explained by conventional TE voltage generation from the temperature gradient remaining after the rapid propagation of thermopower wave has finished. The voltage returns to zero when the temperature across the sample has equilibrated. Comparison between optical microscopy and the electrical signal shows that this region appears to coincide with the self-propagating wave front. There is good agreement between the initial rise time of the thermally induced voltage signal and the optically measured reaction front. The smooth zone appears to be thermoelectric voltage generation due to the residual temperature gradient following the rapidly propagating wave.

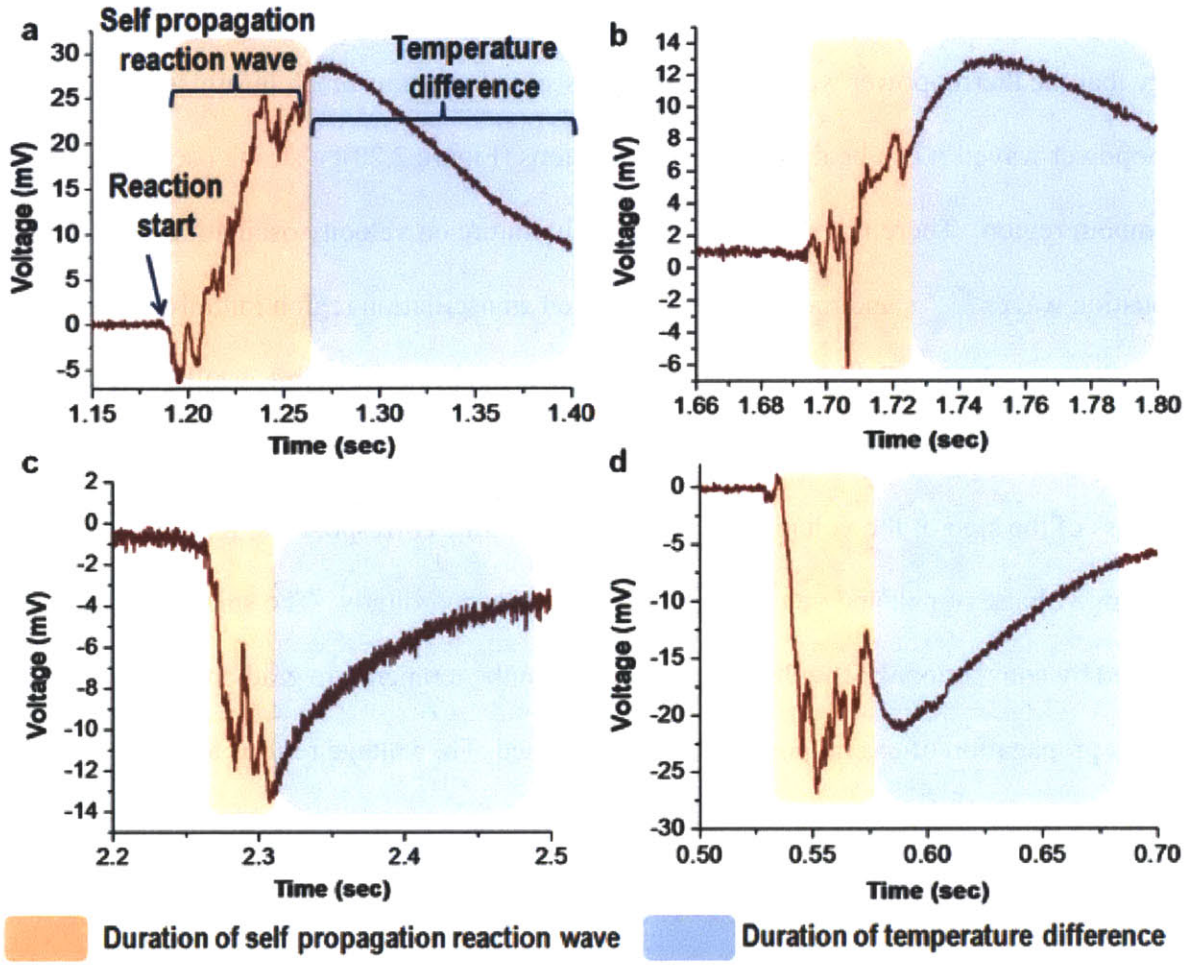

Figure 2.20. Thermopower voltage signal in reaction zone and cooling zone. The thermopower voltage signal is divided into two regions. Initial transient oscillation zone indicates reaction time[107,127], and smooth zone reflects cooling time. (a), (b) Positive voltage generation with clear oscillation and smooth regions. (c), (d) Negative voltage generation with oscillation and smooth zones.

2.5.4. Correlation between Reaction Front Velocity and Thermopower Wave

The reaction velocities determined from thermopower voltage signals appear in Figure 2.21. One reason for the scaling of reaction velocity in Figure 2.21 is orthogonal heat transfer in the TNA-MWNT arrays. Since all the samples had similar lengths (between 3 and 6 mm), a larger sample mass corresponds to a larger cross-sectional area and, therefore, increased orthogonal heat propagation that would eventually cause an overall system loss in an anisotropic

reaction velocity. Schematic in Figure 2.21 explains the 2-dimensional flame dissipation in larger samples. To illustrate this further, high speed video microscopy was used in Figure 2.22 to map the reaction front velocities as a function of orientation angle from the initiation point for an array of relatively large mass. Along the zero-degree axis (parallel to the nanotube orientation), the reaction propagates 6 to 13 times faster than in the orthogonal direction. As the number of parallel nanotubes in the array increase with mass, a greater fraction of heat travels orthogonal to the wave propagation, slowing its velocity and reducing the specific power. It means that increased orthogonal heat transfer slows the reaction wave and hurts the performance (*i. e.* decreases the specific power) of large-mass TNA-MWNT devices. Figure 2.23 is the histogram of reaction front velocity of compiled data sets measured by all 3 methods : High speed microscope, optical fiber setup, and thermopower wave voltage signal.

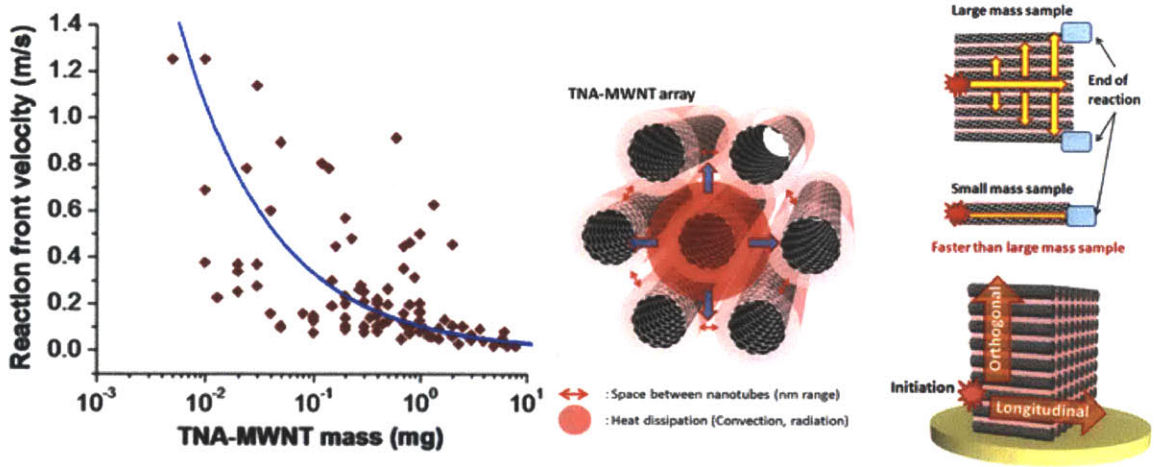

Figure 2.21. Reaction velocity as calculated from thermopower voltage signals (left). The blue line is a curve fit to guide the eye. Illustration of heat transfer in TNA-MWNT array (right). Heat dissipation is blocked between individual nanotubes in the array. Convection or radiation from reacting fuel is absorbed by surrounding MWNT, contributing to their reaction waves. Orthogonal heat transfer is not suppressed in large mass (2D) devices compared to small mass (1D) devices. Orthogonal and longitudinal heat transfer directions in a TNA-MWNT array (bottom right).

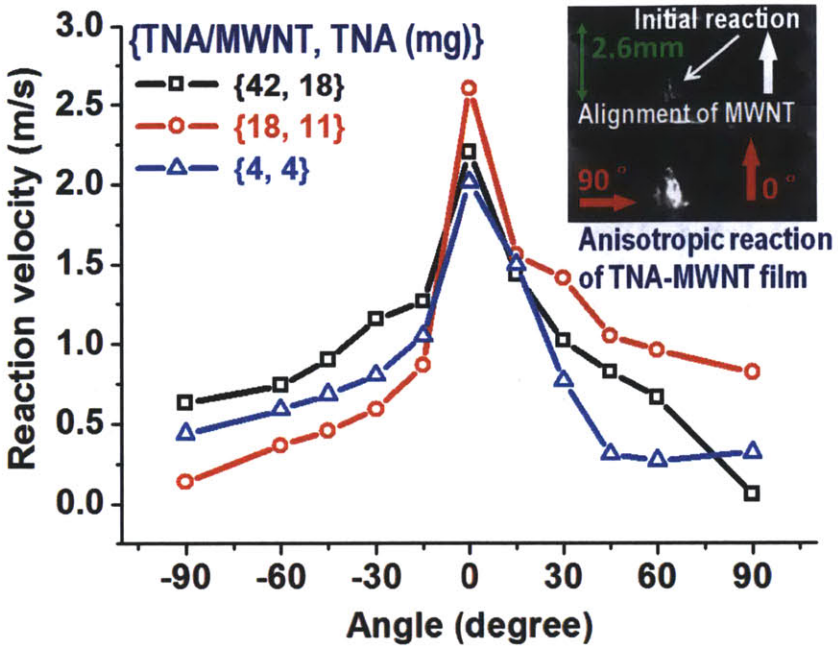

Figure 2.22. Anisotropic reaction propagation. For larger samples, there remains a large axial component to the reaction wave, but also a portion that is orthogonal. The reaction velocities along the aligned (0°) and orthogonal (90°) directions show a discernable peak along the axial direction. (Reactions were initiated at the base.) Parenthetical numbers are the mass ratio and mass of TNA.

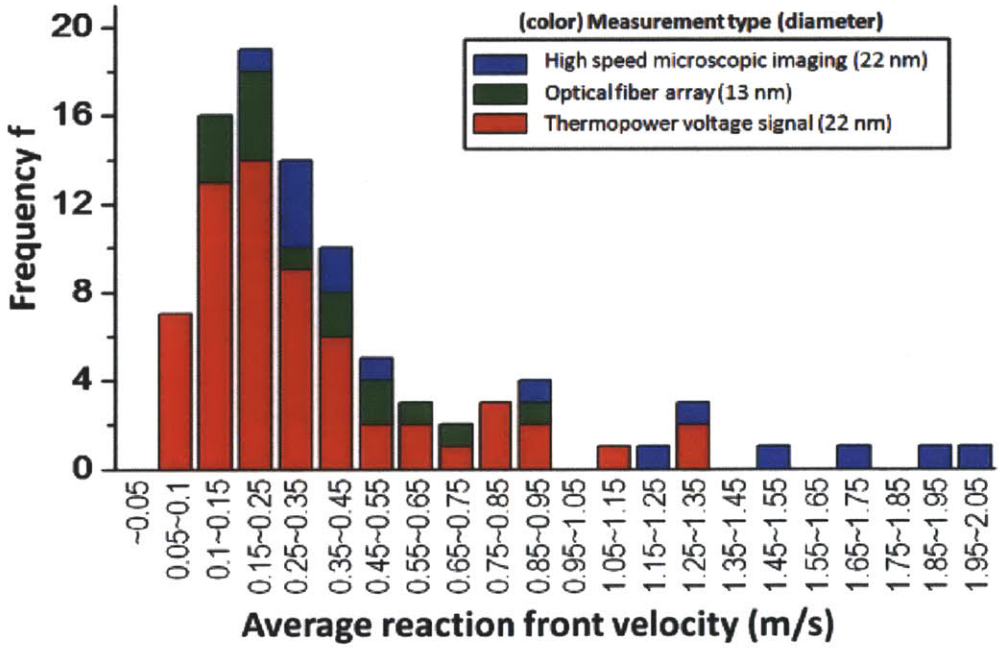

Figure 2.23. Histogram of compiled data sets of TNA-MWNT reaction velocity. This histogram includes results from three different reaction velocity measurement techniques. High speed microscopic imaging or optical fiber array can capture multiple positions of the wave front in time, yielding an accurate velocity. Also, the initial transient rise of the thermopower voltage correlates with the reaction front velocity.

2.5.5. Power Scaling with System Size

Examining the specific power as a function of sample mass (Figure 2.24) for 115 devices demonstrates a significant sample-to-sample variation, mostly due to differences in reaction velocities. However, the maximum values observed exceed 7 kW/kg, and are substantially larger than those for even high performance Li-ion batteries that have much slower discharge rates. Moreover, these high specific power values were observed as the sample mass decreased, a scaling trend that is very favorable for powering micro- and nano-scale devices. The limit of thermopower produced from just the Seebeck effect can be derived from simulated temperature gradients. The scaling trend is somewhat predicted by accounting for the change in reaction velocity with the system size and using a conventional thermopower model. In this case the specific power P/M_t is:

$$\frac{P}{M_t} = \frac{S^2}{R_i \rho \pi r^2 L}\left(\int_0^L \frac{dT}{dL} dL\right)^2 \tag{2-16}$$

$$T_N = \exp\left(-\frac{kA}{\rho C_P V}\frac{L}{v}\right)(T_H - T_L) + T_L \tag{2-17}$$

where P is thermopower, M_t is the mass of TNA-MWNT, S is the Seebeck coefficient of nanotubes, R_i is electrical resistance, ρ is the density of nanotubes, r is the radius of nanotubes, L is the length of the region that the thermal wave propagates, T is temperature (spatially dependent), T_N is the lowest cooled temperature behind the reaction zone, T_H is the temperature of the reaction front, T_L is the ambient temperature, C_p is the specific heat of nanotubes, V is the volume of nanotubes, A is the area in contact with cooling source, k is the coefficient of all cooling effects including thermal contact resistance, convection, radiation, and v is the reaction

velocity of thermal wave. I assume that reaction front temperature T_H is the adiabatic flame temperature. In the case of small mass TNA-MWNT, the reaction velocity is much faster than the time scale of heat diffusion; T_N is nearly the same as T_H. But in the case of large mass TNA-MWNT, the time scale of reaction velocity is similar to the time scale of heat diffusion, and cooling behind the reaction front makes T_N lower than T_H. The temperature gradient between T_N and T_H (the region behind the propagating reaction front) is opposite to the temperature gradient between T_L and T_H (the region ahead of the reaction front), and it causes charge carrier movement and a current in the opposite direction. This trend is stronger with the slow reaction velocities of large mass samples than fast reaction velocities, and specific power has an inverse scaling trend. A relatively fast cooling time with a slow reaction velocity causes a reverse temperature gradient and a diminution of specific power in the direction of wave propagation. While predicting the general trend with system mass, we note that this model under-predicts the observed specific power by as much as 3000 W/kg in some cases. Hence, the nature of the induced thermopower current requires further study. There is an extensive literature on enhanced electron-phonon coupling in 1D-confined systems such as carbon nanotubes. This coupling manifests itself, for example, in the induction of electrical current with polar fluid flow over an array of CNTs [128], and negative differential conductance [129]. The thermopower waves, studied in this work for the first time, seem to propagate at only 0.0002% of a typical Fermi velocity. However, it is possible that the moving thermal gradient can entrain carriers such that a net drift velocity is measurable, and confine charge carriers in a narrow region of the reaction front. The nature of this supplemental power generation will be the subject of further research efforts. The largest chemical to electrical and mechanical energy efficiencies observed in this work are 0.3 % and 0.12 % respectively, with the highest efficiency considering both as 0.42 %.

The Carnot limit, set by the reaction temperature under adiabatic conditions, is a maximum of 80%. At the high decomposition temperatures explored in this work, the dominant parasitic heat loss is radiative. Engineering controls to prevent radiative losses may increase the efficiencies closer to this limit. In addition, conventional TE materials such as Bismuth nanowire or Bismuth based composites would be the core materials with chemical fuel reaction. In this case, these materials has low thermal conductivity, so that the reaction velocity would be slow. However, they have high Seebeck coefficient that can amplify the electrical energy generation. The comparison between fuel/CNT layer and fuel/TE materials would elucidate more detail dynamics of thermopower wave and its efficiency.

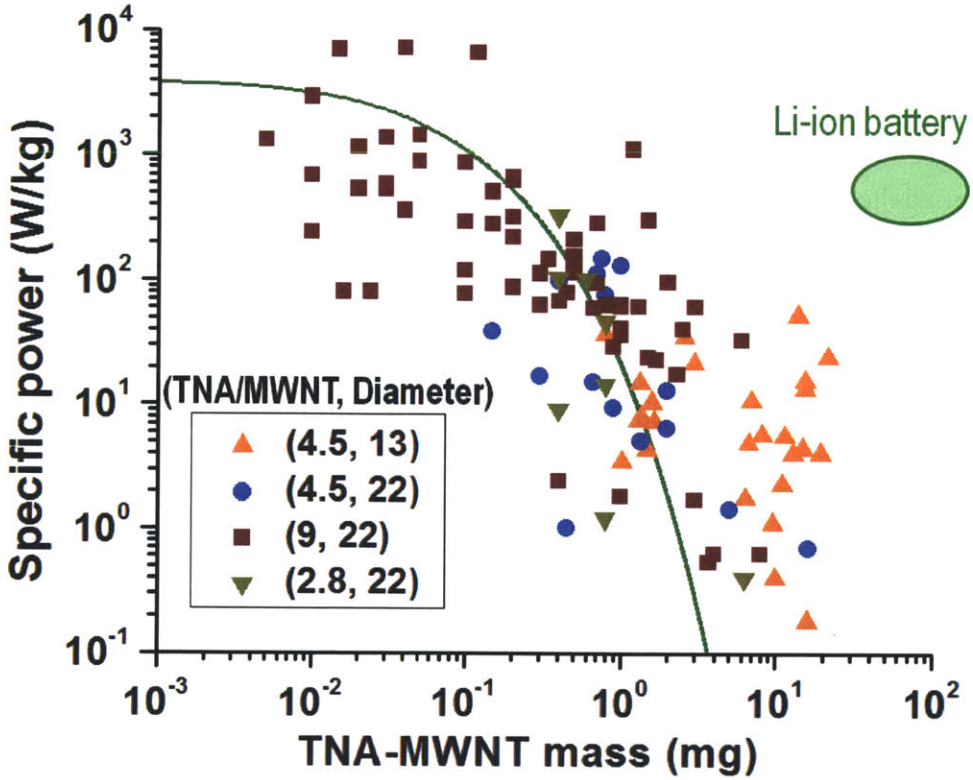

Figure 2.24. The specific peak power plotted as a function of system mass for three different TNA/MWNT mass ratios (9, 4.5, and 2.8) and two different MWNT with diameters (13 and 22 nm) shows an inverse scaling, highlighting that the thermopower wave is enhanced at the micro-nanoscale, and can produce power densities that far exceed conventional energy storage devices. The green line is equation 4 based on the conventional thermoelectric effect and the temperature gradient from reaction (300 K-2800 K).

2.5.6. Thrust Force via Thermopower Wave

In addition to the thermopower wave, the reaction creates a measurable pressure wave that is also of high energy density. The rapidly expanding, gaseous decomposition products from the thermal wave create a strong pressure pulse that is highly anisotropic. We measured the thrust force of this pressure wave using a micro-force sensor configuration (Figure 2.25) to be substantially higher per total propulsion system mass than many other comparable micro-thrust generators in the literature [130-135]. The MWNT array was placed either normal or parallel to the force sensor surface, and immobilized in both directions during testing. The propulsive force generated by the 1-D reaction was measured with a piezoresistive sensor (FlexiForce sensor, under 5 μs response time, force range 0 to 4.4 N, Tekscan). The sample was mounted on the force sensor on a tungsten plate with a lock-up housing to prevent vibration and other movement. The lock-up housing had a small hole to ignite the sample electrically or with a laser. A function generator supplied the electrical signal to the force sensor, and the input and output signals were monitored with a digital oscilloscope (DL 1735E, Yokogawa). The resistance of the sensor increased in proportion to the thrust force generated, which was applied perpendicular to the sensor. Temperature effects were negligible during the short observation period. Figure 2.26a illustrates the anisotropic nature of the thrust force. When perpendicular, the force peaks between 20 to 55 mN with a weak dependence on TNA loading, but in the parallel direction, the force was significantly reduced (< 9 mN). The relatively long duration reaction was obtained with TNA:MWNT mass ratio of 42 (max 47 mN, 175 ms duration) and 23 (max 35 mN, 200 ms duration). A reduction in loading ratio to 18 resulted in a larger peak thrust force (57 mN) for a shorter duration (110 ms). A smaller force is evolved (23 to 29 mN) as the ratio is further reduced to 5, but the reaction duration remains similar. The thrust reaches an optimal value at

intermediate loading (loading ratio of 18) since increasing mass beyond this point increases the orthogonal heat transfer requirement. The broader line-shape of the reaction curves for loading ratios of 23 and 42 supports this. The magnitude of the evolved thrust per unit mass is extremely large in comparison to all other solid propellant microthrusters [130,135]. A free body experiment illustrates the directional nature of the evolved force (Figure 2.26b). In this experiment, the system was released after initiation of the reaction, and its motion was recorded with a synchronized high speed camera. The instantaneous trajectory was compared with the orientation of the MWNT array at each frame, confirming the directional nature of the propulsion. It is an intrinsic property of this material that the thrust is evolved along a single axis, a property not yet realized in any other system. We compare the TNA-MWNT system to other published micro-thrusters with respect to the total and specific impulse per mass ratio (Figure 2.27) since these are the figures of merit for micro- or nano-scale actuator systems. Electrokinetic, ferromagnetic, laser ablation jet, and other systems [131-132,134] require bulky housings to direct and channel thrust, and thus have impulse per mass values many orders of magnitude less than the TNA-MWNT system. The total impulse per mass of TNA-MWNT (300 N-s/kg) is 4 to 100 times of that of other proposed micro-thrusters. The specific impulse per total mass (5.5 s/μg) is over 10 times that of typical solid propellant micro-thrusters [130,132-133,135-136].

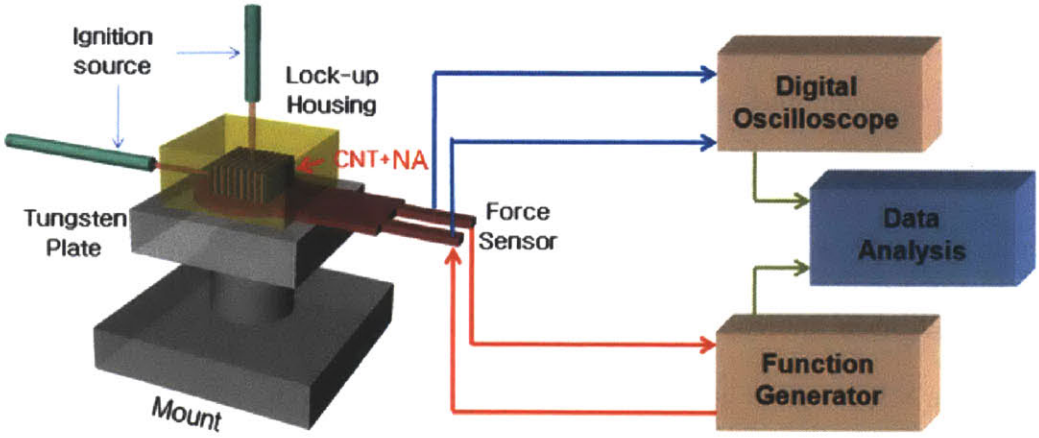

Figure 2.25. Schematic illustration of force and impulse measurement of TNA-MWNT. A TNA-MWNT sample was placed normal to the piezoelectric force sensor. A high speed camera simultaneously captured the reaction images.

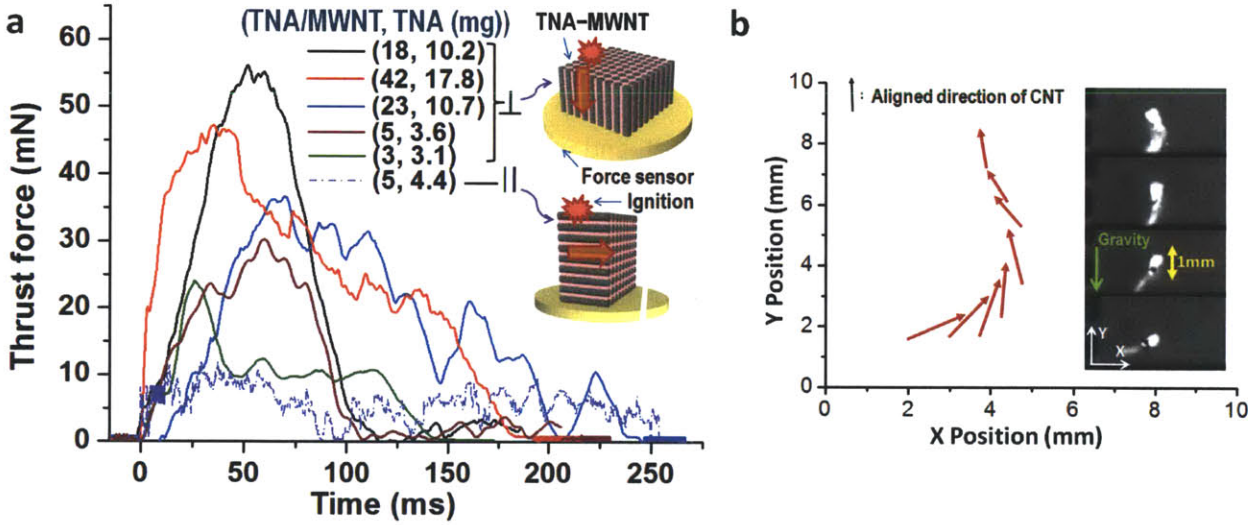

Figure 2.26. (a) The thermopower wave evolves a thrust force of commensurate duration. The transient force response is larger for the 5 samples (5 x 5 x 6 mm, 5–20 mg) aligned perpendicular to the sensor compared with the control aligned parallel to the surface. (b) An illustration of directed thrust: moving as a free body, the TNA-MWNT array (0.4 x 0.3 x 2 mm) proceeds in the direction of its orientation without external confinement.

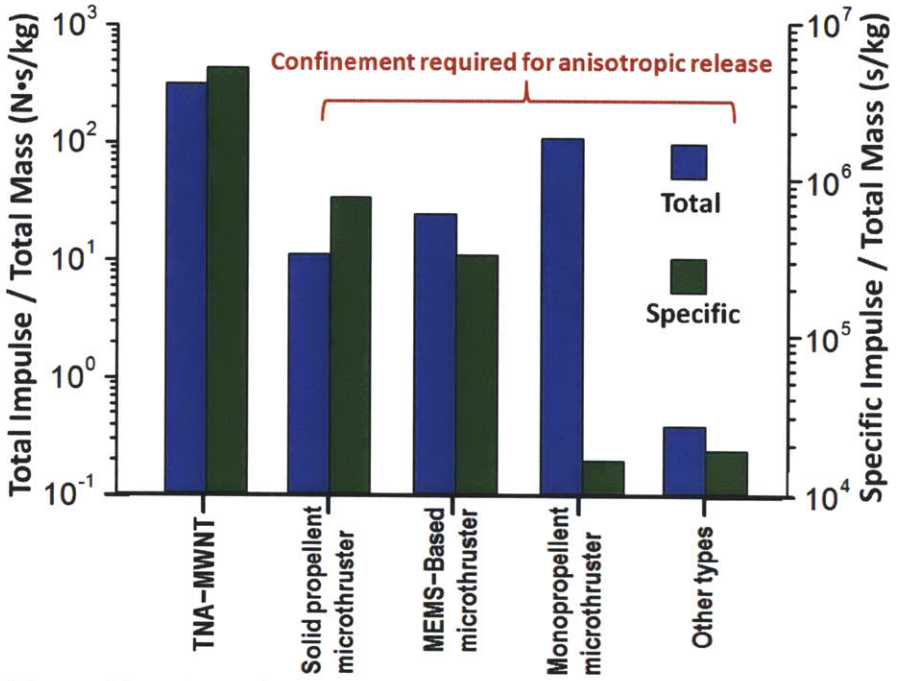

Figure 2.27. The total impulse and specific impulse per total mass of TNA-MWNT is significantly higher than other micro-thruster systems [130-135] because of the lack of a need for external containment, in contrast to electrokinetic [132], ferroelectric plasma [134], and laser ablation jet [131] micro-thruster approaches.

2.5.7. Comparison with Other Energy Storage and Generation methods

Thermopower waves in TNA-MWNT can create electrical pulses of high specific power, up to 7 kW/kg. Even though the duration of electrical discharge is relatively short, the maximum power density can compete even with high- performance Li-ion batteries, demonstrating the utility of thermopower waves. Figure 2.28 shows various electrical energy systems compared on the basis of their power density and volume. Recently, Kang and Ceder[137] reported macroscale Li-ion batteries with power densities up to 25 W/cm^3, far surpassing previous Li-ion technologies. By comparison, NiMH batteries can produce about 1 W/cm^3 at a similar scale[138]. However, the necessity of smaller power sources for MEMS devices has spurred development of electrical energy sources between 10^{-1} and 10^2 mm^3 in size such as MEMS fuel cells[139-140],

supercapacitors[141], and vibration energy harvesters[142]. The power density of these devices has remained lower than that of full-size Li-ion batteries.

However, for so-called "smart dust" applications[143], power sources smaller than 10^{-1} mm^3 are indispensable, as the total device volume must be less than 1 mm^3. For example, a 10^{-3} mm^3 thermoelectric harvester[144] can produce about 200 $\mu W/mm^3$. More recently, Albano *et al.*[145] have designed an even smaller on-chip Zn/AgO battery operating at about 400 $\mu W/mm^3$. Dudney *et al.*[146] have reported a somewhat larger Li microbattery with high power density up to 10000 $\mu W/mm^3$. Notably, the power density of thermopower wave generators (up to 80000 $\mu W/mm^3$) surpasses all these power sources and easily fits within smart dust size limitations, even at this initial stage of research with only one nanocomposite, TNA-MWNT. Moreover, since the scaling trend of thermopower wave generator specific power is inversely proportional to nanocomposite size, the synthesis of materials at extremely small scales is expected to boost maximum peak power. Opportunities for further enhancement also exist in reducing thermal losses, particularly radiation, through systems engineering and design.

While large-scale supercapacitors (not included in Figure 2.28) will generally still produce the highest power pulses of these available technologies, their self-discharge rate is high enough that they are not practical for long-term energy storage. Likewise, self-discharge saps energy stored in batteries, although generally over a longer time scale than capacitors. Thermopower waves, by contrast, use energy stored in the chemical bonds of fuels, which can remain stable for years, providing another advantage over these other power generation systems. Systems like fuel cells also use chemical fuels as energy sources, but have much lower power density compared to thermopower wave generators due to their slower reaction rates.

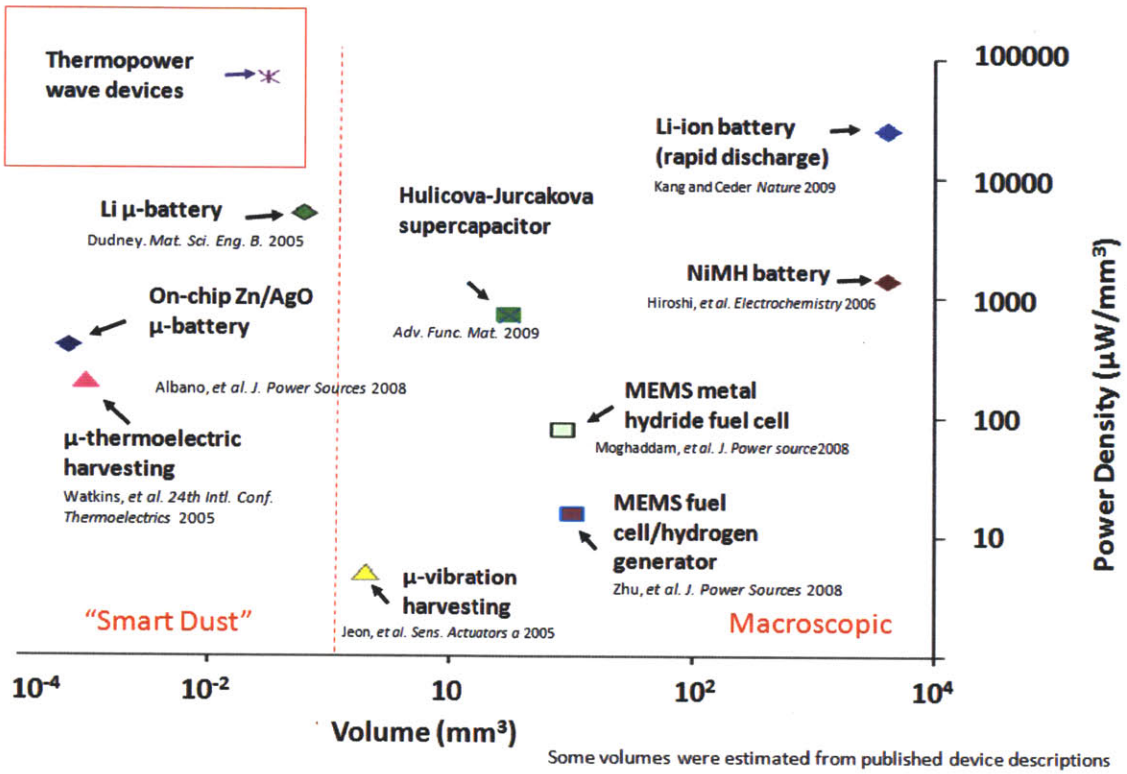

Figure 2.28. Comparison of power densities from various electrical energy sources. (Some volumes were estimated from published device descriptions.) Two different volume scales are presented; "smart dust" is generally defined to be less than 1 mm^3.

2.6. Outlook and Future Challenge

Many interesting directions for future theoretical and applied research exist. For example, more common fuels such as gasoline, ethanol, methane, or formic acid will need to be tested to enable wider applications for thermopower wave generators. These fuels may need catalysts to lower activation energy barriers and increase reaction rates, necessitating more detailed design of the nanostructures that serve as thermal and electrical conduits. The performance of thermopower waves will be affected by the choice of fuel, as shown by the dependence on β in the simulations of Figure 2.15. Differences in thermal diffusivity, specific heat, activation energy, and enthalpy of reaction can thus all play roles.

Another practical research advance would be on-chip initiation of thermopower waves, necessary for their application as micro- and nanoscale power sources. This may involve nanostructures to concentrate diffuse or broadband energy sources. In addition to enabling remote initiation, on-chip integration should increase energy efficiency of thermopower wave devices by minimizing the input energy needed to start the reaction. At present, the peak power output of these devices is excellent, but higher efficiencies are needed.

Energy efficiency would also be significantly increased by insulating against thermal losses. Due to high reaction temperatures, radiation is the largest mode of heat loss in the present device design. One could surround the fuel/thermal conduit composites with layers of insulation to reduce these losses, but the effect on the reaction of the fuel remains to be investigated. It could limit fuel choices to those that do not require oxygen. Moreover, for approximately one-dimensional structures smaller than 1 mm in diameter that operate at high temperature, the increase in diameter from insulation actually increases radiation heat losses by increasing the surface area. Higher energy efficiency will also increase the energy density of thermopower wave devices, making them smaller and more lightweight and thus more desirable for portable applications.

Fundamentally, the science and application of thermopower waves will be driven forward by new nanostructures that can control the direction and speed of these reactions and convert heat to electron motion (*i. e.* current) more efficiently. As shown in Figure 2.15, nanowires with different thermal diffusivities and electrical properties may alter the dynamics of the chemical reaction wave as well as the electricity produced. Materials with large Seebeck coefficients such as silicon nanowires or bismuth telluride could be alternative thermal conduits but may not be the most suitable due to their low thermal diffusivities.

In the theoretical regime, the biggest question is what the figure of merit is for thermopower waves in contrast to static thermopower. What material properties give rise to the additional power observed above the Seebeck limit? What roles do electron-phonon coupling and the Seebeck coefficient itself play? Or are other properties and phenomena the most important? Investigations of these physical principles will clarify what the true nature of the "electron entrainment" effect is and elucidate the design rules for high power, efficient, controllable thermopower wave devices.

3. Part II. Mass Transport within Carbon Nanotubes : Ion Transport

3.1. Introduction to Molecular Transport in Nanochannels

Nanofluidics is interesting field to be explored for many potential applications in nanodevice. In this field, many researchers have reported the results of ion channels with selectivity, nanopores for molecule detection, and transport using nanofluidic channel. Most of all, the ability to actively manipulate and transport single molecules in solution has the potential to revolutionize chemical synthesis, catalysis and sensing. Especially, understanding molecular transport through nanochannels is critical for developing novel platforms for biological detection[147-148], nanoscale reactors,[149] nanoscale injection,[150] and selective membranes [151-152].

3.1.1. Nanopore Sensing

Measurements using the Coulter effect measure the change in background current as particles or molecules pass through a small orifice of comparable size, allowing one to observe single translocation events. The externally applied electric field drives the movement of small charged molecules in solutions (Figure 3.1a). When the pore is blocked by the blocker (normally, large size molecules), the ion current suddenly drops, and generates a characteristic dwell time and the blockade current. The dwell time, and blockade current traces by moving molecules can give the information of which molecules pass through (Figure 3.1b). The Length of dwell time means how long the blocker stays inside of pores. The magnitude of blockade current shows the estimation of the relative size of the blocker. In the system with multi pores, the number of coulter states can give the information of how many pores are activated. When there is more than one possible channel, the Coulter analysis easily indicates multiple states. Multiple pores increase the number of Coulter states that are observed. If one observes only two states, we can

confirm that a single channel is operative. For example, protein based ion channels were studied using a protocol whereby dilute solutions are added to the lipid layer until a two state Coulter effect is observed. If more than one channel is operative, it is obvious from the channel currents. Coulter effect in nanopores has been shown for cells, particles, and more recently DNA, but not for single ions to date.[153-157]

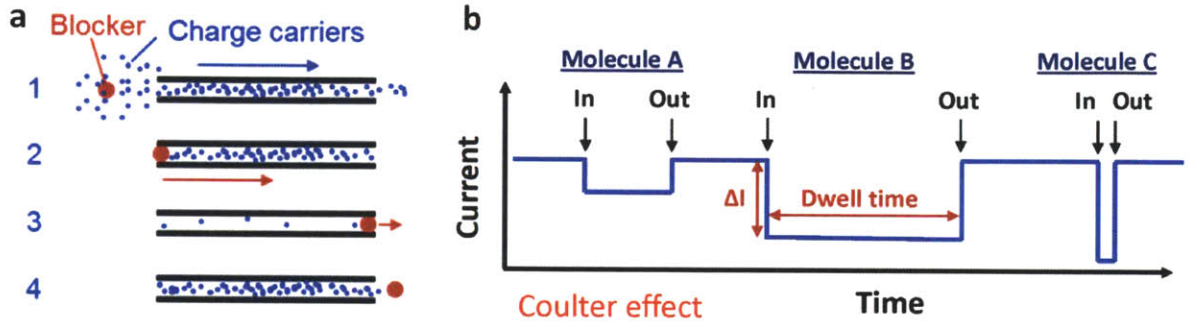

Figure 3.1. Mechanism of nanopore sensing. (a) Baseline current is constructed by charge carriers which can easily pass through the nanopore (1). When the blocker emerges into the entrance of nanopore, the charge carrier flow is blocked (2). While the blocker stay inside of nanopore, the baseline level is lower than normal current (3). After the blocker get out of the nanopore, the charge carrier flow is quickly recovered. (b) Each molecule as a blocker construct its own blockade current (ΔI) and the dwell time depending on its properties.

Figure 3.2. Illustration of # of Coulter states, constructed by # of operating pores. All pores are assumed in same size.

Although Coulter effect have been well known for several decades, it has not been long ago that nanopores or channels have been used to detect the extremely small molecules, such as DNA and

nanoparticles. Single ion-channels have been the most interesting topics in electrophysiology to understand the mechanism of triggering many events inside of cells. In 1996, the biological pore (α-haemolysin) was used to classify proteins using Coulter effect [158]. After four years, Deamer *et al.*[159] proposed nanopores as sensors to detect DNA translocation. Figure 3.3a shows various biological nanopores. Biological nanopores can be easily functionalized by chemical modifications, and controlled in local charge distributions [160]. However, the fixed size and instability of biological nanopores, and the limitation of its substrate like lipid bilayer[160] were the critical barriers for the practical applications. Therefore, there were strong needs for synthetic nanopores that can be utilized on any platform with controlled sizes. Emergence of nanofabrication and sensitive voltage or patch clamp facilitated constructing nanopores and measuring sensitive electrical signal around pA scale induced by the Coulter effect. Li *et al*[161] firstly showed 'ion-beam sculpting', which was able to drill the nanometre scale pores with controlled manner on Si_3N_4 membrane. This was the trigger for the field of the detection of DNA translocation and other nanoscale molecules. Figure 3.3c presents various types of solid state nanopores. That same year, it was proven that voltage-driven DNA translocation through nanopore induced the distinctive coulter effect in pA scale [162]. Not only DNA translocation but also other nanosize materials have been chosen as the targets that can be detected by nanopores. Hall *et al.*[163]. used SiN nanopores to detect the number, length and bundling of SWNTs. Various types of nanoparticles were classified by relatively large nanopore in the range of 50 nm and 500 nm [164]. Also, micro-RNAs in lung cancer patients were also detected by α-haemolysin protein. Recently, engineered nanosize hall in graphene have been explored as an effective platform to detect DNA translocation.[165-167]

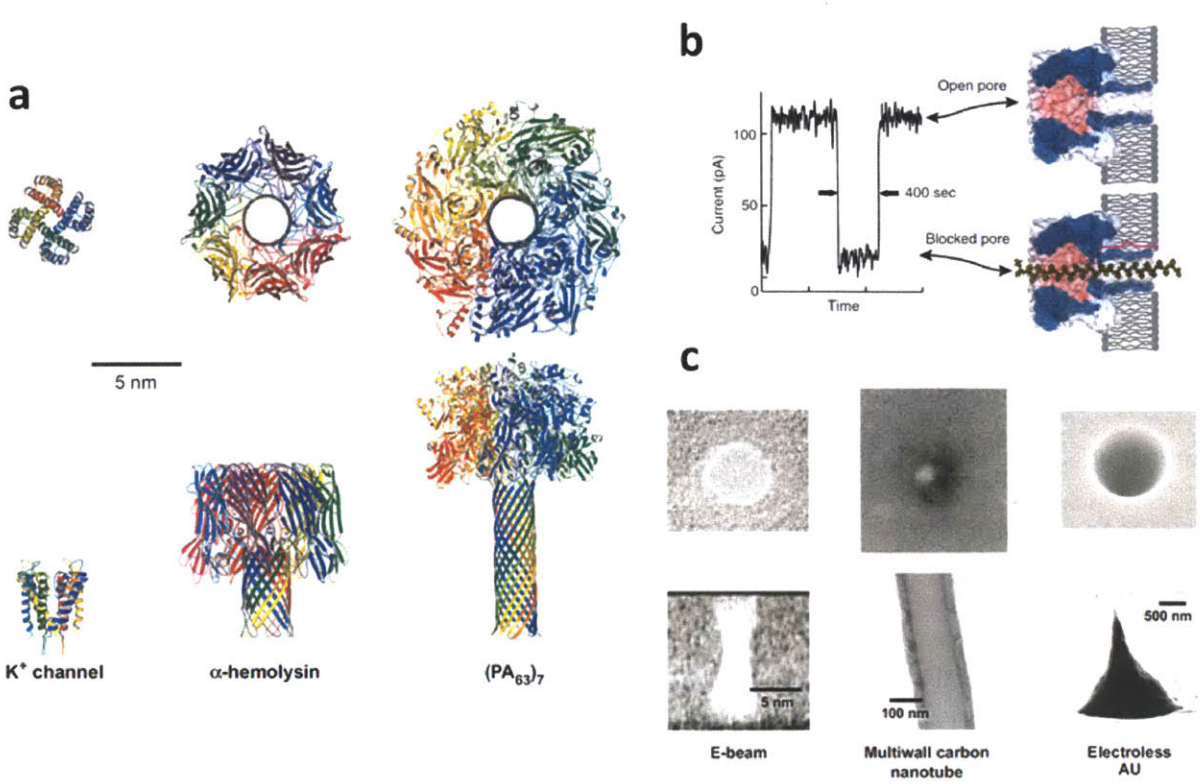

Figure 3.3. Biological and synthetic nanopores. (a) Crystal structures of a K+ selective ion channel, and the channel formed by α-haemolysin and model formed by Bacillus antbracis protective antigen.[148] (b) A typical trace of the ionic current amplitude through α-haemolysin pore.[168] (c) Synthetic silicon nitride nanopore, MWNT in epoxy matrix, and nanopores formed in track-etched polyimide.[148]

3.1.2. CNTs as nanochannels for Transport and Detection

Ion translocation in nanochannels are very intriguing to potentially revolutionize the current biology and membrane sciences. However, singular ion channels have only been realized in biological systems such as potassium, sodium and calcium channels. [169-170] Many synthetic nanopore platforms have been effective to capture and translocate DNA and proteins.[153,155-156,171] But, single, small molecule detection[154] using synthetic nanopores has remained very challenging. Basically, due to the relatively large diameter (3-10 nm) and small aspect ratio ($<10^2$) of typical synthetic nanopores, the electrical signals for both the duration of dwell time and the magnitude of blockade current, induced by single ion translocation are too

small to be measured in current platforms. Moreover, the electrical noise makes a huge disturbance in comparison to meaningful signals. Therefore, the long aspect ratio nanochannels are significant to generate the detection of single ion transport. Also, there have been no synthetic ion channels reproducing fast mass transport, and ion selectivity in biological systems, since the active modulation shedding the hydration shells are only forced by the carbonyl groups in biological ion channels.[157] In this context, single walled carbon nanotube (SWNT) is a promising candidate for simplified ion channel.[172-173] SWNT has extremely small diameter in the range of 0.8 nm and 2 nm, and it can be grown up to several cm. In this case, the aspect ratio of SWNT should be over 10^8, and it is the highest for nanochannels in the synthetic platforms. In addition, SWNTs that are made of graphitic surface with minimum corrugation are atomically smooth surfaces to construct the frictionless platform. Most importantly, the hydrophobic nature of the SWCNT internal surface suggests that decreasing SWCNT diameter should increase the ordering of internal water.[21] Due to these interesting characteristics, molecular simulations expect the interesting phenomena of SWNTs such as ion rejection, rapid proton conduction, and current blockade in electro osmotic flow.[174-175]

Theoretically, water transport through inside of CNTs has been very intriguing. Hummer *et al.*[176] firstly explained how the water conduction can operate in a hydrophobic CNT. Also, the mechanism of fast proton transport in a SWNT was anticipated in the same year. Carbon nanotube membranes were expected to have friction-less flow and the energy barrier at the entry and exit of the CNT pores.[177] Aluru *et al.*[178] modeled water molecules inside a SWNT with increasing diameters (Figure 3.4). The important observation is that under the critical diameter, water molecule chain is like a 1D water network to make high proton conductivity in electroosmotic transport. Above a critical diameter (0.86 nm), water arrangement becomes

more disordered as in bulk. MD simulations[179] predict that in order to produce size-based exclusion of ionic species such as Na+, K+, or Cl– in a uncharged CNT, the diameter should be less than 0.4 nm, which is forced to shedding hydration shell to enter the CNT.[180] Also, another simulation[181] shows that a 0.34 nm diameter CNT constructed with negative charges along its walls excludes Cl- while K+ ions can pass through. More recently, researchers have explored the enthalpy, phase change and water formation in SWNTs as a function of its diameter.[182-184]

Experimentally, others have proven that water can occupy the inside of CNTs by means of Raman spectroscopy[185] and HRTEM[186] (high-resolution transmission electron microscopy). However, there are a few results about the mass transport in SWNTs because of the limitations of experimental platforms and the difficulty of fabricating effective devices. Hinds *et al.*[187] and Holt *et al.*[152] firstly reported fast mass transport of water and gas molecules through MWNTs and DWNTs membranes, experimentally. Also, selective ion rejection[188] between cation and anion up to 98 % were observed in vertically aligned SWNTs embedded in Si_3N_4 substrates.

Experimental examples are lacking and most studies have demonstrated these interesting results in computational and theoretical contributions (Figure 3.5a). Also, most experimental work has been conducted in CNT membranes and MWNTs due to the difficulty of an individual SWNT manipulation and characterization. The more pressing problem is that, for many experimental data sets in literatures, fundamental disagreements are still remain (Figure 3.5b). It is the huge barrier to use a CNT for understanding detail mechanism and applying it in practical nanofluidic devices. In this research, our aim is to designing and fabricating new devices to realize and characterize interesting nanofluidic phenomena and single ion translocation in SWNTs. The development of the working high aspect ratio nanochannels from CNTs will be the breakthrough in the field definitely with many possible applications.

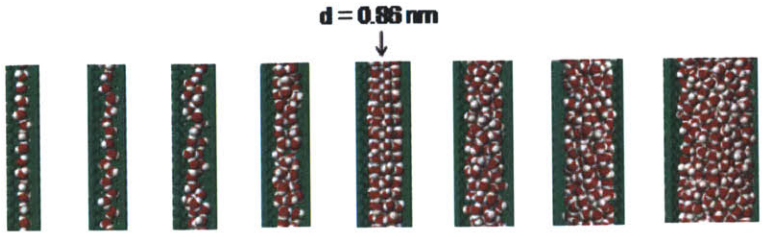

Figure 3.4. Water molecule chain network through interior of SWNTs. [178] Under the critical diameter (<0.86 nm), water molecule forms 1D chain. Above 0.86 nm, the 1D chain is disordered, and close to bulk states.

a **Published Items in Each Year**

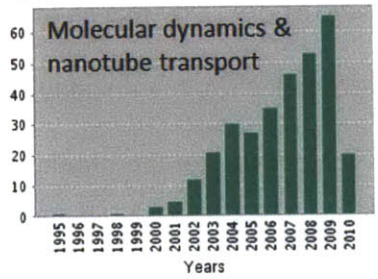

b

	Diameter of CNT (nm)	Enhancement Factor	Slip Length (nm)
X.C. Qin et al	0.81-1.59	51-882	8-53
		21-192	25-4
J. K. Holt et al	1.3-2.0	560-8400	140-1400
B. J. Hinds et al	7	43860-77018	39000-68000
A. J. H. McGaughey et al	0.81-1.66	433-6500	
	1.66-4.99	47-433	30-105

Figure 3.5. (a) The number of publications for studying molecular dynamics and CNT transport. (b) Comparison of enhancement factor and slip lengths obtained with a single SWNT approach.[189]

3.1.3. Concept of Obstructing Charge Carrier Flux by Blocking Ions

The concept of this work is developing a nanopore platform using the interior of a single walled carbon nanotube (diameter = 1.1-2 nm) to demonstrate and study the detection of single cations of Li^+, K^+, Na^+ and Cs^+.[190] Due to the small diameter and the hydrophobic nature of SWNTs, the charge is carried by protons via a 'hop-and-turn' Grotthuss mechanism.[191] By entering the nanotube, these single ions interrupt an otherwise constant proton current that traverses the conduit.[174-175,190] Figure 3.6 is a illustration of single ion blocking in a SWNT at a time that the blocking ions such as cations occupy the inside of SWNTs.

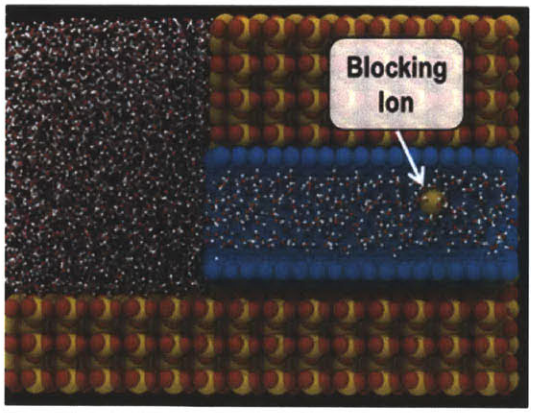

Figure 3.6. Illustration of proton transport and blocking ion in SWNT nanochannel.

3.2. Dynamics of Interior Transport of Ions in SWNTs

3.2.1. Design and Fabrication of the Platform

The platform is constructed using an epoxy structure that acts as both an oxygen plasma mask for the opening of the nanotube ends, and to form two liquid reservoirs at either side.[192] The SWNT are synthesized and aligned using methane CVD in a horizontal quartz tube furnace with an inner diameter of 22 mm (Figure 3.7).[193] After the patterned catalyst layer near the top edge of only one side, 0.5 nm-thick Fe, was deposited on a Si/SiO_2 wafer by electron beam evaporation, the substrate was placed in the quartz tube[193]. Methane (CH_4) was the carbon source. Hydrogen (H_2) and argon (Ar) were used as catalysts and carrier gases, respectively. The flow rate was 3 sccm of H_2 during increase of temperature up to 950 °C for 46 minutes, and the temperature and the flow rate were maintained for 30 minutes. Next, the temperature was increased up to 1015 °C for 33 minutes. After these steps, CH_4 was introduced into the furnace at 1015 °C and 1 atm, and ultra-long aligned SWNTs (Figure S1) were grown for 3 h 30 minutes.

To fabricate the epoxy structure for reservoirs of ionic solution and a mask against plasma etching, the SU- 8 photoresist was used, and we followed the detailed method described in Lin et

al[194]. The epoxy structure was glued onto the silicon wafer containing ultra-long aligned SWNTs using a UV-curing optical adhesive (Norland). The plasma etch removes exposed SWNT leaving 1 mm across the protected section, and opens both ends at the bottom of epoxy reservoirs (Figure 3.8). Only the SWNTs long enough to reach the central portion of the epoxy structure were protected by the divider (Figure 3.7), and all the uncovered portions of the SWNTs were removed by oxygen plasma etching. The duration of oxygen plasma etching was optimized to remove all the exposed SWNTs and not to etch out the SWNTs underneath the epoxy wall. SEM images were taken repeatedly during the process.

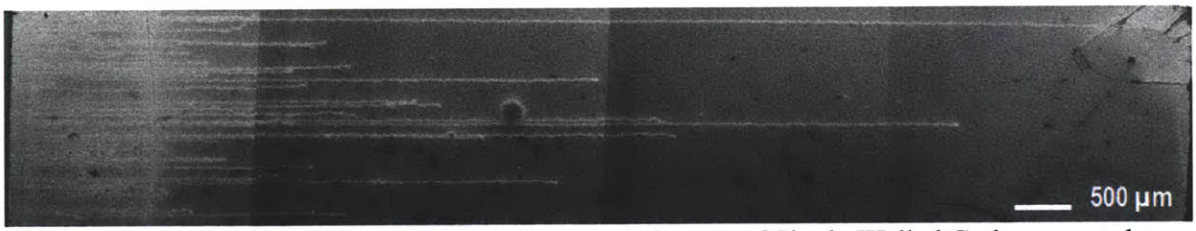

Figure 3.7. A series of Scanning Electron Microscopic images of Single Walled Carbon nanotubes (SWNTs) on Si/SiO_2 wafer grown by CVD method.

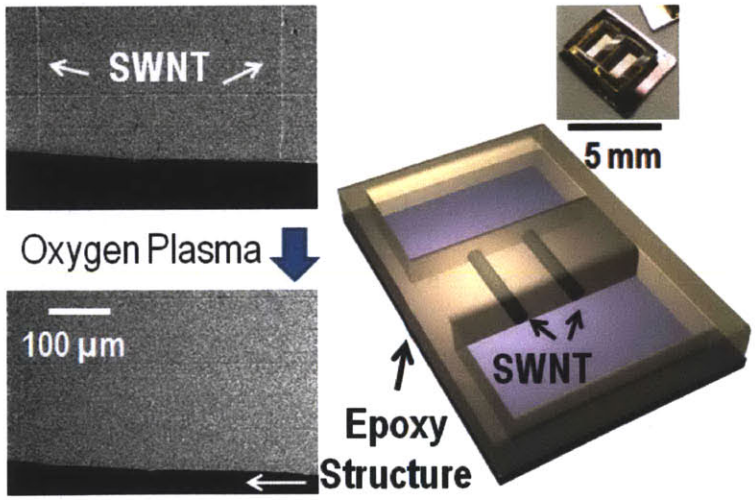

Figure 3.8. Schematic of SWNTs ion channel device. Ultra-long and aligned SWNTs are on silicon wafer, and the epoxy structure is attached to the wafer by UV glue to cover SWNTs during etching.

3.2.2. Ion Current Testing and Characterization of SWNTs Channels

- Ionic current testing

With both compartments filled with ~ 15-20 μL aqueous ionic solution (ex : KCl) ion current across the reservoirs was monitored using Axopatch 200B (Molecular Devices, 2 kHz Bessel low-pass filter, 250 kHz acquisition frequency). Potentiostat (PGSTAT30, Autolab) was used for voltages higher than 1V at 3-10 Hz acquisition frequency.

It is important to understand migration of which ions is causing the current that we measure. Figure 3.9a is a schematic of our experimental platform. Ionic solutions are connected via open-ended SWNT. Ag/AgCl electrodes are used to apply electric field across the reservoirs. Using Ag/AgCl electrodes minimizes the electrode polarization and therefore allows stable ion current measurement[195]. Electrochemical reactions at cathode and anode are shown below.

Cathode (-): $AgCl(s) + e \rightarrow Ag^{o}(s) + Cl^{-}(aq)$

Anode (+): $Cl^{-}(aq) + Ag^{o}(s) \rightarrow AgCl(s) + e$

Chloride ions are consumed at anode (+) and released from AgCl at cathode (-). For channels much larger than the size of ions, there will be counter-migration of cations (Na^{+}, K^{+}, Cs^{+}, or Li^{+}) and anions (Cl^{-}) to the electrodes with opposite polarity. However, for SWNT with the diameter comparable to the size of individual hydrated ions, migration of the ions experience a potential barrier. In this platform with SWNTs, protons are the major charge carriers, whereas individual hydrated cations are the blockers in our system. To confirm the ion transport through CNTs, we checked the current traces before and after adding electrolyte solutions (Figure 3.9b). Before adding the electrolyte solutions, the current trace is flat with small magnitude of intrinsic noise (typical RMS noise level). However, after adding electrolyte solutions like KCl and NaCl within

several minutes, the clear coulter effect was shown with relatively large blockade current in comparison to intrinsic noise. Also, it seems that there was some regular time interval of each pore blocking events like the events in biological ion channels. The flat baseline current without electrolyte were constructed by proton flux through CNTs. However, with electrolyte, cation was the blocker for the path of proton flux, and the repetitive penetrations made this rhythmic current change. At this stage, it is valuable to test that this kind of interesting coulter effect is really generated due to the interior transport of SWNTs. In order to verify the transport from SWNTs, we made two devices for the control experiments. First one is the device without SWNTs. Although other fabrication processes are exactly same with our previous method, we did not include SWNTs. This control experiment was performed to determine if pore blocking was due to the epoxy barrier. We looked at a wide voltage range (0-1000 mV), and there was no blockade current observed at all (Figure 3.9c). In this device, the baseline current (Leakage current) is typically lower than the magnitude from the device with SWNTs (Leakage current + current by SWNTs) when the fabrication conditions are all the same. However, the magnitude of the leakage current was varied from 5 pA to 1500 pA due to the conditions of false fabrications such as wrong curing of epoxy structures, or incomplete sealing of UV glue. Second one is the device with unetched SWNTs. The intention of this experiment was to determine if the act of placing nanotubes (whether open or not) was causing the observed pore blocking phenomenon. During the fabrication process, we left out the oxygen plasma step, which is typically performed to open the exposed nanotubes, leaving capped and unopened nanotubes. As expected, there was no blockade current observed (Figure 3.9d). Next, the series of experiments to characterize SWNTs ion channels will show the proof why proton constructs baseline current and cation is blocker.

Generally, in ion channels where the majority charge carriers are ions, the conductance increases with the ion concentration as observed in all the solid state nanopores [196-197] and nanofluidic channels [198]. In our system, however, the trend is opposite as shown in Figure 3.10a. The result suggests that neither Na^+ nor Cl^- is the majority charge carrier through the SWNT interior, and agrees with theoretical prediction [199-201] and experimental demonstration [157,202] of ion rejection at nanopore-mouth. In addition, we compared water baseline current, KCl baseline current (opened channel) and pore-blocking current (closed channel) for 23 devices in Figure 3.10b. The system that majority charge carriers are ions should show the exponential increase of the baseline current as a function of the concentration of ionic solutions. In our platforms, in spite of using high concentration of ions (3M KCl), this dependence does not appear in Figure 3.10b. In many devices, the water baseline current is larger than that of 3M KCl. It should be noted that the baseline current includes a leakage current through the epoxy structure and UV glue. Also, in some cases, the water baseline current reflects the current at the closed channel, and it turns out the lower current level in comparison to the level of 3M KCl case in an opened channel. Based on this analysis, we can rationalize that the majority charge carriers are H^+ and/or OH^- rather than ions. Proton conduction through 1D water chains can be fast via hop-and-turn [191].

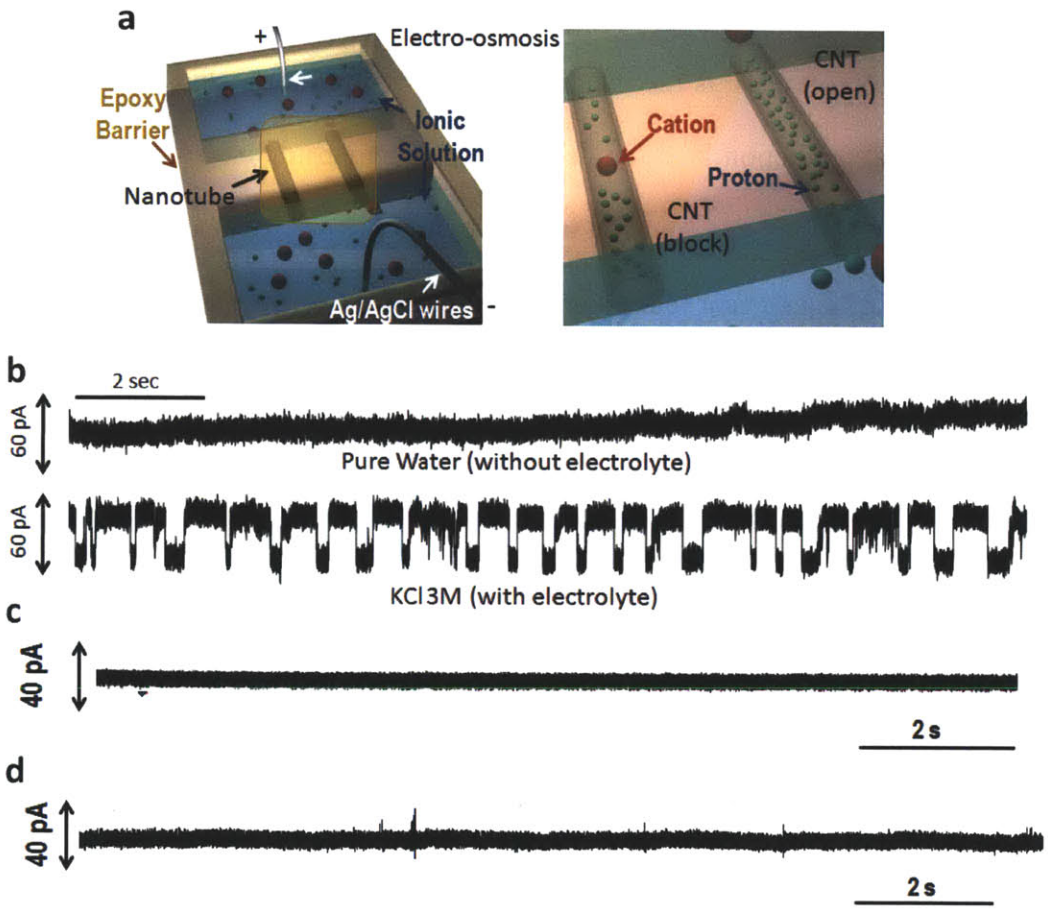

Figure 3.9. (a) Schematic of SWNTs ion channel devices. Two reservoirs of ionic solutions are connected via open nanotubes. Cl^- is released at cathode (-) and consumed at anode (+). Epoxy structures are inhibitors for ionic solution. The central wall blocks molecular transport except through SWNTs in itself. (b) Comparison between pure water (without electrolyte) and KCl 3M ionic solutions (with electrolyte). (c) Current traces with electrolyte in the device without SWNTs. (d) Current traces with electrolyte in the device with unetched SWNTs. The absolute magnitude of the baseline currents (c and d) was around 200 pA in these examples.

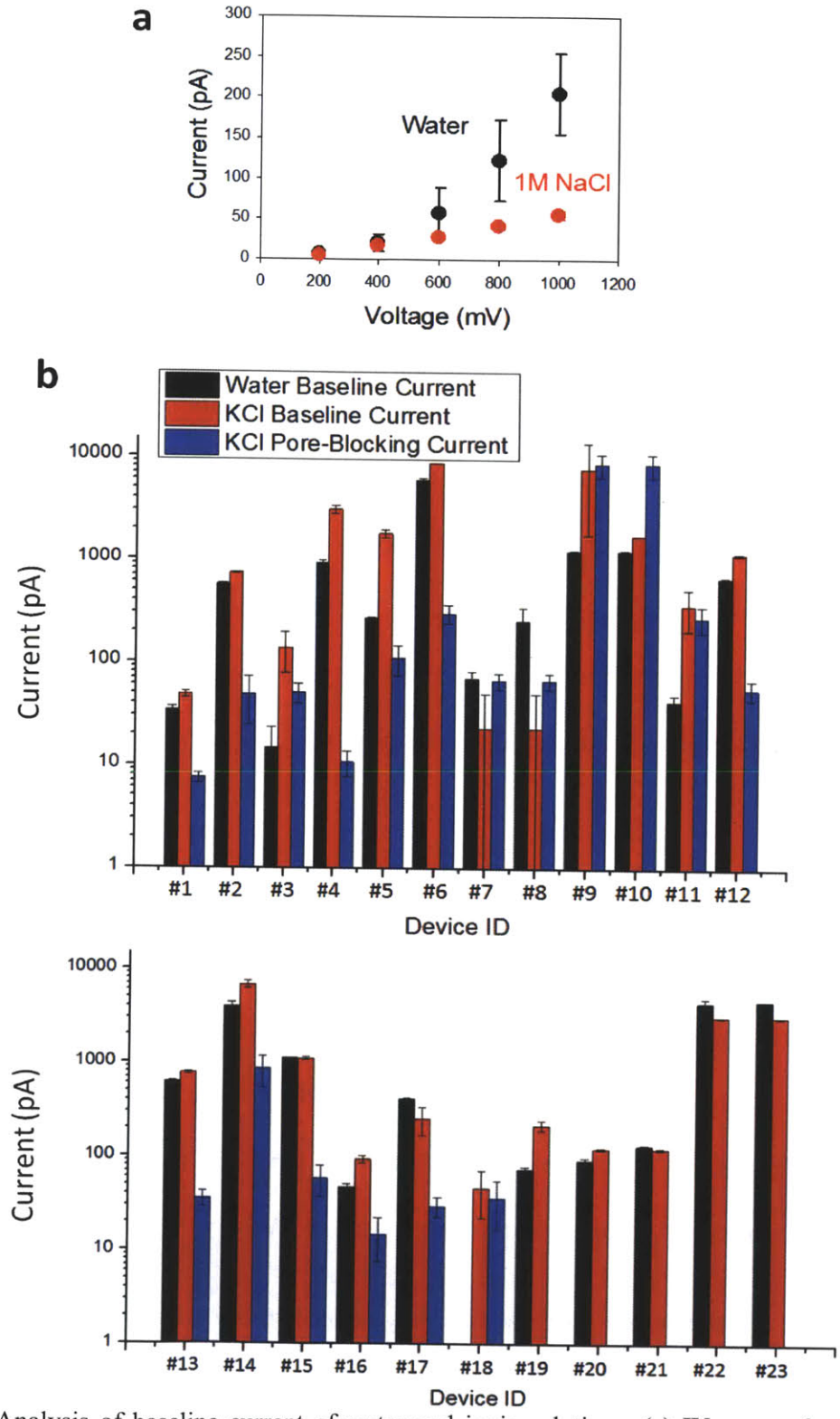

Figure 3.10. Analysis of baseline current of water and ionic solutions. (a) IV curves from one of the devices measured with and without NaCl. Conductance decreases when NaCl is added to the system suggesting little contribution of Na^+ and Cl^- to the ion current. (b) Comparison among water baseline current, KCl baseline current (opened channel) and pore-blocking current (closed channel) for 23 devices.

- Current-voltage (IV) curve

Figure 3.11a shows I-V curves which demonstrate non-linear characteristics. Solid state nanopores without any charged species near the pore mouth normally give linear I-V curves, regardless of the polarity of the applied voltage.[156,203-205] There are two cases in nanopores that can result in non-linear I-V curves. The first case occurs for asymmetric (e.g. conical shaped) nanopores.[206-209] However, CNT nanopores in this platform don't have asymmetric shapes, so this case is ruled out. The second case occurs when there is an asymmetric charge distribution at the pore mouths.[210-212] The oxygen plasma etching step in our device fabrication produced negatively-charged carboxylate groups on both sides of the SWNTs. However, as mentioned, the charged groups might not be identical in number or orientation on the SWNTs. This asymmetry would result in nonlinear I-V curves. Also, unlike hydrophilic pores, hydrophobic pores induce the non-linear I-V curves due to the existence of energy barriers for filling pores[212-213].

If differently charged groups are attached to each side, the I-V curves would show high rectification of current depending on the polarity of the applied voltage. Measured I-V curves in Figure 3.11a show asymmetric current traces, but they still have proper current direction under negative applied voltage. From this data, we reason that the number of carboxylate groups is different for each side, generating non-linear I-V curves. It is well known that oxygen plasma etching shapes carboxylate groups near the pore mouth of SWNTs.

One can observe that the current increased linearly under 600 mV. However, near the 600 mV, the rate of the increase was amplified with non-linear shape. This may be due to the hydrophobic nature of SWNTs. The externally applied voltage near 700 mV may overcome the energy barrier, resulting in accelerated proton transport. Also, the increase of the applied electric

field can induce the increase of available protons following with water dissociation that turns out high current. We conducted the high-voltage I-V measurement to study the effect of applied electric field in detail by potentiostat (Figure 3.11b). The base current by proton conduction rises in a non-linear fashion as the applied electric field increases. If other conditions of the SWNT are kept constant, the magnitude of blockade current during cation transport will increase with the rising base current, as estimated by Figure 3.11b.

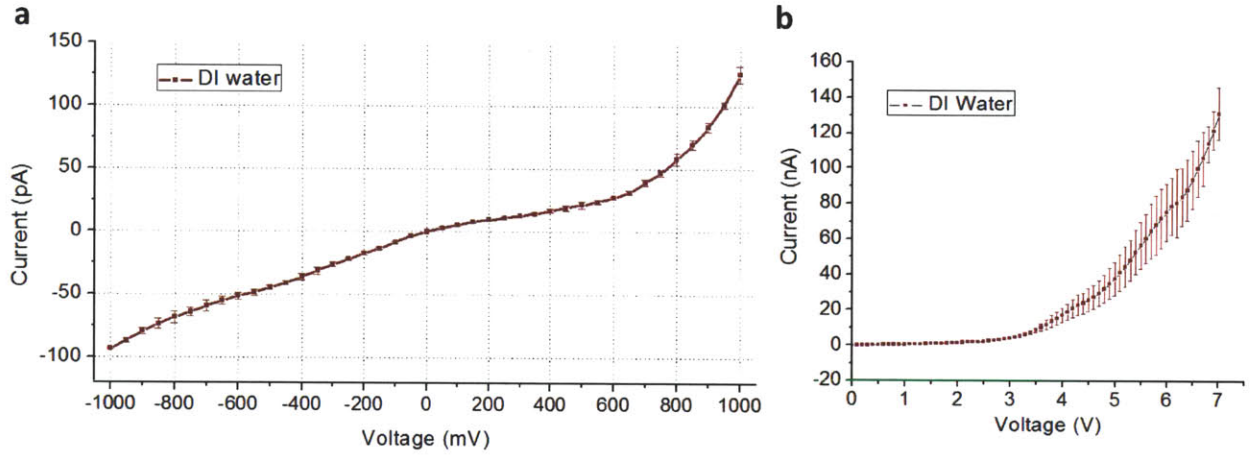

Figure 3.11. (a) Current -Voltage curve for two CNTs nanopores in low voltage range (0-1000 mV). (b) Current -Voltage curve for two CNT nanopores in a high voltage range (0-7 V).

- Threshold voltage

We found that applied voltage across two reservoirs should be over the specific threshold voltages to generate ion transport thorough SWNTs ion channels. For each sample there is an optimal voltage to observe blocking events, and we tune to this region with each experiment. Without the applied voltage, the current remained at 0 pA with intrinsic noise in the measurement setup (Figure 3.12a). The current increase was almost linearly proportional to the applied voltage, linearly (Figure 3.12b). Below the threshold voltages, some SWNTs which were always blocked states could not transport ions. Applied bias between 0 and 695 mV (Figure 3.12) result in only a flat baseline current, demonstrated previously to be proton transport

from the anode to the cathode. At around 700 mV, the electric field was high enough to initiate the transport of ions (Figure 3.13), and above 700 mV, repetitive pore blocking events were observed with varied conductance and dwell time at different electric fields. Since this device had two activated SWNTs as ion channels, two blocked states were observed as shown in Figure 3.12c (one open, and one blocked SWNTs) and Figure 3.12d (two blocked SWNTs). Note that increasing the bias to 800 mV clearly shows the onset of pore blocking. The cations of KCl were shown previously to be the dominant pore-blockers under these conditions.[192] Through a progressive bisection of the interval spanning blocking and non-blocking conditions, an estimate of the threshold potential for pore blocking can be made. Figure 3.13 shows that cycling between 695 and 700 mV results in non-blocking and stochastic blocking intervals in the current trace, respectively. This threshold yields the electrostatic barrier for K+ partitioning into the CNT pore, which is caused by the transfer of charged particles from a high dielectric solvent (bulk water) to a low dielectric environment (interior of the CNT)[214], electrostatic binding to the negatively-charged carboxylate groups near the pore mouth[215], and the partial shedding of hydration shells for ions entering small, hydrophobic pores[199]. In detail, the necessity of partially shedding hydration shells imposes an energetic threshold on ions entering a nanochannel [199]. In protein ion channels this barrier is minimized by carbonyl oxygen mimicking the hydration environment [216], whereas in carbon nanotubes enough activation energy above the potential threshold must be supplied externally. The observed minimum threshold voltage in our study falls into the theoretically predicted free energy of permeation, 80-150 meV [199]. Ensemble measurement by Fornasiero el al. [157] reported percent ion rejection by a nanotube membrane at varied ion concentration and valence. They found that the rejection of anions was more efficient due to a negatively charged pore-mouth. The ability of our system to count single ions allows

precise measurement of the separation factor (proton rate/alkali cation rate). We note that the complete rejection of ions can be achieved below the threshold. This high rejection rate reinforces the notion that membranes based on carbon nanotubes may have applications to desalination of sea water and water purification.

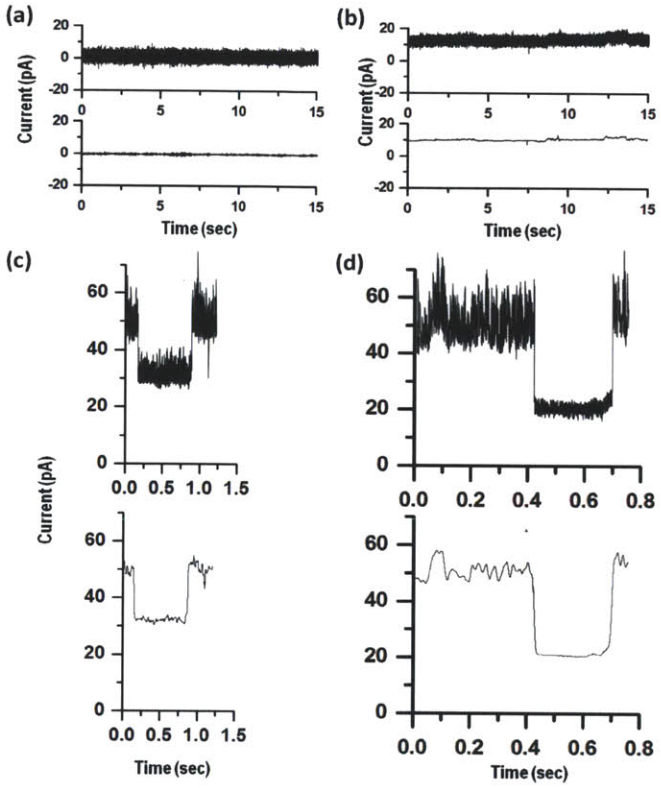

Figure 3.12. Representative current signal of applied electric field between ionic solutions (KCl 3 M). (a) Current trace at 0 V. The base current was zero, and no blockaded current was observed. (b) Current trace at 600 mV. The base current increased, but still, pore blocking did not happen. (c),(d) Current traces at 800 mV (between state 2 and 3 (left), and between 1 and 3 (right)). Only above the threshold voltage (700 mV), did we observe the pore blocking events. State 2 (one SWNT blocked by the cation), and state 1 (two SWNTs blocked by cations) showed the different magnitudes of current.

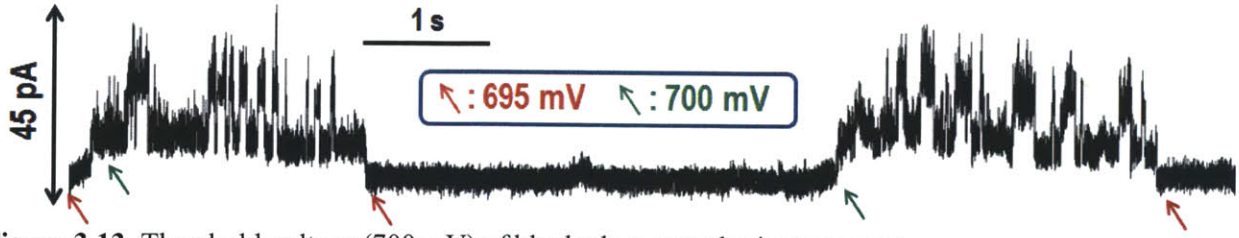

Figure 3.13. Threshold voltage (700 mV) of blockade current by ion transport.

3.2.3. Coherence Resonance in SWNT Ion Channels

- Details of proton transport inside of SWNT

Several researchers predict much faster proton conduction along the hydrogen bonded water network inside the SWNT than in bulk water [217]. The proton conduction can occur via a "hop-and-turn" Grotthuss mechanism along the water chain [191], and does not require physical translocation of protons. Indeed, the current levels are enhanced by the addition of HCl (1 M) and only upon addition to the anode (+). Cations of successively larger hydration radius, with the anion unchanged as chloride, were fed to the nanotube ion channel, and it was found that 1M tetramethylammonium (TMA) chloride (crystallographic diameter of TMA^+ ~ 0.7 nm [218]) yielded no blocking events, despite the fact that the smaller chloride ion should theoretically translocate. The etched ends of nanotubes from the oxygen plasma are known to have carboxylic acid groups with pK_a of about 4.5 [219]. The repulsion of anions is therefore consistent with these observations. Impurities and other artifacts are also easily ruled out [220-221]. The typical current blocking of 100 pA corresponds to 6.25×10^8 protons/s. This value is comparable to the maximum rate reported from water-filled gramicidin proton channels (2.2×10^9 protons/s) under strongly acidic conditions [169]. The result suggests a highly efficient proton conduction through SWNT, enhanced by the expected accumulation of protons near the negatively charged pore-mouth [169]. The high aspect ratio of our nanochannel (> 250,000) is the largest of any synthetic system explored to date, and this appears critical for the detection of single ions in aqueous solution as a technological first. Despite some similarities with biological ion channels, the transport mechanisms in the nanotube are distinct since they do not conduct or gate ions by conformational changes in pore structure [222]. To our knowledge this is the first measurement of the proton conduction through the SWNT interior.

- First observation of coherence resonance

In some instances, we observed durations where the cation blocking events developed highly synchronized, rhythmic patterns, three of which are shown for each ion type in Figure 3.14a. From the all-point histograms, it is clear that these oscillations occur from single nanotube transport. A fast Fourier transform (FFT) of the resulting current output (Figure 3.14b) reveals the oscillator frequencies as 0.046 Hz for NaCl, 2.7 Hz for LiCl, and 8.1 Hz for KCl. These instances appeared meta-stable and particularly sensitive to environmental perturbation, but otherwise observable for durations lasting several minutes. Despite extensive work examining synthetic analogs of the ion channels, sustainable current oscillation [223,224] produced from transport of single ions has not been observed. The productivity of the nanopore in terms of single molecule processing dramatically increases during these periods, counting hundreds of individual cations per minute.

The blocking events provide information about hydrated ion transport in the carbon nanotube, a subject of intense theoretical investigation [199,202]. The histograms (Figure 3.15a) of the blocking currents (ΔG) show Gaussian distributions for Li^+ and K^+ (with too few events for Na^+) and mean values that scale as $Na^+ > K^+ > Li^+$. The ratio of the areas between the hydrated ion cross section and that of the nanopore provides an estimate of the conductance change upon ion partitioning, ΔG, relative to the value at complete blockage, ΔG_{max}.

$$\Delta G = \left(\frac{d_{ion}}{d_{tube} - \sigma_{C-O}} \right)^2 \Delta G_{\max}$$

Here, $\sigma_{C\text{-}O}$ is the Lennard-Jones parameter for C-O interaction (0.0319 nm) [225]. For example, K^+ produces ΔG values that vary between 52-323 pS (with the latter value taken as ΔG_{max}), and d_{ion}/d_{tube} therefore varies between 0.39-0.98 assuming d_{tube} = 1.5 nm. Diameter was in the range

of 1.2 and 1.8 nm, and average value was chosen. For Li^+, the ΔG range is 7.5-145 pS, and d_{ion}/d_{tube} is 0.22-0.98. For Na^+, ΔG is 120-420 pS, and d_{ion}/d_{tube} is 0.52-0.98. The ΔG is the smallest for the Li^+ ion, which has the smallest crystallographic diameter and the largest hydrated diameter in bulk. It is expected that $\Delta G_{Na+} > \Delta G_{K+}$ due to stronger hydration around Na^+, which generally requires larger pore size as observed in protein ion channels [226] although Carrillo-Tripp et al.[227] predict higher hydration numbers for K^+. A rigid, synthetic nanopore capable of single ion detection as introduced in this work may resolve outstanding questions about ion hydration numbers in a confined space [228].

This ordering of the blocking currents is also consistent with what is observed in the mobility histograms in Figure 3.15a, which should instead scale inversely with d_{ion}/d_{tube}. Here the Na^+ mean (5×10^{-8} m^2/Vs) is much smaller than Li^+ and K^+ with values of 8×10^{-6} m^2/Vs. The Gaussian distribution of τ_{dwell} leads to asymmetry in the mobility distribution (mobility ~ $1/\tau_{dwell}$). The smallest ΔG values accompany a large variation in mobility for Li^+ which has a small ionic diameter (0.12 nm). The mobility of Na^+, conversely, is smaller by nearly 3 orders of magnitude by comparison suggesting sterically hindered transport inside the nanotube. These are the first experimental measurements of single ion mobilities in a synthetic nanopore. The values are two orders of magnitude higher than the cation mobility of bulk water and the theoretical mobility through a 3 nm diameter SWNT [229], (both approximately 10^{-8} m^2/Vs). Theoretical treatments describe this high ion mobility as arising from the atomically smooth surface of the SWNT interior and velocity slip at the wall [225]. Plotting ΔG versus mobility at 1M (Figure 3.15b) reveals an inverse relation as expected for Li^+ (red) and K^+ (black), and describing the mean value of Na^+ (blue). Future work will seek to perform these measurements on a consistent series of identical nanotubes with defined radius, to validate the scaling of mobility with pore size

predicted by Liu et al. [230], and also observed for larger molecules such as DNA through solid-state nanopores [231] and SWNT [172].

- Stochastic simulation of coherence resonance

These oscillations are caused by a coupling between the stochastic pore blocking and a proton diffusion limitation that develops at the pore mouth (Figure 3.16a). As stated before, the proton mobility through the nanotube is substantially higher than that of bulk solution. Therefore, an unobstructed proton current in the nanotube will necessarily deplete the proton concentration at the pore mouth. Coupling occurs because the depletion increases the relative blocking ion concentration, thereby increasing its probability of partitioning into the nanotube, an extremely rare event otherwise. Once the nanotube is blocked, the proton concentration at the pore mouth increases rapidly while the blocking cation traverses the nanotube. When the blocker emerges from the other side, the proton current is restored, and a subsequent blocking event is suppressed by the initially high concentration of protons relative to blocking cations. Reformation of the diffusion limitation as the proton flow is restored then allows this cycle to repeat indefinitely. We constructed a stochastic simulation [232] (Figure 3.16b) with 6 equations and rate constants (diffusion of H^+ into (k_s) and out of (k_{sd}) the pore mouth region, partitioning of H^+ (k_1) and blocking cation (k_2) into the nanotube, and the exit of these two species from the nanotube (k_{1d} and k_{2d} for H^+ and blocker respectively)) with a Gaussian dwell time distribution known from experiments. The blocking rate constant (k_2) is small compared to the proton value (k_1). This system reconstructs the oscillation frequencies observed experimentally for certain values of the proton exchange rate constant (k_s), and also the Gaussian distribution in open-channel lifetime, τ_{open}, observed during the oscillations events in Figure 3.14a.

The signature of stochastic resonance is one where the signal to noise ratio of the system maximizes at optimal level of noise or random fluctuations. In a typical demonstration, an external periodic forcing is super-imposed with white Gaussian noise with a resulting increase in the signal to noise ratio at an optimal noise level. In this work, the mechanism is best described by a coherence resonance [233] since the forcing function is intrinsic to the system dynamics. This phenomenon is demonstrated in Figure 3.16c by tuning the rate of proton diffusion into the near-pore region (k_s), which controls the inherent noise in the system. A value of k_s that is too large or too small to create the resonance condition results in a blocking frequency that is Poisson-like and erratic. As k_s approaches an inherent resonance condition, the distribution of open-channel lifetime becomes Gaussian and narrow, and the blocking events occur with a locked frequency. This mathematical system can reproduce the frequency values of the oscillations (Figure 3.16d) by examining the FFT of the blocking cation occupancy.

The coherence resonance condition dramatically increases the single molecule processing rate of the nanotube (480/min in resonance versus 5/min off resonance). This has implications for other nanopore systems, including DNA translocation and sequencing, and Coulter detectors. The largest proton conductivity measured to date opens possibilities for new types of proton conducting membranes for fuel cells and catalysis.

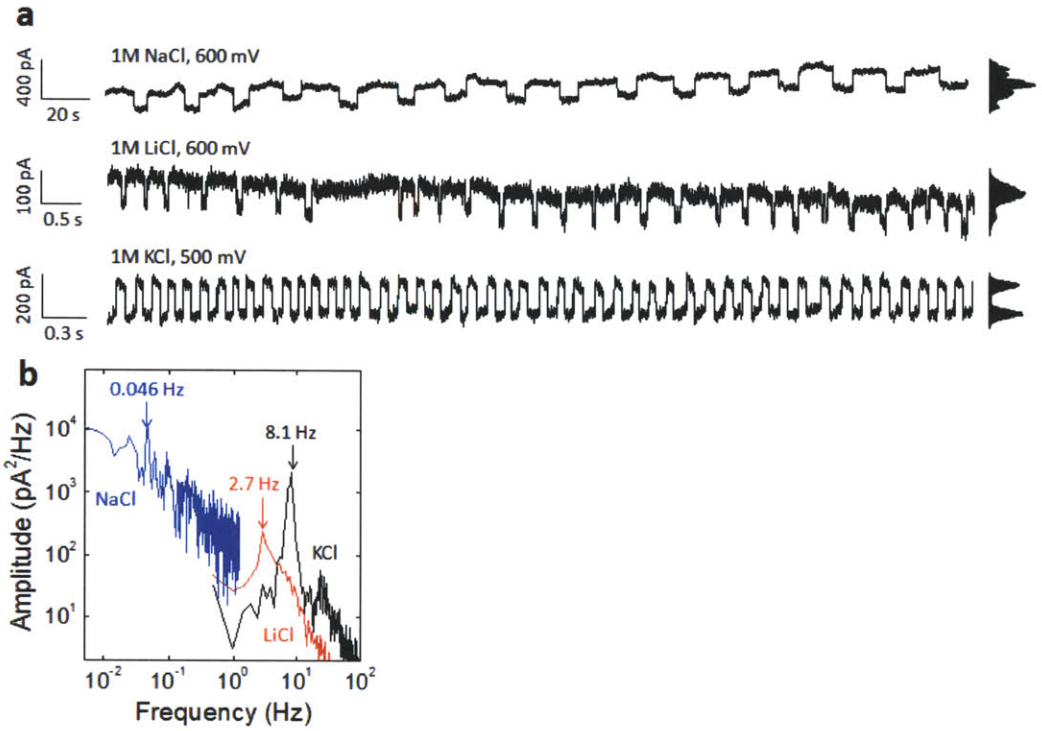

Figure 3.14. Meta-stable oscillations of the electro-osmotic current are observed for durations lasting several minutes. (a) Two defined peaks in the all-point histograms indicate that the phenomena arise from single-tube pore blocking events. The frequency of the oscillations varies with the type of ion. (b) Sharp peaks in fast Fourier transform (FFT) of the electro-osmotic current are pronounced at the oscillation frequencies.

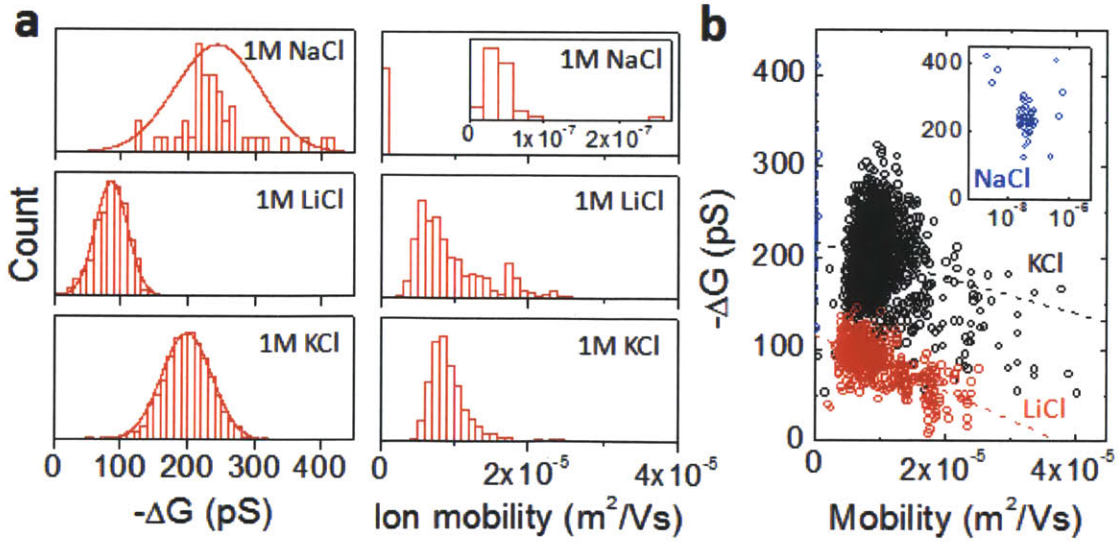

Figure 3.15. Detection of individual cation transport through the interior of a single nanotube. (a) Histograms of the conductance decrease upon pore blocking, ΔG (left), and ion mobility (right) for the tested ions. The ion mobility is 1000 times higher than the value in bulk water. (b) The conductance change with blocking, ΔG, decreases with ion mobility as expected.

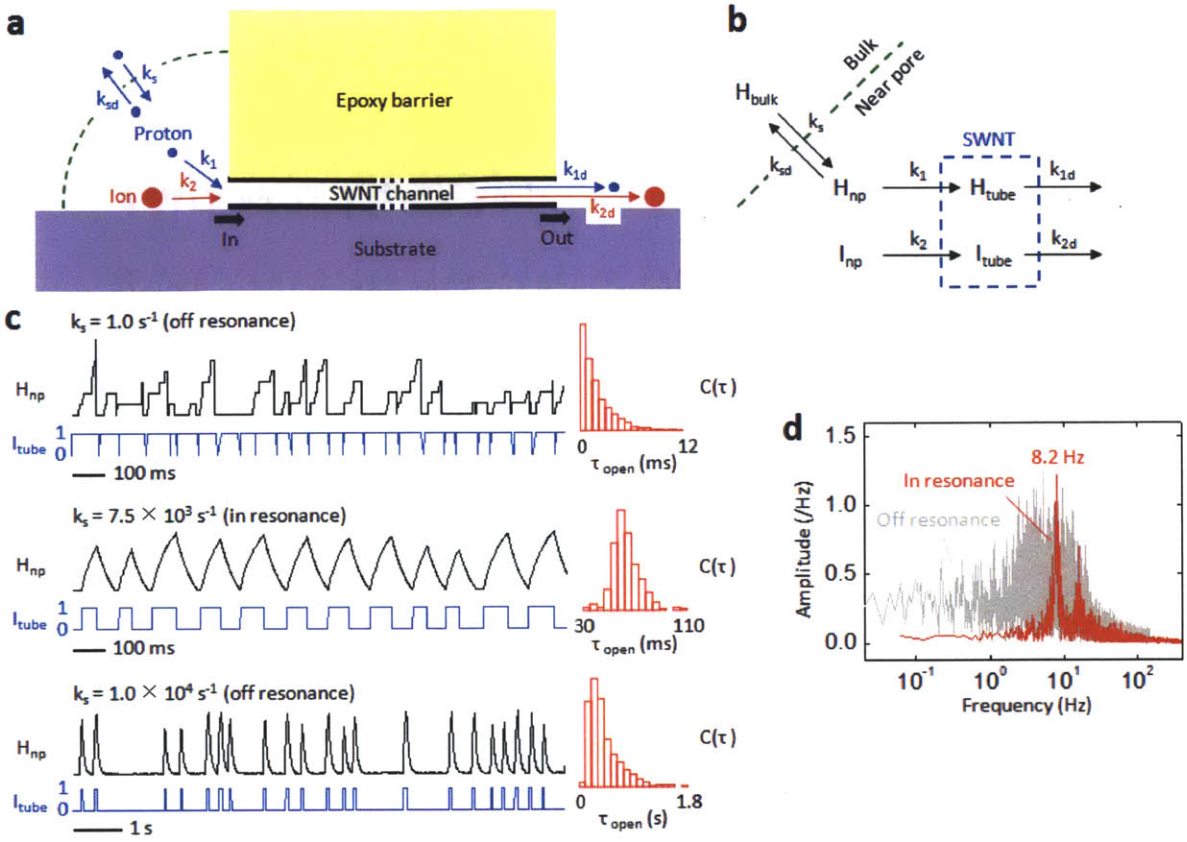

Figure 3.16. Stochastic simulation illustrating the influence of coherence resonance on the oscillatory behavior. (a) Six reaction steps define this system: protons and blocking cations entering and transporting across the channel, proton exchange between bulk and pore-mouth region. (b) Summary of the 6 reactions, (c) Trace of number of protons at near-pore (H_{np}, black) and ion occupancy in the nanotube (I_{tube}, blue) at varied rate constant of proton-in to near-pore (k_s). Histogram of open-channel lifetime, τ_{open} (red), shows Gaussian distributions only at optimal values of k_s (in resonance), and random, exponential distributions at larger and smaller values of k_s (off resonance). Autocorrelation function, $C(\tau)$, shown on the right is pronounced only when the system is in resonance. (d) Sharp peaks in the FFT appear only within the resonance window (red).

3.2.4. Proton Transport through Hydrophobic SWNTs

- Validity of protons as the majority charge carriers

High ionic current can be feasible by first noting that water can form water chains inside the hydrophobic interior, and interrupting this water chain is energetically unfavorable.[176] Because there are carboxylic acid groups (pKa ~ 5) on the ends of the nanotube, there is a local increase in proton concentration at the pore mouth. Thus, it may be expected that the close proximity of protons to the entrance of the water chain, coupled with the electric field, would predominantly drive proton conduction through the nanotube.

To further confirm this, we conducted experiments with 3M KCl at different pH values (1, 5, and 8). We also performed experiments using D_2O as a solvent (pD 5). These results support the idea that protons are indeed the majority charge carriers. In order to avoid any ambiguity due to leakage current, we have examined the conductance change upon pore blocking (ΔG, blockade current) rather than the baseline current (Figure 3.17). From over a hundred blocking events for each pH value, we have found that ΔG increases as the solution becomes more acidic (see histograms). The comparison of D_2O and H_2O experiments with 3M KCl shows that the ΔG of D_2O is smaller than value from the H_2O at pH 5. It is well known that the isotope effect for proton transport can be explored by the comparison between H_2O and D_2O. It is expected that the ratio of blockade current between H_2O and D_2O would correspond to an isotope effect (Y_H/Y_D) of 1.6.[234] In our experiments, this ratio in the experiments is around 1.9 (Figure 3.17b) and it is in a good agreement with our expectation. This strongly supports that the proton transfer is induced by the water wire in the Grotthus mechanism. Also, in theory, the current magnitude should be increased linearly with decreasing pH[235], suggesting that the proton was the principal current carrier. Both of these results provide good evidence of proton conduction through the nanotube.

More acidic solution have higher proton concentrations, which should increase blockaded current by cation. It is reasonable that higher proton concentration induces larger proton flux in an electric field. Also, D_2O proton flux through nanotubes should be lower than that of H_2O. Deuterium is heavier than hydrogen, and it causes the decrease of proton mobility in same electric field.

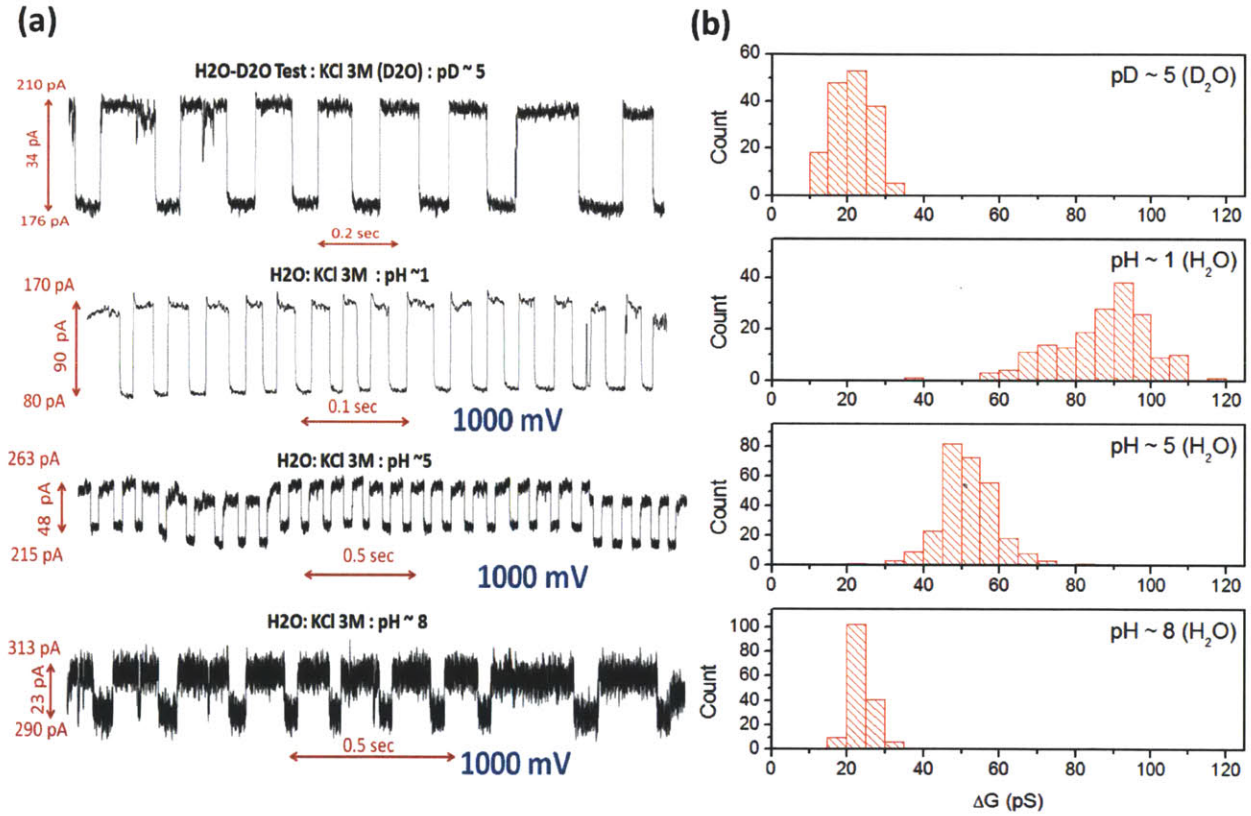

Figure 3.17. (a) Current traces of coherence resonance from D_2O-KCl 3M (pD 5) and H_2O-KCl 3M (pH 1, 5, 8). (b) ΔG values from 3M KCl at different pH. The value is smaller in D_2O than in H_2O. Larger ΔG at acidic pH verifies that protons are the major charge carriers.

- High proton mobility

Proton conduction in this system has been proposed to take place by a Grotthuss mechanism, by which the excess proton charge is transferred along a chain of water molecules

by a hopping mechanism. No MD simulations have been run that examine proton conduction in long nanotubes (more than a few nm), but it is conceivable that many protons could be hopping simultaneously inside the nanotube, as one simulation reported a stabilized water complex which contains the excess proton delocalized over 4 water molecules ($H_9O_4^+$).[236] Also, assuming 10 water molecules in the cross-sectional area of SWNT is conceivable based on the SWNT diameter. The 20 pA blocking current corresponds to a proton transport rate of 1.25×10^8 proton/s. This value is comparable to the maximum rate reported from water-filled gramicidin proton channels (2.2×10^9 protons/s) under strongly acidic conditions.[237] Also, assuming 10 water molecules in the cross-sectional area of SWNT is feasible in the range of SWNT diameter. In this case, the proton transport rate along one bonding network is 1.25×10^7 proton/s.

Thus, if we assume that there is one proton per 4 water molecules, and 10 water molecules in the cross-sectional area, the calculated proton mobility becomes:

$$\mu = \frac{\mathbf{v}}{\mathbf{E}} = \frac{(1 \times 10^7 \mathbf{proton/s})(0.24\ \mathbf{nm}/1\ \mathbf{H_2O})(4\mathbf{H_2O}/1\ \mathbf{proton})}{1\mathbf{V/mm}} = 0.096\ \mathbf{cm^2/V\text{-}s}$$

which is still high, but several orders of magnitude lower than the hole mobility for silicon. The proton mobility in the bulk water is 0.004 cm^2/V-s. However, MD simulation have anticipated 10 to 100 times higher proton mobility (0.04~0.4 cm^2/V-s) in confined nanoscale regions.[176,238-240] This indicates that this high proton mobility is not unrealistic in comparison to simulation.

- Filling water in hydrophobic nanotubes

One would generally question how water would fill a high-aspect ratio, highly hydrophobic carbon nanotube interior. It is true from a continuum dielectric model that moving

a polar species (water) from a high dielectric region (bulk water) to a low dielectric region (the interior of the nanotube) results in a significant free-energy barrier.

According to molecular dynamics simulations by Hummer et al.[176], water molecules will lose 2 out of 4 hydrogen bonds, on average, upon entering a nanotube much smaller than the ones probed in this study (0.8 nm vs. 1.5 nm). The energy from van-der Waals interactions with the nanotube interior makes up a fraction of this loss. In addition, there is still significant entropy, as water molecules can freely rotate around the hydrogen bonds. Water chains have been found to form on the inside of carbon nanotubes, which suppress the formation of three-dimensional hydronium cations and provides one-dimensional hydrogen-bonded networks that enhance fast proton transport.[238]

The main conclusion of the simulation study by Hummer et al.[176] was that water occupancy can be quite significant even in very small hydrophobic channels (and on time scales on the order of nanoseconds). Again, that simulation study was performed for an even smaller nanotube diameter than the ones probed in this study; therefore, water may be expected to fill the hydrophobic interior of the 1.5 nm diameter nanotubes even more favorably due to more hydrogen bonds achievable and more entropy relative to a smaller diameter nanotube.

3.2.5. Observation of Simultaneous, Single Ion Transport in Two SWNTs

The current trace under K+ blocking conditions reveals several interesting details regarding the construction of the nanopore system. Three Coulter states are evident, therefore this system corresponds to two parallel nanopores with approximately equal proton conductances (Figure 3.18b). These states are analyzed in more detail below. We also observe that this

system *fail-closed* when the potential drops below the 700 mV threshold, as it clearly remains in the blocked state. This feature is unique to this nanopore system and indicates that the electrostatic barrier is higher for the exit region than the entrance. Such an imbalance can occur from unequal numbers of charged carboxylic acid groups on either end of the nanopore, a condition easily realized due to the small number of attachment sites at either end of the CNT.[219] Also, the functionalization of positively- and negatively-charged groups at either side of the nanopore may have the potential to draw individual cations and anions in opposite directions. The fail-closed state is intriguing because it allows for the systematic trapping of molecules within the nanopore whereby chemical reactions or further manipulations can be performed before their expulsion by cycling the potential above the threshold. In Figure 3.18a, a short dwell-time state is periodically observed in the two pore system, corresponding to the coincident blockage of two K+ ions in each nanopore. Figure 3.18b confirms that this system demonstrates 3 Coulter states with the short dwell time corresponding to the longest arrival time (or interval between observations). The three distinct current levels indicate specific states of SWNT #1 and #2 (state 1 : #1 block - #2 block, state 2 : #1 open - #2 block or #1 block - #2 open, state 3 : #1 open - #2 open). The two pores have nearly similar magnitudes of blockade currents so that we can only observe 3 states (Figure 3.19). Ion channels with two activated SWNTs should possess three different states (state 1 : two blocked, state 2 : one opened, one blocked, state 3 : two opened).

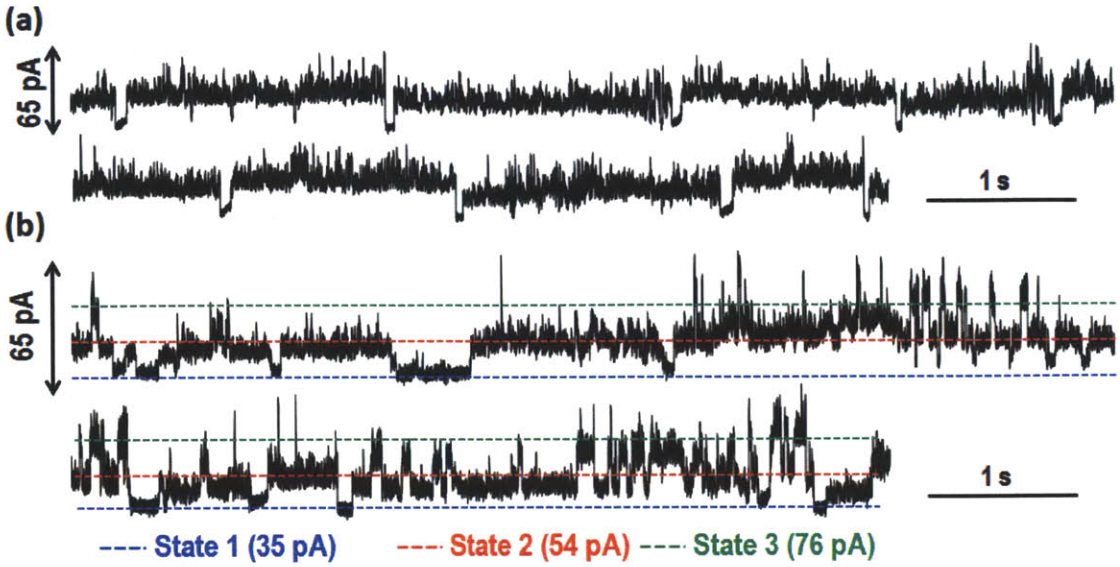

Figure 3.18. (a) Threshold voltage (700 mV) of blockade current by ion transport. (b) Stochastic pore blocking through SWNT #2 (800 mV). Among stochastic events, pore blocking events having short dwell time occur in SWNT #1. (c) Proof of two activated SWNTs in ion channels (800 mV). The blockade current shows 3 states meaning the system of two pores.

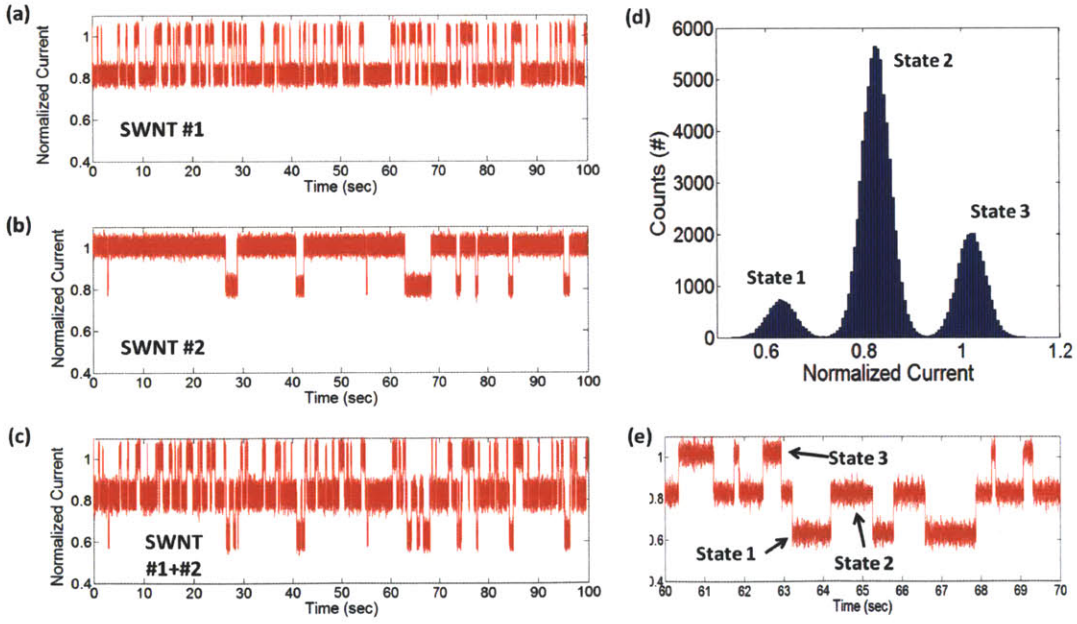

Figure 3.19. Modeling states of ion channels made by two SWNTs. **a,** Data set of pore blocking events from SWNT #1 which has high reaction rate, and short dwell time. **b,** Data set of pore blocking events from SWNT #2 which has low reaction rate, and long dwell time. **c,** Mixed data set of ion channels (a + b). **d,** Histogram of two blocked SWNTs (state1), one opend and one blocked SWNTs (state 2), and two opened SWNTs (state 3). **e,** Expanded data to clarify each state.

This parallel nanopore system provides an opportunity to test the statistical nature of pore blocking events at potentials above the threshold. Specifically, we asked if the dynamics of this system are described by a 3 state Markov chain (Figure 3.20). We applied three different voltages (800, 900, or 1000 mV), generating the current traces and all point histograms shown in Figure 3.21. Again, since two parallel SWNT nanopores are involved in ion transport, the all points histogram should indicate 4 peaks except in the case where the intermediate state (one blocked/one unblocked) is degenerate (Figure 3.19). We find that the ratios of the observed 3 peaks in the all points histogram are consistent with a simple Markov process. Note that the completely closed state displays a large arrival time (18 sec), with a short dwell time (0.07 sec) in all three cases. This state is rare (probability = 0.02) because two K+ must transport coincidently in each nanopore for its observation. Using relative ratios of the 3 peaks, we calculated the probabilities of pore blocking for SWNT #1 and #2. At 800 mV, the probabilities of blockade current for #1 and #2 were 0.73 and 0.066 (Figure 3.21a). At 900 mV, #1 and #2 were 0.78 and 0.019 (Figure 3.21b). At 1000 mV, #1 and #2 were 0.67 and 0.006 (Figure 3.21c).

Note that increasing the electric field is expected to decrease the dwell times of single pore occupancy, since the K^+ will translocate faster. The coincident state in SWNT #2 decreases as expected with increasing potential. However, the increasing electric field also appears to affect the frequency of cation arrival at the negatively charged pore mouth. Since, SWNT #1 is affected by both the dwell time and this frequency, the probability is not inversely proportional to the electric field as one might expect.

This distinct trend between SWNT #1 and #2 from applied voltage can be explained as an interference between the ion dwell time and the arrival frequency. The fast proton conduction through SWNT[20,241] induces the depletion of proton concentration at the pore mouth. Near the

pore entrance, it gradually establishes a relatively high concentration of cations, which leads to pore blocking when a single cation enters the SWNT.[157,199] After the blocking cation translocates, this depletion process is repeated, and another cation continues the process. The frequency of this process is accelerated with increasing applied electric field whereas the dwell time decreases. In SWNT #2 (low probability for blocking), the occupancy of SWNT by the cation is a relatively rare event, and the change in arrival frequency with an increase in applied voltage can be neglected in comparison with the change in dwell time. However, in SWNT #1 (with a high probability for blocking), the frequency of pore blocking events appear sensitive to the applied electric field. Therefore, the probability is affected by both of the frequency of pore blocking events and the dwell time. In SWNT #1, the average dwell time was slightly decreased by the increase of applied voltage (Figure 3.22), whereas the frequency of pore blocking events was increased. This difference can be caused by either the defects-impurities in SWNTs, or the various charged conditions[242] on the pore mouths of SWNTs or slight difference of diameters and chiralities[243]. For example, the end of SWNTs etched by oxygen plasma forms carboxylic acid groups that may not be identically shaped on SWNT #1 and #2.[219]

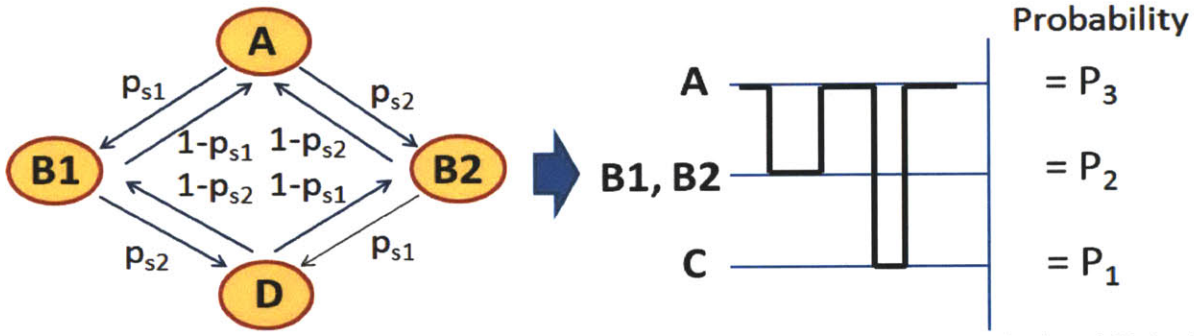

Figure 3.20. Markov chain network with probabilities of pore blocking for SWNT #1 (p_{s1}) and #2 (p_{s2}). A (state 3) : #1 OPEN - #2 OPEN, B1 (state 2) : #1 BLOCK - #2 OPEN, B2 (state 2) : #1 OPEN - #2 BLOCK, D (state 1) : #1 BLOCK - #2 BLOCK.

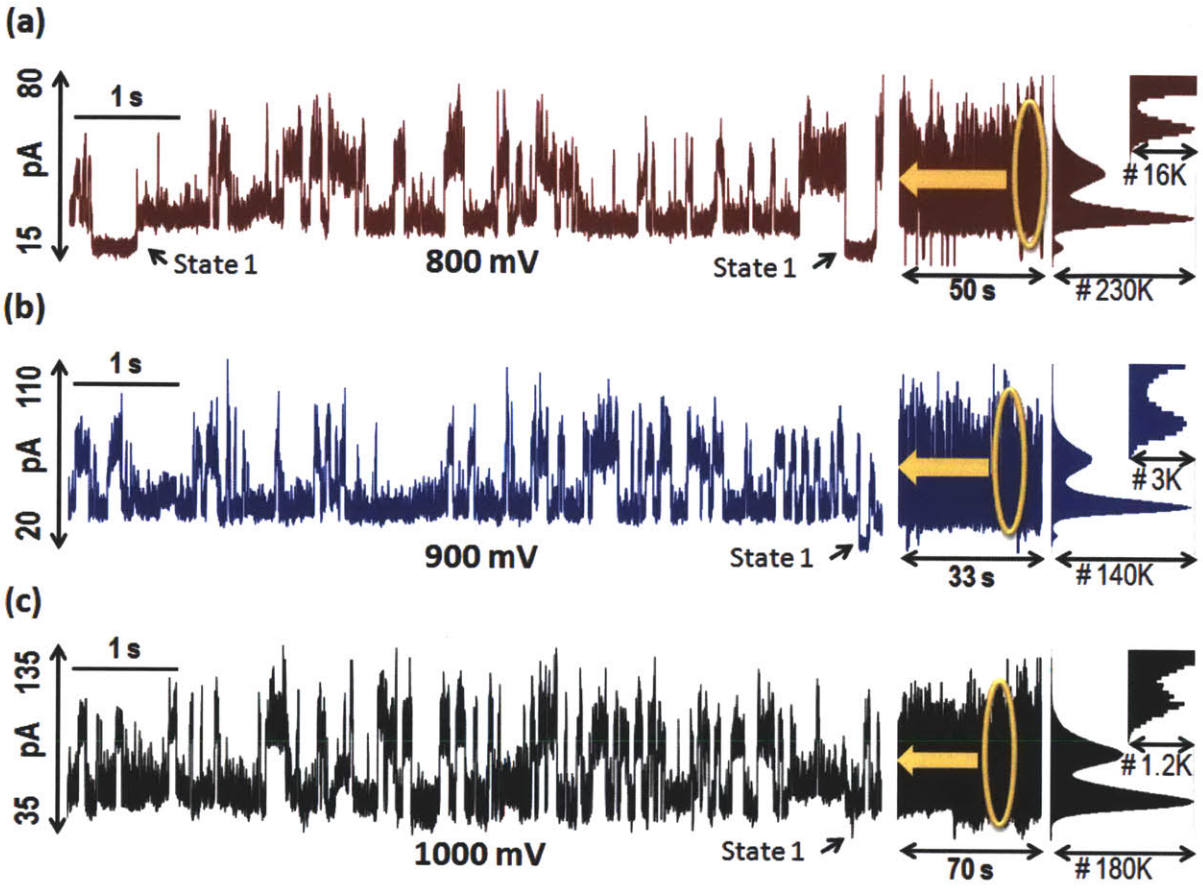

Figure 3.21. Current traces and all-point histograms of (a) 800 mV, (b) 900 mV, and (c) 1000 mV. Inset is extended figure of state 1. Peak heights represent # of data points in state 1, 2, and 3.

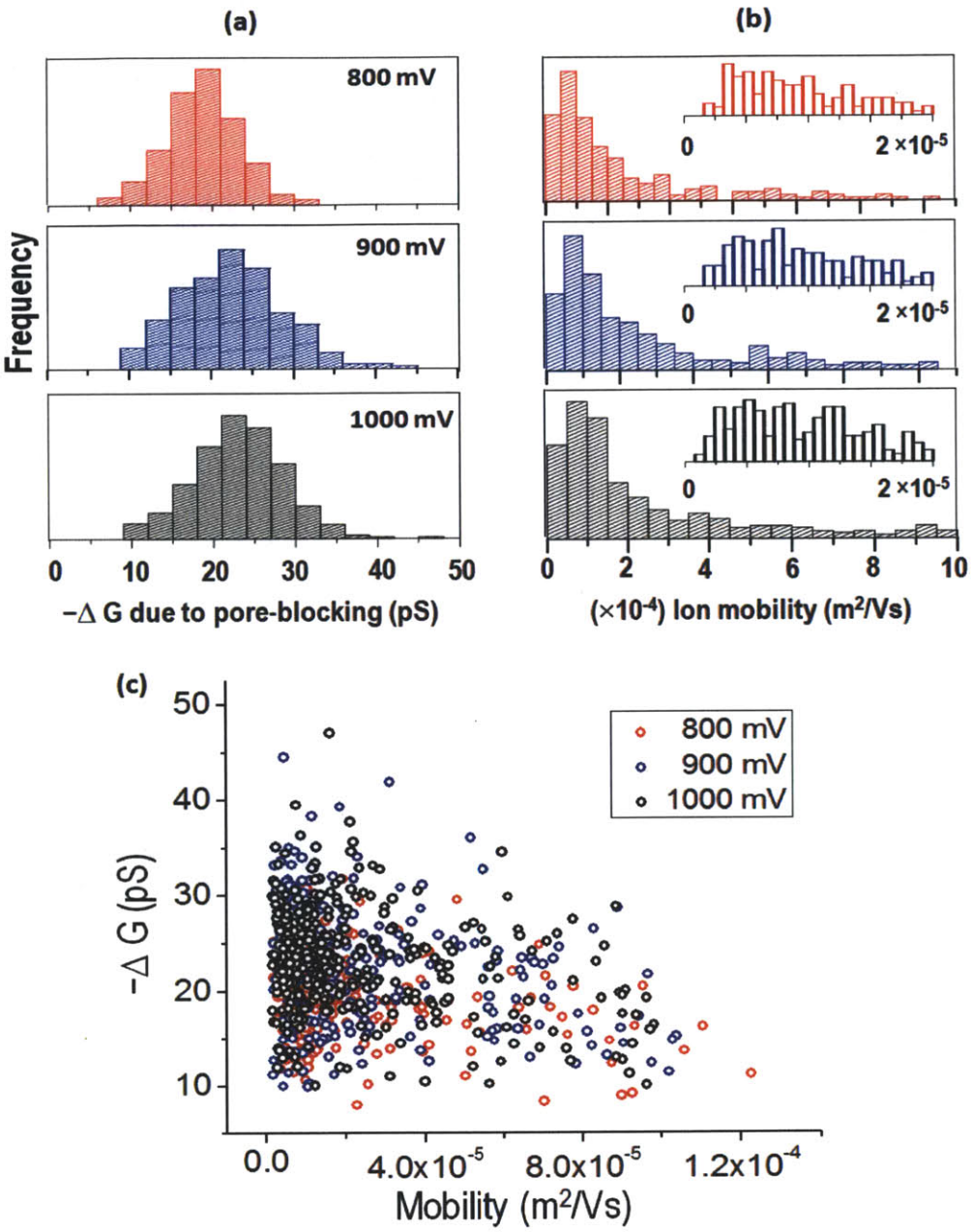

Figure 3.22. Ion mobility, and conductance change by pore blocking, ΔG . (a) Histograms of ΔG as a function of applied voltage. (b) Histograms of ion mobility versus applied voltage. (c) Conductance change by pore blocking decreases with ion mobility.

3.2.6. Model for Simultaneous, Single Ion Transport through Two SWNTs

We analytically describe (Fig. 3.23a) the two ion channels using a simple three state Markov chain governed by two different sets of rate constants. The rate constants for cation blocking in SWNT #1 (k_1) and SWNT #2 (k_2) control the arrival times and depend on the status of each pore mouth. We note that pore blocking in #1 appears to be more frequent than #2 ($k_1 > k_2$). The rate constants for the pores #1 (k_{1d}) and #2 (k_{2d}) should be known from the electric field and the scaling of ion mobility. The expected distribution of states 1, 2, and 3 (Figure. 3.20) are then,

$$P_1 = p_{S1}p_{S2},\ P_2 = p_{S1} + p_{S2} - 2p_{S1}p_{S2} \qquad (3-1)$$
$$P_3 = (1-p_{S1})(1-p_{S2})$$

probabilities of state 1 (P_1), 2 (P_2), 3 (P_3), where, pore blocking for SWNT #1 (p_{S1}), #2 (p_{S2}) that can be described by cation-in (γ_1, γ_2) and cation-out (γ_{1d}, γ_{2d}).

$$p_{S1} = \gamma_1(1-\gamma_{1d}),\ p_{S2} = \gamma_2(1-\gamma_{2d}) \qquad (3-2)$$

Each γ can be calculated by a rate constant according to.

$$\gamma_1 = 1-e^{k_1 t},\ \gamma_{1d} = 1-e^{k_{1d} t},\ \gamma_2 = 1-e^{k_2 t},\ \gamma_{2d} = 1-e^{k_{2d} t} \qquad (3-3)$$

where, t is the time interval for the observation. Rate constant for releasing cations are estimated by,

$$k_{i,d} = \frac{\mu_i (E - E_{th})}{L} \qquad (3-4)$$

where, L is the length of SWNTs, μ is the ion mobility of each SWNT, E is the applied voltage, and E_{th} is the threshold voltage. Figure 3.23b shows that the simulations of relative peak heights nearly correspond with experimental results. The weight of state 1 rapidly decreases from threshold voltage with increase of applied voltage, while state 3 slowly increases (Figure 3.24a, c). The state 1 is dominated by pore blocking of #2 which is a rare event, so that it depends on

ion mobility inversely proportional to the voltage. State 3 shows a gradual increase, because the increase of frequency of pore blocking decays the decrease of ion mobility. Uniquely, the probability of the state 2 increases up to 860 mV, the range which the frequency increase surpasses overall decrease of dwell time. But, the probability of the state 2 decreases over 860 mV, due to the decrease of dwell time over the effect of the rising frequency (Figure 3.24b). We conclude that a simple Markov network with linear electric field dependence of the translocation velocity approximately describes this system.

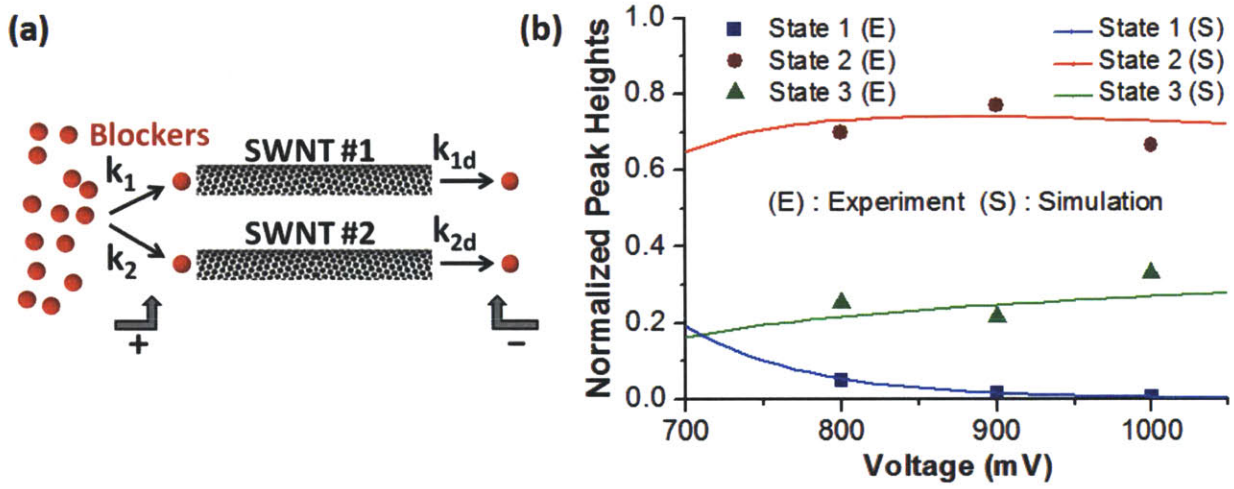

Figure 3.23. (a) Schematic of transports of cations through SWNTs. Each SWNT has different rate constants (k_1 and k_2 : occupied by cations, k_{1d} and k_{2d} : releasing cations) (b) Comparison of 3 states : simulation and experiment at 800, 900, and 1000 mV.

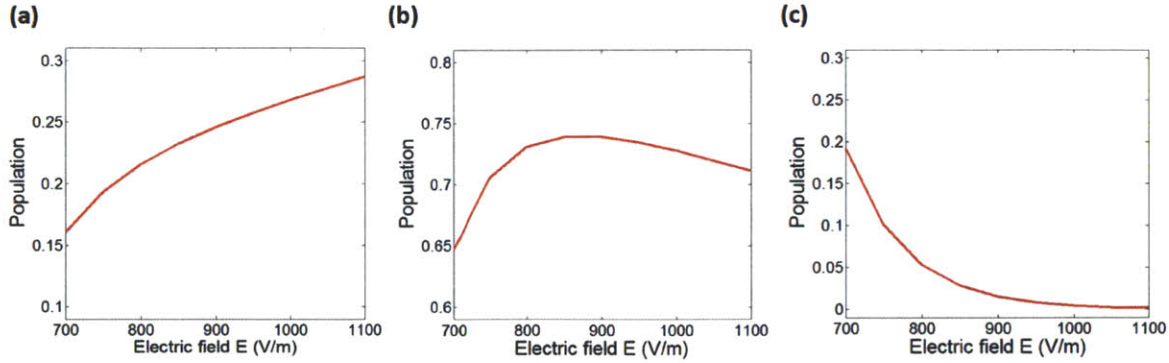

Figure 3.24. The simulations of probabilities of all states (state 3 : (a), state 2 : (b), state 1 : (c)) are shown as a function of applied voltage.

3.3. Ion Correlated Transport Phenomena from a Single Isolated SWNT

3.3.1. Two SWNTs Undergoing Simultaneous Coherence Resonance

The platform we studied was fabricated the same manner as in our previous work.[244] Briefly, horizontally-aligned SWNT were grown using chemical vapour deposition[83,193] and covered by an epoxy structure defining the reservoirs, using UV glue to form a tight seal.[194] The exposed ends of the SWNT were removed using oxygen plasma, leaving open SWNT that span the epoxy barrier. The reservoirs were filled with electrolyte solutions (KCl, LiCl, NaCl, or CsCl), and a fixed voltage drove the current that is detected by Ag/AgCl electrodes. In stochastic pore-blocking, fast proton flux[245] through the interior of SWNT results in a high current level, depleting the proton concentration in the near-pore region and increasing the concentration of cations near the pore mouth (Figure. 3.25a). Next, a cation enters the SWNT and obstructs the proton flux, resulting in a low current level (Figure. 3.25b). Once the ion emerges from the other side, the high current level is rapidly restored due to the high proton concentration near the pore mouth (Figure 3.25c). Under certain conditions, ions enter and translocate at a fixed frequency, resulting in CR being observed for a single SWNT.[192]

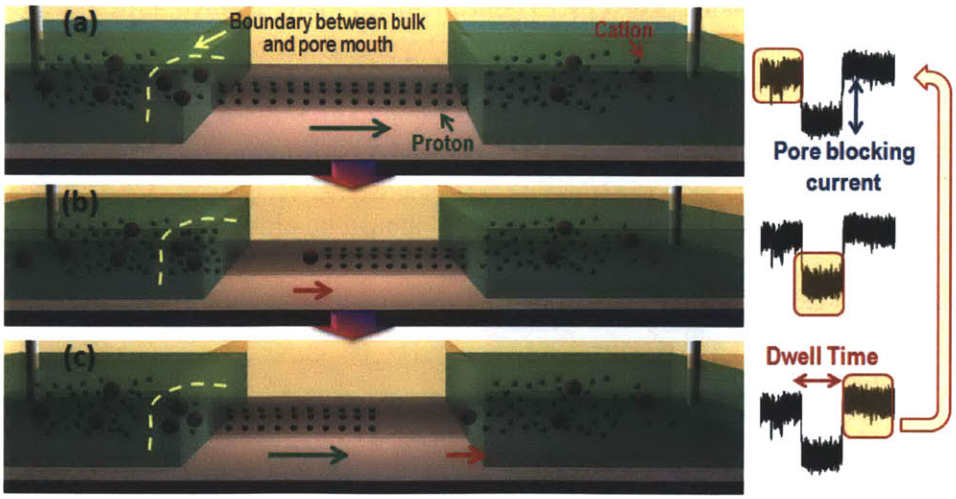

Figure. 3.25. Schematic illustration of ion transport in SWNTs and concomitant electro-osmotic current changes: (a) Proton flux, (b) ion insertion, and (c) recovery of proton flux.

In one of the devices we tested, we observed CR in one SWNT with 3M KCl in the reservoirs. Over time, this developed into two simultaneous CR traces being observed as a second SWNT opened up. The current trace is composed of four distinct current levels and two dwell times which indicate that there are two activated SWNTs (SWNT #1, #2) undergoing high- and low-frequency CR (Figure 3.26a). The differences in CR frequencies, dwell times, and pore-blocking currents between the two channels can be due to different diameters or number of carboxylic groups on the ends. Although the SWNT diameters in the device are 1.2-1.8 nm, a small difference can induce dramatic changes in CR characteristics. The histogram of ΔG (conductance change upon ion partitioning) (Figure 3.26b), and ion mobility(=[channel length]^2/[voltage][dwell time]) (Figure 3.26c) distinctly show the contributions from two SWNTs. SWNT #1 has large ΔG (48 pS) and ion mobility (2.8×10^{-5} m^2/Vs), whereas SWNT #2 generates relatively low ΔG (21 pS) and ion mobility (0.4×10^{-5} m^2/Vs). This result implies that SWNT #1 has greater proton flux and faster cation transport than SWNT #2. Performing FFT on the current trace reveals resonant frequencies centered at 12 Hz (SWNT #1) and 1.4 Hz (SWNT #2), as shown in Figure 3.26d. One hypothesis for this distinct difference can be explained as the bulk to nanoscale transition inside SWNTs. Theoretical simulations have anticipated a transition from bulk to one-dimensionally, confined water chains in SWNT as its diameter decreases.[246-248] Nearer to the transition, ion transport is one-dimensional, resulting in mobilities higher than that in bulk.[249] In this scheme, the diameter of SWNT #1 should be closer to this transition than SWNT #2, which also results in larger ΔG due to enhanced proton flux in one-dimensional water chains.

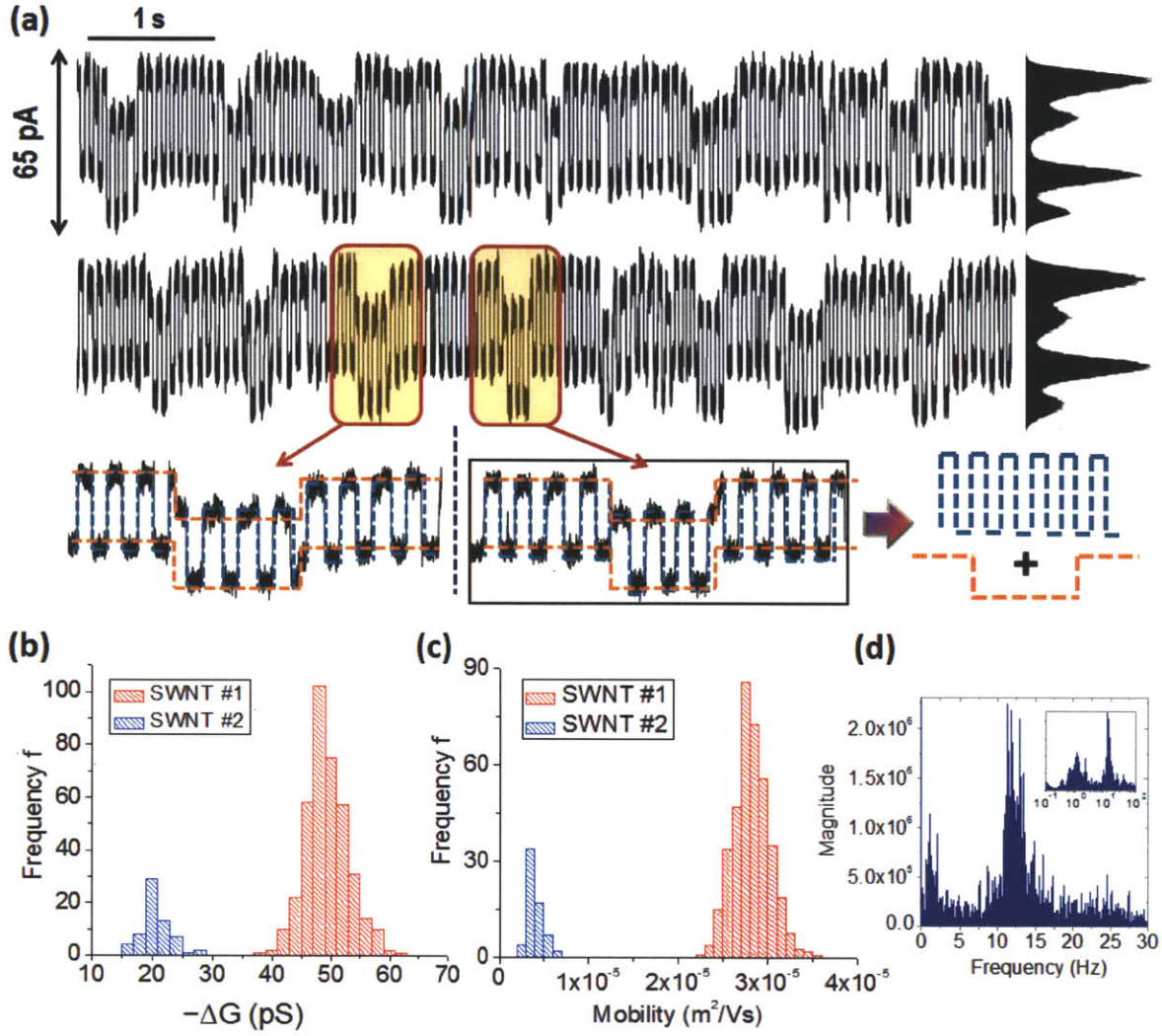

Figure 3.26. Two simultaneous-synchronized coherent resonance (CR) by ion transport at 1000 mV. (a) Representative current traces, all-point histogram and enlarged shapes of a combination of two CR. Histograms of (b) conductance decrease upon ion partitioning, ΔG, and (c) ion mobility for K^+ ion in two SWNTs. (d) Two oscillation frequencies calculated by fast Fourier Transform (FFT) of the electro-osmotic current.

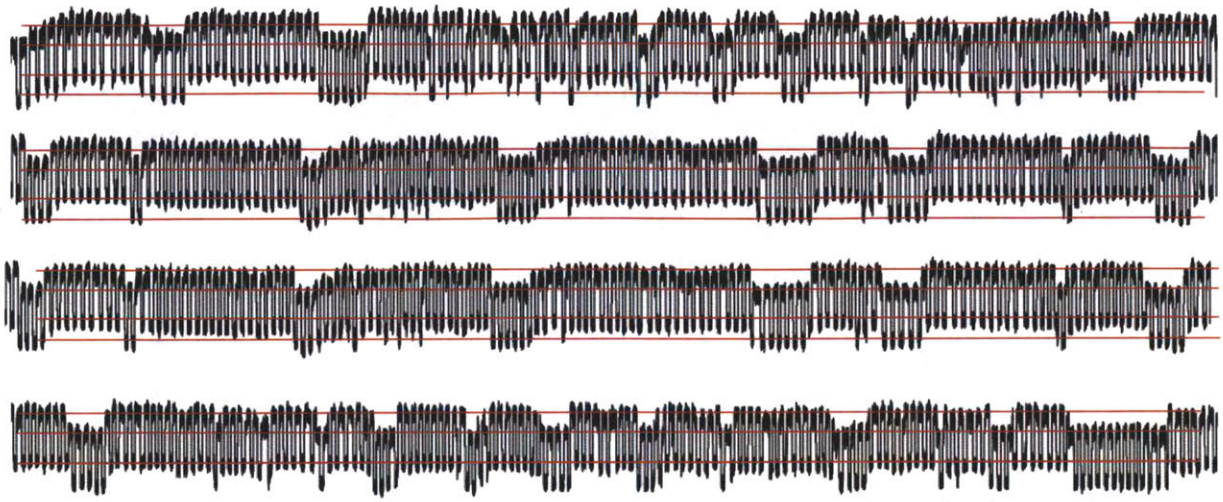

Figure 3.27. More examples of two SWNTs undergoing coherence resonance simultaneously.

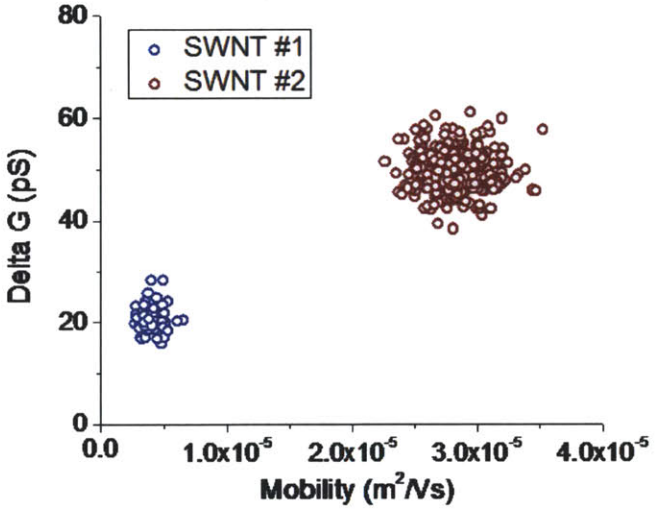

Figure 3.28. The conductance change with blocking, ΔG and ion mobilities of two SWNTs constructing coherence resonance (#1 and #2)

3.3.2. Effects of Ionic Species on the Dynamics in a Single SWNT

The dynamics of ion transport are also correlated with the ionic species. Figure 3.29a shows that K^+, Cs^+, Li^+, and Na^+ produce distinct blockade currents and dwell times. These traces were all observed in the same SWNT device, and the two peaks in the all-points histogram shows that only one nanotube is contributing to the current trace. The distinguishing features are

ΔG (Figure 3.29b), and ion mobility (Figure 3.29c). ΔG reflects the obstructed proton flux by the cation and should be proportional to the hydrated radius inside the SWNT. The ordering for ΔG is $Li^+<Na^+<Cs^+<K^+$, and the ordering for ion mobility is $Na^+<Cs^+<K^+<Li^+$. These orders should be compared to the orders of crystallographic diameters ($Li^+<Na^+<K^+<Cs^+$) and hydrated diameters ($Cs^+<K^+<Na^+<Li^+$) in water.[218] It is well-known that ions need to partially shed hydration shells in order to enter a hydrophobic nanochannel.[250] Shao et al.[251] predicted the anomalous hydration shell order between Na^+ and K^+ inside a CNT. The narrow diameter and hydrophobic nature of SWNTs are critical to the hydration radius and shell numbers, and we observe here that new orders of hydrated radius of cations are implied to be $Li^+<Na^+<Cs^+<K^+$ from ΔG orders. In this case, although the largest ionic size results in the lowest mobility in bulk water, the ion mobility is not inversely proportional to hydrated ion sizes for ion transport through the SWNT interior. For example, except Li+ (the smallest ΔG and the largest mobility), other cations do not follow a normal trend. This can be understood by either the unique structure of hydrogen bonded water in molecular chains, or counter ions on SWNTs. First, in bulk water, molecule chains do not line up in one direction due to no constriction of structures, whereas water molecule chains are aligned inside of SWNTs. Disordering this immovable and stable chain for cations passing through requires completely different dynamics with bulk water. For example, the higher energy barrier would be counted for breaking this substantial chain than that in bulk. Another potential mechanism is that the counter ions are supposed to cancel out the positive charges in SWNTs. When the water molecule chains are unstable, there is a possibility of the existence of hydroxide ions on the SWNT.[252-253] This mechanism might affect the unique order of ion mobility in the SWNT.

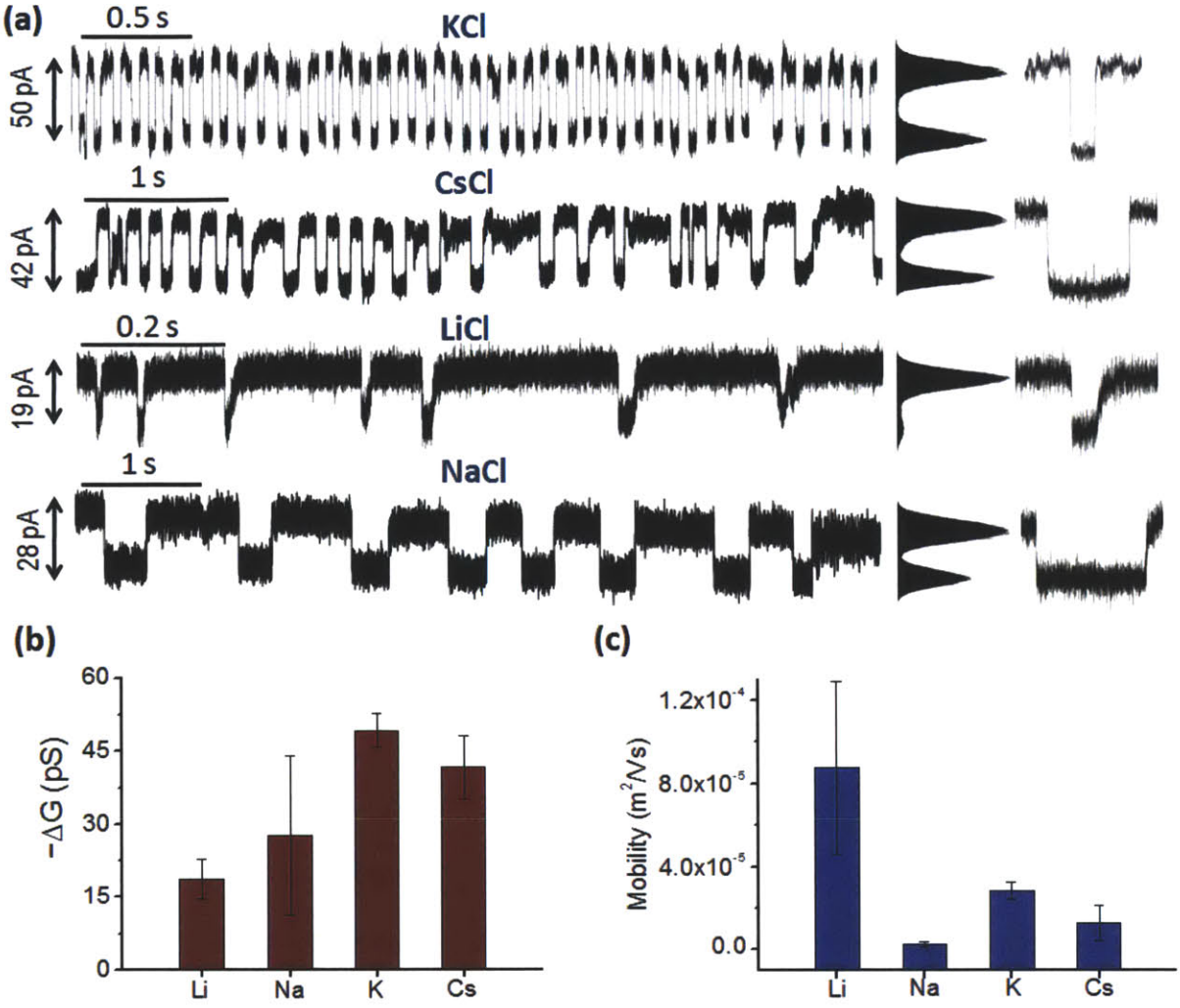

Figure 3.29. Rhythmic oscillations of the electro-kinetic current in various ionic solutions. All data in this figure was collected from the same device. SWNT diameter is unknown. (a) Representative current traces of K^+, Cs^+, Li^+, Na^+, and enlarged shapes of one pore-blocking event at 1000 mV. Histograms of (b) ΔG, and (c) ion mobility induced by the different types of cations. Other 2 devices show the same orders for both blocked conductance and mobility though the absolute magnitudes are varied a little.

3.3.3. Effects of an Applied Electric Field on Dynamics in a Single SWNT

The applied voltage is another critical factor affecting the dynamics of ion transport through SWNTs. While stochastic pore blocking is observed, an increase in the voltage results in an increase in the blockade current and a decrease in the dwell times (Figure 3.30a). The pore-blocking characteristics for K^+ and Cs^+ were explored in more detail from its threshold voltage (the voltage at which pore-blocking events begin[244]) to 1000 mV (Figure 3.30b). In this SWNT the threshold voltages were 500 mV for K^+ and 700 mV for Cs^+. The entire current traces of K^+ and Cs^+ each lasting several minutes are shown in Figure 3.30b. Sometime, when the electric field was suddenly changed, the pore-blocking event disappeared, instantly, and was restored after a while. It is due to the reconstruction of the optimized conditions of CR near the pore mouth such as proton, and cation concentration against new electric potential. Also, during cycling between 500 mV and 1000 mV for K^+, the blockade current was fairly stable at the same electric potential. Figure 3.30c and Figure 3.30d summarize the average ΔG and dwell time, respectively. The observed results show the nonlinear increase in ΔG for both K^+ and Cs^+ as voltage increases (Figure 3.30c). Also, the dwell times decrease (Figure 3.30d), and the ion mobilities slightly increase as applied voltage increases. These results have been observed in many devices, and it is a distinctive trend in high-aspect ratio SWNTs. Theory predicts linear scaling ofΔG, and the constant ion mobility in bulk solutions,[254] whereas other experimental data and simulations have shown the nonlinear scaling of ΔG and the change of mobility under varying electric fields.[255-256] This behaviour in SWNTs is explained by the enhancement of ordered, one-dimensional water structures in nanoscale channel,[257-258] which is also known to occur in the interior of SWNT.[248] This arrangement highly accelerates the proton fluxes in comparison to bulk environments. When the electric potential rises, there is a strong

enhancement of one dimensional arrangement of water molecules from a bulk, disordered configuration to a nanoscale, ordered one, and this results in the nonlinear amplification of proton flux inside SWNTs. This argument also explains the trend in the ion mobility, which should increase in a more ordered, one-dimensional environment induced by higher applied voltage. In addition to that, there might be effects from localization of the electric field near the ion and nonlinear concentration enhancement of protons in the SWNT. All of those reasons should definitely construct the nonlinear amplification of the blocked conductance as a function of the electric field.

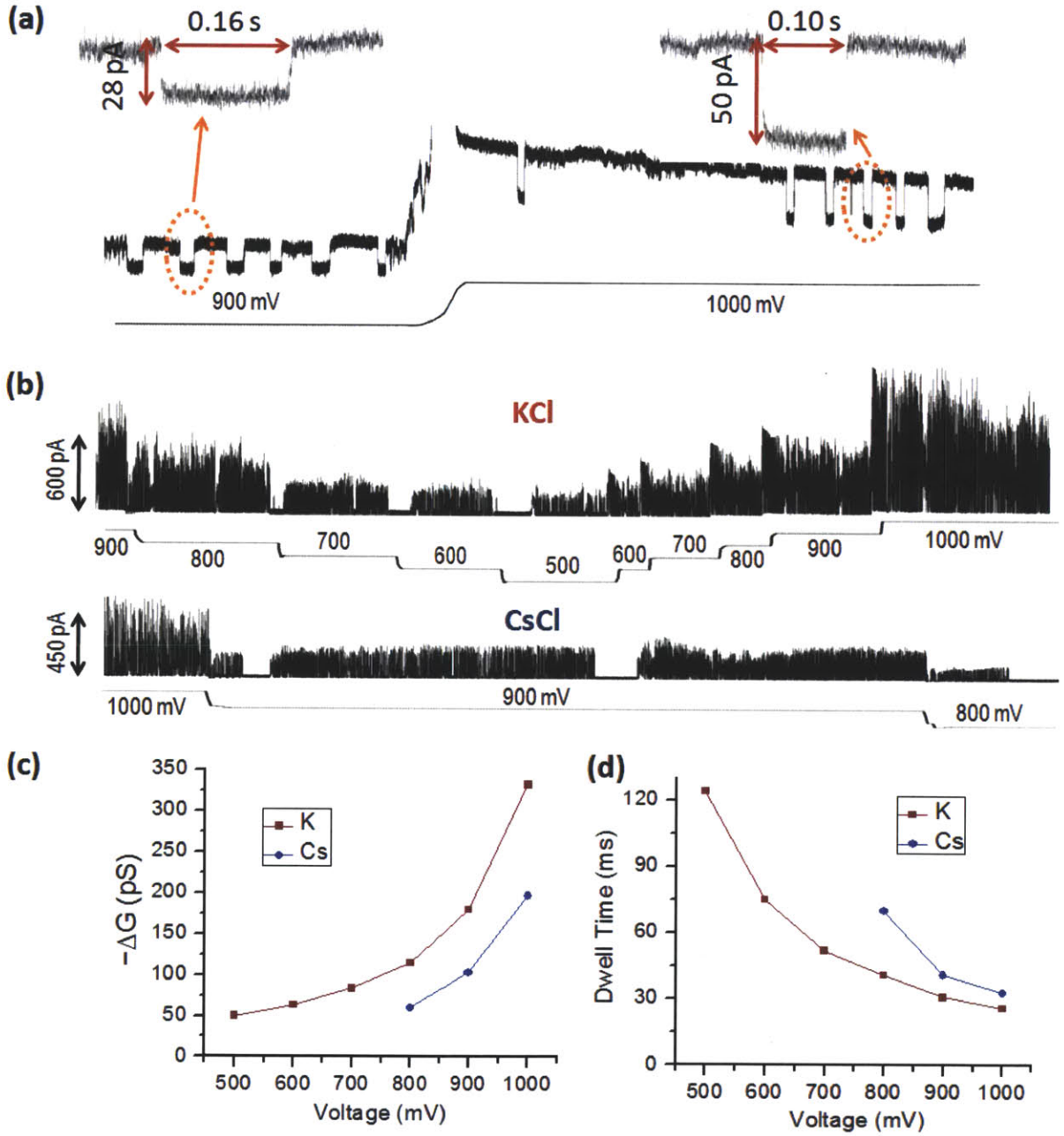

Figure 3.30. Dynamics of ion transport induced by an applied electric field. (a) Real time change of characteristics of ion transport between 900 mV and 1000 mV. (b) Electro-osmotic current traces of KCl and CsCl 3M solutions from the threshold voltage to 1000 mV. Average (c) ΔG and (d) dwell time of K+ and Cs+ depending on an electric field.

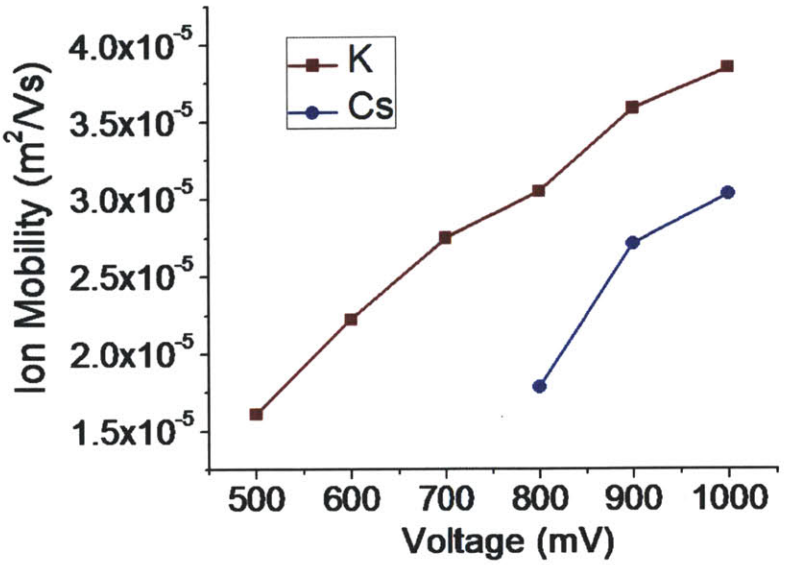

Figure 3.31. Ion mobilities of K^+ and Cs^+ as a function of the applied electric field.

3.4. Effect of Ion Transport upon Diameters of SWNTs

Given the previous data, it is estimated that SWNTs may construct their own blockade current and dwell time. The two parameters are considered to determine the characteristics of ion translocation through SWNTs, which include. The number of carboxylic groups near the pore mouth and the geometric properties and limitations from SWNTs diameters. The former would be controllable by changing the exposure time to oxygen plasma etching, whereas the latter induces complexities. SWNTs in our previous study were in the range of 1.2 nm and 1.8 nm. In spite of the small difference in SWNTs diameters, we observed variations in blockade currents and dwell times. If the correlated phenomena for ion transport inside the SWNTs is formulated as a function of SWNTs diameters, it will provide new insights into understanding the detailed nano-confined effects of hydrophobic channels.

3.4.1. Modified Device Fabrication with a Single SWNT

To explore more detailed dynamics of SWNTs diameters, we modified and fabricated a new device with only one-single SWNT (Figure 3.32). The aligned SWNTs were grown on the silicon wafer by CVD. Specific markers indicating the position of SWNTs on the silicon wafer were deposited by the E-beam evaporation technique. At this stage, SWNTs on the specific area were characterized by Raman spectra, which would give the information of diameters and types (metal or semiconducting) of SWNTs. Based on the information, the only one SWNT was chosen and remained as the specific nanochannel in the device, whereas all other SWNTs were removed by a razor blade etching process (Figure 3.33). On the basis of SEM images for entire silicon wafer and markers, accurate positions of SWNTs relative to markers can be indicated. A razor blade physically etches the area parallel to markers that do not include a target SWNT.

After this selective process, the platform was fabricated by the same manner in our previous work. Briefly, one SWNT and silicon wafer was covered by an epoxy structure (constructed from SU-8 negative photoresist) that defines reservoirs, using UV glue to form a tight sealing. The exposed ends of the SWNT were removed using oxygen plasma, which leaves an open SWNT that spans the epoxy barrier. The reservoirs were filled with electrolyte solutions (KCl, LiCl, NaCl, or CsCl), and a fixed voltage drove the current that is detected by Ag/AgCl electrodes.

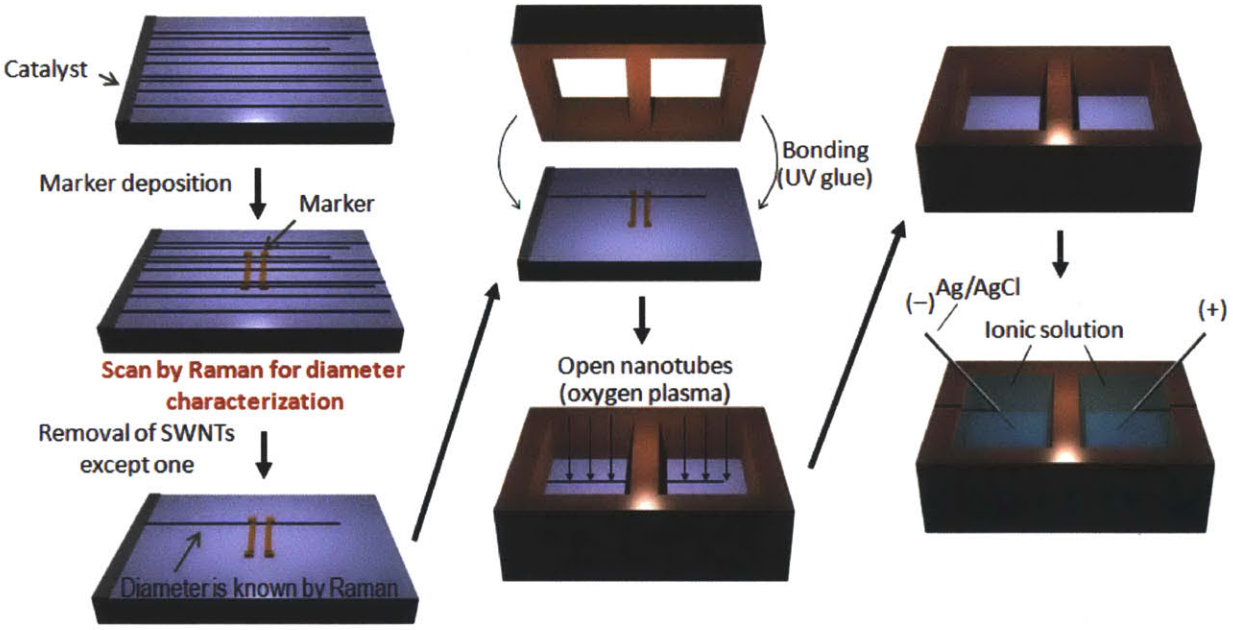

Figure 3.32. Fabrication of a single SWNT ion channel device. After growing SWNTs by CVD method, Raman spectra scans several SWNTs near the specific markers. Except one targeted SWNT, all others are removed. Next procedures follow the fabrication process of multi SWNTs devices in 3.2.1.

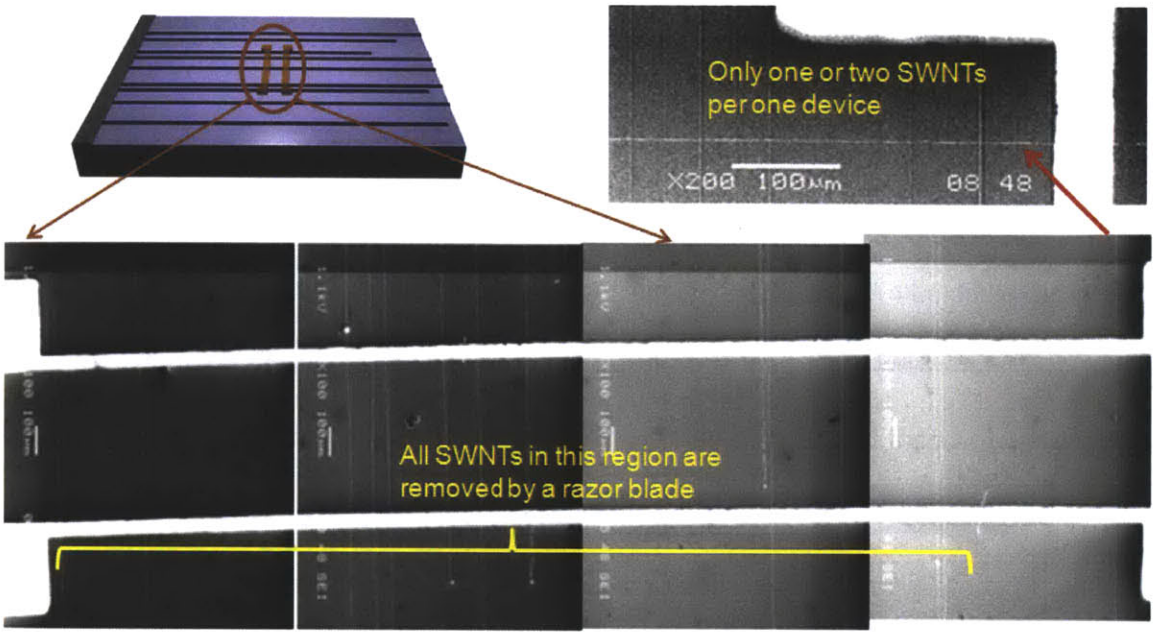

Figure 3.33. Scanning electron microscopic (SEM) images of SWNTs and one selective SWNT. All positions of SWNTs were recorded by SEM images near the specific markers. After characterizing all SWNTs by Raman, only one SWNT remained in the device while others were etched.

3.4.2. Characterization of a Single SWNT by Raman Spectra

SEM images would be able to inform us the exact position between the specific markers and SWNTs (Figure 3.33). Although the optical microscope can detect the position of the specific markers, it is not possible to see an individual SWNT on the silicon wafer due to the limitation of resolutions. Therefore, we roughly estimate the distance between the specific marker and a SWNT based on the entire map prepared by SEM. By scanning few micrometers near the region expected to have a SWNT, we are able to find an individual SWNT on the silicon wafer. The diameter of a SWNT can be collected by either AFM (atomic force microscopy) or Raman spectra. AFM can directly measure the diameter of SWNTs from the difference in height between the surface and SWNTs. However, it needs a large amount of time to scan even a few micrometers. In comparison, Raman spectra needs a relatively small amount of time, and thus it is a more effective method to find the specific SWNT on the silicon wafer in our devices. G mode from Raman scattering indicates whether this scanned area includes a SWNT or not. This G mode corresponds to planar vibrations of carbon atoms and it exists in most graphite-like materials.[259] G peak in SWNTs is shifted slightly to lower frequencies relative to graphite (1580 cm^{-1}), and it shows several seperate peaks depending on the tube structure and its excitation energy. Radial Breathing Mode (RBM) of Raman spectroscopy corresponding to radial expansion-contraction of the nanotube would inform us the diameter according to the relation between its frequency (ω_{RBM}) and a SWNT diameter (d_{SWNT} (nm)). Many empirical fomulas have been available to confirm the scaling of RBM frequency corresponding to a specific diameter. Fanitini et al.[260] studied this scaling of Hipco SWNTs in the solution phase. They demonstrated that this relation would be formulated as $\omega_{RBM}=(223/d_{SWNT})+10$. On the other hand, Jorio et al.[261] developed a formula for an individual SWNT on the silicon wafer

synthesized by CVD as $\omega_{RBM}=(248/d_{SWNT})$. A few years later, Souza et al.[262] confirmed that experimental values measured by AFM are well fitted to this formula with more than one hundred samples. This RBM intensity is normally in the range of 100 and 350 cm^{-1}. We applied this formula to calculate the diameters of SWNTs, while the G peak was used to fix the types of SWNTs. Figure 3.34a is the representative Raman signal for semiconducting SWNTs corresponding to a SWNT in SEM images. The sharp G peak without a large second peak indicates that this SWNT is semiconducting. The RBM peak (180.38 cm^{-1}) is converted to the 1.37 nm diameter by $\omega_{RBM}=(248/d_{SWNT})$. For the metallic SWNT, G peak shows wide distribution (Figure 3.34b). The diameter conversion formula is the same as the semiconducting SWNTs. A 1.57 nm diameter corresponds to the 158.1 cm^{-1} RBM peak. All SWNTs in devices were characterized by the same method, and we were able to explore the diameter scaling of ion translocation through the inside of SWNTs.

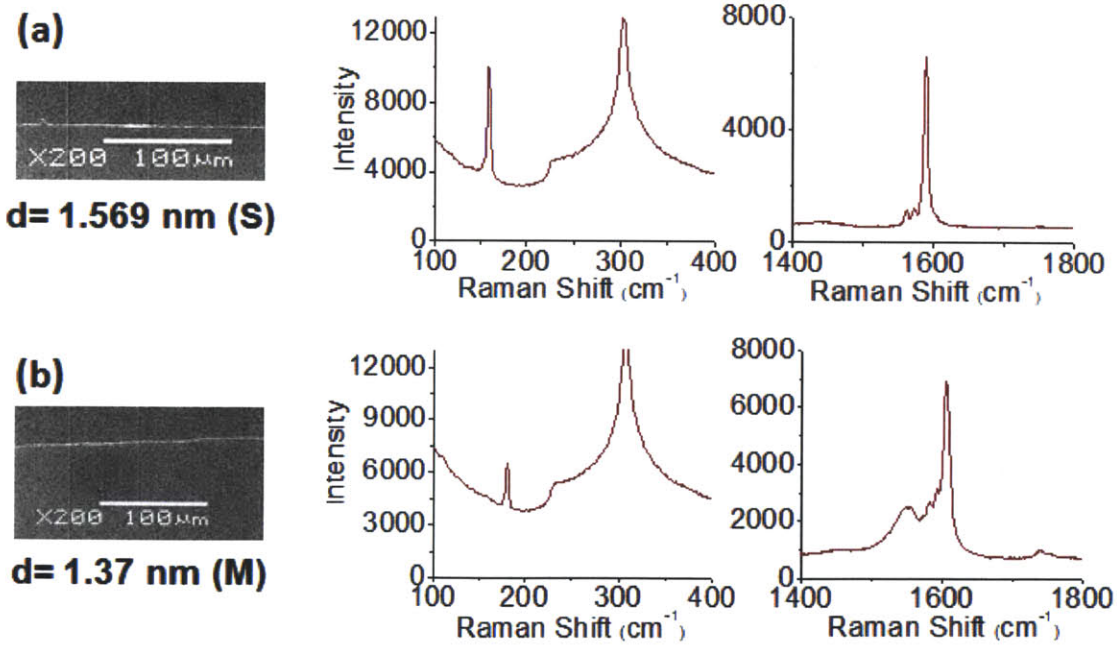

Figure 3.34. Examples of Raman spectra of (a) a semiconducting SWNT and (b) a metal SWNT. RBM peak indicates the diameter of a SWNT and G-peak indicates the type (metal or semiconducting) of a SWNT.

3.4.3. Typical Current Traces of Ion Transport through one SWNT

We reported two simultaneous coherence resonances as two SWNTs opened up at the same time (Figure 3.26). The current trace is composed of four distinct current levels and two dwell times, which indicates that there are two activated SWNTs (SWNT #1, #2) undergoing high- and low-frequency coherence resonance. As indicated, although SWNT diameters in the device are 1.2-1.8 nm, a small difference can induce these dramatic changes in coherence resonance characteristics. Numerical simulations have anticipated a transition from bulk to water chains confined in SWNTs with a single dimension as its diameter changes. Approaching the transition, ion transport is one-dimensional, resulting in mobilities higher than those in bulk. This suggests that the study of coherence resonance in different diameters of SWNTs will give the most intriguing understanding of sub nm, high aspect ratio, hydrophobic nanochannels. A specific diameter of SWNT is expected to construct its distinctive movement of ion and proton transport.

Figure 3.35 shows the representative current traces from many devices in different diameters. Figure 3.35a shows the current trace and histograms in blockade current and dwell time of the 1.74 nm diameter SWNT, while Figure 3.35b is the data from the SWNT with the diameter of 1.67 nm. At some times, during experiments, sometimes, the irregular change of current states might be observed due to the random behaviors of species near the pore mouth. Therefore, in order to confirm successive single cation transports, both dwell time and blockade current should have regular shapes. We can see the well-distributed histograms of both blockade current and dwell time, similar to the Poisson distribution. Moreover, in spite of small change in diameters from 1.74 nm to 1.67 nm, the blockade current increases twice, whereas the dwell time is lowered. It implies that the sensitive change of geometrical constriction in nanoscale may

induce the critical behavior about the dynamic behaviors of nanofluidics. Furthermore, it should be noted that the dwell time is more widely distributed in comparison to the case of blockade current. The blockade current is related to the proton flux through water molecule chains, and the dwell time is affected by cation transport. Water molecule chains are stabilized and nearly immovable in a SWNT, whereas cations pass through a SWNT with breaking the water chains.

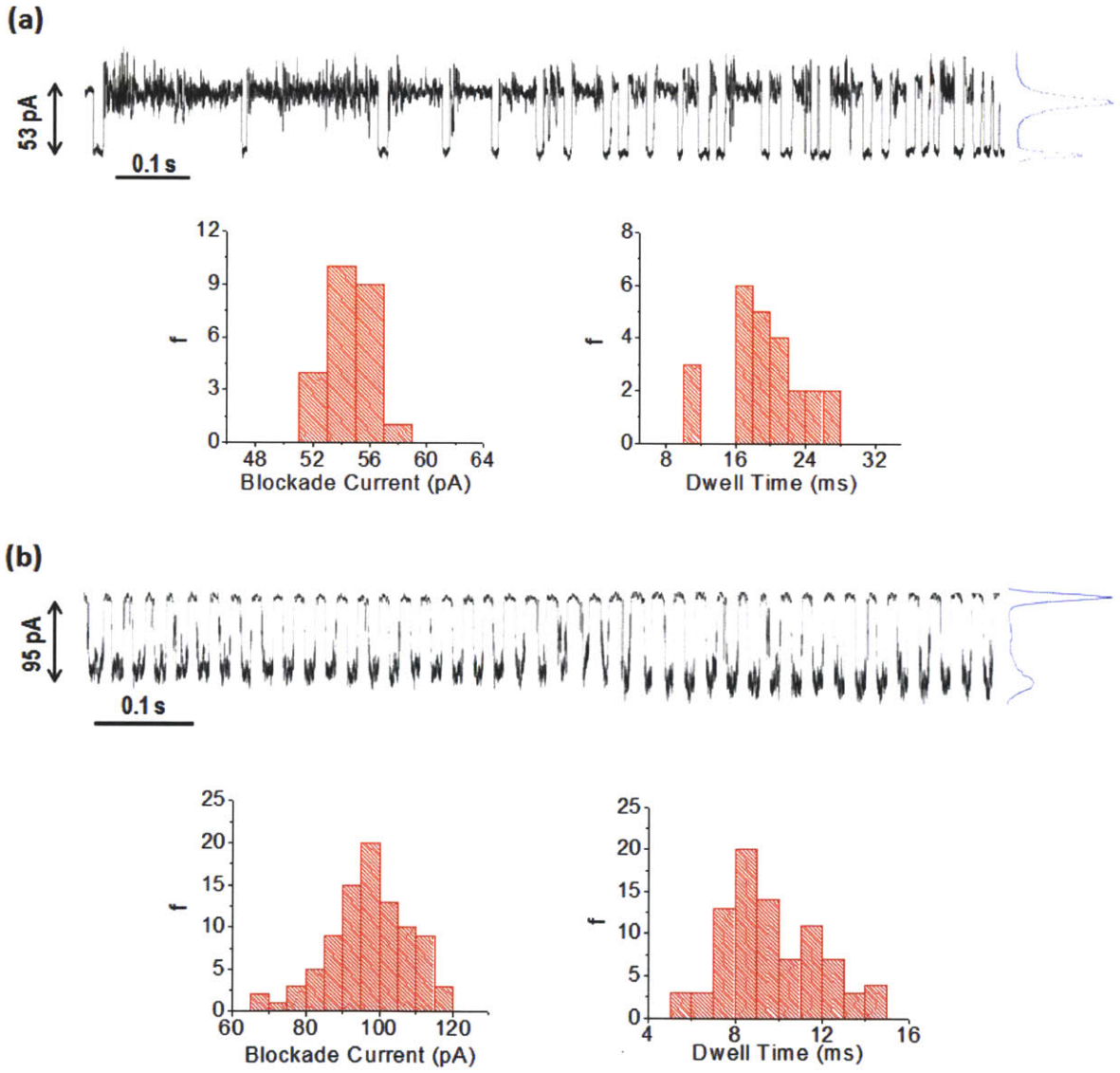

Figure 3.35. Examples of typical current traces and histograms for a specific SWNT diameter. Histogram shows the poisson distribution for both blockade current and dwell time. Data for (a) a 1.74 nm, semiconducting SWNT and (b) a 1.67 nm, semiconducting SWNT. Potassium ions were the blockers for both cases.

3.4.4. Conductance and Dwell Time as a Function of SWNT Diameters

A number of devices with one, two or three SWNTs have been fabricated and tested for ion translocation by the voltage clamp setup. A higher failure rate has been observed in a device with a single SWNT in comparison to multi SWNTs devices. In the previous work, multi SWNTs in one device were fabricated to increase the probability of the observation of ion transport during experiments. Many of multi SWNTs in devices were permanently blocked by impurities or defects from CVD or fabrication processes. Moreover, SWNTs with the high aspect ratio might be bended or damaged during the fabrication, and these uncertain obstructions could block the paths of ions. An applied electric field (max 1000 mV) may also remain below the requisite field to begin ion translocation cleaning the blocking species or to overcome the potential barrier (threshold voltage) near the pore mouth. Therefore, many devices have been fabricated and tested. Pore-blocking events have only been constructed in about 15 devices out of over 100 devices.

First of all, the 12 devices with pore-blocking events in a single SWNT are shown in Figure 3.36. This plot includes all pore-blocking events that are described by its distinctive blockade current and dwell time. It should be noted that the blockade current is shown in a linear scale, while the dwell time is presented in a log scale. In some devices, the blockade current is widely scattered, but the normal distribution follows the Gaussian distribution similar to the histograms in Figure 3.35. The red cross in the scatter plot (Figure 3.36) indicates the average value of blockade current. We can find quite distinctive trends of blockade current as a function of SWNTs diameter from this plot. Interesting phenomena occur near 1.6-1.7 nm. The overall trend under 1.6 nm is an increase in blockade current induced by larger diameters. The maximum values are observed near the range of 1.6 nm and 1.7 nm, and it starts showing the

reduction in the blockade current. The blockade current above 1.7 nm decreases again, and it continues to the area of 2 nm. With respect to dwell time, we can see more widely distributed points than the blockade current, although it seems that dwell time also maintains roughly the general trend. Figure 3.37 represents the average values and the standard deviation of the blockade current (a) and the dwell time (b). The dwell times are in the minimum values around 1.65 and 1.75 nm. It is approximately in the inverse proportion to the blockade current. However, the dwell time is more randomly distributed rather than any clear tendency. The large standard deviation in the dwell time also confirms more irregular distribution in the dwell time.

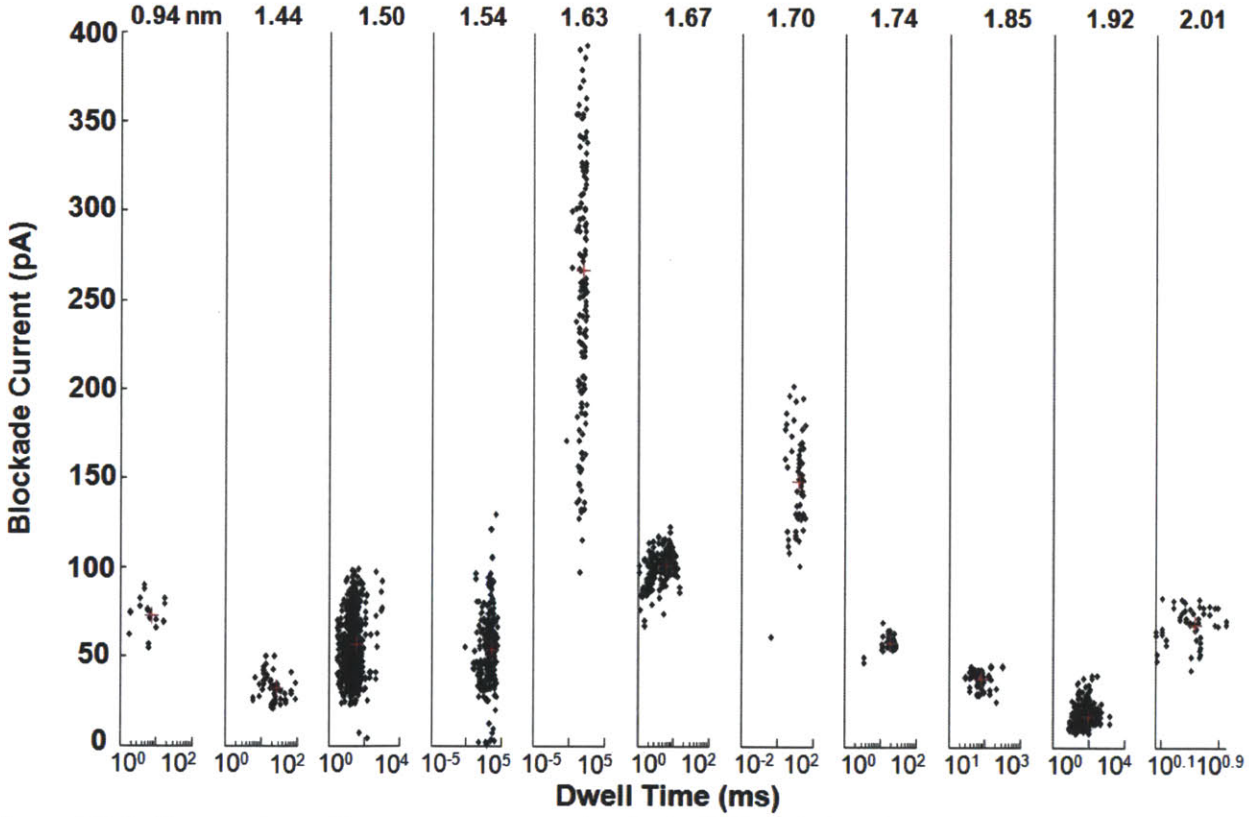

Figure 3.36. Scatter plots of ion transport events for single SWNT devices in 3M KCl solutions. Dwell time VS blockade current. SWNTs diameters are in the range of 1 nm and 2 nm. The red cross for each subplot indicates the average blockade current for one device. Note that dwell time is distributed in different time scale for each device. Potassium chloride solution was used during the experiments.

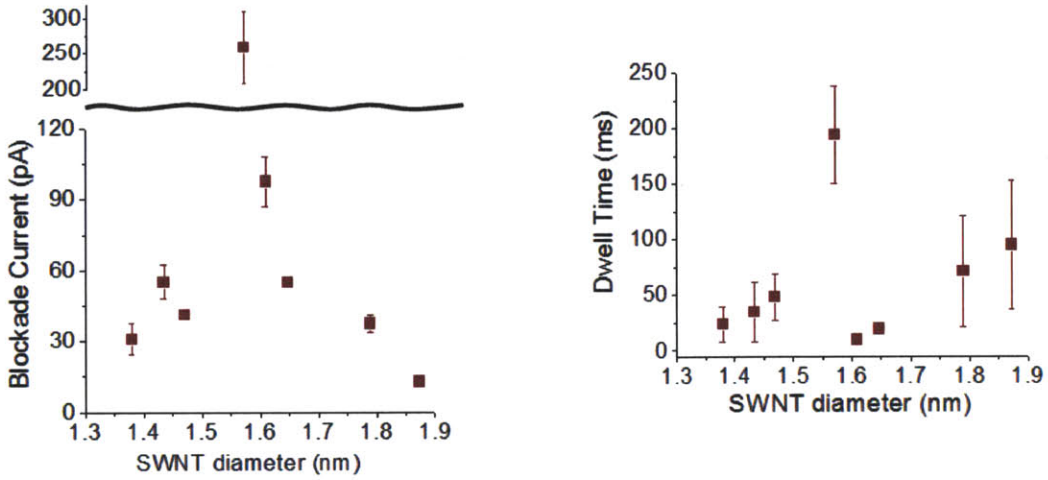

Figure 3.37. Average magnitude and standard deviation of blockade current and dwell time for single SWNT devices.

In different devices, there might be different conditions of negatively charged carboxylic groups near the pore mouth. To examine the accurate effects of different diameters in similar pore mouth conditions, we fabricated many 2 or 3 SWNTs devices with known diameters. Based on the single SWNTs data, we can assign which pore blocking phenomena match up with events in the specific diameter of SWNT. Student's t-test about 1.5 and 1.7 allows the assignment of multi SWNTs devices (In here, 2 or 3 SWNTs). For example, if two distinctive pore-blocking events in a 2 SWNTs device with 1.2 nm and 1.5 nm are observed, we can assign large blockade current events to 1.5 nm SWNT and the small blockade current events to 1.2 nm SWNT. By means of this assignment, the overall four devices (3 devices with 2 SWNTs, 1 device with 3 SWNTs) are added to the master plot as a function of SWNTs diameters (Figure 3.38). We can still see the unique volcano trend for the blocked conductance. From 1.2 to 1.6 nm, the blockade current increases beyond 1.7 nm, whereas the blockade current reduces. The critical observation is sudden, maximized blocked conductance in the range of 1.6 and 1.7 nm. Figure 3.39 shows the average values and the standard deviation of (a) the blockade current and

(b) the conductance change. The most SWNTs diameter were in the range of 1 nm and 2 nm, because we expected this range would show unique behavior with the transition between the ordered structures of nanofluidics and more randomly distributed molecules in nanochannels. Another unique trend becomes possible below 1 nm range or over 2 nm range. However, over 2 nm, the water diffusion in the bulk would be dominant rather than the immovable water structures in SWNTs. In addition, the ionic selectivity may be weakened, so that the massive ionic diffusion would interrupt the current traces. Under 1 nm range, many researchers have reported that about a 0.86 nm diameter SWNT would construct a single water molecule chain SWNT. Therefore, there can exist high possibility to observe another unprecedented change due to the water molecules chains of single water file near 0.86 nm. Figure 3.39 also describes average values and the standard deviation of (c) the dwell time and (d) the ion mobility. We can still observe the overall trend that dwell time decrease from 1.2 nm to 1.65 nm, while the dwell time increases over 1.7 nm. In addition to that, we investigated the effect by the different types of ions whether it is metallic or semiconducting type. There were no specific trends depending on metallic or semiconducting SWNTs. It means that the most parts of distinguishable events might be constructed by geometrical conditions like diameters and lengths rather than the surface structures characterized by the chirality of SWNTs. However, as we discussed in single SWNT devices, this trend is not clear enough to confirm any specific dynamics. Another observation is that the standard deviation of the dwell time in large diameters (low ion mobility) are relatively larger than small one, and it might be due to the diffusive, random movement of cations for all directions inside the SWNTs in a larger diameter channel.

In addition, we investigated the effects of the baseline current on the blockade current. As we informed, the baseline current was constructed by the leakage current. When a SWNT

was activated, the current trace was circulated between the opened state and the closed state as a coulter state. Figure 3.40 shows the comparison of the baseline current, closed state, and opened state. It should be noted that the magnitude of the baseline has not shown any systematic changes being related to the blockade current (Opened state - Closed state). This random tendency is a strong proof that the blockade current was constructed by only a SWNT rather than the leakage current. Also, the leakage current was highly varied due to the different conditions, such as the cross-linking of epoxy structure or UV glue adhesion during the fabrication.

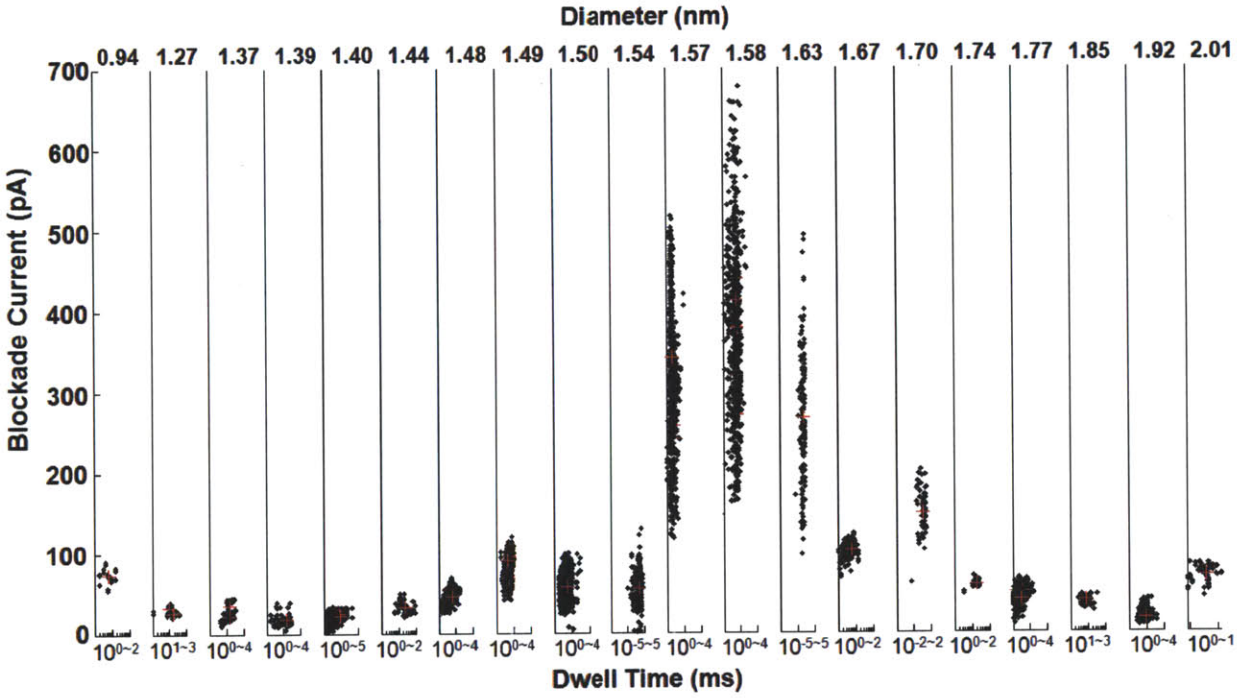

Figure 3.38. Scatter plots of ion transport events for all SWNTs including single SWNT devices and multi SWNTs devices. SWNTs diameters are in the range of 1 nm and 2 nm. The red cross for each subplot indicates the average blockade current for one device. All experiments were conducted in 3M KCl and 1000 mV. The length of SWNTs was 1000 μm for the comparison in the same conditions.

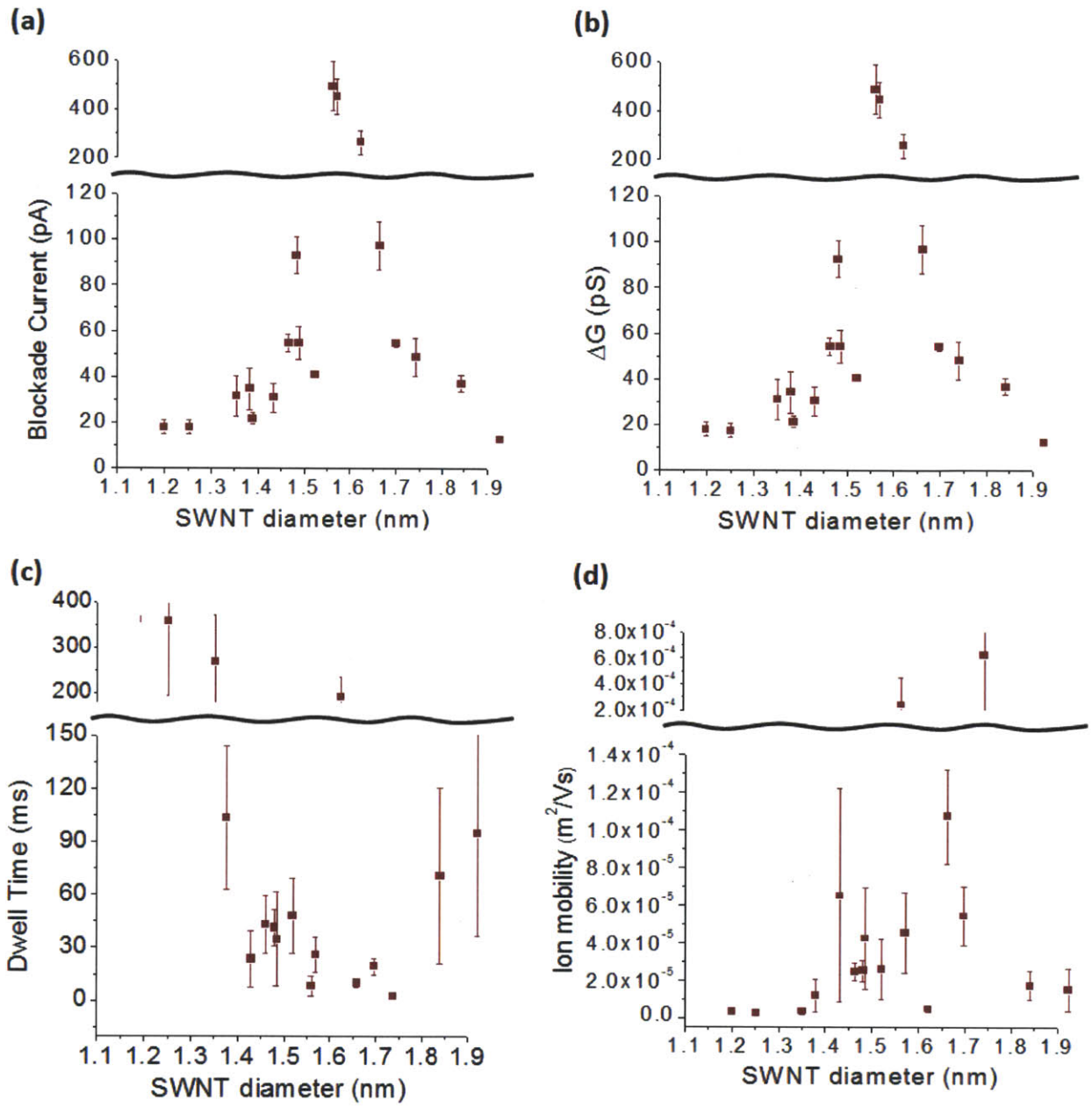

Figure 3.39. Average magnitude and standard deviation of pore-blocking events from one SWNT device and multi SWNTs devices. Test solution was 3M KCl, and all SWNT length was 1000 μm. (a) Blockade current, (b) blocked conductance, (c) dwell time, and (d) ion mobility.

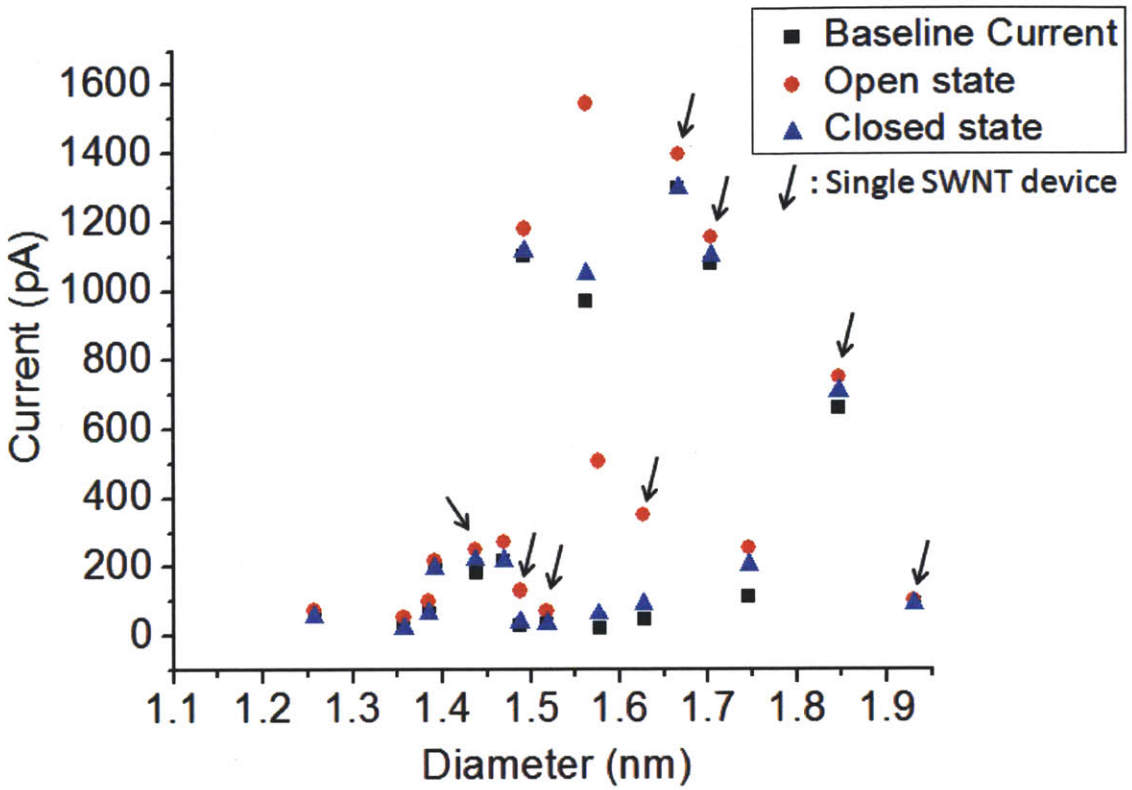

Figure 3.40. Comparison of absolute magnitudes of current traces for baseline current, open state and closed state.

We need to explore detailed analysis and descriptions why we observe this kind of unique trends for the blockade current. The first step is estimating the conductivity and conductance of SWNTs. In an unblocked state, protons flow through the nanotube. Upon complete blockage the proton current will decrease, and generate the blockade current. From the current reduction (ΔI), with known nanotube length (1000 μm) and diameter (1-2 nm), we can calculate the proton conductivity through the nanotube.

$$Conductivity = conductance \times \frac{length}{area} = \frac{\Delta I}{voltage} \times \frac{length}{area} \qquad (3-5)$$

Since the main charge carriers are the protons in the system, the equation gives us the proton conductivity through a single SWNT. Also, the dwell time allows us to calculate the ion mobility and its drifting velocity. It turns out that the proton flux is quite high in comparison to the bulky membranes in solutions. We need to understand how it is feasible to have the high proton flux in SWNTs. First, the proton conduction rate calculated from the blocked conductance is quite high, but it is in the range of other nanochannels. As we described in previous work [192], the proton conduction occurs via proton hopping along continuous water networks (Grotthuss mechanism). The interior is filled with networks of water molecules and does not require any counter ions. Assuming 10 water molecules in the cross-sectional area of SWNT, proton hopping velocity of 5×10^4 m/s and mobility of 5×10^5 cm^2/Vs are estimated. Compared to the experimentally measured proton mobility through a 50 μm diameter capillary [263], the value is 8 orders of magnitude higher, which seems unreasonable. However, the number is not entirely unrealistic when compared with Mann et al.'s molecular dynamics simulation [247] where they report the proton hopping velocity of 1.25nm/150 fs (~10^4 m/s) through a (6,6) SWNT. The fast proton conduction is still valid in this diameter because the electric field reorients water molecules in the desired direction and further facilitates the proton transport. [264]

In a physical model, the trend of the blockade current can be explained by the interaction between ordered water structures and hydrated cation size in this confined SWNT structures. The magnitude of the blocked conductance can be estimated by

$$\Delta G = \left(\frac{d_{ion}}{d_{tube} - \sigma_{C-O}} \right)^2 \Delta G_{\max} \qquad (3-6)$$

where, d_{ion} is the diameter of a cation including hydration shells in a confined space, d_{tube} is the diameter of a SWNT, ΔG is the blocked conductance by a cation, ΔG_{max} is the whole proton flux

through a SWNT, and $\sigma_{C\text{-}O}$ is the Lennard-Jones parameter for C-O interaction (0.0319 nm). in this equation, critical parameters are ΔG_{max} and d_{ion} because other parameters are already fixed in the system. ΔG_{max} depends on the maximum proton flux rate in a SWNT whereas d_{ion} is decided by hydration shell sizes in a sub nanometer scale. Confinement at the molecular scale strongly affects the behavior of water and ions and can lead to effects that are not anticipated from macroscopic descriptions. It is well known that ions need to shed its one or two hydration shells for entering the nanoscale channels. The bulk hydration radius is not the same as that in the confined nanopore. Moreover, in wider pores, which are readily filled by water, there exists considerable midrange ordering of the solvent induced by the ion, i.e. its hydration shell (radius of the second shell 0.53 nm), and by the wall (about two water layers, 0.6 nm). Combining these two ranges, we estimate that the solvent-mediated wall-ion interaction can extend to about 1-2 nm. Thus, ions will still be affected by the pore surface even if the pore is 10 times as wide as the bare ion. Around an ion there exist multiple hydration shells. Ions shed some of their hydration when entering, and remain hydrated inside the nanotube. One of the potential barrier for threshold voltages originates in the high energetic cost for an ion to shed its first or, in wider pores, its second hydration shell. For example, in the narrow selectivity filter of the potassium channels, evolution has demonstrated how to overcome dehydration barriers by solvating ions by carbonyl oxygens, which seamlessly replace water molecules in the first hydration shell, leading to a vanishing barrier for ion permeation.

From the data in Figure 3.38, we can estimate that the transition of shedding hydration shells is near 1.65 nm. The possible explanation is that more hydration shells should be shedded to enter a SWNT under 1.6 nm. Near 1.65 nm, an increase of geometric confinement would reduce the energy to enter the pore, and less hydration shells would be needed to pass through a SWNT. In

this case, d_{ion} would suddenly be increased near this transition point that turns out a significant increase in ΔG. Also, water molecule structures are quite dependent on the diameter of a SWNT. Near 1.65 nm, water molecules construct well-ordered double-cylindrical structures [265] to amplify the proton flux. Over 1.7 nm, water molecule structures show the transition to the bulk states of the radial distribution from the center of a SWNT, and it would significantly decrease the proton flux per the same area (ΔG_{max}/Area). If the blocker only breaks the bulk area near the center, the blocked proton flux would significantly be diminished in comparison to ordered water structures. In addition, in the range of 1.3 nm and 1.6 nm, the number of water molecules in chain networks are small due to its one cylindrical structure surrounding single-chain structure. This reduction in total available hydrogen bonds with D defects in water molecule chains induces a decrease in the overall proton flux, ΔG_{max}. Under 1.3 nm, water structures would be one cylindrical structure, so that the decrease in ΔG_{max} would be promoted in comparison to other ranges. These coinstantaneous dynamics between water structures (ΔG_{max}) and the hydration shell size (d_{ion}) explains the overall trend of conductance as a function of SWNTs diameters.

3.5. Understanding Physical Mechanism of Ion and Proton flux in CNTs

Understanding the physical mechanism of ion and proton flux in a SWNT is critical to why we observe the diameter scaling of ion transport and large conductance in a SWNT. Moreover, it will be the solid foundation to develop more advanced nanofluidic devices, such as synthetic biological channel, proton exchange membranes, high performance fuel cell, DNA sequencing, and energy storage devices. The first step is elucidating the ion and water structures inside of a SWNT. It is true that water structures in a confined nanochannel is relatively immobile in comparison to the bulk states.[266-268] Sometimes, in a specific geometry, the ice or helix formations are constructed inside of it at room temperature [269-270], and these amplify the proton flux by Grotthuss mechanism (Proton 'hop' and 'turn'). Another interesting hypothesis is the formation of special water structures inside of SWNTs depending on the diameter.[265,271] It was already proved in many molecular dynamic simulations that water structures can be changed to various shapes in the diameter range of 1 nm and 2 nm. For the first step, we should confirm whether the water formation at room temperature is immobile in a SWNT or the liquid formation with unique structures.

3.5.1. Set up of Temperature Scaling Experiments relative to Ion Transport

Temperature scaling experiments yield valuable information about water structure in a SWNT with a high aspect ratio. The high proton flux might be induced by either ice-helix water formation or one dimensional proton transport along the unique water molecule chains. The former would be legitimated if we observe the decrease of blockade current via an increase in temperature. On the contrary, if the temperature increase induces the amplification of proton

conductance, the latter hypothesis, the unique water structures with one dimensional proton transport would be persuasive.

To change the temperature of SWNTs and devices, the input of thermal energy is required. However, it is challenging to produce thermal energy without the electrical noise. Most equipments for heat energy generation uses the conversion from electrical to thermal energy. Since the blockade current in ion translocation is in a pA scale, the typical electrical noise from these kinds of electrical equipment (ex : hot plates) would hinder the measurement of sensitive current change. For that reason, the direct heat supply with a torch was chosen as the method for the temperature change. Figure 3.41 shows the modified setup of temperature scaling experiments. The basic components are similar to the previous setup with Ag/AgCl electrodes and voltage clamp. In addition, the thin copper plate (high thermal conductive material) is placed on the bottom of the testing device (Figure 3.41a). The ultrafast responsive thermocouple (Response time < 0.01 sec) is embedded in the copper plate. A torch supplies thermal energy to the copper plate for several seconds. This thermal energy is transferred to the device and a SWNT by means of the similar method using hot plates for baking silicon wafers. All materials are highly thermal conductive, which enables assuming constant temperatures through the heat energy paths. Figure 3.41b is the real image of the temperature scaling setup. The torch is fixed in optical elements on an optical table, and thermocouples are connected to the thermometer that is able to read the temperature in real time.

A torch is turned on when the regular pore blocking events are observed. Figure 3.42 shows the typical response of temperature change by the heat supplies from the torch. The temperature range during this experiment should be under 50 °C since the higher temperature may induce the significant change of water phase as well as the chemical reaction in electrolyte

solutions. According to the calibration process, we found that heat supplies for 7 seconds would be reasonable to change the temperature upto 50 °C. Due to the delay of heat transfer, the temperature reaches the maximum at 20 seconds after stopping the heat supplies from the torch. After the maximum temperature (Figure 3.42), the system is in the cooling process by an environment, and the response is very slow. According to the curve of temperature measurement, we are able to evaluate the ion transport events in the specific temperature range. We divided the temperature range as each 5 °C region and studied the change of dynamics of ion translocation.

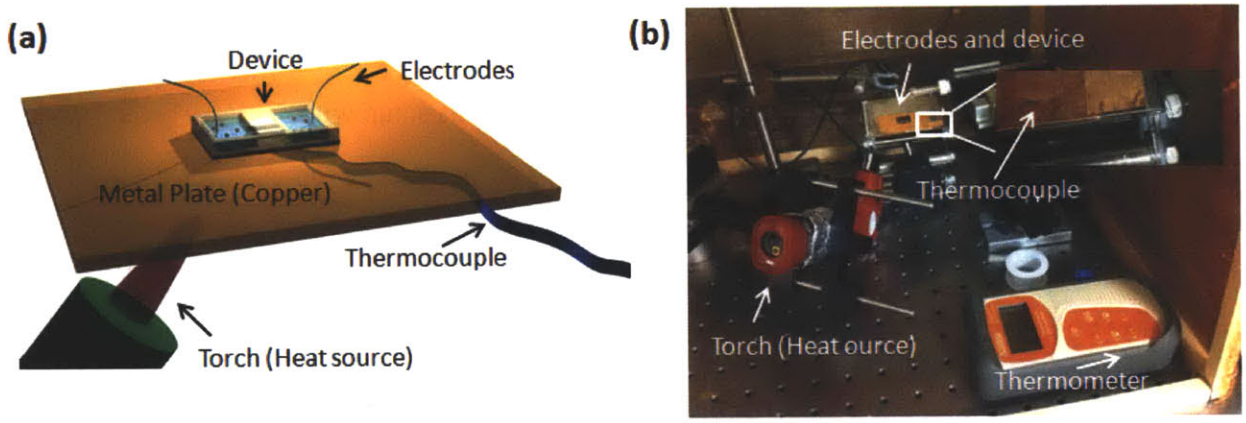

Figure 3.41. Setup for temperature scaling experiments for ion transport in a SWNT. (a) Scheme of the device, heating source (Torch), metal plate and thermocouple. (b) Real image of experimental setup. Ultrafast responsive thermocouple with thermometer for minimizing the delay of temperature measurement.

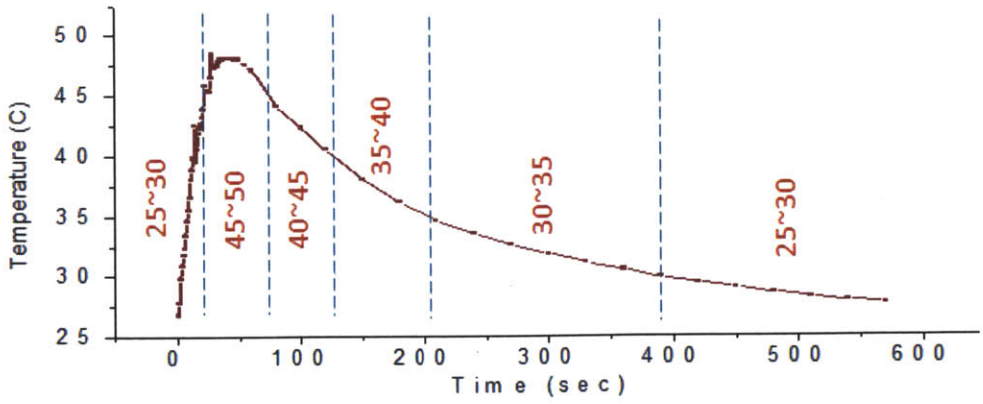

Figure 3.42. Temperature (Celcius) VS Time (sec) plot during the heating by torch and cooling in an environment

3.5.2. Analysis of General Trend of Temperature Scaling

The general trend of temperature scaling experiments is shown in Figure 3.43a. The current traces in our devices are constructed as baseline currents and blockade currents. Although the thick epoxy barrier and UV glue tightly seals the leakage path, it is inevitable to have some leakage current paths through the epoxy structure and UV glue. Thus, the baseline current includes both paths from leakage currents and SWNTs. However, observation of blockade currents clearly indicates the variation of ion transport dynamics as a function of temperature change. When the pore blocking events were observed for a while, we confirmed that the blockade currents and dwell time were in consistent magnitudes. After collecting these data at room temperature (23 °C), the torch was turned on and thermal energy was supplied to devices for several seconds. During the increase in temperature, the blockade current clearly increased while the dwell times were shortened. The increase in baseline currents was originated from both the epoxy structures and SWNTs. After passing the maximum temperature region (≈ 50 °C), the device was cooled down to room temperature. During this cooling process, the blockade current slightly decreased whereas the overall dwell time increased. After long cooling process, the temperature approached the room temperature before heating, and the magnitude of blockade current and dwell time were restored. To collect data, we divided current traces to regions with the span of 5 Celsius degree, such as 25-30, 30-35, 35-40, 40-45 and 45-50 °C. Figure 3.43a and Figure 3.43b are the representative dataset for the blockade current and dwell times in different ranges of temperatures, respectively. In these histograms, the average blockade current increases around 3 times as the temperature increase from 25 to 45 °C. However, for the dwell time, the average value decrease under half of its value at a room temperature. Also, it is true that the blockade current clearly follows this trend with a small deviation whereas the dwell time is

widely distributed. This result is consistent to our previous dataset for SWNTs diameter scaling in 3.4.4.

3 devices were evaluated for this temperature scaling data, and the summary of results are shown in Figure 3.44. One device includes a SWNT with a known diameter, and two devices possesses SWNTs with unknown diameters. The overall trend for the blockade current and conductance are quite clear in all 3 devices (Figure 3.44a, c). Without any outlier point, the conductance increase is consistent in the range of 20 °C and 50 °C. It means that the proton flux inside of SWNTs would be amplified due to an increase in temperature. Also, this result indicates that the water structures through a SWNT in an applied electric field is not either ice or helix formation. It is close to the liquid phase in this temperature range rather than immovable solid structures. It should be noted that the large difference in the blockade current was maintained in each device. In spite of the temperature change, the orders of intrinsic magnitude of blockade current for 3 devices are stable. These results support that the intrinsic properties of SWNTs would be critical to decide proton flux rate in various temperature range. This result can be explained by the increase of proton concentration and D defects in water molecule chains, which enhances the proton flux through the ordered water structures. The overall trend of dwell time and ion mobility is fluctuated whereas the tendency of conductance as temperature increase seems stable. Even though we estimate the overall trend of dwell time and mobility, some outlier events out of overall trend exist in the plot (Figure 3.44b, d). The general trend is due to the fast diffusion and movement of cations through a SWNT nanochannel. The increase of temperature enhances the movement of diffusion and moving velocity of individual species. In addition, it would amplify the random movements of ions to the orthogonal directions in large diameter SWNTs. Depending on the diameter of SWNTs, the space for free motion of ions would be

expandable. This conformational change induces the transition of ion movements from one dimensional to more random motions. It should be noted that the ion mobility is calculated for only one direction along its length axis, while ion diffusion is possible for all directions. Even if the temperature increase certainly promotes the ion diffusion, it may not be counted on ion mobility enhancements due to the random motions in other directions. In this case, the large fluctuation of ion mobility can be observed through the SWNTs. This hypothesis can explain why we observe stable trend of conductance from proton flux and relatively unstable ion mobility from cation transport.

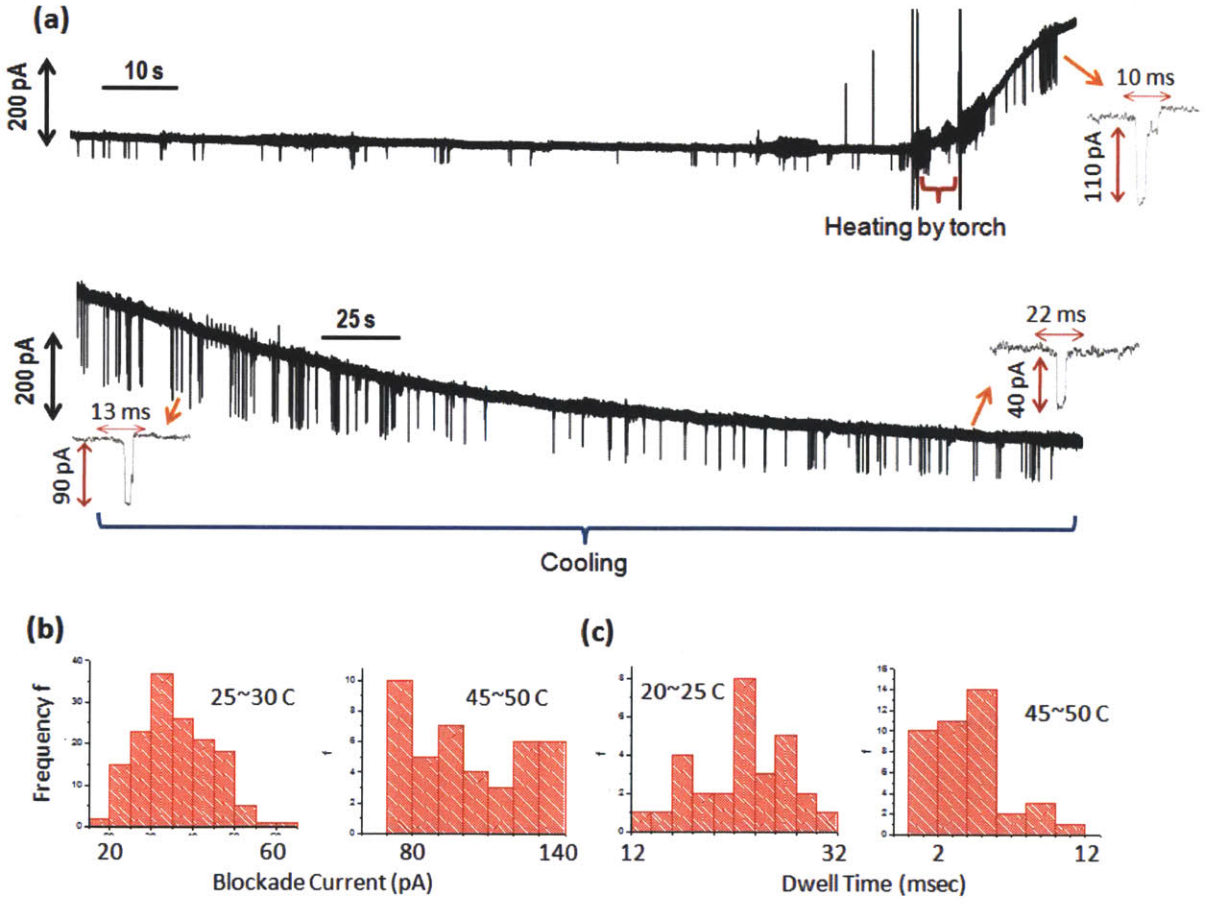

Figure 3.43. Detail trend of temperature scaling experiments in KCl 3M ionic solutions. (a) Representative current traces during heating and cooling for temperature scaling. (b) Example of data processing for blockade current and dwell time. The length of SWNTs was 1000 μm.

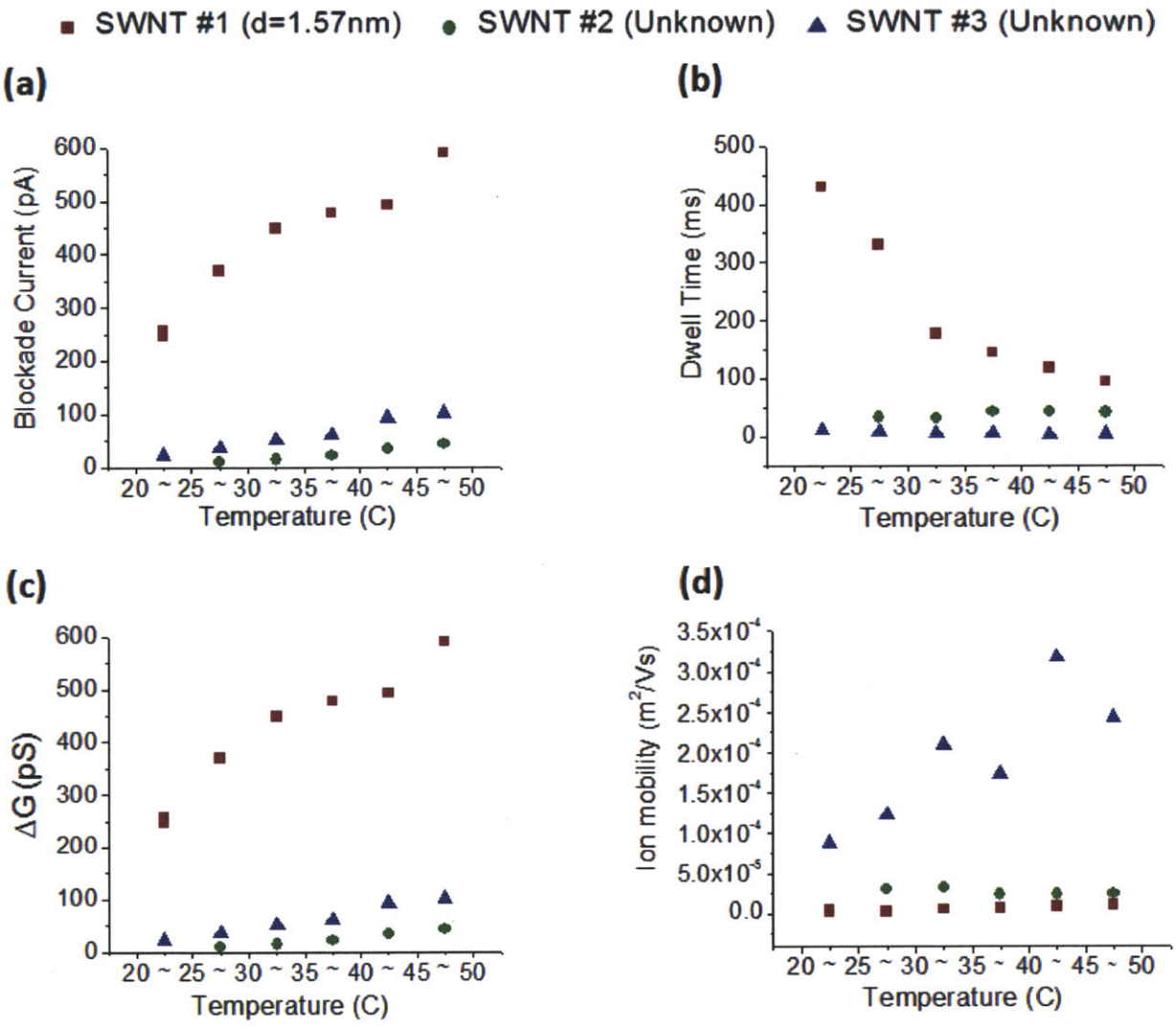

Figure 3.44. Overall Ion transport scaling with temperature dependence.

3.5.3. Activation Energy for Proton Flux

Temperature scaling of transport yields information about the physical mechanism of ion transport through a SWNT. Identification of an activated mechanism, in particular, is revealed. First, we examine the Arrhenius plot (Figure 3.45) for blockade current as a function of reciprocal temperature (1/T (Kelvin)). Using this Arrhenius plot, the activation energy follows as:

$$\ln(\Delta I) = \ln(z) - \frac{E_a}{R}\left(\frac{1}{T}\right) \qquad (3-7)$$

where, ΔI is the blockade current, z is the pre-exponential factor, E_a is the activation energy, R is the gas constant, and T is the absolute temperature. Table 3.1 is the summary of the activation energy. The calculated activation energy from experimental measurements is in the range of 20 and 60 kJ/mol. The activation energy implies the potential barrier to construct the open channel current in SWNTs although it can be varied by pore mouth conditions, such as carboxylic group or impurities. The open channel current might be constructed from proton flux by Grotthuss mechanism (proton hop and turn), or water diffusion, and cation diffusion. The magnitude of activation energy would be critical leading to decide which physical model is validated. Previous research[191,272-274] has explained that the activation energy in the range of 0.1 and 0.5 eV is the proof of proton transfer through water molecule chains by Grotthuss mechanism. This mechanism describes proton transport of excess protons through reforming hydrogen bonds between H_3O^+ and water molecules. This value is in the similar order of hydrogen bond strength in water.[272] The 25-60 kJ/mol activation energy would be converted to 0.26-0.62 eV. This activation energy is in a good agreement with the standard of proton 'hop' and 'turn' mechanism. Moreover, this range is quite similar number for the most well known proton exchange membrane made out of nafion that is described through Grotthuss mechanism , which supports

that our physical model might be from the proton 'hop' and 'turn' mechanism. Other scenarios for the open channel current require the significantly larger activation energy rather than 0.1-0.5 eV.

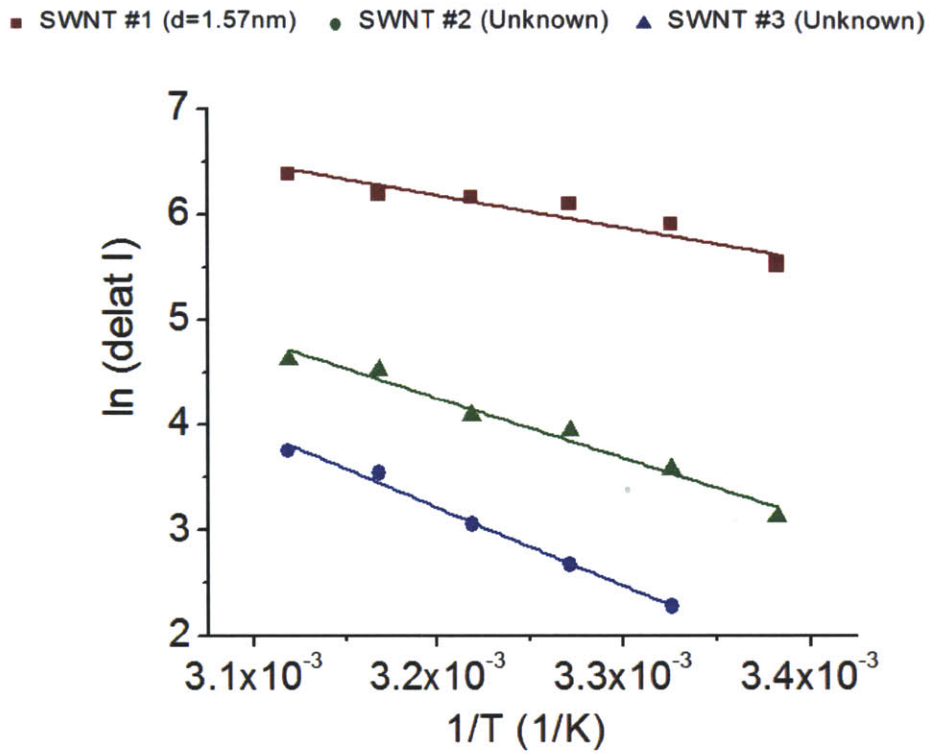

Figure 3.45. Arrhenius plot for blockade current from ion translocation. Activation energy is extracted from this plot.

Table 3.1. Activation energy and slope in Arrhenius plot

	Slope (E_a/R)	Intercept	E_a (kJ/mol)
SWNT #1 :	3075	16.02	**25.57**
SWNT #2 :	5696	26.89	**61.53**
SWNT #3 :	7401	22.48	**47.46**

3.5.4. Correlation between Proton Concentration and Temperature Changes

Temperature scaling experiments confirm that water structures inside the SWNT in an applied electric field are close to a liquid phase rather than an ice phase. In this scenario, the increase of the blockade current in a SWNT can be described by proton concentration change. In proton hop and turn through water molecule chains, the reorientation of water molecules has been accepted as the rate limiting step.[169] Several researchers reported that proton transfer along water molecule chains would be able to the rate limiting step at specific conditions.[169] However, this debate is restricted to the constant proton concentration. If many available protons exist, the conductance would be proportional to the change of proton concentration near the mouth of nanochannels. The ionic solution at either wells in our devices are contacting with the pore mouth of SWNTs. During the temperature scaling experiments, the temperature of ionic solution increased together, and we may assume that the temperature of the solution is that of the thermocouple.

The proton concentration in solution is related to the water dissociation constant, K_w. The water dissociation constant has been explored experimentally, but there is no completed theoretical analysis up to date. In order to anticipate the water dissociation constant in a wide range of temperature, the empirical formula can be used, [275]

$$K_W = 8.754\times10^{-10}\exp\left(\frac{-1.01\times10^{6}}{T^{2}}\right) \qquad (3-8)$$

where T is the absolute temperature. The water dissociation constants as a function of the temperature is plotted in Figure 3.46a. A proton concentration proportional to $\sqrt{K_w}$ and the relation with a temperature is

$$\text{Proton concentration} \propto \left(\exp\left(\frac{-1.01\times10^{6}}{T^{2}}\right)\right)^{\frac{1}{2}} \qquad (3-9)$$

The range of interests is between 293 K and 323 K. The proton concentration, $\sqrt{K_w}$ at 323 K (8.3×10^{-8}) is about 3 times larger than that at 293 K (2.35×10^{-7}), as shown in Figure 3.46b. The proton concentration near the pore mouth and SWNTs would be amplified with temperature increases as well, and the magnitude of amplification, roughly 3 times are quite similar to our measurement between 298 K and 323 K, as seen in Figure 3.44.

Moreover, the amplification of water dissociation can directly change the hydrogen bonded network in both a SWNT and pore mouths. As the applied electric field made more ordered or disordered hydrogen bonds in a SWNT, temperature increase can induce the intrinsic change of the structure of hydrogen bonding. Hanasaki et al. [265] reported that between 300 K and 340 K, the water structure inside of a SWNT is quite stable, and it does not matter for the dynamics of hydrogen bonds. However, in our system, we should consider the effect of the pore mouth. Especially, in the serial circuits of our devices, the narrow, hydrophobic SWNTs would be the dominant factor of the resistance rather than the bulk water region. It turns out that the water impedance in both reservoirs is negligible whereas the impedance between the entrance and the exit of a SWNT channel is high. Therefore, the most of the applied electric field, or the transition of water structures by water dissociation were concentrated on the pore mouth. This large ΔV and Δ of water dissociation at the entrance of a SWNT highly amplify the proton flux inside of a SWNT. It is quite consistent to the mechanism of coherence resonance on the previous chapters, the depletion of proton concentration by means of the fast proton flux in a SWNT.

Figure 3.47 shows the direct comparison between the change of blockade current in experiments and the calculated proton concentration. The variation of the magnitude of blockade current in 3 devices are in the range of 2.5 and 4 times. Furthermore, the overall shape of increase of

blockade current is well following the trend of proton concentration, as shown in Figure 3.47, although the detailed shape is slightly different for each device. As it is informed, this increase might be due to the increase of proton concentration near the pore mouth as well as the local dissociation of water near the pore mouth. In addition, another possible mechanism is the increase of the D defects in water chain structures in a SWNT.[169] Proton is transferred along water chains. This proton transfer is regarded as the transfer of defects along the water chains, and the number of protons in a flux should be fixed in the number of defects occupied by protons. These available defects for protons are normally called as D defects.[169] In the Grotthus mechanism for proton flux, each proton would occupy D defects and be transferred along water structures. It is generally accepted that temperature increase significantly amplifies the number of D defects. The rate limiting step in proton flux is known as water reorientation in bulk water. However, for the narrow hydrophobic channel, the potential barrier near the entrance is another critical rate limiting step. Moreover, an applied electric field would make more oriented water molecule chains, and the weight of reorientation is weakened. In conclusion, the amplification of proton concentration and the number of D defects well describe the increase of blockade current as temperature increases.

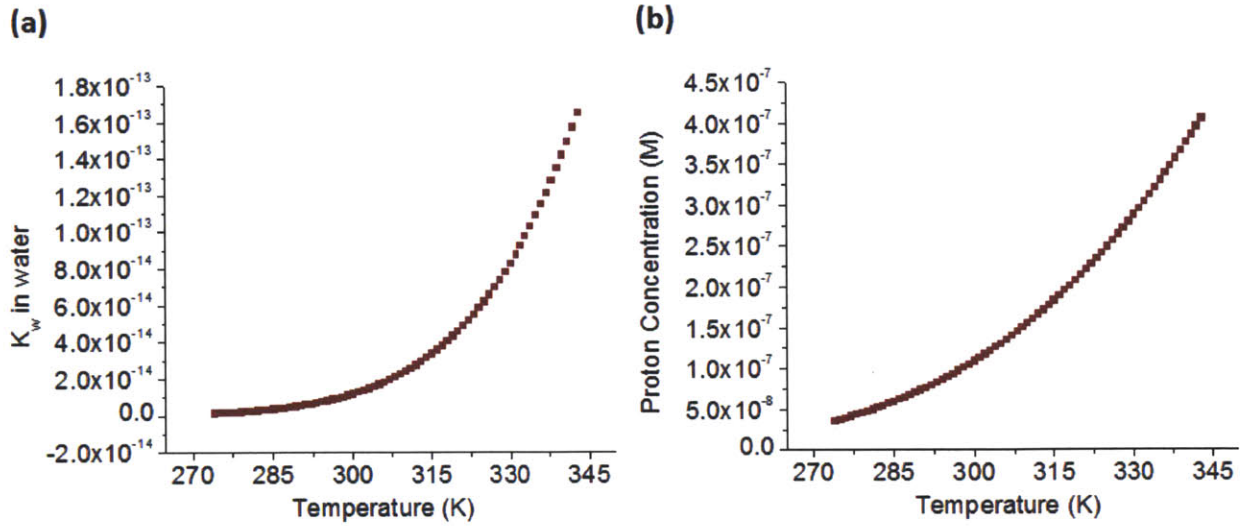

Figure 3.46. Temperature dependence of water dissociation constant and proton concentration

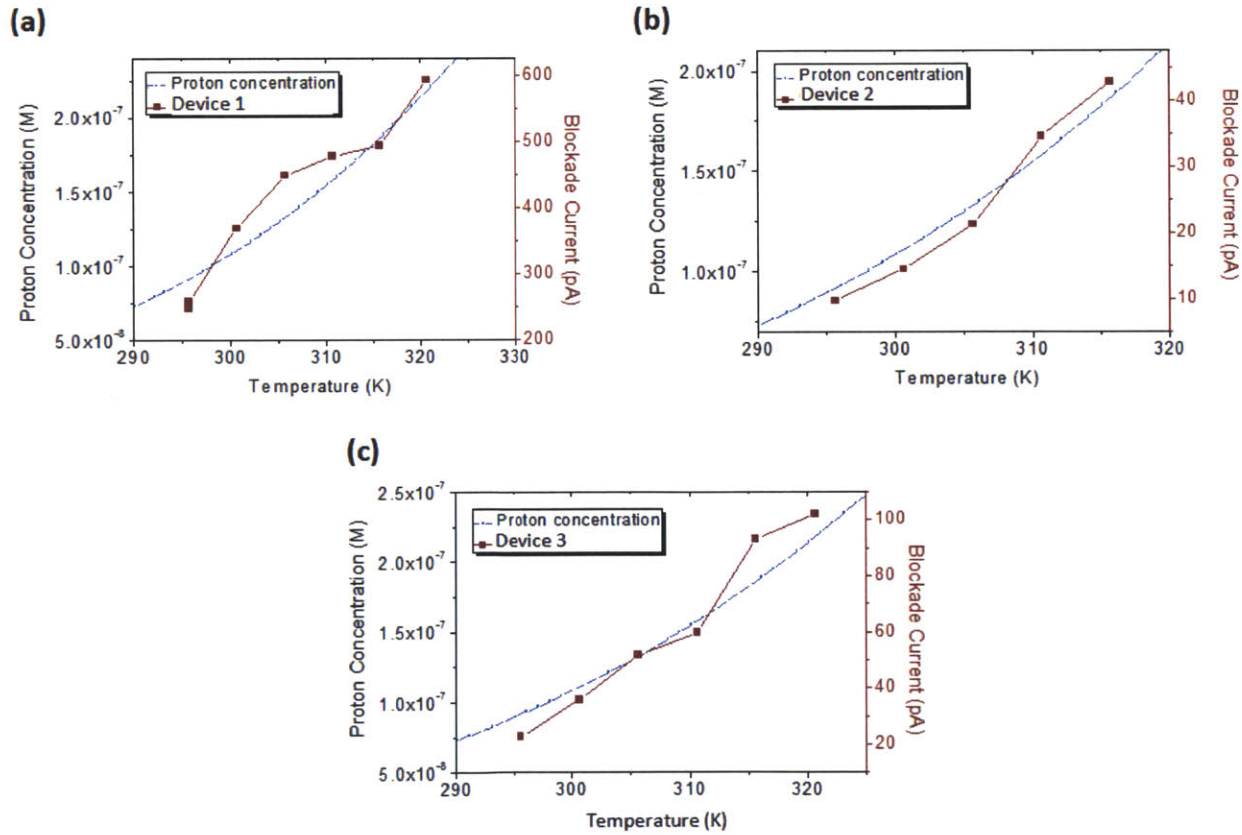

Figure 3.47. Comparison of the blockade current of experimental dataset from SWNTs and calculated proton concentration

3.6. Outlook and Future work

Many interesting directions for future theoretical and applied research exist. First, it should be noted that nanofluidic properties of SWNTs are subjects still under debate in both many theoretical and experimental works. For example, many other numbers have been reported for proton flux inside of SWNTs, experimentally, whereas the transfer mechanism of ions and potential distributions in SWNTs have not been confirmed yet, theoretically. In this work, we mainly explored the experimental verification of nanofluidic behavior of a SWNT with high aspect ratio in an applied electric field. The detail molecular dynamic simulations will give more solid foundation of the dynamics of ion transport in SWNTs. For example, the simulation dealing with SWNTs diameters, an applied electric field, ionic species, and different temperatures will add clear understanding about the behavior of SWNTs ion channels, and it will promote the appearance of the practical applications. Moreover, dynamics in SWNTs ion channels will be affected by the other conditions such as chemistry near the SWNTs, pore mouth conditions, doping effects and so on. Also, the study of proton re-equilibration near the pore mouth from the local pH measurements would elucidate the solid pictures of proton flux in SWNTs.

Another practical research will be the membrane of SWNTs with high aspect ratio. The large proton flux was confirmed in a SWNT. This result suggests that this membrane would be highly proton selective in comparison to relatively slow movement of other species. Also, as the ion Coulter counters, the correct estimation of the number of translocated ions can be expected in this membrane. Also, if the coherence resonance happens in multiple SWNTs and all ion transfers are synchronized, we can construct the molecular waves through the membrane at a

certain point. This molecular wave pulse can be used to design the nanoreactors with controlled numbers of single molecules.

Another interesting subject is the active control of molecule transport in SWNTs. Since cations or most ions are charged molecules in solutions, the externally applied electric field would affect changes of distinct movements of each molecule. It is known that the electromigration wind force exists on the atomic surface of CNTs. Wind force is the electromigration, the transport of material which is caused by the flow of the ions or electrons in a conductor due to the momentum transfer between conducting electrons and atoms. However, there is no proof that the electrical current by external source can control the transport of ions and molecules inside CNTs. The realization of the wind force would give the active control for an acceleration or a deceleration of ion translocation.

For further usability, other interesting molecules may be tested in SWNTs with a high aspect ratio. Current results were collected by a transport of an individual cation. But, this high aspect ratio nano channel may have different ability to detect molecules in comparison to many other nanopores with small aspect ratio, such as silicon nitride nanopores. There are a lot of questions about what kind of molecules can pass through. Also, the vital roles of charged groups near the pore mouth should be explored for the complete understanding. Based on those fundamental aspects, highly selective passage and rejection depending on types of molecules suggests other interesting features, such as desalination. For the further study of the potential usability, transport of nucleobase, biomolecules like protein, and charged amino acid would be quite interesting topics. Also, it has potential application to detect harzardous substances like Arsenic.

4. Conclusion

CNTs have been the most intriguing one-dimensional nanomaterials for a decade. A lot of resources have been invested to study properties and applications of CNTs. It has been proved that CNTs are attractive materials for many future applications of nanodevices. However , in spite of those efforts, there have been still not much uses of CNTs as practical applications due to the lack of the knowledge about the fundamental properties and usability. To overcome this barrier, CNTs have to be explored a lot for both its properties and insights of the practical applications. In this work, we have focused on many intriguing properties and new applications of CNTs that have not been explored up to date.

For the first part, we have developed the unique core-shell nanostructures of CNT/Fuel using the thermal and electrical properties among a lot of useful properties of CNTs. Due to the high thermal conductivity, CNTs are able to produce one-dimensional chain reaction of fuel along its aligned direction. At the same time, the moving thermal wave would induce the movement of electrical charge carriers, which generate the concomitant electrical energy like the pulse. The main contributions in this work are summarized in 1) designing the wet impregnation method for the development of CNT/fuel structures, 2) figuring out the one-dimensional chain reaction in core-shell nanostructures, and 3) realizing thermopower wave as the direct chemical to electrical energy conversion. The most electrical energy generation requires complicated energy conversion systems. The only well-known method is the thermoelectric, but it is limited due to the its low efficiency and large amount of the energy to maintain the temperature difference. Especially, for MEMS or NEMS systems, shrinkable and minuscule power source with high power density would be need for the integration in the extremely small devices. Also, even though some nanomaterials as the additives have been studied to accelerate the chemical

reaction, understanding one-dimensional chemical reaction for CNTs has not be done, and it is important to use CNTs for the practical chemical reactions. We first showed that nanowires with high thermal conductivity would supply the released heat energy on the unreacted regions of fuel which can promote the amplification of a chain reaction. These phenomena were demonstrated in experiment and theoretical study. In the experiments, one-dimensional chemical reaction was realized in core-shell CNT/Fuel layer along its aligned direction with the amplified reaction velocity. This reaction velocity is 1000 times faster than that of bulky fuel layers. Also, it was proven that CNTs would lower the minimum energy to initiate the chemical reaction of fuels. In the theoretical study, the fourier description coupled with energy generation of fuel confirmed that the core-shell nanowire/fuel structures would enhance the efficiency of a reaction depending on the thermal conductivity of nanowire and non-dimensionalized thermal properties of fuel, β. The most central result is the thermopower wave. The one-dimensional chain reaction along nanowire can induce the thermopower wave, which is the electrical energy pulse by the entrained charge carriers in the moving thermal waves. This concept was demonstrated in CNT/Fuel structures. The dynamics being related to the one-dimensional effect and orthogonal heat trasfer in thermopower wave were deeply explored, and the optimal structures were suggested for the maximum power generation. The specific powers were compared to the conventional thermoelectrics and other technologies. From this, we proved the hypothesis that the entrained charge carriers by moving thermal waves would amplify the energy generation. These results suggest that the thermopower wave and amplified 1D chain reaction would be good alternatives for either small scale power source with high power density in small volume and mass or the supportive power source using the wasting energy. Since this work is the first demonstration of thermopower wave without more engineering or further modification, it should be explored in

detail to find the optimal conditions of core materials, chemical fuels, efficient ignition and so on. For example, as the extension of thermopower wave concept, the exploration of other TE materials will be able to open the new area from the chemical to electrical energy conversion combined by the nanostructured materials and classical chemical fuels. CNT is useful to generate the amplified chemical reaction whereas it has relatively low Seebeck coefficient around 80 μV/K. However, many efficient thermoelectric materials like Bismuth telluride has high Seebeck coefficient at 300 μV/K, but low thermal conductivity. In this case, this amplified energy generation in the same temperature gradient may be commensurate with the slow chemical reaction and electrical polarity change during the reaction transfer, and it will add the more fundamental understanding for the interaction between nanowire/fuel structures. Also, the complex structures between CNT and TE materials would be the intriguing structures because their weakness of thermopower wave can be commensurate with their strengths (CNT : low Seebeck coefficient and high thermal diffusivity VS. TE material : high Seebeck coefficient and low thermal conductivity).

For the second part, we have explored SWNTs ion channels using the atomically smooth surface and an originally cylindrical shape with the high aspect ratio in the sub-nanometer range. By means of the confinement in a small diameter and a long travel distance along the length axis of CNTs, the applied electric field was able to drive the transport of individual ions through SWNTs. This movement induces the distinctive current traces depending on the many critical parameters. The main contributions in this work are summarized in 1) developing and modifying new platform for SWNTs ion channels, 2) exploring the dynamics of ion translocation in many different conditions (threshold potential, applied electric field, ionic species, coherence resonance, relation between frequency and dwell time) and 3) resolving the roles of SWNTs

diameter and temperature change for ion transport behavior through a SWNT. Many researchers have reported the results of ion channels with selectivity, nanopores for molecule detection, and transport using nanofluidic channel. These results are very important to make biomimetic ion channel, DNA sequencing, and future nanofluidic applications. However, ion channels were only realized in biological ion channel. Nanopores for molecule detection have been limited in short aspect ratio while the diameter is comparable to 3 to 10 nm. For the nanofluidic channel, the real diameter was in the range of 50 to 1000 nm due to the difficulty of fabrication. In order to overcome these limitations and constructing multifunctional nanofluidic channels, CNTs have been strong candidates. The thorough study for CNTs as nanochannels would form the basis of the practical nanofluidic devices with many intriguing properties such as fast mass trasnport, large proton flux and ionic selectivity. The most previous studies for CNTs were concentrating on the computational/theoretical works due to the difficulty of the fabrication of working SWNTs ion channels. We first developed the high aspect ratio SWNTs ion channels that can realize the transport of an individual single ion transport and detection. In this platform, the dynamics of ion transport through SWNTs ion channels were studied in many aspects. It was shown that the intrinsic current inside of SWNTs would be constructed by proton flux, while the large cations would be the repetitive blockers for the path of proton flux chains. Also, we demonstrated the existence of threshold potential that should be overcome to observe the first pore-blocking events. The increase of an applied electric fields induced the increase of blockade current and decrease of dwell time. It means that the blocker is the charged molecules. The different ionic species made their distinctive behavior of ion translocations. For more detail studies, the ion transports were explored as a function of diameters of SWNTs (1-2 nm) and temperature changes (25-50 °C). The SWNTs diameter dependences proved that the ion and

proton transfer would have the transition points near the 1.6 nm diameter at maximum due to the change of water molecule chain structures and confinements of ion movements. The increase of temperature amplified the number of available protons for the Grotthuss mechanism as the method for proton transfer. It turned out the increase of proton flux as well as the increase of the blockade current. From those detail experimental studies, we believe that all results would form the basis of understanding the nanofluidic properties of SWNTs and give the critical answers about the debate among many computational/theoretical works. The high aspect ratio SWNTs ion channels would have high potential for many intriguing nanofluidic devices, such as molecular counters for ions, high proton flux membranes, water desalination and nanoreactors for an single molecule.

5. Bibliography

1 Iijima, S. Helical Microtubules of Graphitic Carbon. *Nature* **354**, 56-58, (1991).

2 Iijima, S. & Ichihashi, T. Single-Shell Carbon Nanotubes of 1-Nm Diameter. *Nature* **363**, 603-605, (1993).

3 Dresselhaus, M. S. & Avouris, P. Introduction to carbon materials research. *Top Appl Phys* **80**, 1-9, (2001).

4 Olk, C. H. & Heremans, J. P. Scanning Tunneling Spectroscopy of Carbon Nanotubes. *J Mater Res* **9**, 259-262, (1994).

5 Dresselhaus, M. S., Dresselhaus, G. & Saito, R. Carbon-Fibers Based on C-60 and Their Symmetry. *Phys Rev B* **45**, 6234-6242, (1992).

6 Jones, D. E. H. Science of fullerenes and carbon nanotubes - Dresselhaus,MS, Dresselhaus,G, Eklund,PC. *Nature* **381**, 384-384, (1996).

7 Dresselhaus, M. S., Dresselhaus, G. & Saito, R. Physics of Carbon Nanotubes. *Carbon* **33**, 883-891, (1995).

8 Mohamed, A. R., Sivakumar, V. M., Abdullah, A. Z. & Chai, S. P. Role of Reaction and Factors of Carbon Nanotubes Growth in Chemical Vapour Decomposition Process Using Methane-A Highlight. *J Nanomater*, 395191, (2010).

9 Bystrzejewski, M. *et al.* Single-Walled Carbon Nanotubes Synthesis: A Direct Comparison of Laser Ablation and Carbon Arc Routes. *J Nanosci Nanotechno* **8**, 6178-6186, (2008).

10 Mitra, S. & Brukh, R. Mechanism of carbon nanotube growth by CVD. *Chem Phys Lett* **424**, 126-132, (2006).

11 Chang, C. W., Okawa, D., Majumdar, A. & Zettl, A. Solid-state thermal rectifier. *Science* **314**, 1121-1124, (2006).

12 Chang, C. W., Okawa, D., Garcia, H., Majumdar, A. & Zettl, A. Nanotube phonon waveguide. *Phys Rev Lett* **99**, 045901, (2007).

13 Ebbesen, T. W. *et al.* Electrical conductivity of individual carbon nanotubes. *Nature* **382**, 54-56, (1996).

14 Ando, Y., Zhao, X., Shimoyama, H., Sakai, G. & Kaneto, K. Physical properties of multiwalled carbon nanotubes. *Int J Inorg Mater* **1**, 77-82, (1999).

15 Yu, C. H., Shi, L., Yao, Z., Li, D. Y. & Majumdar, A. Thermal conductance and thermopower of an individual single-wall carbon nanotube. *Nano Lett* **5**, 1842-1846, (2005).

16 Adu, C. K. W., Sumanasekera, G. U., Pradhan, B. K., Romero, H. E. & Eklund, P. C. Carbon nanotubes: A thermoelectric nano-nose. *Chem Phys Lett* **337**, 31-35, (2001).

17 Sumanasekera, G. U., Pradhan, B. K., Romero, H. E., Adu, K. W. & Eklund, P. C. Giant thermopower effects from molecular physisorption on carbon nanotubes. *Phys Rev Lett* **89**, 166801, (2002).

18 Cahill, D. G. *et al.* Nanoscale thermal transport. *J Appl Phys* **93**, 793-818, (2003).

19 Fisher, T. S. & Walker, D. G. Thermal and electrical energy transport and conversion in nanoscale electron field emission processes. *J Heat Trans-T Asme* **124**, 954-962, (2002).

20 Holt, J. K. *et al.* Fast mass transport through sub-2-nanometer carbon nanotubes. *Science* **312**, 1034-1037, (2006).

21 Hone, J. Phonons and thermal properties of carbon nanotubes. *Top Appl Phys* **80**, 273-286, (2001).

22 Hone, J. *et al.* Thermal properties of carbon nanotubes and nanotube-based materials. *Appl Phys a-Mater* **74**, 339-343, (2002).
23 Benedict, L. X., Louie, S. G. & Cohen, M. L. Heat capacity of carbon nanotubes. *Solid State Commun* **100**, 177-180, (1996).
24 Hone, J., Whitney, M., Piskoti, C. & Zettl, A. Thermal conductivity of single-walled carbon nanotubes. *Phys Rev B* **59**, 2514-2516, (1999).
25 Cola, B. A., Xu, J. & Fisher, T. S. Contact mechanics and thermal conductance of carbon nanotube array interfaces. *Int J Heat Mass Tran* **52**, 3490-3503, (2009).
26 Zettl, A., Chang, C. W., Okawa, D. & Majumdar, A. Solid-state thermal rectifier. *Science* **314**, 1121-1124, (2006).
27 Yao, Z., Dekker, C. & Avouris, P. Electrical transport through single-wall carbon nanotubes. *Top Appl Phys* **80**, 147-171, (2001).
28 Burke, P. J., Li, S. D., Yu, Z., Yen, S. F. & Tang, W. C. Carbon nanotube transistor operation at 2.6 GHz. *Nano Lett* **4**, 753-756, (2004).
29 Dai, H. J. *et al.* Nanotube molecular wires as chemical sensors. *Science* **287**, 622-625, (2000).
30 Shi, L. *et al.* Measuring thermal and thermoelectric properties of one-dimensional nanostructures using a microfabricated device (vol 125, pg 881, 2003). *J Heat Trans-T Asme* **125**, 1209-1209, (2003).
31 Kunadian, I., Andrews, R., Menguc, M. P. & Qian, D. Thermoelectric power generation using doped MWCNTs. *Carbon* **47**, 589-601, (2009).
32 Kim, P., Shi, L., Majumdar, A. & McEuen, P. L. Thermal transport measurements of individual multiwalled nanotubes. *Physical Review Letters* **8721**, 215502, (2001).
33 Zhang, H. L. *et al.* Electrical and thermal properties of carbon nanotube bulk materials: Experimental studies for the 328-958 K temperature range. *Phys Rev B* **75**, 205407, (2007).
34 Riffat, S. B. & Ma, X. L. Thermoelectrics: a review of present and potential applications. *Appl Therm Eng* **23**, 913-935, (2003).
35 DiSalvo, F. J. Thermoelectric cooling and power generation. *Science* **285**, 703-706, (1999).
36 Chen, G., Dresselhaus, M. S., Dresselhaus, G., Fleurial, J. P. & Caillat, T. Recent developments in thermoelectric materials. *Int Mater Rev* **48**, 45-66, (2003).
37 Chen, G. Nanoscale heat transfer and nanostructured thermoelectrics. *Ieee T Compon Pack T* **29**, 238-246, (2006).
38 Dresselhaus, M. S. *et al.* Low-dimensional thermoelectric materials. *Phys Solid State+* **41**, 679-682, (1999).
39 Minnich, A. J., Dresselhaus, M. S., Ren, Z. F. & Chen, G. Bulk nanostructured thermoelectric materials: current research and future prospects. *Energ Environ Sci* **2**, 466-479, (2009).
40 Dresselhaus, M. S. *et al.* Quantum wells and quantum wires for potential thermoelectric applications. *Semiconduct Semimet* **71**, 1-121, (2001).
41 Dresselhaus, M. S. *et al.* New directions for low-dimensional thermoelectric materials. *Adv Mater* **19**, 1043-1053, (2007).
42 Sun, X., Zhang, Z. & Dresselhaus, M. S. Theoretical modeling of thermoelectricity in Bi nanowires. *Appl Phys Lett* **74**, 4005-4007, (1999).

43 Boukai, A., Xu, K. & Heath, J. R. Size-dependent transport and thermoelectric properties of individual polycrystalline bismuth nanowires. *Adv Mater* **18**, 864-869, (2006).
44 Li, L. *et al.* Fabrication and electronic transport properties of Bi nanotube arrays. *Appl Phys Lett* **88**, 103119, (2006).
45 Poudel, B. *et al.* High-thermoelectric performance of nanostructured bismuth antimony telluride bulk alloys. *Science* **320**, 634-638, (2008).
46 Takashiri, M., Takiishi, M., Tanaka, S., Miyazaki, K. & Tsukamoto, H. Thermoelectric properties of n-type nanocrystalline bismuth-telluride-based thin films deposited by flash evaporation. *J Appl Phys* **101**, 074301, (2007).
47 Yoo, B. Y. *et al.* Electrochemically deposited thermoelectric n-type Bi2Te3 thin films. *Electrochim Acta* **50**, 4371-4377, (2005).
48 Zhao, X. B. *et al.* Bismuth telluride nanotubes and the effects on the thermoelectric properties of nanotube-containing nanocomposites. *Appl Phys Lett* **86**, 062111, (2005).
49 Zhou, J. H., Jin, C. G., Seol, J. H., Li, X. G. & Shi, L. Thermoelectric properties of individual electrodeposited bismuth telluride nanowires. *Appl Phys Lett* **87**, 133109, (2005).
50 Heremans, J. P., Thrush, C. M., Morelli, D. T. & Wu, M. C. Thermoelectric power of bismuth nanocomposites. *Phys Rev Lett* **88**, 133109, (2002).
51 Martin-Gonzalez, M., Prieto, A. L., Gronsky, R., Sands, T. & Stacy, A. M. High-density 40 nm diameter Sb-rich Bi2-xSbxTe3 nanowire arrays. *Adv Mater* **15**, 1003-1006, (2003).
52 Lin, Y. M., Rabin, O., Cronin, S. B., Ying, J. Y. & Dresselhaus, M. S. Semimetal-semiconductor transition in Bi1-xSbx alloy nanowires and their thermoelectric properties. *Appl Phys Lett* **81**, 2403-2405, (2002).
53 Cui, H. M. *et al.* Synthesis of Bi2Se3 thermoelectric nanosheets and nanotubes through hydrothermal co-reduction method. *J Solid State Chem* **177**, 4001-4006, (2004).
54 Hochbaum, A. I. *et al.* Enhanced thermoelectric performance of rough silicon nanowires. *Nature* **451**, 163-165, (2008).
55 Boukai, A. I. *et al.* Silicon nanowires as efficient thermoelectric materials. *Nature* **451**, 168-171, (2008).
56 Ramayya, E. B. & Knezevic, I. Ultrascaled Silicon Nanowires as Efficient Thermoelectric Materials. *Iwce-13: 2009 13th International Workshop on Computational Electronics*, 129-132, 330, (2009).
57 Dames, C. & Chen, G. Theoretical phonon thermal conductivity of Si/Ge superlattice nanowires. *J Appl Phys* **95**, 682-693, (2004).
58 Chen, X., Wang, Y. C. & Ma, Y. M. High Thermoelectric Performance of Ge/Si Core-Shell Nanowires: First-Principles Prediction. *J Phys Chem C* **114**, 9096-9100, (2010).
59 Lee, C. H., Yi, G. C., Zuev, Y. M. & Kim, P. Thermoelectric power measurements of wide band gap semiconducting nanowires. *Appl Phys Lett* **94**, 022106, (2009).
60 Tai, G., Zhou, B. & Guo, W. L. Structural characterization and thermoelectric transport properties of uniform single-crystalline lead telluride nanowires. *J Phys Chem C* **112**, 11314-11318, (2008).
61 Liang, W. J. *et al.* Field-Effect Modulation of Seebeck Coefficient in Single PbSe Nanowires. *Nano Lett* **9**, 1689-1693, (2009).
62 Uryupin, O. N. *et al.* Thermoelectric Properties of InSb Nanowires Over a Wide Temperature Range. *J Electron Mater* **38**, 990-993, (2009).

63 Mingo, N. Thermoelectric figure of merit and maximum power factor in III-V semiconductor nanowires. *Appl Phys Lett* **84**, 2652-2654, (2004).
64 Abramson, A. R. *et al.* Fabrication and characterization of a nanowire/polymer-based nanocomposite for a prototype thermoelectric device. *J Microelectromech S* **13**, 505-513, (2004).
65 Lim, J. R. *et al.* Fabrication method for thermoelectric nanodevices. *Adv Mater* **17**, 1488-1492, (2005).
66 Wang, W., Jia, F. L., Huang, Q. H. & Zhang, J. Z. A new type of low power thermoelectric micro-generator fabricated by nanowire array thermoelectric material. *Microelectron Eng* **77**, 223-229, (2005).
67 Wakim, S., Aïch, B.-R., Tao, Y. & Leclerc, M. Charge Transport, Photovoltaic, and Thermoelectric Properties of Poly(2,7-Carbazole) and Poly(Indolo[3,2-b]Carbazole) Derivatives. *Polymer Reviews* **48**, 432-462, (2008).
68 Hone, J. *et al.* Thermoelectric power of single-walled carbon nanotubes. *Phys Rev Lett* **80**, 1042-1045, (1998).
69 Choi, Y. M. *et al.* Nonlinear behavior in the thermopower of doped carbon nanotubes due to strong, localized states. *Nano Lett* **3**, 839-842, (2003).
70 Vavro, J. *et al.* Thermoelectric power of p-doped single-wall carbon nanotubes and the role of phonon drag. *Phys Rev Lett* **90**, 065503, (2003).
71 Sadanadan, B. *et al.* Synthesis and thermoelectric power of nitrogen-doped carbon nanotubes. *J Nanosci Nanotechno* **3**, 99-103, (2003).
72 Venkatasubramanian, R., Siivola, E., Colpitts, T. & O'Quinn, B. Thin-film thermoelectric devices with high room-temperature figures of merit. *Nature* **413**, 597-602, (2001).
73 Meng, C. Z., Liu, C. H. & Fan, S. S. A Promising Approach to Enhanced Thermoelectric Properties Using Carbon Nanotube Networks. *Adv Mater* **22**, 535-539, (2010).
74 Van, T. D. *et al.* Integration of SWNT film into MEMS for a micro-thermoelectric device. *Smart Mater Struct* **19**, 075003, (2010).
75 Please, C. P., Liu, F. & McElwain, D. L. S. Condensed phase combustion travelling waves with sequential exothermic or endothermic reactions. *Combust. Theor. Model.* **7**, 129-143, (2003).
76 Zel'dovich, Y. B. & Frank-Kamenetskii, D. A. The theory of thermal flame propagation. *Zh. Fiz. Khim.* **12**, 100-105, (1938).
77 Roy, G. D., Frolov, S. M., Borisov, A. A. & Netzer, D. W. Pulse detonation propulsion: challenges, current status, and future perspective. *Prog. Energ. Combust.* **30**, 545-672, (2004).
78 Arimondi, M., Anselmi-Tamburini, U., Gobetti, A., Munir, Z. A. & Spinolo, G. Chemical mechanism of the Zr+O-2->ZrO2 combustion synthesis reaction. *J. Phys. Chem. B* **101**, 8059-8068, (1997).
79 Alexander, M. H. *et al.* Nitramine Propellant Ignition and Combustion Research. *Prog. Energ. Combust.* **17**, 263-296, (1991).
80 Yu, C. H., Shi, L., Yao, Z., Li, D. Y. & Majumdar, A. Thermal conductance and thermopower of an individual single-wall carbon nanotube. *Nano Lett.* **5**, 1842-1846, (2005).
81 Chang, C. W., Okawa, D., Garcia, H., Majumdar, A. & Zettl, A. Nanotube phonon waveguide. *Phys. Rev. Lett.* **99**, 045901-045904, (2007).

82 Akkutlu, I. Y. & Yortsos, Y. C. The dynamics of in-situ combustion fronts in porous media. *Combust. Flame* **134**, 229-247, (2003).
83 Choi, W. *et al.* Chemically driven carbon-nanotube-guided thermopower waves. *Nat Mater* **9**, 423-429, (2010).
84 Hata, K. *et al.* Water-assisted highly efficient synthesis of impurity-free single-waited carbon nanotubes. *Science* **306**, 1362-1364, (2004).
85 Xu, Y. Q., Flor, E., Schmidt, H., Smalley, R. E. & Hauge, R. H. Effects of atomic hydrogen and active carbon species in 1 mm vertically aligned single-walled carbon nanotube growth. *Applied Physics Letters* **89**, 123116, (2006).
86 Han, J. H. *et al.* A mechanochemical model of growth termination in vertical carbon nanotube forests. *Acs Nano* **2**, 53-60, (2008).
87 Liu, K. *et al.* Controlled termination of the growth of vertically aligned carbon nanotube arrays. *Advanced Materials* **19**, 975-978, (2007).
88 Futaba, D. N. *et al.* 84% Catalyst activity of water-assisted growth of single walled carbon nanotube forest characterization by a statistical and macroscopic approach. *Journal of Physical Chemistry B* **110**, 8035-8038, (2006).
89 Futaba, D. N. *et al.* Shape-engineerable and highly densely packed single-walled carbon nanotubes and their application as super-capacitor electrodes. *Nature Materials* **5**, 987-994, (2006).
90 Potvin, H. & Back, M. H. Study of Decomposition of Sodium Azide Using Differential Thermal-Analysis. *Canadian Journal of Chemistry-Revue Canadienne De Chimie* **51**, 183-186, (1973).
91 Williams, M. R. & Matei, M. V. The decomposition of some RDX and HMX based materials in the one-dimensional time to explosion apparatus. Part 1. Time to explosion and apparent activation energy. *Propellants Explosives Pyrotechnics* **31**, 435-441, (2006).
92 Prevo, B. G. & Velev, O. D. Controlled, rapid deposition of structured coatings from micro- and nanoparticle suspensions. *Langmuir* **20**, 2099-2107, (2004).
93 Kulkarni, A. M. & Zukoski, C. F. Nanoparticle crystal nucleation: Influence of solution conditions. *Langmuir* **18**, 3090-3099, (2002).
94 Simchi, A., Ahmadi, R., Reihani, S. M. S. & Mahdavi, A. Kinetics and mechanisms of nanoparticle formation and growth in vapor phase condensation process. *Mater. Design* **28**, 850-856, (2007).
95 Yusa, H. & Watanuki, T. X-ray diffraction of multiwalled carbon nanotube under high pressure: Structural durability on static compression. *Carbon* **43**, 519-523, (2005).
96 Maniwa, Y. *et al.* Anomaly of X-ray diffraction profile in single-walled carbon nanotubes. *Jpn. J. Appl. Phys., Part 2* **38**, 668-670, (1999).
97 Cao, A. Y., Xu, C. L., Liang, J., Wu, D. H. & Wei, B. Q. X-ray diffraction characterization on the alignment degree of carbon nanotubes. *Chem. Phys. Lett.* **344**, 13-17, (2001).
98 Ajayan, P. M. *et al.* Nanotubes in a flash - Ignition and reconstruction. *Science* **296**, 705-705, (2002).
99 Manaa, M. R., Mitchell, A. R., Garza, R. G., Pagoria, P. F. & Watkins, B. E. Flash ignition and initiation of explosives-nanotubes mixture. *J Am Chem Soc* **127**, 13786-13787, (2005).
100 Volkov, E. N., Paletsky, A. A. & Korobeinichev, O. P. RDX flame structure at atmospheric pressure. *Combust. Explo. Shock.* **44**, 43-54, (2008).

101 Aleksandrov, V. V., Tukhtaev, R. K., Boldyrev, V. V. & Boldyreva, A. V. Mechanism of Catalytic Additive Effects on Diethylnitramine Dinitrate Combustion Rates. *Combust. Flame* **35**, 1-15, (1979).
102 Homan, B. E., Miller, M. S. & Vanderhoff, J. A. Absorption diagnostics and modeling investigations of RDX flame structure. *Combust. Flame* **120**, 301-317, (2000).
103 Zenin, A. Hmx and Rdx - Combustion Mechanism and Influence on Modern Double-Base Propellant Combustion. *J. Propul. Power* **11**, 752-758, (1995).
104 Miyamoto, Y., Berber, S., Yoon, M., Rubio, A. & Tomanek, D. Onset of nanotube decay under extreme thermal and electronic excitations. *Physica B* **323**, 78-85, (2002).
105 Begtrup, G. E. *et al.* Probing nanoscale solids at thermal extremes. *Physical Review Letters* **99**, 155901-155904, (2007).
106 Ivanov, I. *et al.* Fast and highly anisotropic thermal transport through vertically aligned carbon nanotube arrays. *Appl Phys Lett* **89**, 223110, (2006).
107 Weber, R. O., Mercer, G. N., Sidhu, H. S. & Gray, B. F. Combustion waves for gases (Le=1) and solids (L->infinity). *Proceedings of the Royal Society of London Series a-Mathematical Physical and Engineering Sciences* **453**, 1105-1118, (1997).
108 Parr, T. & Hanson-Parr, D. RDX ignition flame structure. *Twenty-Seventh Symposium (International) on Combustion, Vols 1 and 2*, 2301-2308, 3274, (1998).
109 Li, S. C., Williams, F. A. & Margolis, S. B. Effects of 2-Phase Flow in a Model for Nitramine Deflagration. *Combustion and Flame* **80**, 329-349, (1990).
110 Oyumi, Y. Melt phase decomposition of RDX and two nitrosamine derivatives. *Propell. Explos. Pyrot.* **13**, 42-47, (1988).
111 Liau, Y. C., Kim, E. S. & Yang, V. A comprehensive analysis of laser-induced ignition of RDX monopropellant. *Combust. Flame* **126**, 1680-1698, (2001).
112 Richard E. Sonntag, G. J. V. w. *Introduction to thermodynamics: classical and statistical.* 3rd ed edn, (John Wiley & Sons, 1991).
113 Begtrup, G. E. *et al.* Probing nanoscale solids at thermal extremes. *Physical Review Letters* **99**, 155901, (2007).
114 Gong, Q. M., Li, Z., Li, D., Bai, X. D. & Liang, J. Fabrication and structure: a study of aligned carbon nanotube/carbon nanocomposites. *Solid State Commun* **131**, 399-404, (2004).
115 Li, C. Y. & Chou, T. W. Quantized molecular structural mechanics modeling for studying the specific heat of single-walled carbon nanotubes. *Physical Review B* **71**, 075409, (2005).
116 Mingo, N. & Broido, D. A. Carbon nanotube ballistic thermal conductance and its limits. *Physical Review Letters* **95**, 096105, (2005).
117 Hanson-Parr, D. M. & Parr, T. P. Thermal properties measurements of solid rocket propellant oxidizers and binder materials as a function of temperature. *J. Energetic Mat.* **17**, 1-47, (1999).
118 Li, S. C., Williams, F. A. & Margolis, S. B. Effects of 2-phase flow in a model for nitramine deflagration. *Combust. Flame* **80**, 329-349, (1990).
119 Long, G. T., Vyazovkin, S., Brems, B. A. & Wight, C. A. Competitive vaporization and decomposition of liquid RDX. *Journal of Physical Chemistry B* **104**, 2570-2574, (2000).
120 Abrahamson, J. T., Nair, N. & Strano, M. S. Modelling the increase in anisotropic reaction rates in metal nanoparticle oxidation using carbon nanotubes as thermal conduits. *Nanotechnology* **19**, 195701, (2008).

121 Liau, Y. C., Kim, E. S. & Yang, V. A comprehensive analysis of laser-induced ignition of RDX monopropellant. *Combust Flame* **126**, 1680-1698, (2001).
122 Volkov, E. N., Paletsky, A. A. & Korobeinichev, O. P. RDX flame structure at atmospheric pressure. *Combust Explo Shock+* **44**, 43-54, (2008).
123 Kim, P., Shi, L., Majumdar, A. & McEuen, P. L. Thermal transport measurements of individual multiwalled nanotubes. *Phys. Rev. Lett.* **8721**, 215502-215505, (2001).
124 Takashiri, M., Takiishi, M., Tanaka, S., Miyazaki, K. & Tsukamoto, H. Thermoelectric properties of n-type nanocrystalline bismuth-telluride-based thin films deposited by flash evaporation. *J. Appl. Phys.* **101**, 074301-074305, (2007).
125 Venkatasubramanian, R., Siivola, E., Colpitts, T. & O'Quinn, B. Thin-film thermoelectric devices with high room-temperature figures of merit. **413**, 597-602, (2001).
126 Zhang, H. L. *et al.* Electrical and thermal properties of carbon nanotube bulk materials: Experimental studies for the 328-958 K temperature range. *Phys. Rev. B* **75**, 205407-205415, (2007).
127 Please, C. P., Liu, F. & McElwain, D. L. S. Condensed phase combustion travelling waves with sequential exothermic or endothermic reactions. *Combustion Theory and Modelling* **7**, 129-143, (2003).
128 Ghosh, S., Sood, A. K. & Kumar, N. Carbon nanotube flow sensors. *Science* **299**, 1042-1044, (2003).
129 Pop, E. *et al.* Negative differential conductance and hot phonons in suspended nanotube molecular wires. *Physical Review Letters* **95**, 155501, (2005).
130 Zhang, K. L., Chou, S. K., Ang, S. S. & Tang, X. S. A MEMS-based solid propellant microthruster with Au/Ti igniter. *Sensors and Actuators A-Physical* **122**, 113-123, (2005).
131 Phipps, C., Luke, J., Lippert, T., Hauer, M. & Wokaun, A. Micropropulsion using a laser ablation jet. *J. Propul. Power* **20**, 1000-1011, (2004).
132 Patel, K. D. *et al.* Electrokinetic pumping of liquid propellants for small satellite microthruster applications. *Sens. Actuators, B* **132**, 461-470, (2008).
133 Kuan, C. K., Chen, G. B. & Chao, Y. C. Development and ground tests of a 100-millinewton hydrogen peroxide monopropellant microthruster. *J. Propul. Power* **23**, 1313-1320, (2007).
134 Kemp, M. A. & Kovaleski, S. D. Ferroelectric plasma thruster for microspacecraft propulsion. *J. Appl. Phys.* **100**, 113306-113311, (2006).
135 Chaalane, A., Rossi, C. & Esteve, D. The formulation and testing of new solid propellant mixture (DB plus x%BP) for a new MEMS-based microthruster. *Sens. Actuators, A* **138**, 161-166, (2007).
136 Patel, K. D. *et al.* Electrokinetic pumping of liquid propellants for small satellite microthruster applications. *Sensors and Actuators B-Chemical* **132**, 461-470, (2008).
137 Kang, B. & Ceder, G. Battery materials for ultrafast charging and discharging. *Nature* **458**, 190-193, (2009).
138 Kuriyama, N. *et al.* Hydrogen storage alloys for nickel/metal-hydride battery. *Vacuum* **47**, 889-892, (1996).
139 Moghaddam, S., Pengwang, E., Masel, R. I. & Shannon, M. A. A self-regulating hydrogen generator for micro fuel cells. *J Power Sources* **185**, 445-450, (2008).
140 Zhu, L. *et al.* Integrated micro-power source based on a micro-silicon fuel cell and a micro electromechanical system hydrogen generator. *J Power Sources* **185**, 1305-1310, (2008).

141 Hulicova-Jurcakova, D. *et al.* Nitrogen-Enriched Nonporous Carbon Electrodes with Extraordinary Supercapacitance. *Adv Funct Mater* **19**, 1800-1809, (2009).
142 Jeon, Y. B., Sood, R., Jeong, J. H. & Kim, S. G. MEMS power generator with transverse mode thin film PZT. *Sensor Actuat a-Phys* **122**, 16-22, (2005).
143 Sailor, M. J. & Link, J. R. "Smart dust": nanostructured devices in a grain of sand. *Chem Commun*, 1375-1383, (2005).
144 Watkins, C., Shen, B. & Venkatasubramanian, R. Low-grade-heat energy harvesting using superlattice thermoelectrics for applications in implantable medical devices and sensors. *ICT: 2005 24th International Conference on Thermoelectrics*, 250-252, 533, (2005).
145 Albano, F. *et al.* A fully integrated microbattery for an implantable microelectromechanical system. *J Power Sources* **185**, 1524-1532, (2008).
146 Dudney, N. J. Solid-state thin-film rechargeable batteries. *Mat Sci Eng B-Solid* **116**, 245-249, (2005).
147 Kowalczyk, S. W., Grosberg, A. Y., Rabin, Y. & Dekker, C. Modeling the conductance and DNA blockade of solid-state nanopores. *Nanotechnology* **22**, 315101, (2011).
148 Kasianowicz, J. J., Robertson, J. W. F., Chan, E. R., Reiner, J. E. & Stanford, V. M. Nanoscopic Porous Sensors. *Annu Rev Anal Chem* **1**, 737-766, (2008).
149 Pan, X. *et al.* Enhanced ethanol production inside carbon-nanotube reactors containing catalytic particles. *Nat Mater* **6**, 507-511, (2007).
150 Svensson, K., Olin, H. & Olsson, E. Nanopipettes for Metal Transport. *Physical Review Letters* **93**, 145901, (2004).
151 Majumder, M., Chopra, N. & Hinds, B. J. Mass Transport through Carbon Nanotube Membranes in Three Different Regimes: Ionic Diffusion and Gas and Liquid Flow. *Acs Nano* **5**, 3867-3877, (2011).
152 Bakajin, O. *et al.* Fast mass transport through sub-2-nanometer carbon nanotubes. *Science* **312**, 1034-1037, (2006).
153 Kowalczyk, S. W., Hall, A. R. & Dekker, C. Detection of Local Protein Structures along DNA Using Solid-State Nanopores. *Nano Lett* **10**, 324-328, (2010).
154 MacKinnon, R. Potassium channels and the atomic basis of selective ion conduction (Nobel lecture). *Angewandte Chemie-International Edition* **43**, 4265-4277, (2004).
155 Heng, J. B. *et al.* Stretching DNA using the electric field in a synthetic nanopore. *Nano Letters* **5**, 1883-1888, (2005).
156 Heng, J. B. *et al.* Sizing DNA using a nanometer-diameter pore. *Biophys J* **87**, 2905-2911, (2004).
157 Fornasiero, F. *et al.* Ion exclusion by sub-2-nm carbon nanotube pores. *P Natl Acad Sci USA* **105**, 17250-17255, (2008).
158 Kasianowicz, J. J., Brandin, E., Branton, D. & Deamer, D. W. Characterization of individual polynucleotide molecules using a membrane channel. *P Natl Acad Sci USA* **93**, 13770-13773, (1996).
159 Deamer, D. W. & Akeson, M. Nanopores and nucleic acids: prospects for ultrarapid sequencing. *Trends Biotechnol* **18**, 147-151, (2000).
160 Dekker, C. Solid-state nanopores. *Nat Nanotechnol* **2**, 209-215, (2007).
161 Li, J. *et al.* Ion-beam sculpting at nanometre length scales. *Nature* **412**, 166-169, (2001).
162 Meller, A., Nivon, L. & Branton, D. Voltage-driven DNA translocations through a nanopore. *Phys Rev Lett* **86**, 3435-3438, (2001).

163 Hall, A. R., Keegstra, J. M., Duch, M. C., Hersam, M. C. & Dekker, C. Translocation of Single-Wall Carbon Nanotubes Through Solid-State Nanopores. *Nano Lett* **11**, 2446-2450, (2011).
164 White, H. S., Lan, W. J., Holden, D. A. & Zhang, B. Nanoparticle Transport in Conical-Shaped Nanopores. *Anal Chem* **83**, 3840-3847, (2011).
165 Golovchenko, J. A. *et al.* Graphene as a subnanometre trans-electrode membrane. *Nature* **467**, 190-193, (2010).
166 Drndic, M. *et al.* DNA Translocation through Graphene Nanopores. *Nano Lett* **10**, 2915-2921, (2010).
167 Dekker, C. *et al.* DNA Translocation through Graphene Nanopores. *Nano Lett* **10**, 3163-3167, (2010).
168 Branton, D. *et al.* The potential and challenges of nanopore sequencing. *Nat Biotechnol* **26**, 1146-1153, (2008).
169 DeCoursey, T. E. Voltage-gated proton channels and other proton transfer pathways (vol 83, pg 475, 2003). *Physiological Reviews* **83**, 1067-1067, (2003).
170 Armstrong, C. M. & Hille, B. Voltage-gated ion channels and electrical excitability. *Neuron* **20**, 371-380, (1998).
171 Kowalczyk, S. W., Tuijtel, M. W., Donkers, S. P. & Dekker, C. Unraveling Single-Stranded DNA in a Solid-State Nanopore. *Nano Lett* **10**, 1414-1420, (2010).
172 Liu, H. T. *et al.* Translocation of Single-Stranded DNA Through Single-Walled Carbon Nanotubes. *Science* **327**, 64-67, (2010).
173 Ito, T., Sun, L., Bevan, M. A. & Crooks, R. M. Comparison of nanoparticle size and electrophoretic mobility measurements using a carbon-nanotube-based coulter counter, dynamic light scattering, transmission electron microscopy, and phase analysis light scattering. *Langmuir* **20**, 6940-6945, (2004).
174 Gong, X. J., Li, J. C., Xu, K., Wang, J. F. & Yang, H. A Controllable Molecular Sieve for Na+ and K+ Ions. *Journal of the American Chemical Society* **132**, 1873-1877, (2010).
175 Shao, Q. *et al.* Anomalous Hydration Shell Order of Na+ and K+ inside Carbon Nanotubes. *Nano Letters* **9**, 989-994, (2009).
176 Hummer, G., Rasaiah, J. C. & Noworyta, J. P. Water conduction through the hydrophobic channel of a carbon nanotube. *Nature* **414**, 188-190, (2001).
177 Hummer, G., Kalra, A. & Garde, S. Osmotic water transport through carbon nanotube membranes. *P Natl Acad Sci USA* **100**, 10175-10180, (2003).
178 Aluru, N. R. & Qiao, R. Atypical dependence of electroosmotic transport on surface charge in a single-wall carbon nanotube. *Nano Lett* **3**, 1013-1017, (2003).
179 Hummer, G. & Peter, C. Ion transport through membrane-spanning nanopores studied by molecular dynamics simulations and continuum electrostatics calculations. *Biophys J* **89**, 2222-2234, (2005).
180 Noy, A. *et al.* Nanofluidics in carbon nanotubes. *Nano Today* **2**, 22-29, (2007).
181 Aluru, N. R., Park, J. H. & Sinnott, S. B. Ion separation using a Y-junction carbon nanotube. *Nanotechnology* **17**, 895-900, (2006).
182 Goddard, W. A., Pascal, T. A. & Jung, Y. Entropy and the driving force for the filling of carbon nanotubes with water. *P Natl Acad Sci USA* **108**, 11794-11798, (2011).
183 Koga, K., Takaiwa, D., Hatano, I. & Tanaka, H. Phase diagram of water in carbon nanotubes. *P Natl Acad Sci USA* **105**, 39-43, (2008).

184 Terzyk, A. P. *et al.* Molecular dynamics of zigzag single walled carbon nanotube immersion in water. *Phys Chem Chem Phys* **13**, 5621-5629, (2011).
185 Wenseleers, W., Cambre, S., Culin, J., Bouwen, A. & Goovaerts, E. Effect of water filling on the electronic and vibrational resonances of carbon nanotubes: Characterizing tube opening by Raman spectroscopy. *Adv Mater* **19**, 2274-2278, (2007).
186 Gogotsi, Y. *et al.* Environmental scanning electron microscopy study of water in carbon nanopipes. *Nano Lett* **4**, 989-993, (2004).
187 Majumder, M., Chopra, N., Andrews, R. & Hinds, B. J. Nanoscale hydrodynamics - Enhanced flow in carbon nanotubes. *Nature* **438**, 44-44, (2005).
188 Bakajin, O. *et al.* Ion exclusion by sub-2-nm carbon nanotube pores. *P Natl Acad Sci USA* **105**, 17250-17255, (2008).
189 Liu, Z. F., Qin, X. C., Yuan, Q. Z., Zhao, Y. P. & Xie, S. B. Measurement of the Rate of Water Translocation through Carbon Nanotubes. *Nano Lett* **11**, 2173-2177, (2011).
190 Chang Young Lee, J.-H. H., Wonjoon Choi, and Michael S. Strano Coherence resonance in a single walled carbon nanotube ion channel. *Science*, **329**, 1320-1324, (2010).
191 Agmon, N. The Grotthuss Mechanism. *Chemical Physics Letters* **244**, 456-462, (1995).
192 Lee, C. Y., Choi, W., Han, J. H. & Strano, M. S. Coherence Resonance in a Single-Walled Carbon Nanotube Ion Channel. *Science* **329**, 1320-1324, (2010).
193 Huang, S. M., Cai, X. Y. & Liu, J. Growth of millimeter-long and horizontally aligned single-walled carbon nanotubes on flat substrates. *Journal of the American Chemical Society* **125**, 5636-5637, (2003).
194 Lin, C. H., Lee, G. B., Chang, B. W. & Chang, G. L. A new fabrication process for ultra-thick microfluidic microstructures utilizing SU-8 photoresist. *J Micromech Microeng* **12**, 590-597, (2002).
195 Zhe, J., Jagtiani, A., Dutta, P., Hu, J. & Carletta, J. A micromachined high throughput Coulter counter for bioparticle detection and counting. *Journal of Micromechanics and Microengineering* **17**, 304-313, (2007).
196 Ho, C. *et al.* Electrolytic transport through a synthetic nanometer-diameter pore. *Proceedings of the National Academy of Sciences of the United States of America* **102**, 10445-10450, (2005).
197 He, Y. *et al.* Tuning Transport Properties of Nanofluidic Devices with Local Charge Inversion. *Journal of the American Chemical Society* **131**, 5194-5202, (2009).
198 Vermesh, U. *et al.* Fast Nonlinear Ion Transport via Field-induced Hydrodynamic Slip in Sub-20-nm Hydrophilic Nanofluidic Transistors. *Nano Letters* **9**, 1315-1319, (2009).
199 Beckstein, O., Tai, K. & Sansom, M. S. P. Not ions alone: Barriers to ion permeation in nanopores and channels. *Journal of the American Chemical Society* **126**, 14694-14695, (2004).
200 Song, C. & Corry, B. Intrinsic Ion Selectivity of Narrow Hydrophobic Pores. *Journal of Physical Chemistry B* **113**, 7642-7649, (2009).
201 Liu, H. M., Murad, S. & Jameson, C. J. Ion permeation dynamics in carbon nanotubes. *Journal of Chemical Physics* **125**, 084713, (2006).
202 Corry, B. Designing carbon nanotube membranes for efficient water desalination. *Journal of Physical Chemistry B* **112**, 1427-1434, (2008).
203 Ito, T., Sun, L. & Crooks, R. M. Simultaneous determination of the size and surface charge of individual nanoparticles using a carbon nanotube-based coulter counter. *Anal Chem* **75**, 2399-2406, (2003).

204 Skinner, G. M., van den Hout, M., Broekmans, O., Dekker, C. & Dekker, N. H. Distinguishing Single- and Double-Stranded Nucleic Acid Molecules Using Solid-State Nanopores. *Nano Lett* **9**, 2953-2960, (2009).
205 Zhang, B., Wood, M. & Lee, H. A Silica Nanochannel and Its Applications in Sensing and Molecular Transport (vol 81, pg 5541, 2009). *Anal Chem* **82**, 3404-3404, (2010).
206 Yameen, B. *et al.* Single Conical Nanopores Displaying pH-Tunable Rectifying Characteristics. Manipulating Ionic Transport With Zwitterionic Polymer Brushes. *J Am Chem Soc* **131**, 2070-2071, (2009).
207 Wang, L. *et al.* Nanofluidic Diode Generated by pH Gradient inside Track-etched Conical Nanopore. *Inec: 2010 3rd International Nanoelectronics Conference, Vols 1 and 2*, 568-569, 1483, (2010).
208 Kalman, E. B., Sudre, O., Vlassiouk, I. & Siwy, Z. S. Control of ionic transport through gated single conical nanopores. *Anal Bioanal Chem* **394**, 413-419, (2009).
209 Cervera, J., Schiedt, B., Neumann, R., Mafe, S. & Ramirez, P. Ionic conduction, rectification, and selectivity in single conical nanopores. *J Chem Phys* **124**, 104706, (2006).
210 Okazaki, T., Sakoh, M., Nagaoka, Y. & Asami, K. Ion channels of alamethicin dimer N-terminally linked by disulfide bond. *Biophys J* **85**, 267-273, (2003).
211 Fulinski, A., Kosinska, I. & Siwy, Z. Transport properties of nanopores in electrolyte solutions: the diffusional model and surface currents. *New J Phys* **7**, 132, (2005).
212 Radenovic, A., Trepagnier, E., Csencsits, R., Downing, K. H. & Liphardt, J. Fabrication of 10 nm diameter hydrocarbon nanopores. *Appl Phys Lett* **93**, 183101, (2008).
213 Beattie, J. K. The intrinsic charge on hydrophobic microfluidic substrates. *Lab Chip* **6**, 1409-1411, (2006).
214 Peter, C. & Hummer, G. Ion transport through membrane-spanning nanopores studied by molecular dynamics simulations and continuum electrostatics calculations. *Biophys J* **89**, 2222-2234, (2005).
215 Joseph, S., Mashl, R. J., Jakobsson, E. & Aluru, N. R. Electrolytic transport in modified carbon nanotubes. *Nano Lett* **3**, 1399-1403, (2003).
216 Zhou, Y. F., Morais-Cabral, J. H., Kaufman, A. & MacKinnon, R. Chemistry of ion coordination and hydration revealed by a K+ channel-Fab complex at 2.0 angstrom resolution. *Nature* **414**, 43-48, (2001).
217 Dellago, C., Naor, M. M. & Hummer, G. Proton transport through water-filled carbon nanotubes. *Physical Review Letters* **90**, 105902, (2003).
218 Nightingale, E. R. Phenomenological Theory of Ion Solvation - Effective Radii of Hydrated Ions. *Journal of Physical Chemistry* **63**, 1381-1387, (1959).
219 Wong, S. S., Joselevich, E., Woolley, A. T., Cheung, C. L. & Lieber, C. M. Covalently functionalized nanotubes as nanometre-sized probes in chemistry and biology. *Nature* **394**, 52-55, (1998).
220 Smeets, R. M. M., Keyser, U. F., Wu, M. Y., Dekker, N. H. & Dekker, C. Nanobubbles in solid-state nanopores. *Physical Review Letters* **97**, 088101, (2006).
221 Georgalis, Y., Kierzek, A. M. & Saenger, W. Cluster formation in aqueous electrolyte solutions observed by dynamic light scattering. *Journal of Physical Chemistry B* **104**, 3405-3406, (2000).
222 Berneche, S. & Roux, B. Energetics of ion conduction through the K+ channel. *Nature* **414**, 73-77, (2001).

223 Powell et al. observe oscillations from divalent ions precipitating at the pore mouth of a 2-6 nm Si nanopore. These oscillations are distinct from those observed in this work in that they are formed from an unstable (precipitating) system`, difficult to sustain without reversible formation and dissolution of the precipitates.
224 Powell, M. R. *et al.* Nanoprecipitation-assisted ion current oscillations. *Nature Nanotechnology* **3**, 51-57, (2008).
225 Alexiadis, A. & Kassinos, S. Molecular Simulation of Water in Carbon Nanotubes. *Chemical Reviews* **108**, 5014-5034, (2008).
226 Carrillo-Tripp, M., Saint-Martin, H. & Ortega-Blake, I. Minimalist molecular model for nanopore selectivity. *Physical Review Letters* **93**, 168104, (2004).
227 Carrillo-Tripp, M., Saint-Martin, H. & Ortega-Blake, I. A comparative study of the hydration of Na+ and K+ with refined polarizable model potentials. *Journal of Chemical Physics* **118**, 7062-7073, (2003).
228 Varma, S. & Rempe, S. B. Coordination numbers of alkali metal ions in aqueous solutions. *Biophysical Chemistry* **124**, 192-199, (2006).
229 Chen, Y. F., Ni, Z. H., Wang, G. M., Xu, D. Y. & Li, D. Y. Electroosmotic flow in nanotubes with high surface charge densities. *Nano Letters* **8**, 42-48, (2008).
230 Liu, H., Qian, S. Z. & Bau, H. H. The effect of translocating cylindrical particles on the ionic current through a nanopore. *Biophysical Journal* **92**, 1164-1177, (2007).
231 Wanunu, M., Sutin, J., McNally, B., Chow, A. & Meller, A. DNA Translocation Governed by Interactions with Solid-State Nanopores. *Biophysical Journal* **95**, 4716-4725, (2008).
232 Gillespie, D. T. Exact Stochastic Simulation of Coupled Chemical-Reactions. *Journal of Physical Chemistry* **81**, 2340-2361, (1977).
233 Pikovsky, A. S. & Kurths, J. Coherence resonance in a noise-driven excitable system. *Physical Review Letters* **78**, 775-778, (1997).
234 DeCoursey, T. E. & Cherny, V. V. Deuterium isotope effects on permeation and gating of proton channels in rat alveolar epithelium. *J Gen Physiol* **109**, 415-434, (1997).
235 Vijayvergiya, V. *et al.* Proton conductance of influenza virus M2 protein in planar lipid bilayers. *Biophys J* **87**, 1697-1704, (2004).
236 Mann, D. J. & Halls, M. D. Water Alignment and Proton Conduction inside Carbon Nanotubes. *Phys. Rev. Lett.* **90**, 195503, (2003).
237 DeCoursey, T. E. Voltage-Gated proton channels and other proton transfer pathways (vol 83, pg 475, 2003). *Physiol Rev* **84**, 1479-1479, (2004).
238 Cao, Z. *et al.* Mechanism of Fast Proton Transport along One-Dimensional Water Chains Confined in Carbon Nanotubes. *J Am Chem Soc* **132**, 11395-11397, (2010).
239 Mann, D. J. & Halls, M. D. Water alignment and proton conduction inside carbon nanotubes. *Phys Rev Lett* **90**, 195503, (2003).
240 Dellago, C., Naor, M. M. & Hummer, G. Proton transport through water-filled carbon nanotubes. *Phys Rev Lett* **90**, 105902, (2003).
241 Dellago, C., Naor, M. M. & Hummer, G. Proton transport through water-filled carbon nanotubes (vol 90, art no 105902, 2003). *Phys Rev Lett* **91**, 105902, (2003).
242 Majumder, M., Zhan, X., Andrews, R. & Hinds, B. J. Voltage gated carbon nanotube membranes. *Langmuir* **23**, 8624-8631, (2007).

243 Won, C. Y., Joseph, S. & Aluru, N. R. Effect of quantum partial charges on the structure and dynamics of water in single-walled carbon nanotubes. *J Chem Phys* **125**, 114701, (2006).
244 Choi, W., Lee, C. Y., Ham, M. H., Shimizu, S. & Strano, M. S. Dynamics of Simultaneous, Single Ion Transport through Two Single-Walled Carbon Nanotubes: Observation of a Three-State System. *J Am Chem Soc* **133**, 203-205, (2011).
245 Dellago, C., Naor, M. M. & Hummer, G. Proton transport through water-filled carbon nanotubes. *Phys Rev Lett* **90**, (2003).
246 Thomas, J. A. & McGaughey, A. J. H. Water Flow in Carbon Nanotubes: Transition to Subcontinuum Transport. *Phys Rev Lett* **102**, 184502, (2009).
247 Mann, D. J. & Halls, M. D. Water alignment and proton conduction inside carbon nanotubes. *Phys Rev Lett* **90**, 195503, (2003).
248 Yan, T. Y. *et al.* Mechanism of Fast Proton Transport along One-Dimensional Water Chains Confined in Carbon Nanotubes. *J Am Chem Soc* **132**, 11395-11397, (2010).
249 Qin, X. C., Yuan, Q. Z., Zhao, Y. P., Xie, S. B. & Liu, Z. F. Measurement of the Rate of Water Translocation through Carbon Nanotubes. *Nano Lett* **11**, 2173-2177, (2011).
250 Gong, X. J., Li, J. C., Xu, K., Wang, J. F. & Yang, H. A Controllable Molecular Sieve for Na(+) and K(+) Ions. *J Am Chem Soc* **132**, 1873-1877, (2010).
251 Shao, Q. *et al.* Anomalous Hydration Shell Order of Na(+) and K(+) inside Carbon Nanotubes. *Nano Lett* **9**, 989-994, (2009).
252 Liu, H. T., Steigerwald, M. L. & Nuckolls, C. Electrical Double Layer Catalyzed Wet-Etching of Silicon Dioxide. *J Am Chem Soc* **131**, 17034-17035, (2009).
253 Miller, S. A., Young, V. Y. & Martin, C. R. Electroosmotic flow in template-prepared carbon nanotube membranes. *J Am Chem Soc* **123**, 12335-12342, (2001).
254 Sen, Y. H. & Karnik, R. Investigating the translocation of lambda-DNA molecules through PDMS nanopores. *Anal Bioanal Chem* **394**, 437-446, (2009).
255 Xie, Y. H., Kong, Y., Soh, A. K. & Gao, H. J. Electric field-induced translocation of single-stranded DNA through a polarized carbon nanotube membrane. *J Chem Phys* **127**, 225101, (2007).
256 Pelta, J. *et al.* Dynamics of polyelectrolyte transport through a protein channel as a function of applied voltage. *Phys Rev Lett* **100**, 158302, (2008).
257 Duan, C. H. & Majumdar, A. Anomalous ion transport in 2-nm hydrophilic nanochannels. *Nat Nanotechnol* **5**, 848-852, (2010).
258 Choi, W., Abrahamson, J. T., Strano, J. M. & Strano, M. S. Carbon nanotube-guided thermopower waves. *Mater Today* **13**, 22-33, (2010).
259 Eklund, P. C., Holden, J. M. & Jishi, R. A. Vibrational-Modes of Carbon Nanotubes - Spectroscopy and Theory. *Carbon* **33**, 959-972, (1995).
260 Fantini, C. *et al.* Optical transition energies for carbon nanotubes from resonant Raman spectroscopy: Environment and temperature effects. *Phys Rev Lett* **93**, 147406, (2004).
261 Jorio, A. *et al.* Structural (n, m) determination of isolated single-wall carbon nanotubes by resonant Raman scattering. *Phys Rev Lett* **86**, 1118-1121, (2001).
262 Souza, A. G. *et al.* Stokes and anti-Stokes Raman spectra of small-diameter isolated carbon nanotubes. *Phys Rev B* **69**, 115428, (2004).
263 Duso, A. B. & Chen, D. D. Y. Proton and hydroxide ion mobility in capillary electrophoresis. *Anal Chem* **74**, 2938-2942, (2002).

264 Han, J. H., Zhou, X. Y. & Liu, H. T. Ab initio simulation on the mechanism of proton transport in water. *J Power Sources* **161**, 1420-1427, (2006).
265 Hanasaki, I. & Nakatani, A. Hydrogen bond dynamics and microscopic structure of confined water inside carbon nanotubes. *J Chem Phys* **124**, 174714, (2006).
266 Pan, C. F. *et al.* Nanowire-based high performance "micro fuel cell": One nanowire, one fuel cell. *Adv Mater* **20**, 1644-1648, (2008).
267 Bocquet, L. & Charlaix, E. Nanofluidics, from bulk to interfaces. *Chem Soc Rev* **39**, 1073-1095, (2010).
268 Daiguji, H. Ion transport in nanofluidic channels. *Chem Soc Rev* **39**, 901-911, (2010).
269 Takaiwa, D., Hatano, I., Koga, K. & Tanaka, H. Phase diagram of water in carbon nanotubes. *P Natl Acad Sci USA* **105**, 39-43, (2008).
270 Gauden, P. A. *et al.* Molecular dynamics of zigzag single walled carbon nanotube immersion in water. *Phys Chem Chem Phys* **13**, 5621-5629, (2011).
271 Mamontov, E. *et al.* Dynamics of water confined in single- and double-wall carbon nanotubes. *J Chem Phys* **124**, 194703, (2006).
272 Decoursey, T. E. Voltage-gated proton channels and other proton transfer pathways. *Physiol Rev* **83**, 475-579, (2003).
273 Dong, B., Gwee, L., Salas-de la Cruz, D., Winey, K. I. & Elabd, Y. A. Super Proton Conductive High-Purity Nafion Nanofibers. *Nano Lett* **10**, 3785-3790, (2010).
274 Wilson, S. M. & Jones, G. C. Investigation of the Grotthuss mechanism via water conductivity. *Abstr Pap Am Chem S* **221**, 222-222, (2001).
275 John A.K, E. W. P. *Stewart's Textbook of Acid-Base*. 2nd edition edn, (2009 Acidbase.org, 2009).

Appendix A: Control Experiments in the Device without SWNTs

Typical current traces with electrolyte in the device without SWNTs

To perform control experiments, we fabricated more than 30 devices without SWNTs. It is shown that current traces with electrolyte in the device without SWNTs predominantly construct flat baseline current. Although they fluctuate with the existence of external perturbation, current traces recover rapidly their original baseline current. At a few times during the measurement, the current level was maintained above or below the average of current traces. In these cases, a gradual increase or decrease in current traces was observed rather than sharp changes. It is due to a flow of ionic solutions through the leakage path of either epoxy or UV glue. The leakage path might be activated by the applied electric field or deactivated by impurities. Because the epoxy barrier did not form the straight, narrow hydrophobic channel, it would not shape multiple coulter states.

Figure A1. A typical current trace with 3M KCl in the device without SWNTs.

Variance of background and leakage currents and non-stochastic pore-blocking

It should be noted that the absolute magnitude of the baseline current without SWNTs is largely varied by the conditions of the epoxy barrier and UV glue in electrolyte and DI water. To minimize such background and leakage impedance, lower baseline current in the control device without SWNTs could be obtained by employing thicker and larger sealant barriers. In the case of 1mm epoxy barrier thickness, dominant baseline currents were approximately from 20 to 50

pA. However, some control devices establish a higher current level up to 500 pA. To elucidate this peculiar result, we compared the curing time for epoxy structures made out of SU-8 negative photo resist. Insufficient curing time leads to more leakage currents because of the solvent residue in the ultra-thick layer of SU-8 photo resist. In addition, imperfect sealing or wide spreading of UV glue generated an extremely large leakage path. In the case of high background and leakage impedance, without the presence of a SWNT, our devices showed no stochastic pore-blocking events.

Comparison of the absolute magnitude of baseline current in the devices with and without SWNTs

Devices using epoxy structures in the same batch, in general, maintained similar background and leakage current levels in control devices. To investigate the effects of SWNTs on the baseline current, devices with SWNTs are compared to those without SWNTs fabricated by epoxy structures in the same batch. Figure A2 illustrates that the device with many SWNTs (~13) obtain a higher current level than that of the device without SWNTs. Impurities in the device or the defect appearing during fabrication could make permanently or instantly blocked SWNTs. However, the baseline current upto 365 pA in a device with SWNTs is much larger than 32 pA in a device without SWNTs. It shows that a flow current through the interior of SWNTs is added to the background and leakage path in sealant barriers.

Figure A2. Comparison of the absolute magnitude of the current level in the devices without (a) SWNTs and (b) with SWNTs constructed by the epoxy structure in same batch.

Common artifacts 1 : False ground in a voltage clamp setup

In the course of control experiments, we observed two or more random state changes in a device without SWNTs. Figure A3a shows current traces in a device without SWNTs. Even when DI water is being used, current fluctuation can be found in the same device (Figure A3b).

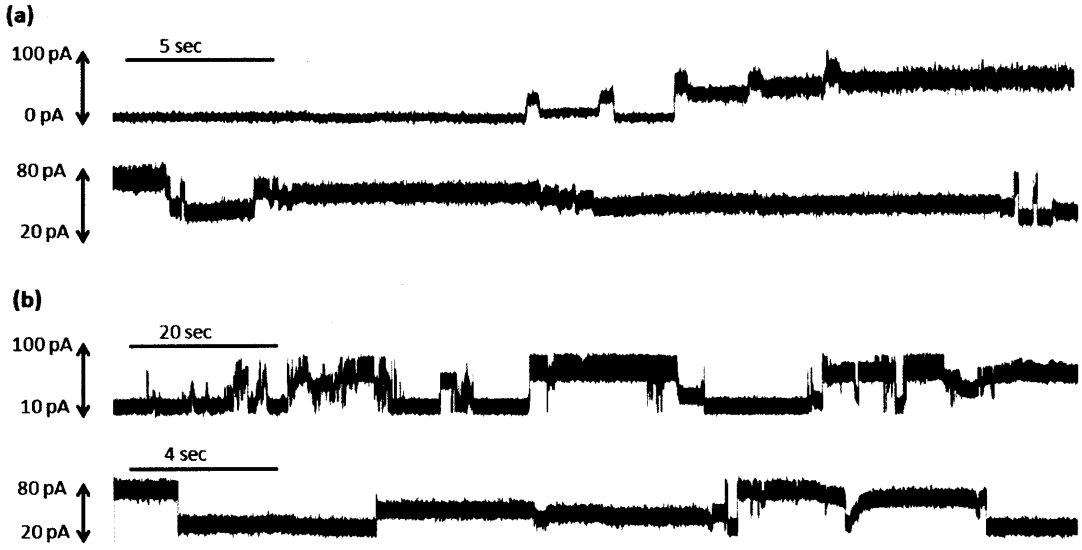

Figure A3. Changes of coulter states in a device without SWNTs in 3M KCl (a) and DI water (b).

These state changes in control devices can be explained by the false ground in the voltage clamp setup. The voltage clamp setup uses two electrodes (active electrode and ground). The ground electrode is connected to the substrate of the whole setup. To measure the accurate current level and apply only the electric field between two reservoirs, the device should be perfectly insulated from the ground. Nonconductive materials such as rubber pad can prohibit the false ground during experiments. However, when we measured current traces shown in Figure A3, no insulating material was used between the device and the substrate. Figure A4 shows the comparison between the voltage clamp setup without and with the rubber pad. In the case of no rubber pad (Figure A4a), we measured the shift of current traces as well as current fluctuation by means of the continuous perturbation from the false grounding situation. On the contrary, with the rubber pad (Figure A4b), both current shift and fluctuation disappeared. Therefore, the entire measurements for studying ion transport through a SWNT have been conducted with the insulating material between the device and the ground state, as shown in Figure A5.

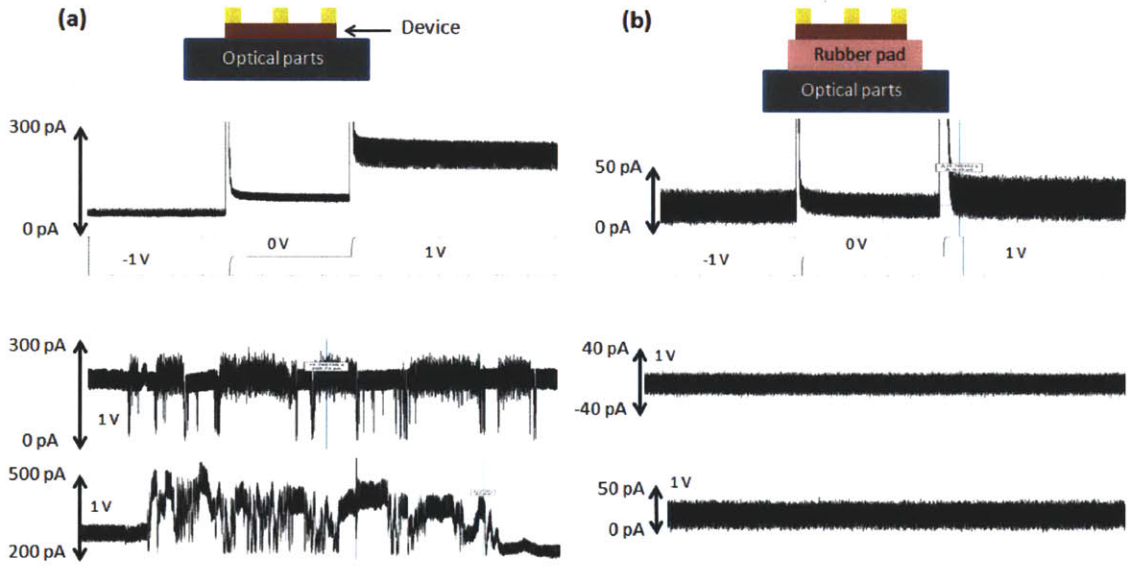

Figure A4. Comparison of the current traces (a) without a rubber pad (false grounding) and (b) with a rubber pad (Normal setup) between the device and the ground.

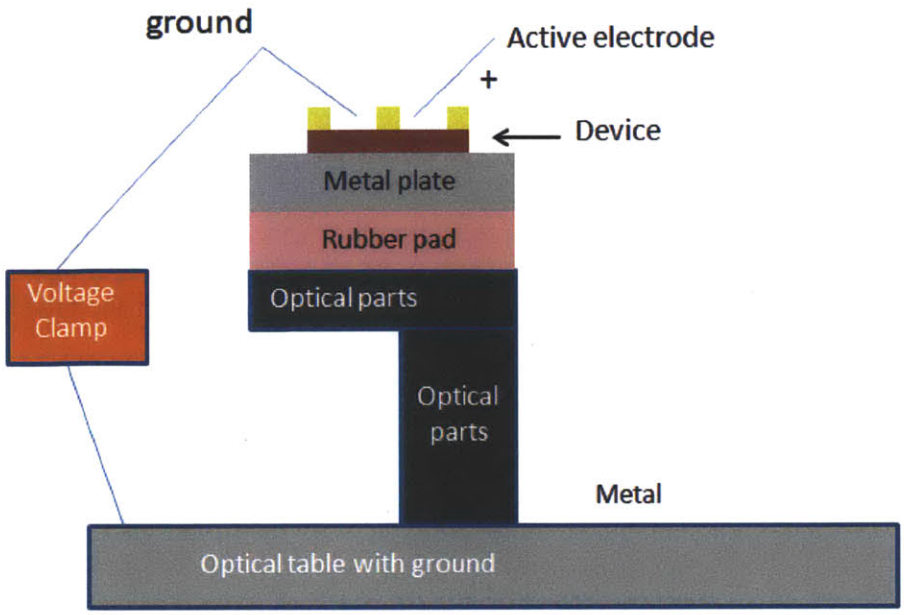

Figure A5. Schematic of the normal voltage clamp setup without the false grounding situation. The rubber pad was inserted to insulate between the device and the ground.

Common artifacts 2 : Disconnection between the anode and solutions

As a source of another artifact, the disconnection between the anode and ionic solutions or DI water could make the current fluctuation. Solutions in reservoirs of the device were evaporated during the measurement. When the measurement was taken above 40 minutes, a gradual decrease in the solution level in each reservoir was found. Figure A6 illustrates that the reduction in the solution level in each reservoir would cause the disconnection between the anode and the solution. When we observed this specific situation during the measurment, the curent was highly shifted up to 1500 pA, and it made the current fluctuation. In addition, the oscillation between contact and non-contact situations induced the repetitive change of current between the baseline current and the highly shifted current level. To prohibit this phenomenon, we have conducted our measurements for 30 minutes, and checked the stable connection at the end of each measurement.

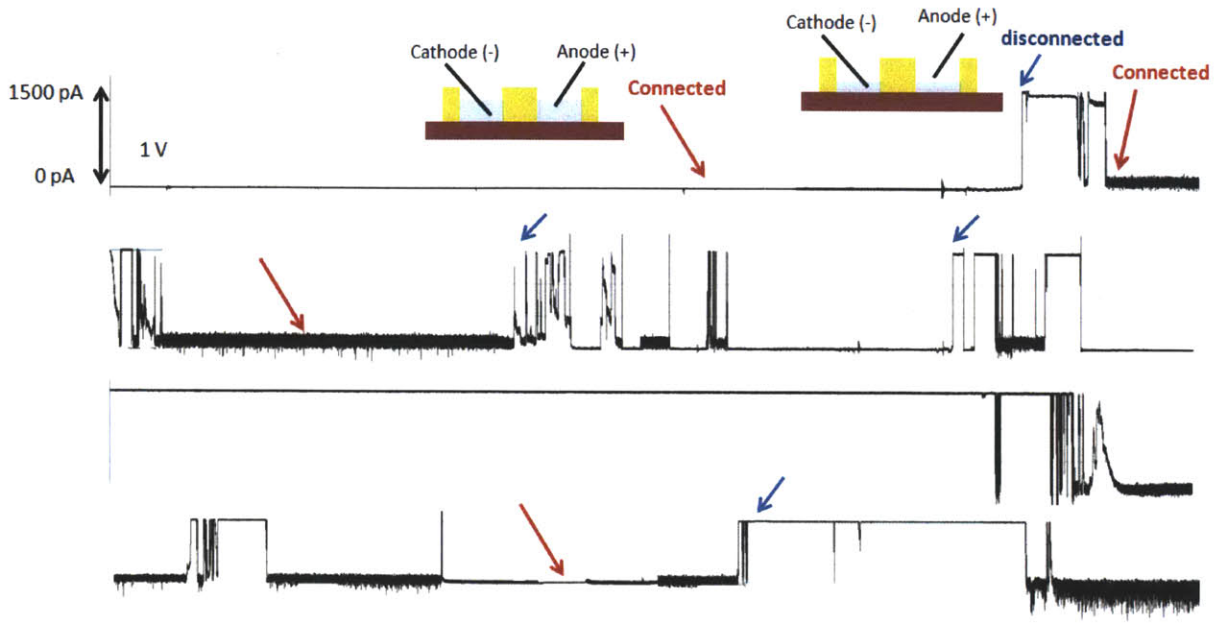

Figure A6. Shift of the current traces during the cycling the connection and disconnection between an anode and an ionic solution. Red and blue arrows indicate the situation of connection and disconnection, respectively.